Quantum-Degenerate Cesium: Atoms and Molecules

Dissertation

zur Erlangung des Doktorgrades an der
Fakultät für Mathematik, Informatik und Physik
der Leopold-Franzens-Universität Innsbruck

vorgelegt von

Jens Herbig

durchgeführt am Institut für Experimentalphysik
unter der Leitung von
Univ.-Prof. Dr. Rudolf Grimm

April 2005

Zusammenfassung

In einem Bose-Einstein Kondensat (BEC) aus Cäsium besteht die Möglichkeit, die Wechselwirkung zwischen den Atomen abzustimmen. Diese außergewöhnliche Eigenschaft entsteht durch die Kopplung an zahlreiche molekulare Zustände und durch das daraus resultierende Spektrum von Feshbach-Resonanzen bei einfach zugänglichen Magnetfeldern. In dieser Arbeit wurde ein BEC aus Cäsium-Atomen erzeugt, dessen Abstimmbarkeit in neuartigen Experimenten mit kondensierten Atomen und in der Erzeugung von ultrakalten Cs_2-Molekülen angewendet wird.

Zur Erzeugung des BECs verwenden wir optische Dipolfallen, um die Vorteile der Abstimmbarkeit auszunutzen. Mit einer Folge von zwei optischen Fallen erreichen wir sowohl gute Ladebedingungen als auch effiziente evaporative Kühlung. Die erste Falle wird durch zwei gekreuzte CO_2-Laser erzeugt. Das großvolumige Fallenpotential ist bestens geeignet, um eine große Zahl lasergekühlter Atome zu laden und dient als Reservoir für den nächsten Schritt: Ein stark fokussierter Laserstrahl erzeugt eine Mikrofalle im großvolumigen Fallenpotential. Diese Falle bietet die Möglichkeit einer effizienten Evaporation durch Absenken der Laserleistung des fokussierten Strahls. Mit dieser Strategie haben wir das erste Cäsium Bose-Einstein Kondensat realisiert. Durch eine Optimierung des Lade- und Evaporationsvorgangs können wir BECs mit mehr als 10^5 Atomen erzeugen, die einen idealen Ausgangspunkt für weiterführende Experimente darstellen. Wir zeigen die Abstimmbarkeit der Selbstwechselwirkung des Kondensats in Expansionsmessungen bei verschiedenen Streulängen. Durch Expansion am Nulldurchgang der Streulänge erzeugen wir ein „gefrorenes“ Kondensat mit einer fast verschwindenden Expansionsenergie von 50 pK.

Wir erzeugen ultrakalte Moleküle durch eine Magnetfeldrampe über eine Feshbach-Resonanz. Dadurch werden Atome aus dem BEC in den gebundenen molekularen Zustand überführt, der die Resonanz erzeugt. Um Moleküle und Atome räumlich zu trennen, legen wir ein magnetisches Gradientenfeld in vertikaler Richtung an. Durch eine umgekehrte Magnetfeldrampe können wir die Moleküle wieder in Atome dissozieren. Eine Abbildung der resultierenden Atome ergibt einen direkten Rückschluss auf die Dichteverteilung der reinen molekularen Wolke. Indem wir die Stärke des Gradientenfeldes anpassen, können wir die Schwerkraft für die Moleküle exakt kompensieren und zusätzlich das molekulare magnetische Moment präzise bestimmen. Die dadurch ermöglichten langen Beobachtungszeiträume erlauben uns die Messung sehr geringer Expansionsenergien, die die Annahme einer Quantenentartung der molekularen Wolke nahe legen. Eine genauere Untersuchung des Erzeugungsprozesses führt zu einer verbesserten Magnetfeldrampe mit einer Konversionseffizient von 30%, drei Mal höher als bisher mit konventionellen Rampen erreicht wurde. Wir können durch die Ausnutzung vermiedener Kreuzungen zwischen molekularen Zuständen die Moleküle in andere gebundene Zustände überführen. So ist es uns sogar möglich, Zustände mit hohem Drehimpuls zu bevölkern. Erste Experimente zeigen, dass wir die Moleküle in der CO_2-Laser Falle fangen können. Dies ist richtungweisend für die Realisierung eines gefangenen molekularen BECs.

Abstract

A Bose-Einstein condensate (BEC) of cesium atoms features extraordinary possibilities to control interatomic interactions. These outstanding properties result from various couplings to molecular states, which occur at easily accessible magnetic fields and show up in a rich spectrum of low-field Feshbach resonances. In the frame of this thesis, we create a BEC of cesium and exploit its tunability for new experiments on Cs atoms and in the creation of Cs_2 molecules.

To produce the BEC we employ an optical trapping approach to take full advantage of the tunability of cesium. With a sequence of two optical traps we realize good loading conditions as well as efficient evaporation. For the first optical trap, two crossed CO_2 lasers form a large volume trapping potential suited for loading a large number of pre-cooled atoms. This trap serves as a reservoir for the next step: A tightly focussed laser beam creates a "dimple" in the optical potential. In the dimple trap efficient evaporation can be performed by lowering the optical potential. With this strategy we were able to create the first BEC of cesium. Optimization of the loading and evaporation process yields a pure BEC with more than 10^5 atoms, which serves as a starting point for several experiments. We demonstrate the tunability of the mean-field interaction in the condensate by measuring the release energy as a function of the scattering lengths. By switching the scattering length to zero, we realize a non-expanding "frozen condensate" with an extremely low release energy corresponding to 50 pK.

We use the BEC to create ultracold Cs_2 molecules by applying a magnetic field ramp over a Feshbach resonance. The ramp transfers two colliding atoms into the molecular bound state that causes the resonance. We separate atoms from molecules in a Stern-Gerlach type scheme by applying a vertical magnetic field gradient. A reversed magnetic field ramp dissociates the molecules into atoms and allows to image the density distribution of the molecular sample. We precisely determine the molecular magnetic moment by matching the gradient field to exactly cancel the gravitational force for the molecules. We can thus monitor the dynamics of the molecular sample on extended time scales and observe ultra low expansion energies, consistent with the presence of a macroscopic molecular matter wave. A further investigation of the molecular creation process results in a novel magnetic field ramping scheme. The achieved conversion efficiency of 30% is a factor of three higher than obtained by conventional magnetic field ramps. In first experiments we transfer molecules to different internal molecular states using avoided level crossings. In this way we can populate a molecular state with high orbital angular momentum. Finally, we demonstrate trapping of molecules in the CO_2-laser trap, which offers a prospect for a trapped molecular BEC.

Laß die Moleküle rasen,
was sie auch zusammenknobeln!
Laß das Tüfteln, laß das Hobeln,
heilig halte die Ekstasen.

Christian Morgenstern (1871-1914)

Contents

1. Introduction

The early advances of physicists towards absolute zero temperature have soon been rewarded with imposing discoveries, such as superconductivity in 1911 and superfluidity in 1938 at temperatures of a few Kelvin. Another leap towards colder temperatures originated in the advent of laser cooling, which enabled the preparation of dilute clouds of atoms in the microkelvin range. This discovery was recognized with the nobel prize in 1997.

In this ultracold world the behavior of atoms is significantly different from that at room temperature. To characterize the system, classical physics has to give way to quantum mechanics, in which particles are treated as wave-packets. With lower temperature the extent of the wave-packet, the de Broglie wavelength, becomes larger, i.e. the wave character becomes more pronounced. In such quantum gases, the interatomic interaction can be characterized by a single parameter, the so called *s*-wave scattering length [Dal99c]. The intriguing potentiality that this interaction could be influenced by external fields, was offered by the observation of magnetic Feshbach resonances in ultracold atomic gases [Ino98]. This has been a point of intense, but rather disappointing study in room temperature atomic gases. A Feshbach resonance arises when the energy of a bound molecular state is brought into degeneracy with the total energy of two colliding atoms, normally by magnetic tuning. The scattering length varies dispersively around the resonance position. Feshbach resonances exist in most alkali species, but are typically found at fields as high as a few hundred Gauss as in ^{87}Rb [Mar02] or 900 G in Na [Ino98].

Ultracold gases were the first step towards another interesting phenomenon: In 1924 M. Bose and A. Einstein predicted an elusive new state of matter, a Bose-Einstein condensate (BEC). The pase transition to BEC is reached, when the atomic wave-packets start to overlap. However, the required temperatures are typically in the sub-microkelvin regime, which cannot be achieved by laser cooling techniques alone. Thus, to further cool the atoms, forced evaporative cooling has been implemented which relies on the evaporation of the most energetic particles. This led to the first experimental realization of a BEC of a dilute gas of ^{87}Rb in 1995 [And95], which again was rewarded with the nobel prize. The realization of BEC accomplished several long-standing goals. All atoms are in their motional ground state, thus subjecting them to ultimate control, only limited by Heisenbergs uncertainty relation. Furthermore, the creation of a coherent quantum sample, which implies that a BEC is to matter what a laser beam is to light: a coherent state in which the usually microscopic laws of

quantum mechanics govern the behavior of a macroscopic system. The field of Bose-Einstein condensation of dilute atomic gases has continued to progress rapidly, driven by the combination of new experimental techniques evolving along with theoretical advances. Using BECs, many exciting phenomena have been studied, such as atom laser [Mew97], four-wave mixing with matter waves [Den99] as well as observation of vortices [Mat99, Mad00] and solitons [Bur99, Den00, Kha02]. Furthermore, they have been used as a model system to address solid-state physics problems, e.g. the Mott-insulator phase [Gre02, Stö04].

Alkali atoms were and still are used in the majority of quantum optic experiments, since they have the simplest electronic structure, due to their single valence electron,. As a result of its good applicability in laser cooling, cesium was a prime candidate for BEC [Tie92]. Although other alkali species could soon be condensed, Cs did not follow until 8 years after the first realization of a BEC [Web03b]. Cesium exhibits exotic interaction properties. An unusually high two-body loss rate was detrimental for all experiments relying on evaporation in magnetic traps [Söd98, GO98]. But it also features a combination of broad and narrow Feshbach resonances at technically easily accessible magnetic fields of a few ten Gauss [Chi00]. This offers a great tunability of the interaction. In contrast to magnetic traps, an optical trapping approach allows trapping of the lowest internal quantum state of cesium which is immune to inelastic two-body processes, and also permits to fully exploit the tunability.

The unique tunability of Cs can be used to realize “designer condensates” where the interaction energy in the BEC can be externally adjusted. By tuning to an attractive or large repulsive interaction, imploding and exploding BECs can be realized. Even non interacting quantum matter, by tuning to zero scattering length, is possible. In this model system, the theoretical frontiers can be approached by studying the system at extreme values of the scattering length.

Molecules are composite objects and, in contrast to atoms, have a complex internal structure. They can possess permanent vector or tensor properties, such as electric dipole moments, rotational angular momentum, and even chirality. For the past few years, creating a molecular condensate has become one of the main targets in BEC physics. If such a condensate were made, it might reveal new molecular spectroscopy and collision physics, and could open the door to new applications in ultracold quantum chemistry, or even quantum computing [DeM02]. However, the laser cooling techniques developed for atoms do in practice not apply to molecules. Several avenues have been pursued, like cooling of molecules using a buffer gas [Wei98] as a “refrigerator”. Another approach is to start with an atomic BEC and convert it into molecules. In photo-association, laser light is used to transfer two colliding atoms into a molecular bound state [Wyn00]. An alternate route is to utilize the natural atom-molecule coupling, that arises from a Feshbach resonance [Don02]. Cesium with its many Feshbach resonances of different strength at low magnetic fields is a very good candidate for the Feshbach creation of molecules. Also here an optical trapping approach is advantageous since trapping of molecules has already been demonstrated in such a trap.

2. Basic Concepts

Our special interest in ultracold cesium is founded in its unusual properties, which include the tunability of the interaction and the possibility to create ultracold molecules but also frustrated many attempts towards Bose-Einstein condensation (BEC) of cesium. In Sec. 2.1 the basic concepts of interaction in ultracold gases are given, which will then be used to explain the unusual properties of cesium. After a review of the standard way to BEC, Sec. 2.2, the difficulties arising with cesium and our approach are summarized in Sec. 2.3. In Sec. 2.4 the properties of a BEC with tunable interaction are given.

2.1. Interactions in ultracold cesium

All experiments in this work are done using $^{133}_{55}$Cs, the only stable cesium isotope. With an average atomic mass of 132.905 amu and an atomic number of 55, it is the heaviest stable alkali atom. Of all atoms in the periodic table cesium has the lowest ionization energy of 3.894 eV, the largest polarizability of h 0.10 Hz/(V/cm)^2, where h denotes Planck's constant, and the strongest van der Waals interaction strength of 6859 atomic units, because its single valence electron is loosely bound. Due to its large mass and its single unpaired electron, cesium has a strong relativistic electron-nucleus coupling and a simple electronic scheme. The nuclear spin of $7/2$ together with the spin of the unpaired electron of $1/2$ make Cs a boson. Compared to other ultracold alkali gases, cesium shows an exotic scattering behavior, which will be explained throughout this section.

Scattering is a result of the interaction between two colliding particles. Such collision processes play a key role in the understanding of the properties of ultracold gases. Elastic collisions, lead to a redistribution of kinetic energy, which is important for evaporative cooling - the last cooling step for Bose-Einstein condensation. The interaction also determines the dynamics in and the density distribution of a Bose-Einstein condensate. For a detailed description of the basic principles I refer the reader to one of many review articles on this subject, e.g. [Dal99c].

To characterize scattering of ultracold atoms the complex interaction potential can be reduced to one parameter, the *s*-wave scattering length which will be defined in the following section, Sec. 2.1.1, and with some simple models its behavior will be illustrated. In the subsequent section, Sec. 2.1.2, the basic concepts of a Feshbach

resonance will be given, which has become an important tool to tune the interatomic interaction and for the formation of ultracold molecules. Feshbach resonances arise due to the coupling to molecular states, which is covered in Sec. 2.1.3 with special attention to the mechanism relevant for cesium. These concepts can then be used to explain the exotic scattering spectrum of cesium, including many Feshbach resonance, Sec. 2.1.4.

2.1.1. Concept of the scattering length

To describe the scattering of two particles the incident and the scattered particle wavefunctions can be decomposed into a radial part and a set of spherical harmonic functions with different angular momenta. All scattering experiments within this work are done with ^{133}Cs atoms at temperatures at or below 1 µK. To overcome the centrifugal barrier an energy of 192 µK is needed. Thus, for this low energy scattering only waves without orbital angular momentum, *s*-waves, contribute. Accordingly, the scattering cross-section for bosons becomes [Dal99c]

$$\sigma(k) = \frac{8\pi}{k^2} \sin^2 \delta_l(k) \quad \text{with} \quad a = -\lim_{k\to 0} \frac{\tan \delta_0(k)}{k}. \tag{2.1}$$

Here $\hbar k$ is the relative momentum between two particles. The parameter a is called the *s-wave scattering length*. This means that the complex interaction potential can be reduced to this one parameter a, from which the macroscopic behavior of the gas can be deduced.

A Taylor expansion of Eq. (2.1) including quadratic terms in k then gives

$$\sigma_0(k) = \frac{8\pi a^2}{1 + k^2 a^2} \tag{2.2}$$

for the elastic cross section at low energies. This leads to two asymptotic results for different limits:

$$ka \ll 1, \qquad \sigma(k) \simeq 8\pi a^2, \tag{2.3}$$

$$ka \gg 1, \qquad \sigma(k) \simeq 8\pi/k^2. \tag{2.4}$$

Eq. (2.3) is a simple formula for the limit for scattering at ultra-low energies (small k), while Eq. 2.4 describes scattering at higher energies or large values of the scattering length and gives the maximum value of the cross-section for *s*-wave scattering: the *unitarity limit*. Figure 2.1 shows the scattering length as described by (Eq. (2.2)), for the approximation at low energy (Eq. (2.3)), and for a more elaborate calculation including a correction for the effective range of the potential r_{eff} [Chi01a].

Behavior of the the scattering length

The physical meaning of the scattering length can be seen from the asymptotic behavior of the radial part of the wave function. For $r > b$ (outside the interaction region b),

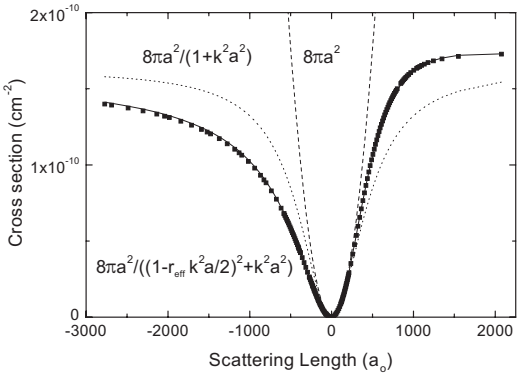

Figure 2.1.: The dependence of the elastic cross-section on the scattering length, given by different approximations. All coincide at small values of the scattering length. Figure taken from [Chi01a].

the wave function is $u_{k,0}(r) \propto \sin(kr + \delta_0(k))$. For small r the wave function resembles $u_{k,0}(r) \simeq kr \cos\delta_0(k) + \sin\delta_0(k)$. This wave function approximates a straight line with a zero-crossing at $a = -\tan\delta_0(k)/k$. Figure 2.2 shows the results of a detailed calculation of the scattering of two sodium atoms [Jul02] which illustrates the asymptotic behavior of the scattering wave function.

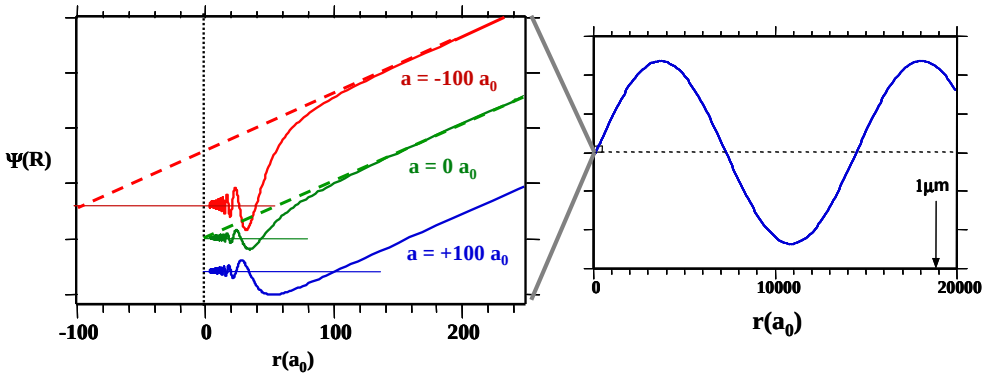

Figure 2.2.: Scattering wave function taken from [Jul02] of two sodium atoms colliding with an energy corresponding to 1.4 μK. The right side shows the wave function outside the range of interaction. The left side is a blow-up of the interaction region. The zero-crossing of the asymptotic wave function is the scattering length. Three different potentials result in three values for the scattering length.

Scattering length and bound states

Using a square potential where the potential is $-V(0)$ for $r < b$ and 0 for values $r \geq b$, the behavior of the scattering length can be analyzed quantitatively. The scattering

length at a given potential depth is [Dal99c]

$$a = b - \frac{\tan(k_0 b)}{k_0} \qquad \text{with} \qquad k_0 = \sqrt{2\mu b^2 V_0}/\hbar. \tag{2.5}$$

As shown in Fig. 2.3, the scattering length is always negative when the potential is

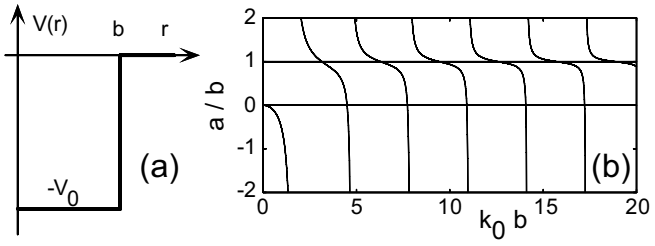

Figure 2.3.: (a) shows the shape of the model potential well with depth V_0. (b) shows the scattering length a as a function of the potential depth $k_0 = \sqrt{2\mu b^2 V_0}/\hbar$.

too small to support a bound state, i.e. $k_0 b < \pi/2$. When the depth of the potential well is increased, the scattering diverges whenever $k_0 b = (2n + 1)\pi/2$, that means whenever a new bound state appears in the potential well. This relation, the Levinson theorem, is quite general. These divergences of the scattering length are called *zero-energy resonances*. When the energy of the bound state is a little above (below) the potential well the scattering length is large and positive (negative). For weakly bound states, i.e. large positive scattering length, the binding energy of the last bound state can be calculated to be [Lan77]

$$E_B = -\frac{\hbar^2}{ma^2}. \tag{2.6}$$

Sign of the scattering length

Since the scattering cross-section is proportional to the square of the scattering length, the sign of a can not be deduced from collision experiments. However, the sign can be of significant importance, e.g. a stable BEC can only exist for positive scattering length. The box potential, as shown in Fig. 2.4, illustrates nicely the relation of the sign of the scattering length and the interaction. For $a \neq 0$ the bounding condition of the wave function is changed. For a positive scattering length the wave function is spatially compressed and the energy is higher. Therefore the particles repel each other: a positive scattering length means repulsive interaction. Analogously a negative scattering length implies attractive interaction.

2.1.2. Feshbach resonances

So far we have considered only elastic collisions of particles with no internal structure. With an internal structure inelastic collisions are also possible where the atoms

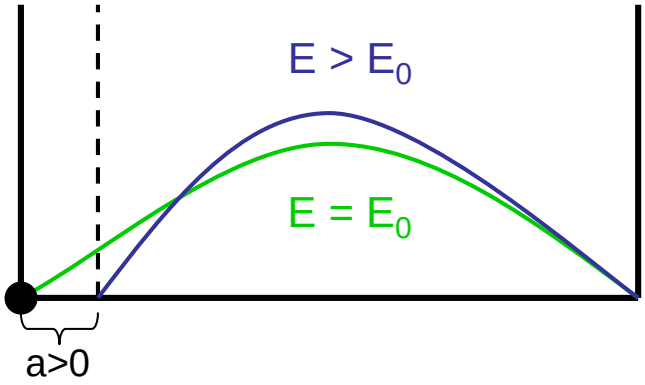

Figure 2.4.: The scattering wave function in a box potential. The left boundary is the scattering potential. For positive scattering length a the interaction energy E is higher than the energy without interaction E_0.

can change their internal state during the collision, provided that there is a coupling between the states. The incident and outgoing scattering wave functions experience a different interaction potential. These potentials are also called incident and outgoing channels. If the energy of an outgoing channel is lower than the total energy of the incident channel, inelastic exothermic collisions to those channels are possible. This channels are called an open channels. If the energy of the outgoing channel is higher, inelastic scattering to this channel is not possible. It is therefore called a closed channel. All experiments in this work are done with ^{133}Cs atoms in the absolute electronic ground state, $F = 3$, $m_F = 3$. Since the two colliding atoms have the lowest internal energy, there are no open channels available. However, closed channels can also alter the (elastic) scattering parameters dramatically.

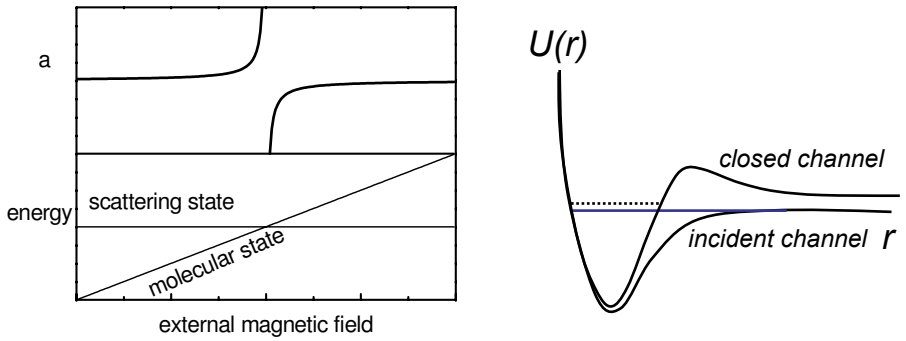

Figure 2.5.: By applying an external magnetic field, the molecular potential can be shifted and a molecular state can be brought into degeneracy with the scattering state. The scattering length a shows a dispersive behavior, a Feshbach resonance. Note that above the scattering continuum, the molecules are unstable and dissociate into free atoms.

Although the dissociation energy of a closed channel is higher than the total energy of the incident channel, a bound molecular state in this potential can have similar or, of

course, a lower energy than the incident channel. If this molecular state has a different magnetic moment compared to that of the incident state, the two states can be brought into degeneracy by applying an external magnetic field of the correct magnitude. When the molecular state is close to the scattering state, quasi-bound molecules are formed. The effect is similar to the zero-energy resonances described above: if the molecular state is close to but below (above) the energy of the incident state, the scattering length is large and positive (negative). This is called a *Feshbach resonance*. Named after Herman Feshbach, who used this model to describe scattering resonances in high-energy physics [Fes62], it was later adapted to explain resonant scattering phenomena in cold atomic collisions [Tie92]. In our case, i.e. in the absence of open channels, the Feshbach resonance only changes the elastic cross-section, if only binary collisions are considered.

The width ΔB of a Feshbach resonance is determined by the magnetic moment of the bound state and the coupling strength between the two states. If the scattering length far from the resonance is a_{bg} then the scattering length around the resonance position B_{res} can be calculated by

$$a(B) = a_{bg}\left(1 - \frac{\Delta B}{B - B_{res}}\right). \tag{2.7}$$

The coupling of the scattering state to a molecular state and the coupling between different internal molecular states leads also to avoided level crossings. For the coupling to the scattering continuum this shifts the observed resonance position depending on the coupling strength. From Fig. 2.5 it is obvious that the measured resonance position also depends on the position of the scattering state, i.e. the energy of the colliding particles. Measurements at different energies allow to extrapolate the position of the resonance for zero energy.

Feshbach resonances offer the possibility to adjust the scattering length and thus the interatomic interaction. This additional degree of freedom can be used to offer the experimentalist further control over experimental conditions. Examples include the optimization of the evaporation process by adapting the elastic cross-section, tuning the mean-field interaction in a BEC, or the production of ultracold molecules.

2.1.3. Coupling to molecular states

In the following the different coupling mechanisms between atomic and molecular states are discussed. More details can be found in [Mar03b, Chi01a]. At the magnetic fields used in the experiment the Zeeman splitting is always small compared to the hyperfine splitting, therefore the atomic scattering states can be labelled using the quantum numbers F of the total angular momentum $\boldsymbol{F}$ of one atom, and m_F the projection of $\boldsymbol{F}$ onto the axis of the magnetic field. For Cs atoms in the absolute internal ground-state these are $F = 3, m_F = 3$.

The Feshbach resonances in cesium can be labelled according to the molecular state which causes the resonance. The molecular states are identified by the following quantum numbers.

f**:** Quantum number of the internal angular momentum $\boldsymbol{f}$ of the molecule.

m_f**:** The projection of $\boldsymbol{f}$ on the magnetic field axis.

l : The quantum number of the molecular orbital angular momentum $\boldsymbol{l}$.

m_l : The projection of the molecular orbital angular momentum $\boldsymbol{l}$ on the magnetic field axis.

In all collisions in our experiment the incoming waves are s-waves. As will be explained below, coupling to molecular channels with $l = 0, 2, 4, 6, ...$ is, however, possible. Accordingly, the molecular states and the Feshbach resonances can be denominated $s-, d-, g-$ and $l-$wave states (resonances).

Coulomb interaction

The Coulomb interaction leads at very short interatomic distances to a repulsive wall in the interaction potential of the colliding atoms. At larger distances it is responsible for the splitting of the interaction potential in the triplet ($^1\Sigma_g^+$) and singlet potential ($^3\Sigma_u^+$). The fully stretched states ($F = 4, m_F = \pm 4$ in the cesium ground state) form a pure triplet potential. For scattering of atoms in other internal states, both potentials contribute. In Fig. 2.6 the singlet and triplet potential for Cs are displayed. Both poten-

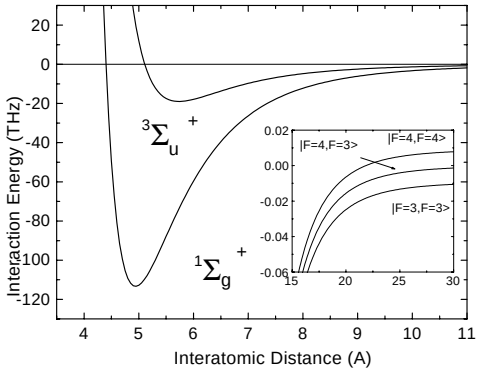

Figure 2.6.: The triplet and singlet potential for cesium atoms in the electronic ground state. The inset shows the energy splitting when one of the colliding atoms is in another hyperfine state. Figure adapted from [Chi01a].

tials can support molecular bound states. The asymptotes of the scattering potentials for atoms in different hyperfine states have an energy difference equal to the hyperfine splitting of the ground state. The degeneracy of the m_F magnetic sub-states is lifted in

the presence of an external magnetic field. Since the $F = 4, m_F = 4$ state has the highest energy, no bound states can exist above and consequently no Feshbach resonances are observed in this state [Chi01a]. For larger interatomic distances the potentials are dominated by the attractive van der Waals interaction.

For coupling to molecular states by the Coulomb interaction, l is conserved. Therefore atoms colliding in an s-wave ($l = 0$) state atoms can only couple to molecular s-wave states ($l = 0$).

Relativistic interactions

The weak relativistic interactions include the magnetic spin-spin dipole interaction and the second-order spin-orbit interaction. While in other alkali metals, e.g. rubidium, the two contributions have different signs and almost completely cancel, the second order spin-orbit term dominates in cesium [Chi01a, Kot00]. This coupling is responsible for the exotic scattering properties of cesium, described in the next section and the unusually high loss rates described in Sec.2.3.1.

For the spin-spin interaction only the total angular momentum is conserved, whereas the orbital angular momentum can change by $|\Delta l| = 0, 2$ [Thr93]. However, in the case of incoming s-waves the coupling from $l = 0 \rightarrow l = 0$ is forbidden [Mar03b]. Thus, in our case, spin-spin coupling leads to coupling to d-wave molecular states ($l = 2$).

The spin-orbit interaction can lead to a redistribution between spin and orbital angular momentum. This can lead to a coupling to molecular states with higher l. In the presence of a magnetic field only $M = m_f + m_l$ is conserved. This means that in our experiment two colliding atoms can couple to any state with $M = 6$. However, due to the higher order spin-orbit coupling g-wave resonances have a width of only a few milligauss [Chi04]. Resonances with higher l-states are expected to be even more narrow.

2.1.4. Scattering properties of cesium

The scattering behavior of the absolute electronic ground state of cesium, $F = 3, m_F = 3$, make it an interesting candidate for experiments with tunable atom interaction. The data on scattering properties and Feshbach resonances is taken from [Chi00, Leo00] and from a more recent and comprehensive collection [Chi04].

Since the two colliding cesium atoms can form a singlet or a triplet state, with the two electron spins aligned parallel or antiparallel. The resulting scattering potential is a combination of the singlet and triplet potential, depending on the projection of the states of the free atoms onto the potentials. The scattering length of cesium in the state $F = 3, m_F = 3$ is thus a combination of the singlet and triplet scattering length. In the analysis of the above mentioned data the deduced value for the singlet scattering

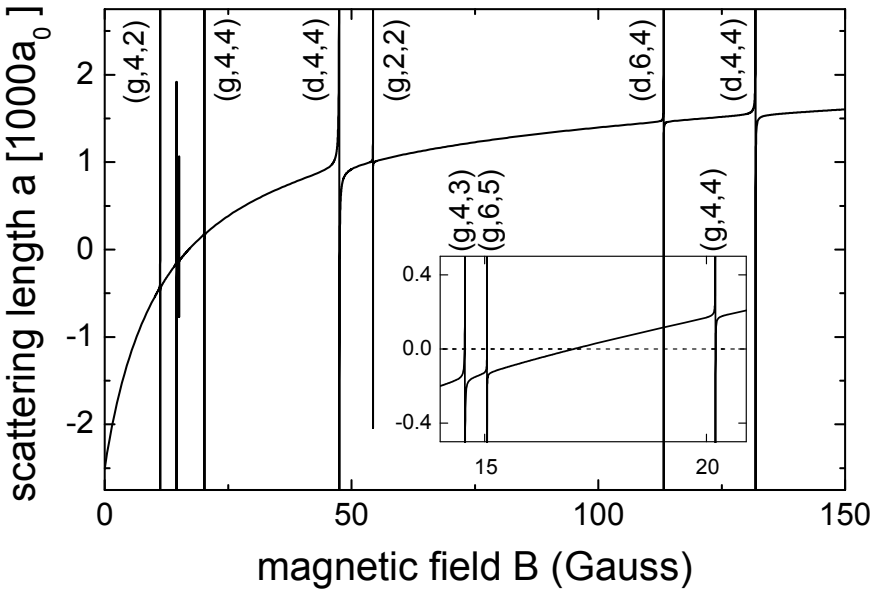

Figure 2.7.: Scattering length as a function of magnetic field for the state $F = 3, m_F = 3$. There is a Feshbach resonance at 48.0 G due to coupling to a d-wave molecular state. Several very narrow resonances at 11.0, 14.4, 15.0, 19.9 and 53.5 G are visible, which result from coupling to g-wave molecular states. The quantum numbers characterizing the molecular states are indicated, here as (l, f, m_f).

length is $a_S = 280.37\ a_0\ \pm 0.02\%$ and $a_T = 2440\ a_0\ \pm 1\%$ for the triplet scattering length[1].

Feshbach resonances in cesium

However, the scattering behavior for fields up to a few hundred Gauss is completely dominated by Feshbach resonances. As shown in Fig. 2.7 the scattering length varies from large negative values over a zero crossing at 17.064 G to large positive values. This behavior is caused by a large Feshbach resonance at ~ -5 G. The broad range of this variation (over a few ten Gauss) allows for precise tuning of the scattering length. This can be utilized to optimize the elastic cross-section in evaporative cooling. Above 17 G, in the range of positive scattering lengths, the interatomic interaction is repulsive, which is fundamental for a stable BEC. Narrower resonances can be used for fast tuning of the scattering length. In Fig. 2.7 one relatively broad resonance with a width of 120 mG is visible at 48.03(3) G. Since the g-wave resonances are induced by the higher-order spin-orbit interactions they show narrow resonance widths of a few mG, as expected. So far, a zoo of over 60 elastic and inelastic Feshbach resonances

[1] a_0 denotes Bohr's radius $1a_0 = 0.0529177$ nm.

has been discovered in cesium, some at relatively low magnetic fields. Even today the number is still growing, as a recent publication by [Mar04] shows.

Molecular bound states

To understand the complex behavior of the scattering length, as plotted in Fig. 2.7, we have to look below the dissociation continuum. As described in Sec. 2.1.2, a Feshbach resonance occurs when a molecular state is brought into degeneracy with the continuum by the application of an external magnetic field. From the measured resonance position it is possible to determine the energy structure of the molecular states below the dissociation continuum. The two plots in Fig. 2.8 show the energy difference be-

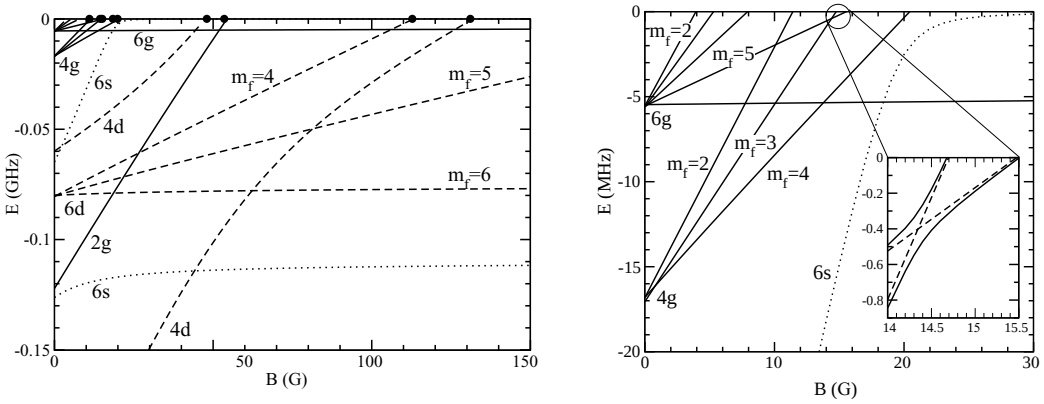

Figure 2.8.: The molecular binding energies of various molecular states are plotted as a function of magnetic field. The left plot covers the whole range from 0 to 150 G. The right plot is a blow up of the range up to 30 G; note the different energy scales. The inset in the right plot is a magnification of the avoided level crossing at ∼ 14.5 G. The plot is adapted from [Chi04]. The labelling of the states is explained in the text.

tween the bound states and the dissociation limit, i.e. the binding energy, as a function of magnetic field. The dissociation limit, the zero-line in the plots, constitutes the energy of two free particles in the state $F = 3$, $m_F = 3$. The molecular states in the figure are labelled with quantum numbers fl, according to the previous section. For the states $fl = 6d$ (left plot) and $4g$ (right plot), the different magnetic quantum numbers m_f are also displayed. The corresponding m_L quantum numbers can be calculated by $m_L + m_F = 6$.

Avoided crossings

The slope of the lines is directly related to the magnetic moment of each state at the given magnetic field. Some lines do not show the expected linear behavior. Their curved shape is due to broad avoided crossings of states with the same fl. This can shift the resonance position which would be expected without coupling, i.e. the $4d$

states in the left plot. Another remarkable feature is the $6s$ state which is shown in the left and right plot of the figure. This state has a binding energy of 65 MHz at zero magnetic field. It rises up to $\sim$ 20 G and then proceeds just below the dissociation limit. This has a strong influence on the scattering length of atoms in $F = 3, m_F = 3$. The slowly approaching state just below the continuum leads to a large and slowly growing scattering length above the zero crossing at 17 G, see Fig. 2.7. A weak coupling of states with different fl also leads to an avoided crossing, but in the case of $6g, m_f = 5$ and $4g, m_f = 3$ it does not necessarily shift the resonance position, as the inset in the left plot shows.

2.2. Standard way to BEC

In this section I will outline the important considerations which require attention in order to reach Bose-Einstein condensation. Since many comprehensive reviews on this topic have been published (e.g. [Ket99]), the focus will be on the topics relevant to this work.

Reaching the phase-space density for Bose-Einstein condensation by cooling methods that rely on the scattering of photons seems not to be possible [Ket99]. The standard path has been to collect and pre-cool atoms in a magneto optical trap, followed by other laser cooling techniques, e.g. optical molasses. The laser cooling mechanisms are not discussed here. Details can be found in various works [Ket99, Met99]. The last cooling step is done by evaporative cooling, which has been employed in the creation of all BECs produced to date.

2.2.1. Evaporative cooling

Evaporative cooling was first invented for hydrogen [Hes86] and was later adapted and used to cool a sample of alkali atoms [Dav95b]. Shortly after its first demonstration, it was used to create the first BEC [And95]. With this technique samples can be cooled over even orders of magnitude in phase-space density.

The pre-cooled sample is loaded into a conservative potential, which can be characterized[2] by the trap depth U and the trapping frequencies $\omega_{x,y,z}$. Evaporative cooling is done by the continuous removal of the high-energy tail of the thermal energy distribution of a trapped sample. The truncation parameter of the high-energy tail is defined as $\eta = U(t)/(k_B \times T)$. The removed atoms carry away more than the average in kinetic energy, effectively cooling the sample. Elastic collisions rethermalize the sample and constantly repopulate the high-energy tail. Without lowering the potential a "hot" sample evaporates typically until $T = U/(10k_B)$ is reached; this is called *plain evaporation*. To speed up the evaporation, the potential depth $U(t)$ is continually lowered (*forced evaporation*). The process can be optimized in discrete evaporation steps. Empirically, optimizing each step only for phase-space density is a dead end street: one is usually left with a a sample of only a few very cold atoms. Instead the efficiency of forced evaporation [Ket96] can be measured using the following formula

$$\epsilon \equiv \frac{\ln(D'/D)}{\ln(N/N')}. \tag{2.8}$$

Here, D and D' are the phase-space densities at the beginning and end of the evaporation step, while N and N' denote the respective particle numbers. The gain in phase-space density is compared to the number of lost atoms, on a logarithmic scale. In a typical experiment a value of $\epsilon \sim 2$ is reached. Two orders of magnitude in phase-space density are gained with a loss of 90 % of the atoms.

[2] For simplicity we assume a harmonic potential. Which is a good approximation in most experiments.

Elastic collisions

The elastic collision rate γ_{el} determines how fast the sample rethermalizes and thus how fast the potential can be lowered without sacrificing efficiency.

$$\gamma_{el} \quad = \bar{n} \cdot \sigma(\bar{v}_{rel}) \cdot \bar{v}_{rel} \quad \propto \quad \sigma(k) \cdot T^{-\frac{3}{2}} \cdot \omega^2 \tag{2.9}$$

The average density is denoted by $\bar{n}$ while $\bar{v}_{rel}$ is the mean relative velocity of the particles in the sample. The elastic collision rate depends on the temperature T, the elastic cross-section (see (Eq. 2.2)) and the average trap frequency $\omega = \sqrt[3]{\omega_x \omega_y \omega_t}$, see also [Ket96]. A Monte Carlo simulation of the process [Arn97] yields an estimate for the thermalization time

$$t_{th} \approx \frac{11}{\gamma_{el}}. \tag{2.10}$$

This means, the sample is in thermal equilibrium after 11 collisions.

Hydrodynamic regime

By adjusting the trapping frequencies or the scattering length, the elastic collision rate can be maximized. The upper limit for this is given by the unitarity limit, see Eq. (2.4). If the collision rate exceeds the trapping frequencies $\gamma_{el} > \omega_{x,y,z}$ the sample is in the *hydrodynamic regime*. The sample thermalizes locally fast, but the overall thermalization is no longer sped up. Working in the hydrodynamic regime is to be avoided since no improvement in thermalization is to be expected whereas three-body losses are increased. Additionally, if "hot" byproducts are generated (see Sec. 2.2.3 below) they have a higher possibility to collide with trapped atoms and thereby heat the sample.

Dimensionality of evaporation

Another important parameter determining the efficiency of the evaporation process is the solid angle under which atoms can escape from the trap. If, for example, the trap depth is lowered only in one dimension, atoms moving with a large kinetic energy in another direction are not removed. Therefore the cooling of other dimensions has to proceed through elastic collisions alone. Such a one-dimensional evaporation is less efficient. Again, in case of "hot" collision byproducts, the sample can be heated dramatically. To ensure an efficient evaporation it is fundamental to provide a large evaporation surface.

2.2.2. Standard trapping schemes

Magnetic traps

In most experiments up to now the trapping potential is created by magnetic fields, which can be conveniently produced by coils. The use of magnetic traps is limited to

the trapping of low-field seeking states, which are trapped in the local minimum of the magnetic field. High-field seeking states would require a local maximum of the field, which cannot be created [Win84]. Magnetic traps have the advantage that the potential depth can be effectively lowered using a radio-frequency knife [Ket96].

Optical traps

In optical dipole traps all magnetic sublevels of a species can be trapped, including high-field seekers and even molecules [Tak98]. For a comprehensive review on optical dipole traps see [Gri00]. Lowering the potential is usually accomplished by decreasing the laser intensity. The disadvantage here is that a lower intensity also leads to lower trap frequencies resulting in a lower elastic collision rate, see Eq. (2.9). This problem can be circumvented by simultaneously decreasing the trapping volume with a zoom-lens system, which requires a more complex setup [Han01].

Certain configurations of optical traps allow for the use of a rf-knife to selectively remove atoms. However, so far it has only been possible to implement one-dimensional rf-evaporation in an optical trap [Han01, Web03c], see also Sec. 3.7.1.

Gravitational sag

In both, optical and magnetic traps, the gravitational potential starts to play a role at low trap depths, i.e. at the end of the evaporation. Gravity tilts the trapping potential in the vertical direction, that means the trap depth is lower on the bottom side of the trap. The energetic particles can still escape through this "hole", but the evaporation becomes only one-dimensional. Lowering the trap depth faster to increase the evaporation surface would expel to many particles. By balancing the gravitational force it is possible to overcome this obstacle, see [Han01, Web03b, Kra04] and Sec. 3.2.6.

2.2.3. Loss and heating mechanisms

Without losses, which predominantly arise from inelastic collisions, evaporative cooling would be straightforward. In reality these losses reduce the efficiency of the evaporation. Therefore, the ratio between "good" elastic and "bad" inelastic collisions is crucial and determines the success of the procedure. Additionally, heating processes can counteract the evaporative cooling.

The main loss and heating mechanisms are described in the following.

Background gas collisions

Collisions with the room temperature background gas in the experimental chamber transfer a large momentum onto an atom, which is subsequently lost from the trap. This induces an exponential decay of the number of the trapped atoms, characterized by τ, the $1/e$ time-constant of this decay. Therefore the experimental setup has to provide a

sufficiently good vacuum so that this mechanism does not noticeably contribute on the time-scale of the evaporation.

Off-resonant scattering

In optical dipole traps the off-resonant scattering of photons can transfer momentum upon a trapped atom. If this momentum is large enough to kick the atom out of the trapping potential it leads to an exponential loss, a lower transferred momentum results in a "hot" particle, which can heat the sample.

Inelastic two-body processes

As outlined in the previous chapter, in a collision between two atoms the internal states can change. In this exothermic process potential energy is converted into kinetic energy[3]. Typically, this leads to the loss of both atoms involved due to the large amount of released energy or if the new internal state is no longer trapped.

The rate of inelastic binary collisions is proportional to the average density. The proportionality factor of this rate is K_2. The cross-section for binary collisions is proportional to a^2, as discussed in section 2.1.1.

Three-body losses

The rate of inelastic collisions involving three atoms is proportional to $\langle n^2 \rangle$, with a proportionality factor K_3. Such processes are only prominent at high density or in the absence of two-body loss. In such a three-body recombination process, three trapped atoms collide, two of them form a molecule while the third takes away the binding energy and momentum, according to momentum and energy conservation. The three-body rate scales with the scattering length as a^4. The experimental confirmation of this scaling law is part of this project, see [Web03c].

Normally all three atoms are lost from the trap. However, if the binding energy of the formed molecule is small enough, the third atom remains trapped and can heat the sample. This effect can be severe at very low temperatures.

Total loss rate

The total loss rate for a trapped gas is given by the differential equation

$$\frac{\dot{N}}{N} = -\frac{1}{\tau} - K_2 \langle n \rangle - K_3 \langle n^2 \rangle \tag{2.11}$$

where the average density is given by $\langle n \rangle = (1/N) \int n^2(\boldsymbol{r})\ d^3r$ and $\langle n^2 \rangle = (1/N) \int n^3(\boldsymbol{r})\ d^3r$. In a harmonic trap the peak density is given by $\hat{n} =$

[3] Endothermic processes are in principle possible. Here, kinetic energy is converted into internal energy. This process is energetically forbidden for scattering in the μK regime.

$(m\omega^2/(2\pi k_B T))^{3/2} N$, with the average trap frequency ω. This is related to the average density by $\langle n \rangle = \hat{n}/\sqrt{8}$ and $\langle n^2 \rangle = \hat{n}^2/\sqrt{27}$.

Anti-evaporation

All density dependent loss mechanisms cause heating by *anti-evaporation*. As opposed to evaporation, particles with an energy smaller than the average are lost from the center of the trap, because there the density reaches its maximum. Effectively, this leads to a higher temperature of the remaining atoms.

Parametric heating

Instabilities in the trap center or geometry (trap frequencies) can feed energy into the system. In magnetic traps this can be caused by fluctuations in the current. In optical traps the beam pointing, size or most likely the laser intensity can vary. In any case, mechanical vibrations of the setup can also cause this effect. This becomes dramatic when the frequency spectrum of the fluctuation has components close to any harmonics of the trap frequencies (*parametric heating*).

2.3. BEC of cesiums

Cesium is an atom of particular interest in physics. It has various important applications in fundamental metrology, such as measurements of the fine-structure constant [Hen00], the electric dipole moment of the electron [Chi01b], parity violation [Bou82], and the Earth's gravitational field [Sna98]. Furthermore, due to its large hyperfine splitting in the ground state, it serves as our primary frequency standard [BIP98]. By definition one second is 9192631770 periods of the microwave transition (9.19... GHz) of the ground state.

Cesium is very suitable for laser cooling applications, due to its large mass, the recoil energy is very low. This and the technical significance made cesium an interesting and the most promising candidate for Bose-Einstein condensation [Tie92]. However, the first successful attempt to condense Cs was part of this work, seven years after the first realization of Bose-Einstein condensation of ^{87}Rb atoms in 1995 [And95].

2.3.1. Review of earlier attempts

Early approaches towards BEC of Cs used magnetic traps to trap atoms in the low-field seeking hyperfine ground state $F = 4$ and magnetic sublevel $m_F = 4$. In this so called *stretched state*, the nuclear spin and the electron spin are aligned. In this state the destructive loss mechanism, the two-body spin-exchange collisions to the lower hyperfine state, are forbidden. Surprisingly, Dalibard and co-workers observed a spin relaxation rate that was three orders of magnitude higher than predicted [Söd98, Arl98]. A theoretical inspection of the problem [Leo98] concluded, that the high relaxation rates were caused by the second-order spin-orbit coupling, also called indirect spin-spin coupling. In contrast to Cs, no such effect was observed in ^{87}Rb because here the terms for direct and indirect spin-spin coupling partly cancel, as mentioned earlier. The relaxation rates are therefore much lower. In cesium the two terms also have opposite sign, but the second-order contribution is so much larger that it completely dominates the process [Mie96, Leo98].

In the lower hyperfine state the discussed hyperfine changing collisions are endothermic and are thus fully suppressed. This approach was followed by groups in Paris [GO98] and Oxford [Hop00]. Using the low-field seeking state $F = 3$ and magnetic sublevel $m_F = -3$ and operating at low magnetic bias fields of ~ 1 G the dipolar relaxation rates to other magnetic substates could be somewhat suppressed, but were still too high. The group in Paris raised the question "Is Bose-Einstein condensation of atomic cesium possible?", title of [GO98]. Both experiments were two orders of magnitude below the necessary phase-space density for BEC.

A conclusion of the observed unusually high inelastic two-body collisions is to completely evade this problem by working with the lowest internal ground state, $F = 3$, $m_F = 3$. As this is the lowest magnetic sublevel, which has no internal energy, inelastic two-body collisions are completely forbidden. Since this state is a high-field seeker, the use of magnetic traps was no longer possible. Therefore, optical dipole traps have

to be used, which trap atoms irrespective of their magnetic properties [Gri00]. This path has been pursued by various groups: in Berkeley [Han01] Weiss and co-workers used a similar setup to the one presented in this thesis. By implementing a radio-frequency evaporation scheme in an optical dipole trap, a phase-space density only a factor of two away from BEC was reached, but in the end the evaporation was limited by three-body loss [Wei02]. Also our group followed this approach by implementing a Gravito Optical Surface Trap (GOST) for cesium [Man99, Ham02]. In an experiment in Stanford an optical dipole trap was used to measure the collision properties of various internal states of cesium [Vul99].

Most experiments started when the scattering properties of cesium were poorly understood. An *ab initio* calculation of the scattering length for such a heavy atom is not possible and the experimental data was still fragmentary. Due to the experimental work of mainly the Stanford group [Vul99, Chi00] and subsequent theoretical analysis by Julienne and co-workers at NIST [Leo00], more information was gathered on the exotic scattering behavior of cesium, which has been presented in the previous section.

The new results for the state $F = 3$, $m_\mathrm{F} = -3$, which predict low relaxation rates at certain bias fields, encouraged Foot and co-workers in Oxford to continue the attempts of evaporating cesium in this state in a magnetic trap. This experiment reached a phase-space density which was only a factor of four away from BEC [Tho03]. Nevertheless, the efficiency at the end of the evaporation was not sufficient to succeed.

Additionally, the extended knowledge on the scattering behavior of cesium also helped in the creation of a two-dimensional cesium BEC in the above mentioned GOST-experiment [Ryc04].

2.3.2. Our scheme

The knowledge about the scattering properties of cesium was fundamental for the design of our experiment. We employ an optical trapping approach to trap and cool the absolute internal ground-state of cesium, $F = 3$, $m_F = 3$. However, omitting the standard magnetic trap leaves a serious concern with regard to loading a pre-cooled sample to the final optical trap. Direct loading of an optical trap produces a small condensate with typically 10^4 atoms compared to 10^6 condensed atoms in typical magnetic traps. Our strategy to achieving large condensates is thus to employ a sequence of optical traps in such a way that the loading from one stage to the next can be performed efficiently.

For pre-cooling we employ several standard techniques which in combination allow for an excellent loading of the first optical dipole trap. This trap is created by two weakly focussed crossed CO_2-laser beams. The large detuning of the lasers implies negligible heating due to low photon scattering rates. In the vertical axis the optical potential is too weak to hold atoms against gravity. With an additional magnetic levitation field, gravity is exactly balanced for one magnetic substate. In this way a large and shallow optical dipole trap with inherent spin-polarization is realized. The trap provides excellent loading due to a large phase-space overlap with the pre-cooled sample.

The low density in the trap suppresses higher order loss processes such as three-body recombination. This trap serves as a reservoir for loading the second optical dipole trap.

For efficient evaporation we transfer the atoms to a tighter optical dipole trap. A tightly focussed red-detuned laser beam creates a dimple in the optical potential. This dimple is loaded by elastic collisions with atoms from the larger reservoir. The density in the tight trap becomes high while the temperature remains almost constant due to the thermal contact with the reservoir. After the loading of the dimple trap, forced evaporation can be realized by decreasing the laser power in the dimple beam. This evaporation is almost three-dimensional and thus very efficient. Additionally, the evaporation is aided by the magnetic levitation field which prohibits gravitational sag. The large evaporation surface provides a quick removal of "hot" byproducts, created in three-body recombination processes, which would otherwise limit the cooling process, as discussed in Sec. 2.2.1. The optical dimple trap provides all the flexibility to explore the tunability of the self-interaction of the BEC: The trapping potential can be easily varied and the magnetic offset field is a free parameter in order to change the scattering length.

Through the whole process the elastic collision rates can be optimized by magnetic tuning of the scattering length. In the presence of the levitation field time-of-flight measurements can be carried out with long observation times of several hundred milliseconds.

2.4. Properties of a tunable BEC

One of the most intriguing phenomena in quantum mechanics is Bose-Einstein condensation (BEC), the so called "fifth state of matter". It was predicted by M. Bose [Bos24] and A. Einstein [Ein25] and can be derived from basic quantum mechanical statistics. In an atomic BEC an ensemble of atoms (bosons) constitutes a coherent macroscopic matter wave, strikingly demonstrating the wave nature of matter.

After the first realization of Bose-Einstein condensation in a dilute atomic gas of ^{87}Rb in 1995 by [And95] other alkali metals followed: ^{23}Na [Dav95a] and ^{7}Li [Bra95] in 1995, hydrogen in 1998 [Fri98], ^{85}Rb in 2000 [Cor00], ^{41}K in 2001 [Mod01] and more recently ^{133}Cs in 2002 [Web03b]. Also, BEC of non-alkali species such as metastable ^{4}He in 2001 [Rob01], ^{174}Yb in 2003 [Tak03] and recently ^{52}Cr [Gri] have been observed.

A number of review articles [Ket99, Dal99b, Cor99, Pit99] and comprehensive textbooks, for instance [Pit03], have been published on this topic. Here, I will briefly outline the basic concepts of a BEC and how it can be derived from quantum statistics. The properties of an atomic BEC in certain limits are given with special attention to an atomic BEC with a tunable interaction, since cesium offers this interesting possibility.

2.4.1. Origin of BEC

Simple model

Bose-Einstein condensation can be illustrated using a simple model. At room temperature atoms behave like point-like particles. Due to Heisenbergs uncertainty principle,

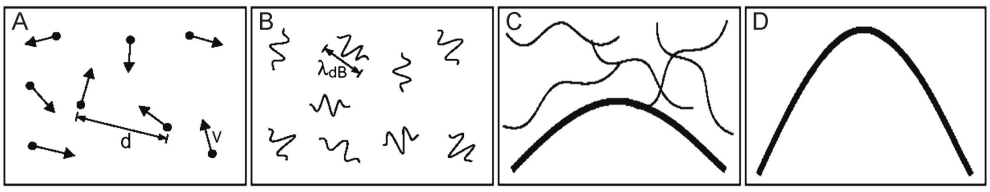

Figure 2.9.: The behavior of particles at different temperatures is illustrated. A) at room-temperature the particles behave as point-like objects. B) At low temperatures the wave nature of the particles starts to play a role. When the wave packets start to overlap at lower temperatures, the onset of BEC is reached (C) until all particles are in a BEC and form a coherent matter wave (D). Figure adapted from [Ket99].

a high velocity (high temperature) implies a well defined localization, see Fig. 2.9 A. Lowering the temperature leads to a higher uncertainty in the localization and the atoms are better described as wave packets (see Fig. 2.9 B) with the characteristic

thermal de Broglie wave length, λ_{dB}.

$$\lambda_{\mathrm{dB}} = \sqrt{\frac{2\pi\hbar^2}{mk_BT}}, \tag{2.12}$$

were T is the temperature of the gas and m the mass of the particles. The extent of the wave packet is thus given by the temperature, i.e. the momentum, of the particle. The volume occupied by the wave functions of an ensemble of cold atoms is known as the phase-space density D

$$D = \hat{n}\lambda_{\mathrm{dB}}^3. \tag{2.13}$$

This is the peak density of the ensemble $\hat{n}$ multiplied by the extent of the wave function. If the wave functions start to overlap ($D \sim 1$, Fig. 2.9 C), a phase transition occurs and the individual wave functions collapse into a single macroscopic one. This is the wave function of the Bose-Einstein condensate. At zero temperature all the particles are condensed, see Fig. 2.9 D.

Quantum statistical derivation

For an appropriate quantum statistical approach we consider a gas of bosons with temperature T. Following Bose statistics, the occupation number of a single atom state is given by

$$N_\nu = \frac{1}{e^{(\varepsilon_\nu-\mu)/(k_BT)} - 1}, \tag{2.14}$$

with ε_ν being the energy of this state and μ the chemical potential. For a given temperature μ is fixed by

$$N = \sum_\nu N_\nu. \tag{2.15}$$

At high temperatures the atoms are distributed among many states and the occupation number of any given state is much less than one, $N_\nu \ll 1$, which implies $\mu \ll \varepsilon_\nu$. Furthermore, Eq. (2.14) also provides the physical constraint $\mu < \varepsilon_0$. A chemical potential equal to the energy in the ground state ($\nu = 0$) would lead to a diverging or negative occupation number, which is in practice impossible. Nevertheless, this is the mechanism behind Bose-Einstein condensation. To avoid the diverging particle numbers in the ground state, we split the sum in Eq. (2.15) into two parts: N_0, the occupation number in the ground state, and N_{th} the sum over all other states, also called the *thermal component*.

$$N = N_0 + N_{\mathrm{th}} = N_0 + \sum_{\nu=1}^{\infty} \frac{1}{e^{(\varepsilon_\nu-\mu)/(k_BT)} - 1}. \tag{2.16}$$

When the particle number is kept constant, a change in temperature implies a change in μ in order to fulfill Eq. (2.15), i.e. when the temperature is lowered, μ has to increase in value. Let us consider N_{th} when the temperature is lowered and therefore $\mu \to \varepsilon_0$.

At a certain temperature N_{th} drops far below N, this is called the *critical temperature* T_c. This implies that the "missing" atoms have to be in the ground state (N_0), in order to fulfill Eq. (2.15). This is the onset of Bose-Einstein condensation: the macroscopic occupation of the ground state. When the temperature drops further below T_c, the occupation number in the ground state N_0 can become very large, until $N_0 = N$ is reached.

2.4.2. BEC in a harmonic trap

Assuming a three-dimensional harmonic trapping potential, the conditions for Bose-Einstein condensation can be calculated. A useful expression for the critical temperature is

$$T_c \approx 4.5 \left(\frac{\omega/2\pi}{100\ \mathrm{Hz}} \right) N^{1/3}\ \mathrm{nK}. \tag{2.17}$$

This equation is adapted from [Sak94]. We use $\omega \equiv \sqrt[3]{\omega_x \omega_y \omega_z}$ as the average trap frequency. The critical temperature depends on the trap frequencies and the particle number. Since both can vary during the (evaporative) cooling process, the critical temperature is not a constant.

Using the expression for the peak density $\hat{n}$ in the trap:

$$\hat{n} = N\omega^3 \left(\frac{m}{2\pi k_B T} \right)^{3/2}, \tag{2.18}$$

we can express the phase space density in Eq. (2.13) in the above defined terms.

$$D = N \left(\frac{\hbar\omega}{k_B T} \right)^3. \tag{2.19}$$

However, temperatures T close to or below T_c [Dal99b] uses a semiclassical approximation to calculate the density n_{th} of a gas of thermal bosons in a trap.

$$n_{\mathrm{th}}(\boldsymbol{r}) = \lambda_{\mathrm{dB}}^{-3}\, g_{3/2}(e^{-V_{\mathrm{ext}}(\boldsymbol{r})/(k_B T)}) \quad \text{for} \quad T \lesssim T_c, \tag{2.20}$$

with the corresponding peak density $\hat{n} = n_{\mathrm{th}}(\boldsymbol{r} = 0)$. Here $g_{3/2}(\boldsymbol{r})$ is a function of the form $g_a(z) = \sum_{n=1}^{\infty} z^n/n^a$ and $V_{\mathrm{ext}}(\boldsymbol{r})$ is the trapping potential. Using the critical temperature (Eq. (2.17)) to calculate the critical phase space density, we get

$$D_c \approx 2.612. \tag{2.21}$$

It is remarkable that this is similar to the value ~ 1 we derived earlier from a simple model.

By integrating Eq. (2.20) over space, a useful expression for the fraction of condensed atoms can be derived

$$\frac{N_0}{N} = 1 - \left(\frac{T}{T_c} \right)^3. \tag{2.22}$$

This means that the number of particles in the ground state becomes macroscopic at low temperatures ($T \ll T_c$). However, this is different from the microscopic criterion for the occupation of the ground state $k_B T < \varepsilon_1 - \varepsilon_0$, which would be much harder to achieve.

So far the calculations have not taken the interaction between the particles into account. However, the corrections, for e.g. the critical temperature, are only of the order of a few percent [Pet02, Bon02].

Ideal gas condensate

In the absence of any interaction between the atoms, the BEC constitutes an ideal gas with all atoms in the ground state of the harmonic trapping potential $U(\boldsymbol{r})$. This is described by the ground state wave function of a three-dimensional harmonic oscillator:

$$\phi(\boldsymbol{r}) = \left(\frac{m\omega}{\pi\hbar}\right)^{3/4} \exp\left(-\frac{m}{2\hbar}(\omega_x x^2 + \omega_y y^2 + \omega_z z^2)\right). \tag{2.23}$$

The shape of the density distribution of the condensate, determined by $n(\boldsymbol{r}) = \phi^2(\boldsymbol{r})$ is a three-dimensional Gaussian with the extension $\sigma_i = a_{\mathrm{ho},i} = \sqrt{\hbar/(m\omega_i)}$, where $i = x, y, z$ and a_{ho}. The average harmonic oscillator length is a useful length scale in the system, where ω is the average trap frequency:

$$a_{\mathrm{ho}} = \sqrt{\frac{\hbar}{m\omega}} \qquad \approx 8.72\ \mu\mathrm{m} \Big/ \sqrt{\frac{\omega}{2\pi}/\mathrm{Hz}}\ \text{ for } {}^{133}\mathrm{Cs}. \tag{2.24}$$

The momentum spread is then determined by the Heisenberg uncertainty relation to be

$$\sigma_{p_i} = \frac{\hbar}{\sigma_i} = \frac{\hbar}{a_{\mathrm{ho},i}} = \sqrt{\hbar m \omega_i}. \tag{2.25}$$

The average release energy per particle for a non-interacting BEC is therefore given by

$$E_{\mathrm{rel}} = \frac{1}{2}\hbar(\omega_x + \omega_y + \omega_z), \tag{2.26}$$

which is independent of N.

Bogoliubov approximation

To directly calculate the properties of a BEC of interacting particles, the many body hamiltonian for N particles in an external potential can be used. For systems with a large N this is very tedious and impractical. To circumvent this problem, Bogoliubov formulated a *mean-field description* of a dilute Bose gas [Bog47]. The generalization of this description is

$$\hat{\Psi}(\boldsymbol{r}, t) = \Phi(\boldsymbol{r}, t) + \hat{\Psi}'(\boldsymbol{r}, t). \tag{2.27}$$

The field operator $\hat{\Psi}(\boldsymbol{r}, t)$ is decomposed into the complex function $\Phi(\boldsymbol{r}, t)$, defined by the expectation value of the field operator $\Phi(\boldsymbol{r}, t) = \langle\hat{\Psi}(\boldsymbol{r}, t)\rangle$, and $\hat{\Psi}'(\boldsymbol{r}, t)$ which can be regarded as a first order perturbation term. The density distribution of the condensate is given by $n(\boldsymbol{r}, t) = |\Phi(\boldsymbol{r}, t)|^2$. Φ is often called the *wave function of the condensate*.

Gross-Pitaevskii equation

In a dilute gas the main contribution of particle interaction arises from binary collisions. The condition for a dilute or weakly interacting system is given by $n|a|^3 \ll 1$, with n being the average density and a being the scattering length (Sec. 2.1.1). The independently developed ansatz of Gross and Pitaevskii [Gro61, Pit61], substitutes the interaction potential between the particles by an effective interaction potential

$$V(\boldsymbol{r} - \boldsymbol{r}') = g\delta(\boldsymbol{r} - \boldsymbol{r}') \quad \text{with} \quad g = \frac{4\pi\hbar^2 a}{m}, \tag{2.28}$$

where, a is the scattering-length. For $T \ll T_C$ the term $\hat{\Psi}'$ can be neglected, and thus $\hat{\Psi}$ can be replaced by Φ. Writing Φ as $\phi(\boldsymbol{r}, t)e^{(-i\mu t/\hbar)}$ results in a time dependent variant of the *Gross-Pitaevskii equation*:

$$\left(-\frac{\hbar^2\nabla^2}{2m} + U(\boldsymbol{r}) + g\phi^2(\boldsymbol{r})\right)\phi(\boldsymbol{r}) = \mu\phi(\boldsymbol{r}). \tag{2.29}$$

Due to the nonlinear term $\phi^2 = n(\boldsymbol{r})$, this has the form of a "nonlinear Schrödinger equation". Without any interaction, $g = 0$, it reduces to the usual Schrödinger equation.

The energy in the ground state is a function of the density.

$$E[n] = \int d\boldsymbol{r}\left[\frac{\hbar^2}{2m}|\nabla\sqrt{n}|^2 + nU(\boldsymbol{r}) + \frac{gn^2}{2}\right] = E_{\text{kin}} + E_{\text{ho}} + E_{\text{int}} \tag{2.30}$$

The different terms can be be distinguished:

E_{kin} This term corresponds to the quantum kinetic energy which derives from the uncertainty principle. It is often referred to as "quantum pressure".

E_{ho} The harmonic oscillator energy is the potential energy in the system.

E_{int} The mean-field energy, arising from the interaction between the particles.

A useful expression is found by directly integrating Eq. (2.29) which relates the chemical potential to the different energy contributions:

$$\mu = \frac{E_{\text{kin}} + E_{\text{ho}} + 2E_{\text{int}}}{N}. \tag{2.31}$$

By summing up the energies in different directions [Dal99b] derives a viral relation for the energies:

$$2E_{\text{kin}} - 2E_{\text{ho}} + 3E_{\text{int}} = 0. \tag{2.32}$$

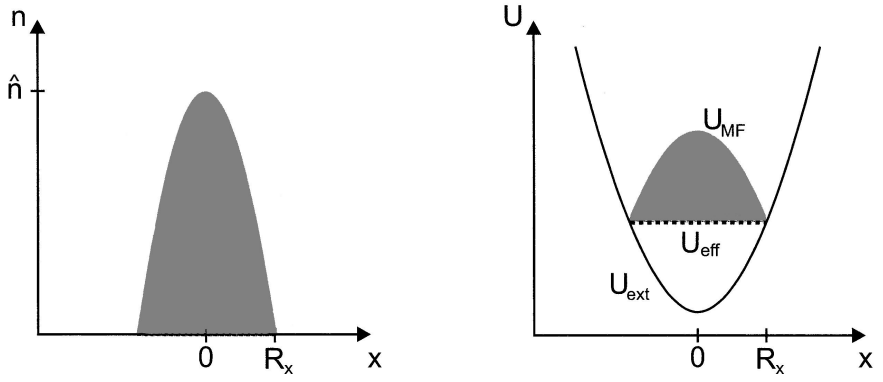

Figure 2.10.: (*Left*) Density distribution of a BEC in the TF limit in a harmonic potential. The point where the density distribution reaches zero defines the Thomas-Fermi radius R_x. (*Right*) The mean field potential U_{MF} resembles the shape of the external potential U_{ext}. Together they add up to an effective potential U_{eff}. Figure taken from [Bon02].

The energy of the BEC can be measured by instantly switching off the trapping potential and integrating over the observed velocity distribution. At the first phase of the expansion both the quantum kinetic energy and the mean-field energy are converted into expansion energy. The measured *release energy* therefore consists of two components.

$$E_{\mathrm{rel}} = E_{\mathrm{kin}} + E_{\mathrm{int}} \tag{2.33}$$

2.4.3. BEC in the Thomas-Fermi limit

For an interacting Bose gas the density distribution can differ significantly from a Gaussian. A repulsive interaction ($a > 0$) will lead to a lower density in the center. A useful expression to estimate the influence of interatomic interaction is

$$\frac{E_{\mathrm{int}}}{E_{\mathrm{kin}}} = \frac{N|a|}{a_{\mathrm{ho}}}. \tag{2.34}$$

Under typical experimental conditions, this ratio is much larger than one. Consequently the quantum kinetic energy E_{kin} does not noticeably affect the system. In the *Thomas-Fermi approximation* (TF) the term representing E_{kin} is set to zero in the Gross-Pitaevskii equation, Eq. (2.29). Solving for ϕ we obtain the following expression for the density:

$$n(\boldsymbol{r}) = \begin{cases} \dfrac{\mu - U(\boldsymbol{r})}{g} & \text{for } \mu - U(\boldsymbol{r}) > 0, \\ 0 & \text{otherwise.} \end{cases} \tag{2.35}$$

In figure 2.10 the behavior of the density for a BEC in the TF approximation is dis-

played. The density reflects the shape of the potential. For a harmonic potential this is an inverted parabola. The classical turning points for which the density vanishes ($\mu = U(\boldsymbol{r})$) are the Thomas-Fermi radii R_{TF}:

$$R_{\mathrm{TF}i} = \sqrt{\frac{2\mu}{m\omega_i^2}} = a_{\mathrm{ho}} \frac{\bar{\omega}}{\omega_i} \left(\frac{15Na}{a_{\mathrm{ho}}} \right)^{1/5}, \tag{2.36}$$

where $i = x, y, z$ denotes the respective axis with a trap frequency of ω_i.

The peak density in the center of the trap $\hat{n}$ can be read directly from Eq. (2.35) by inserting $U(\boldsymbol{r} = \boldsymbol{0}) = 0$

$$\hat{n} = \frac{\mu}{g} = \frac{\mu\, m}{4\pi\hbar^2 a}. \tag{2.37}$$

Using the normalization condition for $n(\boldsymbol{r})$ the chemical potential for a BEC in the TF limit can be calculated

$$\mu = \frac{\hbar\bar{\omega}}{2} \left(\frac{15Na}{a_{\mathrm{ho}}} \right)^{2/5} \tag{2.38}$$

When the quantum kinetic energy is neglected, the release energy in equation (2.33) consists only of the interaction energy. Integrating over the density distribution we get the average energy and the release energy per particle in the TF limit

$$E = \frac{5}{7}\mu \quad \text{and} \quad E_{\mathrm{rel}} = \frac{2}{7}\mu, \quad \text{respectively.} \tag{2.39}$$

An experimental demonstration of the dependency of the release energy on the particle number has been done by [Hol97, Mew96]. Another experiment [Kra04] has shown the the influence of the scattering length, see also Sec. 4.2.

2.4.4. A tunable quantum gas

The above energies have been calculated for a BEC in an equilibrium state. In the special case of cesium and some other alkali gases, the scattering length can be tuned [Cor00, Web03b]. If the scattering length is changed adiabatically $\dot{R_{\mathrm{TF}}}/R_{\mathrm{TF}}(0) \ll \omega$ the density distribution can adapt and the above equations are valid. The release energy is given by Eq. (2.39) and scales with $a^{2/5}$.

For a sudden (non-adiabatical) change in scattering length, e.g. a sudden switch from a, the scattering length of the euilibrium state, to a', the interaction energy between the particles changes according to a', whereas the density distribution has no time to adapt and is thus determined by a. The resulting average release energy per particle can be calculated using Eq. (2.39) and Eq. (2.37):

$$E_{\mathrm{rel}}(a') = \frac{2}{7}\, \hat{n}(a)\, g(a') = \frac{2}{7}\, \mu(a)\, \frac{a'}{a}. \tag{2.40}$$

In the case of non-adiabatic changing of the scattering length, the release energy scales linear with a'.

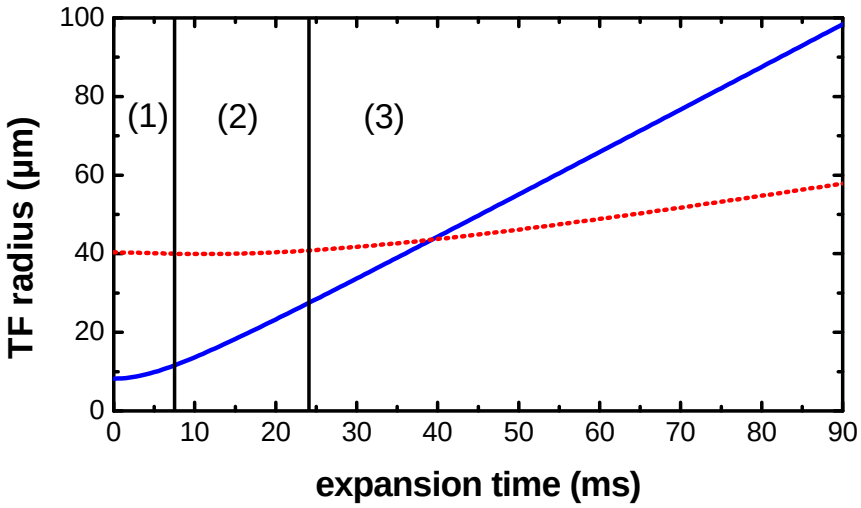

Figure 2.11.: The expansion of a BEC in the TF regime is illustrated. The red curve is the slow axial and the blue the faster radial expansion. Here, the trap frequencies are $\omega_{\mathrm{rad}} = 2\pi\times 21.2$ Hz in radial and $\omega_{\mathrm{ax}} = 2\pi \times 4.4$ Hz in axial direction The particle number is $8.5 \cdot 10^4$ and the scattering length is 210 a_0. These values are typical for our experiment. Three different stages of expansion can be distinguished, which are explained in the text.

It is worth noting, that for a sudden step to vanishing scattering length, the observed energy distribution can be even smaller than the quantum kinetic energy of the ground state. Since the spatial distribution is larger, the uncertainty in momentum spread can be smaller.

Condensate expansion

When a condensate is released from the trap its shape evolves as a rescaling of its parabolic form [Cas96, Kag96, Dal97]. Rather than being isotropic, most traps constitute a cigar-shaped trapping potential with trapping frequencies ω_r in the radial (x and y) direction and ω_{ax} in the axial (z) direction. In this case, according to [Cas96], the evolution of the TF radii during the free expansion is then given by

$$R_{\mathrm{rad}}(t) = R_{\mathrm{rad}}(0)\,\sqrt{1+\tau^2} \tag{2.41}$$

$$R_{\mathrm{ax}}(t) = R_{\mathrm{rad}}(0)\epsilon^{-1}\left(1+\epsilon^2\left[\tau\arctan\tau - \ln\sqrt{1+\tau^2}\right]\right). \tag{2.42}$$

The initial size $R_{\mathrm{rad}}(0)$ can be calculated using Eq. (2.36). Here, $\epsilon = \omega_{\mathrm{rad}}/\omega_{\mathrm{ax}}$ is the ratio of the trap frequencies and $\tau = \omega_{\mathrm{rad}}t$. Equations Eq. (2.41) and Eq. (2.42) only apply when $\epsilon \gg 1$.

The expansion of a BEC is shown in Fig. 2.11. Three stages can be distinguished: (1) The first stage $\tau < 1$ results only in an accelerated radial expansion, the release energy is converted into kinetic energy. (2) The second stage ($1 < \tau < \epsilon^2$) shows weak radial expansion and little axial expansion beyond the initial axial size. (3) Finally, in

the last stage the radial and axial expansion proceed at a constant asymptotic aspect ratio of $R_{\mathrm{ax}}/R_{\mathrm{rad}} = \pi\epsilon^2/2$. The inversion of the aspect ratio is typical for a BEC, in contrast to a thermal gas where the expansion is isotropic.

From the asymptotic radial expansion the chemical potential can be measured directly. For $\tau \gg 1$, the slope of the expansion asymptotically approaches $\tau/t = \omega_{\mathrm{rad}}^2 R_{\mathrm{rad}}^2$. By rewriting Eq. (2.36) we obtain:

$$\mu = \frac{1}{2} m\, \omega_{\mathrm{rad}}^2 R_{\mathrm{rad}}^2. \tag{2.43}$$

BEC with attractive interaction

repulsive interaction described above, an attractive interaction $a < 0$ results in a higher density and thus in a smaller condensate size in order to reduce the interaction energy. The attraction is balanced only by the quantum kinetic energy, which rises for smaller spatial extent. However, due to the different scaling of the two energies width particle number, a critical value N_{cr} can be calculated [Rup95].

$$N_{\mathrm{cr}} = 0.575 \frac{a_{\mathrm{ho}}}{|a|}. \tag{2.44}$$

The numerical prefactor was calculated for spherical traps and can vary for different geometries. For $N > N_{\mathrm{cr}}$ the BEC is unstable, the density grows until inelastic loss processes become dominant. As an example, the scattering length of ^{7}Li is negative and the critical number of atoms N_{cr} was about 1700 in the first experiments [Bra95].

In the case of a tunable quantum gas, a large stable BEC can be produced at positive scattering lengths. When the scattering length is tuned to an attractive interaction, an implosion of the condensate can be observed [Cor00, Web03b] accompanied by a dramatic loss of particles. Due to the inelastic exothermic processes, it is often referred to as “bosanova”.

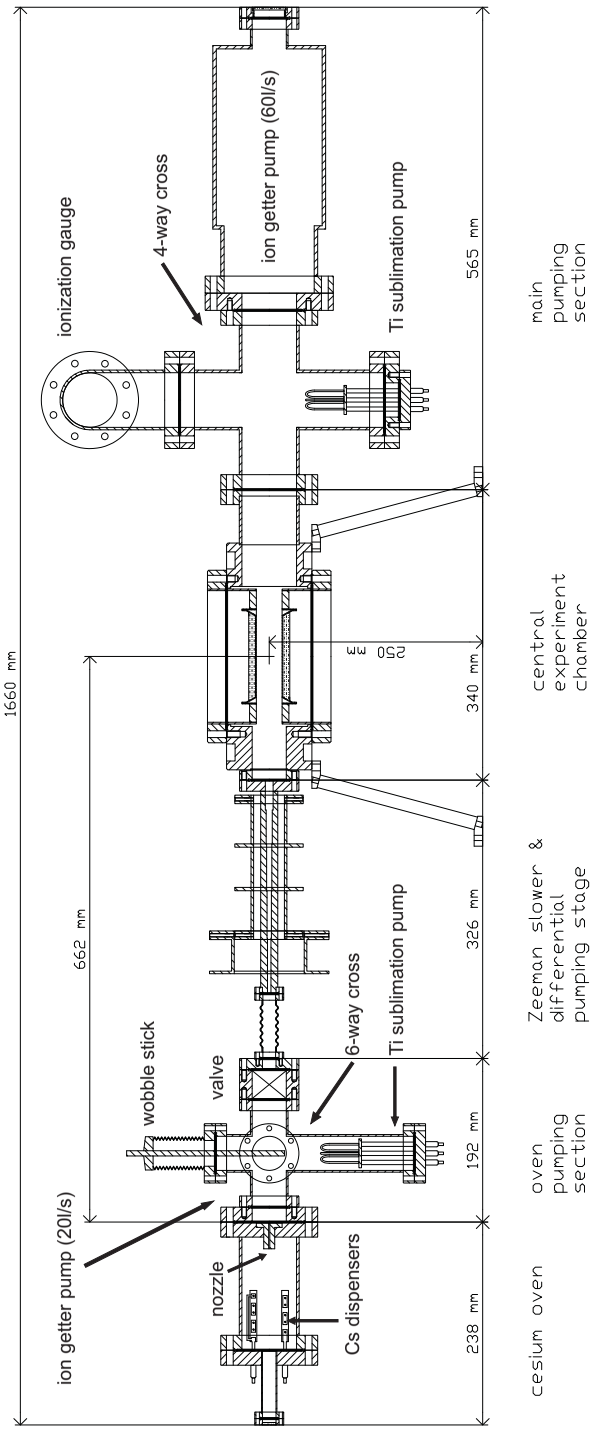

Figure 2.12.: Schematic cross-section through the apparatus.

3. Setup and Methods

In this chapter I will describe the experimental setup and the techniques for atom and molecule manipulation and analysis. The first section (Sec. 3.1) covers our vacuum setup. In the subsequent section, Sec. 3.2, details on the coil configuration and the production of the magnetic fields are given, as an excellent control over the magnetic fields is important in many steps of the experiment. The techniques used for precooling of the atoms are covered in Sec. 3.3.

The heart of the experiment is the Levitated Trap (LevT). It consists of an large and shallow optical dipole trap created by two crossed CO_2-laser beams in combination with a magnetic levitation field that counterbalances gravity for the atoms (Sec. 3.4). The setup of the dimple trap where the BEC is produced is described in Sec. 3.5. The last two sections give an overview over the computerized experimental control, Sec. 3.6, and the techniques we implemented for detection and diagnosis, Sec. 3.7.

3.1. Vacuum setup

All experiments on ultracold atomic gases are carried out in an ultra high vacuum environment, which is essential in order to minimize collisions with room temperature background gas, see Sec. 2.2.3.

The apparatus consists of various stainless steel parts and viewports, all interconnected with UHV copper-ring seals. In order to maintain an excellent vacuum environment, the afflux of gas has to be minimized by adequate preparation and assembly and by the persistent removal of the background gas using vacuum pumps. The vacuum setup can be divided in two parts. Figure 2.12 shows a schematic cross section. The left part consists of the *cesium oven* pumped by the *oven pumping section*, the right part is the *experimental chamber* together with the *main pumping section*. The two parts are interconnected by the *Zeeman slower section* which, in addition, serves as a *differential pumping stage*. Due to the small cross section of the connecting vacuum tube it limits the gas flow and shields the experimental chamber from the higher pressure in the oven section. The two parts can also be physically isolated by closing a viton sealed gate valve (VAT series 01), which serves two purposes: First, the cesium reservoir in the oven section can be replenished without breaking the vacuum in the main chamber and second, the valve is automatically closed if the pressure raises above a certain value in order to prevent pollution of both parts if one has a vacuum

leak. To prevent tension a flexible tube has been installed between the oven section and the Zeeman slower.

A description of the preparation, the bake-out procedure and calculations of the conductances together with estimations on the pumping rates are given in [Web03a].

3.1.1. Vacuum pumps

The pumping is accomplished by the combination of two different pump types.

Titanium sublimation pumps

Titanium sublimation pumps consist of wires made of a Ti-Mo alloy. To activate the pump, a current of 60 A is sent through the wires which produces a high enough temperature to sublimate the titanium. In about one minute enough titanium is sublimated to sputter the surrounding surfaces with a thin film. Titanium is a surface getter for almost all active gases which simply stick to the surface once they come into contact with it. The pumping speed per area is approximately 5 l/(s cm^2). The estimated pump rate for the titanium sublimation pump in the oven section is $\sim$ 900 l/s, reducing the gas load in this part. The pumping speed of the counterpart in the main section is much higher, approximately 3500 l/s. However, in this case, the connection to the main chamber reduces the pumping speed at the experimental region to about 200 l/s.

During the sublimation process, the surrounding parts were cooled using layers of tissue soaked in volatile liquids, such as acetone. This prevents the metal vacuum parts from overheating and supports the adsorption of titanium on the inside surfaces.

Once a good vacuum has been obtained, the above described activation procedure was carried out less than once a year, to restore a fresh layer of titanium on the surface.

Ion getter pumps

The sublimation pumps do not absorb inert gases like helium. For this purpose an ion getter pump is installed in each pumping section. A 20 l/s ion getter pump (Varian Vacion Plus 20 StarCell) is attached to the oven section. The main section is pumped by a 80 l/s ion getter pump (Varian VacIon 911-5034).

Background pressure

The pressure in both sections is measured with ionization gauges. In the oven section the pressure gauge is installed in the six-way cross opposite to the ion getter pump. The pressure is $< 10^{-11}$ mbar with the oven switched off and raises to $\sim 1 \cdot 10^{-10}$ mbar under typical operation of the cesium dispensers. The pressure inside the oven, which is separated from the pumping region by the copper nozzle, can only be assumed to be on the order of the vapor pressure of cesium of $6 \cdot 10^{-4}$ mbar [Ste02].

The position of the ionization gauge in the main chamber in the 4-way cross, as indicated in Fig. 2.12. The gauge controller typically shows an out-of-range error which indicates a pressure below 10^{-11} mbar.

3.1.2. The cesium oven

The oven is the source of cesium atoms for the experiment. It consists of a stainless steel tube with a diameter of 64 mm. Towards the chamber it is closed by a metal plate containing a copper nozzle. The other end consists of a flange with a viewport and the current feed-throughs. Two sets, each consisting of five cesium dispenser (Cs/NF/10.8/25/FT10+10), are mounted on the four current feed-throughs, see Fig. 3.1. They contain a total of 108 mg (10.8 mg per dispenser) of Cs. Initially a current of $\sim$ 7 A has to be applied to activate the dispensers and evaporate enough cesium to cover the inner surface of the oven. Under normal operation condition a current of 3 A is applied to only one of the dispenser sets. To raise the vapor pressure of cesium in the oven, it is thermally insulated and kept at 100 °C using heating tape. The nozzle with a length of 30 mm and a diameter of 1.5 mm collimates the cesium atoms leaving the oven to an effusive beam with an opening angle of 6°.

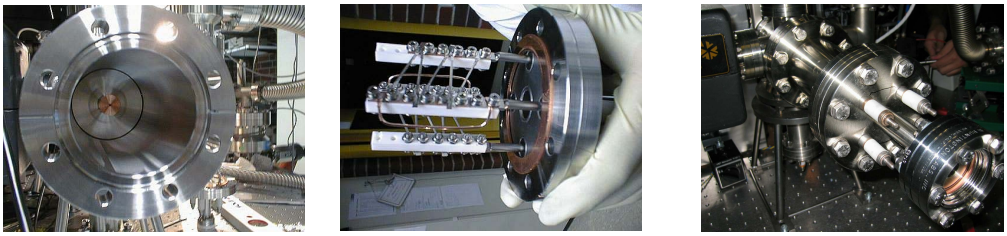

Figure 3.1.: The *left* picture shows the inside of the oven with the copper nozzle at the end. The two sets of cesium dispensers are shown in the *center* picture. The *right* picture shows the oven assembled.

After two years of operation some alterations were required to the oven section. Due to the exposed position of the viewport window, its temperature was slightly below that of the oven. Therefore cesium aggregated at the window and corroded the glass-to-metal junction. This finally lead to a massive leak. In September 2003 the oven was opened and fresh dispensers were installed. The CF16 window has been replaced by a CF40 window mounted on an adapter flange. It has a more robust glass-to-metal junction which is not in direct view of the dispensers, see Fig. 3.1 right image. A separate heating tape has been installed in order to independently control the temperature of the window which is now kept a few degrees above that of the central oven part. Furthermore, an erratic shorting of the dispenser circuit was observed, which we attributed to the wire connecting the top of the dispenser mount to the current feed-through. The wire was therefore relocated further away from the metal chamber walls.

After a bake-out of the oven section the old conditions could be restored. No shortening of the dispenser circuits has been observed since.

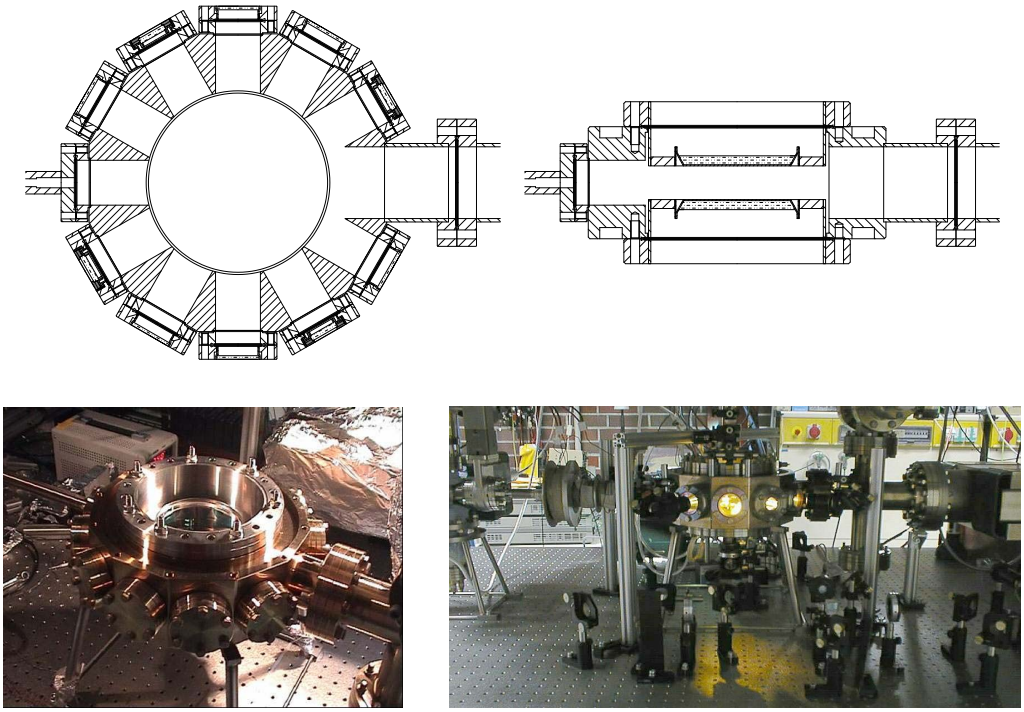

Figure 3.2.: A schematic drawing of the main chamber in top view (*upper left*) and in side view (*upper right*) image. The top re-entrant viewport is clearly visible on the *lower left* image. The *lower right* image shows the main chamber with some optical components, the two different types of viewports can be distinguished.

3.1.3. Main chamber

All experiments are carried out in the center of the experimental chamber. In plan view it is a twelve-sided polygon with each edge having a length of 70 mm. The height of the polygon is 100 mm. All sides have a bore with a diameter of 40 mm. CF40 flanges have been welded into each bore. The bore in the polygon side which connects the main chamber to the pumping section has been opened to 64 nm for better pumping. The opposite side connects to the Zeeman slower. The other ten sides are occupied by viewports. Four viewports are made of ZnSe (Larson, AR coating 10.6 µm), which is transparent for the wavelength of CO_2-laser light. They have a clear view of 22 mm. The optical paths between opposing pairs of ZnSe viewports lie perpendicular to one another. The other viewports are made of quartz (Larson Electronic Glass VQZ-150-F2-AR, AR coating 850 – 1050 nm) and have a clear view of 35 mm. The distance from the outer side of the viewports to the center amounts to 145 mm.

The top and bottom closures are custom-made re-entrant viewports (United Kingdom Special Techniques Group; AR coating 852 – 1064 nm by Laseroptik Garbsen). Enclosed in the center are 95 mm glass windows, which provide excellent optical access. Additionally, the viewports have encampments to mount magnetic field coils

close to the experimental area.

3.2. Magnetic fields

Precise control over the magnetic fields plays a key role in our experimental setup in several respects: to cancel external stray fields, to generate a quadrupole field for the MOT and a homogeneous bias field for Feshbach tuning, and to provide a gradient field for magnetic levitation.

3.2.1. Offset fields

It is crucial to provide the possibility to cancel the static environmental fields such as the earth's magnetic field and fields from components close to the experimental region, such as the ion getter pumps. This is done by three sets of coils, one for each axis in space. The coils are shown in Fig. 3.3. The fields in the horizontal plane, where the

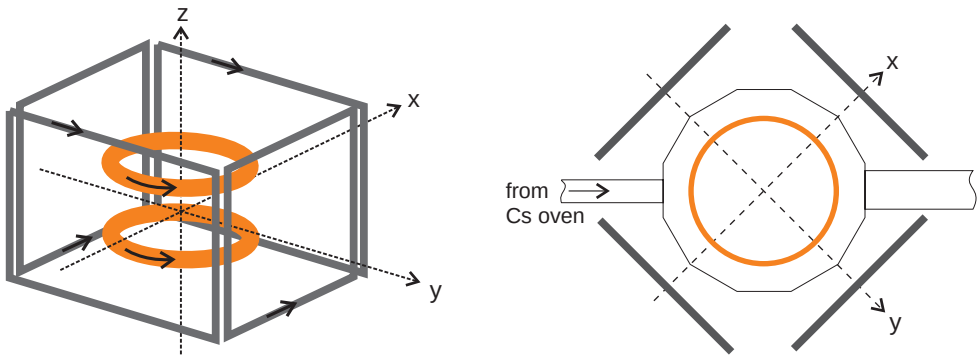

Figure 3.3.: Schematic drawing of the assembly of compensation coils, from the side (*left*) and in tow view (*right*). The x, y and z-axis are shown and the directions of the currents are indicated by arrows.

axes are labeled x and y, are created by two sets of rectangular coils with each side of length 500 mm. The distance between the coil center and the center of the main chamber is 385 mm. Each coil has 70 windings. For the two coils in Helmholtz configuration this results in a measured inductance of 33 mH and a resistance of 6 Ω. The current in the coils is supplied by two precise power supplies (HighFiness BCS 2/20) which can produce currents of ±2 A and a maximum voltage of 20 V. The specified current stability is 10^{-4}. At the maximum current each set produces a field of 1.6 G. The calculated inhomogeneity of 10^{-4} over 1 cm in the trap center is sufficient for our purposes.

The coils for the vertical offset field are integrated in the Helmholtz coils described in the next section. They consist of 23 windings and have a measured inductance of 137 µH and a resistance of 0.5 Ω. The resistance is increased to 3 Ω with external

resistors to reduce the load within the power supply. The power supply (HighFiness BCS 3/15) allows for a maximum current of ±3 A and a maximum voltage of 15 V. The maximum field is 5.5 G in the trap center.

The power supplies are programmable which allow the currents to be computer controlled. Jumpers can be used to adapt the internal PID-controller of each power supply to the inductance of the coils. With external resistors in the circuits a high power dissipation in the power supply is prevented. The switching times of the currents (10% - 90%) are 3 ms for the coils in x- and y-direction and < 1 ms in the z-direction. The carriers of the coils are slit in order to avoid eddy currents.

3.2.2. Residual ambient magnetic fields

The static environmental magnetic fields can be reduced using the offset coils to below 1 mG. Since most experiments are carried out at fields of several Gauss, the much lower residual static offset fields can simply be included by the calibration technique.

Alternating fields are a more complicated problem when trying to cancel them actively. Therefore we chose to reduce the sources of alternating fields in the experimental region and to synchronize our experimental cycle with the phase of the power line, see Sec. 3.6.3.

Residual alternating magnetic fields

Most electronic devices produce electric and magnetic fields, which can be shielded to a certain extent. However stray magnetic fields on the order of a few ten mG in the vicinity of the devices are quite common. Using a magnetic field probe, we measured these fields by individually switching on all electronic devices around the experiment. The main sources are:

Power supplies Power supplies with transformers generate fields up to 20 mG at a distance of 1 m and subsequently were moved further away.

Cooling fans A cooling fan approximately 80 cm from the experimental region generates a field up to 4 mG. The van is essential for one of the ADwin-cards and cannot be removed. It is therefore shut off during crucial phases of the experiment.

Flow box The flow box at a distance of 1 m directly above the experimental region produces a field of 20 mG. It is also turned off during measurements.

With the improvements we measure a width of 4 mG for the residual magnetic field variations. We use 100 ms RF pulses [1], which average over 5 periods of the power line. For experimental interrogations much shorter than the power line cycle the synchronization to the power line suppresses the magnetic field variations to less than 1 mG.

[1] This technique is described in Sec. 3.7.1.

3.2.3. Main coil setup

As shown in the construction drawing of the main chamber with the reentrant viewports, Fig. 3.4, the two pairs of coils are placed in designated recesses. Both sets are nearly in perfect Helmholtz configuration. The aluminum coil frames containing the coil windings are slit and isolated from the main chamber in order to reduce eddy currents. The wire used has a rectangular cross-section of 1.25×2.75 mm^2, which allows tight packing and good heat conductance. The frames contain several sub-coils, each with its own connectors to be used for different applications or to be interconnected in parallel or in series. At typical operation conditions the energy dissipation in the

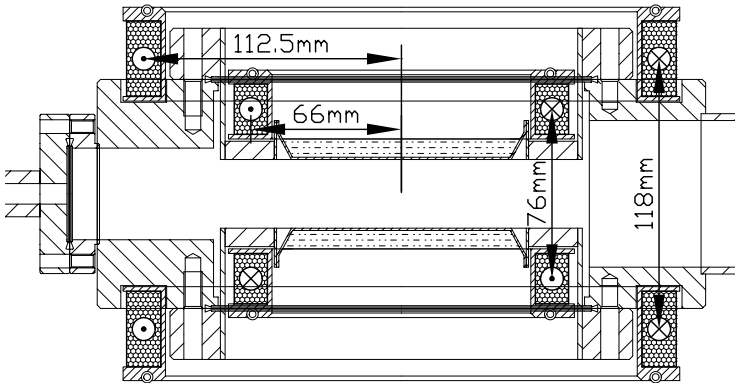

Figure 3.4.: Side view of a cross section trough the main chamber with the two sets of coils. The coil frames, the windings, and the directions of the currents are shown.

coils amounts to 0.25 kW. At maximum currents the energy dissipation is 1.1 kW. To dissipate the heat, water-conveying copper tubes are integrated into the frames.

The **outer pair** of coils with an average radius of 112.5 mm is placed at an average distance of 118 mm between the coils. Each frame accommodates six sub-coils. Counting from inside to outside, the first sub-coil (O1) has 23 windings and a resistance of 240 mΩ. O2 - O6 have 24 windings, with a resistance of 250 mΩ of each coil.

The **inner pair** has a mean radius of 66 mm and a mean distance of 76 mm. Each frame accommodates three sub-coils. The inner most sub-coil (I1) has 48 windings which amounts to a resistance of 62 mΩ, the other two (I2,I3) have 31 windings and a resistance of 40 mΩ each.

3.2.4. Bias fields

By applying an adjustable homogenous magnetic field, the interatomic interaction in an ultracold atomic cesium gas can be tuned. This requires high fields and fast and precise tuning. For that we use two different sets of coils.

High bias field

To create a high bias field, the sub-coils O2 - O6 in the outer carriers are taken together in parallel to reduce the resistance. The upper and lower coil set is connected in Helmholtz-configuration, resulting in a resistance of 56 mΩ (this includes 6 mΩ for the connections) and an inductance of 500 µH. The connected programmable power-supply (DELTA SM 30-100D) with a maximum voltage of 30 V provides up to 100 A which corresponds to a field of 190 G at the experimental region. The power supply is operated in constant current mode and has a measured current ripple of 6 mA equivalent to 11 mG. The time scale for switching on the current[2] is limited by the voltage reserve in the power supply to 360 µs, the field is stable after 1.5 ms. In order to step to a lower value the current has to be dissipated by resistance of the coils, which takes several ms. In order to switch off the fields, the circuit can be opened and the current is dissipated by varistors (EPCOS Scheibenvaristor S20K25). The current drops within 5 µs. However, due to eddy currents in the stainless steel chamber the field takes approximately 7 ms to drop to zero. For fast and precise ramping with millisecond precision, this is unacceptable.

Fast bias field

The inner set of coils induces less eddy currents. Therefore the sub-coils I2 are also connected in Helmholtz-configuration and have a inductance of 500 µH. A self-made highly stable current supply enables precise linear ramps and a maximum field of 60 G. At a sudden switch the current is stable within 10 µs. To precisely measure the time constant we apply a (large) jump of the magnetic field and probe the field response at the position of the atoms with 100 µs absorption imaging pulses. The measured data is presented in Fig. 3.5. The switch is applied at $t = 0$. For every data point the absorption

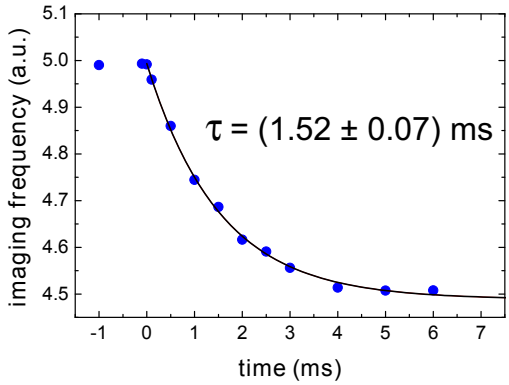

Figure 3.5.: The time constant of the magnetic field response of the fast coils is determined using short absorption imaging pulses, see text.

[2] This is the time it takes for the current to rise from 10% to 90% of its final value.

laser frequency is varied and the frequency of maximum absorption is determined. A fit reveals an $1/e$ response time of the magnetic field of (1.52 ± 0.03) ms. This method is well suited to probe the field response of a large change in bias field, but due to the linewidth of the absorption resonance it is insensitive to small magnetic field changes. Thus to precisely measure the strength of a static field we use the method described in Sec. 3.7.1.

To further improve the magnetic field response another set of coils is in preparation, which will be located directly over the glass surface of the reentrant viewports, further away from the metal parts of the chamber.

3.2.5. Anti-Helmholtz fields

The inner sub-coils I2 and I3 are taken together in parallel to reduce the resistance. The upper and lower coil set are connected in Anti-Helmholtz configuration, resulting in a resistance of 100 mΩ and an inductance of 250 μH. These coils are used to produce the quadrupole field for the MOT and the magnetic gradient field for levitation. The strength of the field increases going upwards along the vertical axis.

A programmable power supply (DELTA SM 45-70) can produce a maximum voltage of 45 V and a maximum current of 70 A, which is equivalent to a vertical field gradient of 58 G/cm. The current can be switched on within 120 μs and is stable within 1 ms. The current can be switched off by an identical circuit as in the case of the high field bias coils.

3.2.6. Magnetic levitation

The potential experienced by particles with a magnetic moment $\boldsymbol{\mu}$ in a magnetic field $\boldsymbol{B}$ is given by $U_{mag} = -\boldsymbol{\mu} \cdot \boldsymbol{B}$. Here we assume that the atomic spin can follow the magnetic field adiabatically, which is true for slowly changing non-zero fields. For an atom in the state $F = 3$, $m_F = 3$, the magnetic potential is given by

$$U_{mag,3,3} = -\frac{3}{4}\mu_B B + \frac{15}{16}\frac{\mu_B^2}{\Delta E_0}B^2, \tag{3.1}$$

here $\Delta E_0 = h \cdot 9.19...$ GHz is the hyperfine energy splitting of the cesium ground state. The first term in Eq. (3.1) is the Zeeman energy and the second term is due to the quadratic Zeeman effect. To estimate the magnetic moment including the quadratic term in Eq. (3.1) the following equation can be used

$$\mu(B) = \left(\frac{3}{4} + \frac{15}{8}\frac{\mu_\mathrm{B}}{\Delta E_0}\, B\right) \mu_\mathrm{B} \tag{3.2}$$

$$\mu(B) \approx \left(0.7500000 + 2.916 \times 10^{-4}\, B\right) \mu_\mathrm{B} \tag{3.3}$$

Here, B is the magnetic field set in the experiment which includes the configuration of the fields.

The gravitational potential for a cesium atom with mass m is

$$U_{grav} = mgz, \tag{3.4}$$

with the gravitational constant g and the vertical coordinate z. The magnetic field gradient needed to counteract the gravitational force for a cesium atom in the state $F = 3, m_F = 3$ can be calculated by comparing Eq. (3.1) and Eq. (3.4):

$$\frac{\partial B}{\partial z} = \frac{mg}{\mu(B)} \approx 31.137 \frac{\mathrm{G}}{\mathrm{cm}} - \frac{0.0119}{\mathrm{cm}} B, \tag{3.5}$$

where $g = 9.80636$ is the gravitational acceleration calculated for Innsbruck and m is the mass of ^{133}Cs. The approximation is a first order Taylor expansion. The deviation of this approximation is less than 5×10^4 for magnetic fields below 60 G.

The field gradient for levitation can be easily produced by the anti-Helmholtz coils described in Sec. 3.2.5. According to the Maxwell's equation (div$\boldsymbol{B} = 0$), a radially symmetric vertical gradient implies also a horizontal gradient half as much.

$$\mathrm{div}\boldsymbol{B} = 0 \quad \rightarrow \quad \frac{\partial B}{\partial x} = \frac{\partial B}{\partial y} = -\frac{1}{2}\frac{\partial B}{\partial z} = -\frac{2}{3}\frac{mg}{\mu_B} \tag{3.6}$$

Using the bias coils a vertical homogenous bias field B_{bias} can be applied. This effectively shifts the center of the quadrupole field. In the vertical direction the magnetic and the gravitational force cancel, whereas in the horizontal plane this leads to an outward pointing force. As illustrated in Fig. 3.6, a large bias field effectively reduces

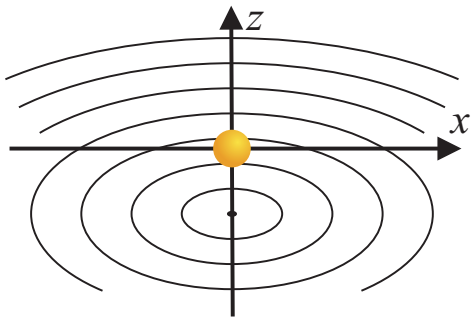

Figure 3.6.: The combined magnetic field of a quadrupole field and a homogeneous bias field in z-direction. The equipotential lines are plotted; the force due to the field gradient is always perpendicular to these lines.

the outward forces. The field in the horizontal plane is given by a superposition of the bias field and the gradient field. Due to the z-symmetry of both fields it is practical to

introduce the radial coordinate $\rho = \sqrt{x^2 + y^2}$.

$$B(\rho) = \sqrt{B_{bias}^2 + \left(\frac{2}{3}\frac{mg}{\mu_B}\rho\right)^2} \tag{3.7}$$

$$\approx B_{bias}\left[1 + \frac{1}{2}\left(\frac{2}{3}\frac{mg}{\mu_B B_{bias}}\rho\right)^2\right] \tag{3.8}$$

$$= B_{bias} + \frac{2}{9}\frac{m^2 g^2 \rho^2}{\mu_B^2 B_{bias}} \tag{3.9}$$

Substituting Eq. (3.9) in Eq. (3.1) and neglecting the quadratic Zeeman term gives the magnetic potential in the horizontal plane:

$$U_B(\rho) = -\frac{3}{4}\mu_B B(\rho) = -\frac{3}{4}\mu_B B_{bias} - \frac{1}{6}\frac{m^2 g^2}{\mu_B B_{bias}\rho^2}. \tag{3.10}$$

This can be written as an inverse harmonic trapping potential with (anti-)trapping frequency α

$$U_B(\rho) = U_{B_{bias}} - \frac{1}{2}m\alpha^2\rho^2 \quad \text{where} \quad \alpha = g\sqrt{\frac{m}{3\mu_B B_{bias}}}. \tag{3.11}$$

When the levitation gradient cancels gravity, only the optical trapping potential remains in the vertical direction. In the horizontal direction however, the trapping potential is superimposed with the anti-trapping potential given by Eq. (3.11), which is weak at high bias fields. At low fields this can reduce the effective trapping potential of a shallow trap (see Sec. 3.4.4) and it effects the motion of free atoms after release from the trap.

According to the equation of motion $F_x = m\alpha^2 x$ for the horizontal degrees of freedom, a particle released at $t = 0$ in the levitation field with an initial horizontal position ρ_0 and an initial horizontal velocity v_0 follows

$$\rho(t) = \rho_0 \cosh(\alpha t) + \alpha^{-1} v_0 \sinh(\alpha t)\,, \tag{3.12}$$

$$v(t) = \alpha\rho_0 \sinh(\alpha t) + v_0 \cosh(\alpha t)\,. \tag{3.13}$$

The vertical motion is not affected.

Table inclination

The axis of the levitation field is defined by the orientation of the coils. Since the coil frames are fixed to the main chamber (see Fig. 3.4) their axis and thus the direction of the produced force on the atoms is perpendicular to the experimental table. The assumption of perfect levitation is only true, when the table lies in the horizontal plane. A small inclination of the table from the horizontal plane leads to residual horizontal forces. The effect of a small inclination of the table is not noticeable in a deep trap of a few μK but at trap depth of $\leq$ 1 μK (e.g. in the dimple trap at the end of the

evaporation) this force can render the trap unstable. The vibration isolation of the optical table relies on an air suspension mechanisms in the table legs. We found that the table inclination can drift due to pressure fluctuations, which led to large day-to-day fluctuation in the number of atoms in the BEC of up to 60%. Therefore we installed an inclination sensor, which allows to recover the original table position. We found that it is necessary to restore the original value with an accuracy of ~ 0.5 mrad to reestablish the original conditions. Additionally, the installation of a more precise suspension system is planned.

3.3. Laser cooling

For Bose-Einstein condensation atoms have to be cooled from about room temperature down to a few ten nK. The largest step is accomplished in the pre-cooling phase. We employ several standard pre-cooling methods to prepare a large ensemble of ultracold atoms: a magneto-optical trap (MOT) in combination with a Zeeman slower is used to cool and collect atoms from the room-temperature atomic beam. Subsequent Raman-sideband cooling (RC) in an optical lattice cools the atoms to below 1 μK and polarizes the ensemble in the state $F = 3$, $m_F = 3$. This is an ideal basis to load the atoms into an optical dipole trap, see Sec. 3.4 and the following, where evaporative cooling can be performed.

Due to its large mass, the recoil energy imparted by a single photon is very low, namely $k_B \times 200$ nK. This makes Cs very suitable for laser cooling applications. As

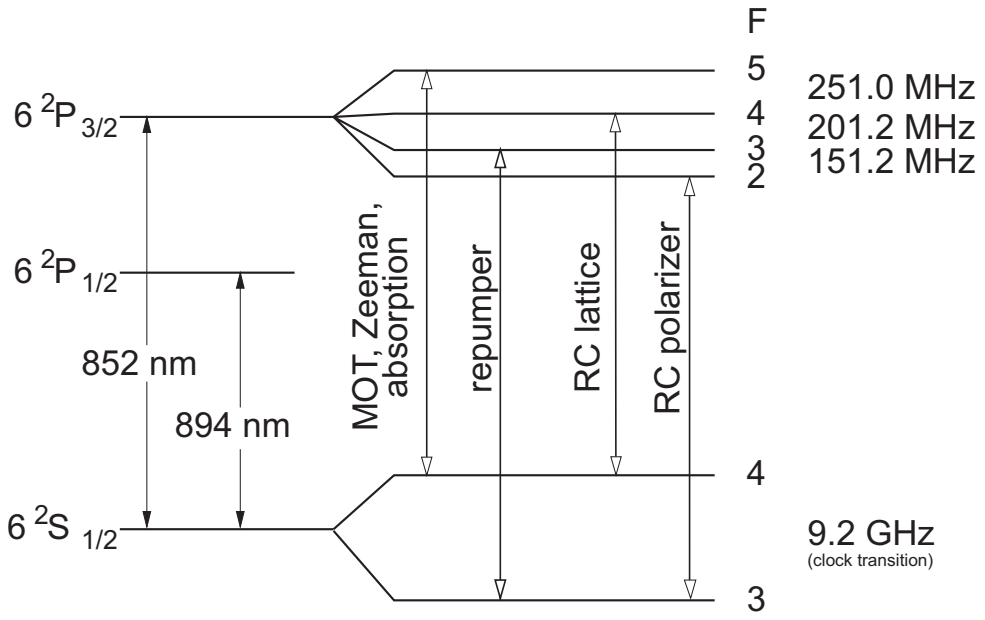

Figure 3.7.: Level scheme of ^{133}Cs. Indicated are the transitions used in the experiment.

shown in Fig. 3.7 the lowest optical transitions are the D_1-line from $6\,^2S_{1/2}$ to $6\,^2P_{1/2}$ with a natural linewidth of $\Gamma_1 = 2\pi\times 4.56$ MHz, and the D_2-line from $6\,^2S_{1/2}$ to $6\,^2P_{3/2}$, which has a linewidth of $\Gamma_1 = 2\pi \times 5.22$ MHz and is used as the primary laser-cooling transition in our experiment.

All frequencies used for laser cooling in our setup, for Zeeman slowing, the magneto-optical trap, Raman-sideband cooling, and also absorption imaging are produced with diode-laser systems, which are described in detail in appendix A.1. Since one of the wavelengths used for telecommunication was around 850 nm, laser diodes for cesium were readily available.

All diode laser frequencies are resonant to the cesium D_2-line at a wavelength of 852 nm. The transitions used in the experiment are indicated in the level scheme Fig. 3.7. I will refer to the transitions as $F \rightarrow F'$, where this represents an atom being exited from the ground state, F, to the excited state, F'.

3.3.1. Standard pre-cooling techniques

Since its first demonstration [Raa87] the magneto-optical trap (MOT) has become a standard tool to capture and cool atoms in modern cold atom experiments. The cooling in the MOT relies on the scattering of photons from a red-detuned laser beam propagating against the atomic motion. With a Zeeman slower atoms in the atomic beam from the oven are slowed down below the capture velocity of the MOT [Phi82], which enhances the loading rate dramatically.

Details on the Zeeman slower and the MOT setup can be found in [Web03a]. Here only the important facts are summarized. Our MOT is operated at a detuning of -7 MHz from the $F = 4 \rightarrow F' = 5$ and a field gradient of 6.5 G/cm is applied. Atoms have a finite probability to decay to $F = 3$, which would lead to a significant loss. Therefore in the MOT and the Zeeman slowing beam, additional light from the repumper is added, which is resonant to the $F = 3 \rightarrow F' = 3$ transition. After 6 s of loading more than 10^8 atoms are collected, for which we measure a temperature of ~ 10 μK.

After the loading phase we compress the MOT by increasing the field gradient over 40 ms by a factor of five to 33 G/cm. Simultaneously the detuning is linearly changed to -30 MHz. The compressed cloud has a spatial extension of 360 μm which is the measured $1/e$-radius of the Gaussian density distribution. After the compression we measure a temperature of 40 μK. The tradeoff between smaller size and higher temperature pays off, as will be outlined in the following sections.

3.3.2. Raman-sideband cooling

The implementation of Raman-sideband cooling (RC) in our setup serves two purposes: The atoms are polarized in the state $F = 3$, $m_F = 3$ which is necessary to load them into the CO_2-laser trap, see Sec. 3.4. Simultaneously it cools samples with several ten μK to temperatures well below 1 μK.

The RC scheme in our setup follows the approach by [Tre01, Ker00]. The basic technique is illustrates in Fig. 3.8. Atoms in the state $F = 3$ are captured in a three-dimensional optical lattice. A magnetic field shifts the energy of the the different m_F substates. The magnetic field is chosen such that the energies of the vibrational trap level ν of an atom in state m_F is in degeneracy with $\nu + 1$ of the state $m_\mathrm{F} + 1$. A circular component in the polarizations of the two counter-propagating lattice beams drives Raman transitions between the degenerate energy levels. The light of the *polarizer* has a strong σ^+ and a weak π polarized component. The atoms are pumped to the state $F' = 2$. In the Lamb-Dicke regime ν is conserved during this process. The π component is used to depopulate the state $m_\mathrm{F} = 2, \nu = 0$, which is not resonant for the σ^+ light. Eventually all atoms end up in the energetically lowest state $m_\mathrm{F} = 3, \nu = 0$ which is a dark state in this scheme. The weak π component suppresses reabsorption heating of atoms in this state. By slowly lowering the potential the atoms are adiabatically released into free space, this reduces the free-space temperature of the ensemble [Kas95]. The 65 mW available from the RC lattice laser is split up into

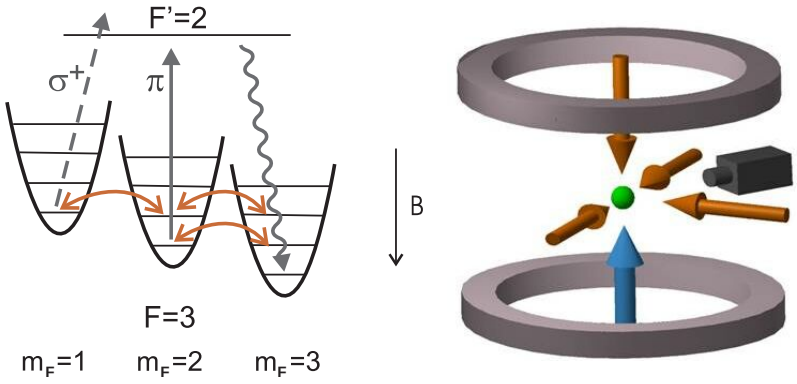

Figure 3.8.: (*Left*) the optical pumping scheme and (*right*) the laser beam configuration for Raman-sideband cooling. Vibrationally excited atoms undergo degenerate Raman transitions (double-sided arrows) stimulated by the lattice beams. The polarizer from below is mainly σ^+ polarized, which provides fast optical cooling. The additional weak component of π polarized light, completes the final cooling step.

four laser beams with $1/e^2$ beam radii of 1 mm. The ratios of the intensities and the polarizations are originally chosen according to [Tre01] and were later optimized by monitoring the cooling performance. The four beams are overlapped in the center of the experimental area, see Fig. 3.8, and create the three-dimensional optical lattice. The level spacing is estimated to be of the order of 100 kHz. Using four beams ensures the stability of the lattice potential under phase fluctuations of the laser light [Gry93]. The RC lattice laser is resonant to the $F = 4 \rightarrow F' = 4$ transition. Therefore it can also serve as a repumper for atoms which end up in the $F = 4$ ground state manifold. However, without the cooling process the relatively small detuning of only ~ 9.2 GHz would lead to a strong loss.

The polarizing beam is 7 MHz blue detuned from the $F = 3 \rightarrow F' = 2$ transition to account for the light shift due to the lattice potential. The beam enters the chamber from below and proceeds vertically. The offset coils in the z-direction produce the main component of the magnetic field in the order of a few hundred mG. The polarizer is circularly polarized to produce σ^+ light. Due to imperfections, the polarization is slightly elliptical. This can be understood as an additional σ^- component counteracting the cooling process. Using the x- and y-offset fields the direction of the magnetic field can be slightly tilted. In this way the elliptical polarization can be converted into σ^+ polarized light with a small component of π polarized light. This is optimal since the σ^- component is eliminated and the π light is needed for the cooling process. By iterating we optimize the strength and the direction of the magnetic field. Typically every few weeks the fields have to be reoptimized.

After 6 ms of cooling, 95 % , or equivalently $4 \cdot 10^7$ atoms, are polarized in the state $F = 3$, $m_F = 3$. The sample has a temperature of about 0.7 µK, corresponding to a phase space density of 1×10^{-3}. This is a perfect starting condition for the loading of the Levitated Trap (LevT), see next Sec. 3.4.

The implementation of RC greatly improved the number of atoms loaded into the LevT. First of all, other techniques to polarize the atoms in the desired state caused heating in the order of a few µK. Second, the cloud can be compressed for a better phase space matching with the LevT while the additional heating caused by the compression is diminished. Finally, the spatial localization in the RC lattice ensures reproducible loading conditions for the LevT.

3.4. The LevT – Levitated Trap

The central part of our experiment is the Levitated Trap (LevT). It features a large and shallow optical trapping potential allowing for efficient loading. The use of CO_2 lasers for the dipole trap gives a negligible heating rate from resonant photon scattering due to the large detuning. The gravitational force is eliminated using magnetic levitation, as described in Sec. 3.2.6. A weak trap together with the levitation ensures perfect spin polarization of the atoms. The levitation field is matched to levitate Cs atoms in the state $F = 3$, $m_F = 3$, for which two-body losses are fully suppressed, see Sec. 2.3.1. Furthermore it allows for RF-induced forced evaporation in an optical trap (Sec. 3.7.1).

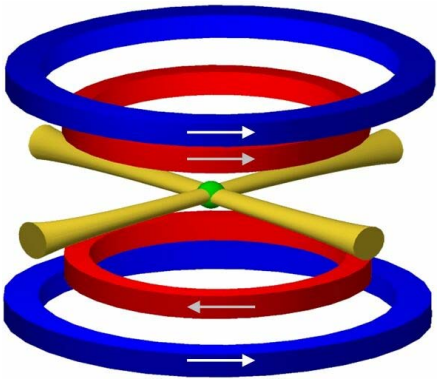

Figure 3.9.: Scheme for the Levitated Trap (LevT). The two CO_2 lasers propagate in the horizontal plane. The leviation field is created by the inner coils in anti-Helmholtz configuration, which produce a magnetic field gradient in the vertical direction to counterbalance gravity for the atoms. A variable homogeneous bias field is applied in the vertical direction by the outer coils configuration. The direction of the currents in the coils is indicated by arrows.

The trapping of atoms in an optical dipole trap using the ac Stark shift from a red detuned laser beam was first demonstrated by Chu and co-workers [Chu86]. The detuning of only a few hundred GHz from the atomic dipole transition led to significant photon scattering rate from the trapping beam. In contrast, a Far Off-Resonant Trap (FORT) relies on a larger detuning, thus reducing the photon scattering rate. Such a trap is also used in a later step in our experiment, see Sec. 3.5. A FORT was first realized for Rb atoms using a laser beam with a detuning of 65 nm [Mil93]. A quasi-electrostatic trap (QUEST) is a variant of the FORT, where the frequency of the trapping laser is less than half of the frequency of the lowest electric dipole transition. Takekoshi et al. [Tak95] implemented a QUEST for cesium atoms employing the focused beam of a 18 W cw CO_2 laser with a wavelength of 10.6 µm. This wavelength is very far detuned from the optical transitions of all alkali atoms. Trapping of molecules has also been reported in such a trap [Tak98]. In a similar approach, a QUEST was implemented in our group using commercial CO_2-lasers [Eng00, Web00]. No signif-

icant heating due to laser intensity fluctuations, beam pointing, or photon scattering was observed, encouraging the approach presented in this thesis.

3.4.1. QUEST – QUasi-ElectroStatic Trap

A detailed derivation of the photon scattering rate and the potential depth in a QUEST can be found in [Web03a] and in the comprehensive review [Gri00]. The potential depth and the photon scattering rate in a QUEST can be calculated from:

$$U_{\mathrm{dip,QUEST}} = -\frac{3\pi c^2}{\omega_{\mathrm{eff}}^4}\Gamma_{\mathrm{eff}} \cdot I, \tag{3.14}$$

$$\Gamma_{\mathrm{sc,QUEST}} = \frac{6\pi c^2}{\hbar\omega_{\mathrm{eff}}^5}\left(\frac{\omega}{\omega_{\mathrm{eff}}}\right)^3 \Gamma_{\mathrm{eff}}^2 \cdot I. \tag{3.15}$$

Here $\omega_{\mathrm{eff}} = 1/3\ \omega_1 + 2/3\ \omega_2$ accounts for the two possible dipole transitions D_1 and D_2 of the Cs atom in the ground state with the transition frequencies ω_1 and ω_2, respectively. The pre-factors are determined by the relative transition line strength. Analogously the effective line strength Γ_{eff} is obtained. I is the intensity of the beam.

The potential depth can also be calculated by using the measured *static polarizability* of the ground state of the cesium atom of $\alpha_{\mathrm{stat}} = 6.63 \cdot 10^{-39}$ Cm^2/V [Lid97]. The relation between potential U and light intensity I is then given by the simple expression

$$U_{\mathrm{dip,QUEST}} = -\frac{\alpha_{\mathrm{stat}}}{2\epsilon_0 c} \cdot I, \tag{3.16}$$

which results in values about 5% higher than obtained from Eq. (3.14). The photon scattering rate in our CO_2-laser trap can be calculated to be $4.1 \cdot 10^{-5}$ s^{-1}. This is equivalent to 3.6 photons/day which is negligible in every step of the experiment.

3.4.2. The CO_2 lasers

Our optical trapping potential is formed by the crossed beams of two CO_2 lasers intersecting under an angle of 90°. I will denote Laser1 as having its beam propagating along the y-axis, and Laser2 as having its beam propagating along the x-axis. The definition of the axes is consistent with the axes for the magnetic offset fields introduced in Sec. 3.2.1. The beams are produced by two commercial CO_2 lasers (Coherent-DEOS GEM-100L) which have a specified cw output power of 100 W each. The $1/e^2$ radius of the Gaussian beam profile is 3 mm, with a specified beam quality of $M^2 = 1.1$. The directly measured output powers were 118 W for Laser1 and 101 W for Laser2 on installation in August 2001. However, the powers degraded and were measured to be 115 W and 90 W in August 2003. The laser heads are pumped by two 1 kW RF-drivers running at 100 MHz. The drivers have been modified to receive their power from two highly stable power supplies (Agilent 6573A). The lasers run on a single longitudinal line of the CO_2 emission spectrum with a free spectral range (FSR) of $\sim$ 66 MHz. The

end mirror of the laser cavity is mounted on a piezo electric crystal, which allows for tuning of the frequency.

Water cooling

The laser heads must be water cooled. A temperature change of 0.15 °C leads to a mode hop which is accompanied by a strong loss in atom number in the LevT. Since the two heat exchangers supplying the cooling water show temperature variations of up to 0.3 °C, the cooling cycle is equipped with additional stabilization. A temperature sensor together with a run-through water heater is installed directly before each laser head. A heater consists of a 150 mm long, 16.5 mm diameter aluminum tube encased in heating tape which can deliver a power of 240 W. Together with a microprocessor temperature controller the temperature can be stabilized to ±0.01 °C. The piezo electric crystal can be used to tune the frequency of the laser to the middle of the gain profile. A slow drift over a few hours requires re-adjustment to avoid mode hops. Since the efficiencies of the heat exchangers dropped gradually over two years, both were subsequently replaced to restore the initial efficiencies.

Acousto-optical modulators

In order to maintain a stable low noise power output, the CO_2 lasers have to be run continuously. Changing the laser intensity is therefore accomplished by AOMs (IntraAction AGM-408BB1M). For an aperture of 8 mm in diameter the beam radii do not need to be adjusted. The drivers for the AOMs deliver up to 50 W of RF at 40 MHz. The AOMs have been adjusted to shift the frequency by +40 MHz for one laser and by −40 MHz for the other. This 80 MHz difference is always larger that the 66 MHz FSR of a CO_2 laser which makes interference impossible. The first order efficiencies are 78% for Laser1 and 72% for Laser2. This is a combined effect from the insertion loss (12%), the 90% deflection efficiency, and the geometrical cut off of a few percent.

The beams are directed into the chamber using gold coated copper mirrors (Laser Beam Products SNICU50-10-00) with a diameter of 50 mm.

Beam parameters

Even though the AOMs are water cooled, the RF power and several Watts of absorbed laser power lead to strong thermal effects. As a result, the first order of each beam becomes strongly astigmatic. In addition, the beam pointing changes with varying RF power, which complicates the option of lowering the trapping potential. The beams are focused by ZnSe lenses (Laser Beam Products LZ38-7-190) with a focal length of 190.5 mm and a diameter of 38 mm. To characterize the astigmatism, the beam waists have been measured in horizontal and vertical direction for various distances after the lenses. In the test setup for this measurement the beam path was composed of the same optical elements as were used later in the experiment. The results are shown in

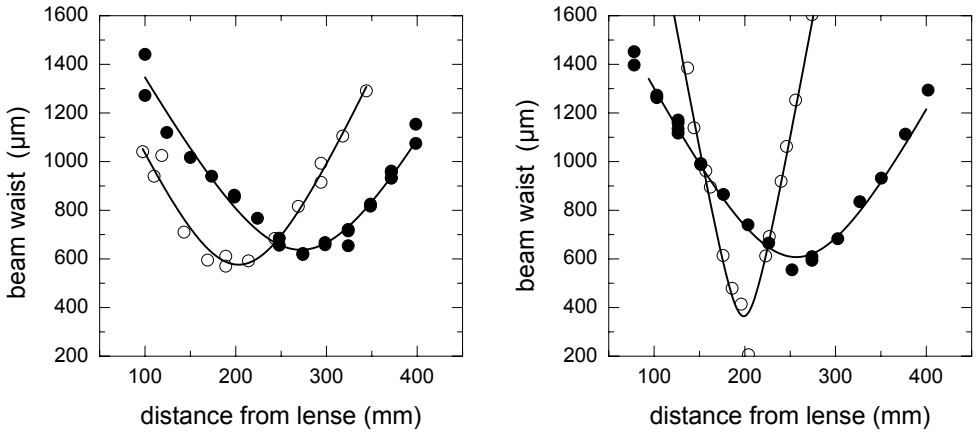

Figure 3.10.: Horizontal (open symbols) and vertical (full symbols) beam waists along the beam path. The left plot displays the data for Laser1, the right plot for Laser2. The astigmatism is clearly visible.

Fig. 3.10. The astigmatism shifts the foci between the horizontal and vertical direction up to 70 mm apart. The lenses are mounted on 3D translation stages for adjustment. The distances from the lenses to the trap center are adjusted to the distances where the lines in Fig. 3.10 cross, i.e. where the radii are equal. For the lens in Laser1(2) this is at a distance of 240 ± 3 mm (232 ± 3 mm) where the radius is w_0 = 637 ± 15 µm (w_0 = 672 ± 15 µm). The error in the distance derives from the uncertainty of the actual crossing point of the laser beams in the experimental chamber where the trap is formed.

Laser power at the experimental region

The beams enter and leave the main experimental chamber through the ZnSe viewports. The loss from one viewport was measured separately to be $\leqslant$ 2 %. Taking into account the respective power in the first order of each beam reduced by the loss at the viewport, the total laser power at the experimental region amounts to 85 ± 5 W for Laser1 and 65 ± 5 W for Laser2.

All beams (the first order emerging from the main chamber and the zeroth order) have to be dumped in water cooled beam dumps.

3.4.3. Optical potential

The optical dipole potential in the LevT is proportional to the light intensity (cf. Eq. (3.16)) which is determined by the superimposed Gaussian beam profiles of Laser1 and Laser2. Both beams have in good approximation a Gaussian intensity distribution.

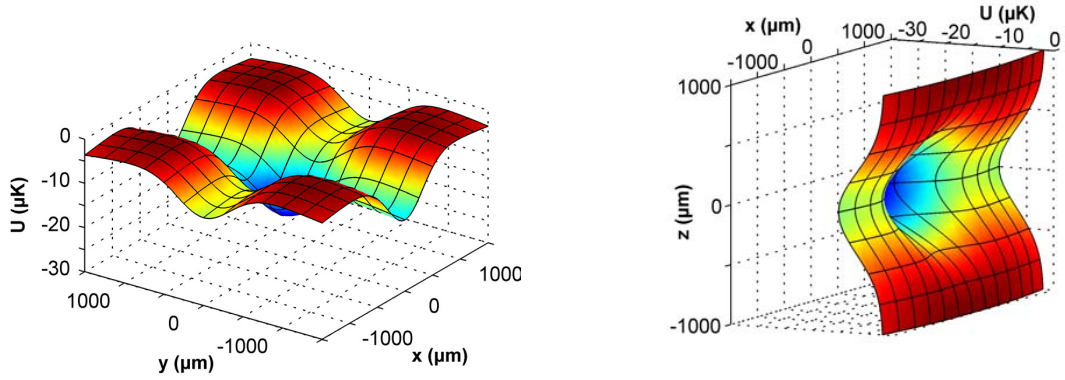

Figure 3.11.: Potential of the CO_2-laser trap in the horizontal x-y plane at $z = 0$ (*left*) and in the vertical x-z plane at $y = 0$ (*right*). The calculation includes the transversal magnetic forces of the levitation field at a high bias field of $B_{bias} = 75$ G, where their effects are negligible.

The intensity in a beam with a Gaussian profile is given by

$$I(r,a) = \frac{2P}{\pi w^2(a)} e^{-2r^2/w^2(a)}. \tag{3.17}$$

The total laser power is denoted P, a is the axial coordinate along the beam axis, and r is the radial coordinate. The beam waist $w(a)$ depends on the position by the relation

$$w(a) = w_0 \sqrt{1 + \left(\frac{a}{z_R}\right)^2}, \tag{3.18}$$

where w_0 is the minimum beam waist in the focus, and the *Rayleigh range* $z_R = \pi w_0^2/\lambda$ is a measure of the axial extension of the focal region. For a minimal beam waist of ~ 600 μm and the corresponding Rayleigh range is about 10 cm. This leads to a negligible axial confinement. We can therefore safely assume $w(a) = \text{const.}$ throughout the following considerations.

The two laser intensity distributions can be simply added, since interference of the two beams is not possible due to the large frequency difference. The resulting potential is then

$$U_{\mathrm{CO_2}}(x,y,z) = -\hat{U}_1 e^{-2(x^2+z^2)/w_1^2} - \hat{U}_2 e^{-2(y^2+z^2)/w_2^2}, \tag{3.19}$$

with the trap depths given by Eq. (3.16)and Eq. (3.17)

$$\hat{U}_{1,2} = \frac{\alpha_{\mathrm{stat}}}{\pi \epsilon_0 c} \frac{P_{1,2}}{w_{1,2}^2} = k_B \cdot 5.76 \cdot 10^4\ \mu\mathrm{K} \cdot \frac{P_{1,2}/\mathrm{W}}{w_{1,2}^2/\mu\mathrm{m}^2}. \tag{3.20}$$

With the radii w_1, w_2 and the intensities of Laser1 and Laser2 given above, the potential depths for the two beams result to $\hat{U}_1 = k_B \cdot (12.1 \pm 1)$ μK and $\hat{U}_2 = k_B \cdot (8.3 \pm 1)$ μK. The potential in the trap center is $\hat{U}_1 + \hat{U}_2 \cong k_B \cdot 20.4$ μK. The effective trap depth is given by the direction with the lowest potential $\hat{U}_{CO_2,\mathrm{eff}} = \hat{U}_2$.

	calculated
$\omega_x/2\pi$	13.7 Hz
$\omega_y/2\pi$	10.8 Hz
$\omega_z/2\pi$	17.4 Hz

Table 3.1.: Calculated trap frequencies in the LevT.

For an ensemble with a temperature much lower than the trap depth the Gaussian potential can be approximated by a radially symmetric harmonic potential,

$$U(r) \approx -\hat{U}\left(1 - 2\frac{r^2}{w^2}\right), \tag{3.21}$$

from which the trap frequencies can be calculated. In table 3.1 the calculated trap frequencies are displayed. The trap frequencies can be measured using the methods described in Sec. 3.7.4. To check the consistency we measure the vertical trap frequency: The obtained value of $\sqrt{\omega_x^2 + \omega_y^2} = 2\pi \cdot 17.0$ Hz agrees well with the prediction. The previously found systematically lower values [Web03a], were probably caused by the above mentioned degrading of the laser power.

3.4.4. Levitating the trap

So far the gravitational potential $m_{\mathrm{Cs}}gz$ along the vertical axis has not been taken into account, its force is by far stronger then the optical trapping force. Using magnetic levitation, as explained in Sec. 3.2.6, gravity is counterbalanced and the potential in the z-axis is determined only by Eq. (3.19). The trap frequency remains unchanged in this direction. However, the anti-trapping potential (Eq. (3.11)) caused by the gradient field contributes to the potential in the horizontal direction. The resulting potentials for the vertical direction and for one horizontal direction at high and low bias field is displayed in Fig. 3.12.

In the harmonic approximation (Eq. (3.21)) the horizontal potential under the influence of the levitation field can be easily calculated, e.g. for the x-axis:

$$U(x) = 2\frac{\hat{U}_1}{w_1^2}x^2 - \frac{1}{2}m\alpha^2x^2 = \frac{1}{2}m\left(\omega_x^2 - \alpha^2\right)x^2. \tag{3.22}$$

This gives an expression for the trap frequencies along the horizontal axes,

$$\omega'_{x,y} = \sqrt{{\omega_{x,y}}^2 - \alpha^2}. \tag{3.23}$$

The trap frequencies in the horizontal direction are reduced by the anti-trapping frequency α to an effective frequency ω'. Since the value of α varies with the applied bias field B_{bias} through Eq. (3.11), the effective trap frequency depends on B_{bias}. Fig. 3.13

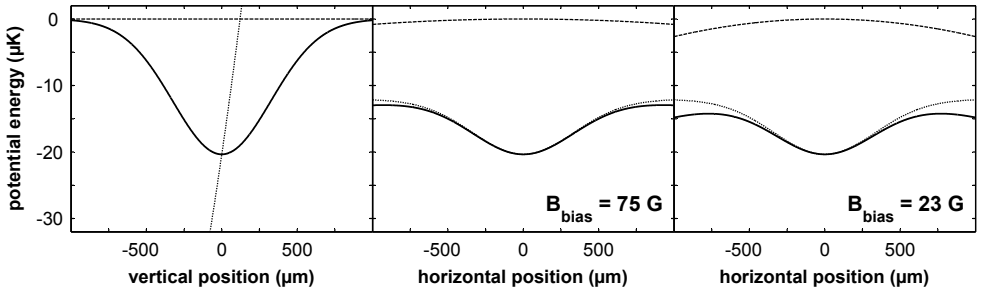

Figure 3.12.: The potentials in the LevT along the vertical and one horizontal axis under the influence of transversal forces caused by magnetic levitation are shown. (*Left*) in the vertical direction the gravitational potential is exactly canceled. The dashed line is the potential caused by the magnetic forces. The dotted line is the optical potential without levitation, which would not be confining. (*Middle*) at high bias fields (75 G) the vertical potential is almost unaffected. (*Right*) At a bias field of 10 G the potential depth is notably reduced by 40 %.

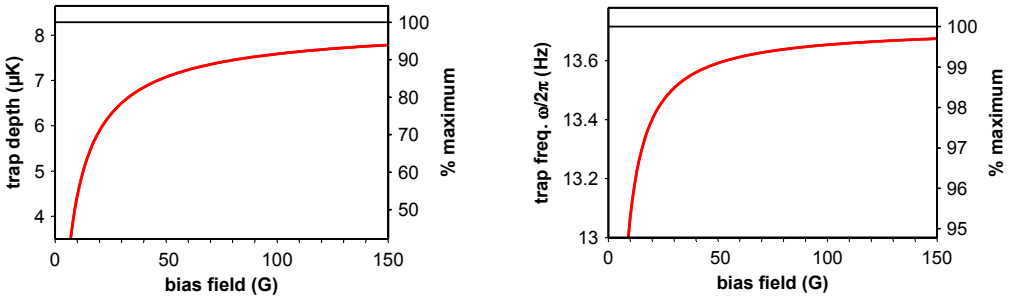

Figure 3.13.: Calculated LevT trap depth and average trap frequency as a function of the bias field. Note that different scales for trap depth and trap frequency. At 75 G, the trap depth is 7.4 μK (90 % of the maximum), the average trap frequency is almost unaffected, $\bar{\omega}/2\pi$ = 13.6 Hz (> 99 %). At a bias field of 10 G, the trap depth is remarkably reduced to 4.4 μK whereas the reduction in the average trap frequency to 13.06 Hz, 95% of the maximum value, is still small.

shows the dependence of the average trap frequency on B_{bias}. The reduction in potential depth due to the magnetic forces at a certain bias field is obtained by comparing the potential minimum in the center to the maximum value, see Fig. 3.12, right plot.

3.4.5. Loading the LevT

The LevT is loaded with the ensemble cooled and polarized by Raman-sideband cooling. For transfer of the pre-cooled atoms into the optical dipole trap, we leave the light of the two CO_2 lasers on during the entire pre-cooling phase. This is because of the strong variations in beam pointing and beam shape as a function of radio-frequency power to the AOMs (Sec. 3.4.2). We have checked that the small light shift introduced

by the lasers does not affect the initial loading and cooling efficiency. The LevT is then activated by ramping up the magnetic bias field and the gradient field. The $1/e$-rise time of the magnetic fields is limited to 1.5 ms because of eddy currents in the stainless steel chamber. We therefore do not expect the transfer to be fully adiabatic.

We find that the atoms are heated to about 2.2 μK by the transfer into the LevT. A clear measurement on the trapped sample is only possible after about 50 ms since the system initially is not in thermal equilibrium and since the untrapped atoms need to disappear from the field of view. We largely attribute the heating to imperfect phase space matching. The atomic cloud, after Raman-sideband cooling to 0.7 μK, has a $1/e$-radius of $\sim$ 350 μm. In comparison, an equilibrium distribution in the reservoir trap at 0.7 μK would have a $1/e$-radius of $\sim$ 100 μm. Potential energy is thus gained which is then turned into kinetic energy, effectively heating the cloud of atoms. In fact, without compression of the MOT (Sec. 3.3.1), the extension of the density distribution in the Raman lattice is much larger and the heating effect is even more severe, as Fig. 3.14 demonstrates. The introduction of the compression phase improved the remaining atom number after the plain evaporation by more than a factor of two.

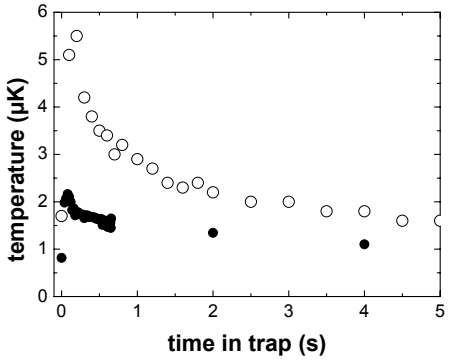

Figure 3.14.: Temperature evolution in the LevT after loading, with subsequent plain evaporation. The initial heating is attributed to phase-space mismatching between the LevT and the Raman-sideband cooled cloud (data at $t = 0$ s). The compressed cloud is heated to 2.2 μK (solid symbols). In contrast, the maximum temperature of the uncompressed cloud (open symbols) is more than a factor of two higher.

Subsequently, the hot atoms evaporate out of the trap. This phase of plain evaporation at a scattering length of 1200 a_0, corresponding to a bias field of 75 G, leads to a temperature reduction to less than 1 μK within 10 s. This is roughly $0.1 \cdot \hat{U}_{CO_2,\mathrm{eff}}$, as expected (cf. Sec. 2.2). At this point, we measure more than 4×10^6 atoms, corresponding to a peak phase space density of 2×10^{-3}.

3.4.6. Improving the loading

The inadequate phase-space matching suggests further improvements.

Adjusting the trap geometry

For a Raman-sideband cooled cloud with a temperature of 0.7 μK and a initial $1/e$-radius of 360 μm of the Gaussian density distribution, the corresponding trap frequency is calculated to be about 4 Hz. At the given powers of the CO_2 lasers this would correspond to a beam-radius of $\sim$ 1200 μm which could be accomplished by exchanging the lenses in the beam paths.

Alternatively, the radio-frequency for the AOMs could be modulated by a frequency much larger than the trap frequencies. This would effectively increase the trapping volume in the horizontal direction. The amplitude can then be adjusted for optimal phase space matching. Moreover, by lowering the modulation amplitude, an adiabatic compression of the trap to its current shape is possible. However, since the AOMs deflect the beams only in the horizontal plane the vertical extension cannot be adapted in this way.

Additional Raman-cooling sequence

Another approach to compensate for the imperfect transfer has been demonstrated by [Han01] in a setup similar to ours. After the transfer the atoms start to oscillate in the trap. After a quarter of the trap frequency the kinetic energy of the oscillating atoms is at maximum. At this point an additional phase of Raman-sideband cooling is applied to cool the ensemble.

The switching times of the magnetic fields in our setup of 1.5 ms complicate this approach. The levitation field is indispensable in the LevT but it needs to be turned off in order to apply the right field for RC. Without the cooling process the lifetime in the RC lattice is only in the order of a few milliseconds.

3.4.7. Standing-wave problem

The measurement of the beam waists of the CO_2 lasers (Fig. 3.10) shows that the optical potential by a single beam would not be confining. Even without the astigmatism, the foci of the beams would provide only a weak confinement due to their large Rayleigh length.

Nevertheless, when one of the beams is switched off, a part of the atoms stays trapped in the remaining beam. We assume that a small fraction of the light is back-reflected from the exit viewport and forms a weak standing-wave potential. The depth of this potential can be estimated by measuring the temperature of the atoms that are trapped in this potential to be in the order of 300 nK. It is assumed that here plain evaporation is suppressed due to the low density of the small number of remaining atoms. Readjusting the lasers has some influence on this effect, but does not extinguish it.

This corrugation of the optical potential is negligible in most experiments carried out in the LevT. However, in the first implementation of the *dimple trap*, which consisted of the dimple laser beam and one CO_2-laser beam, this proved to be a problem. The

measured trap frequencies could be seen to deviate significantly from the prediction at low temperatures where the corrugation starts to play a role. Furthermore, the lattice spacing of $\lambda_{CO_2}/2 = 5.3$ µm is in the order of the size of the spatial extension of the BEC thus complicating the precise determination of the properties of the BEC.

Therefore the CO_2-laser in the dimple trap had to be replaced by another laser beam, as described in the next section.

3.5. Dimple trap

When the shape of a harmonic trapping potential is adiabatically transformed to another (e.g. a tighter) harmonic potential, the density and the temperature rise, while the phase-space density remains constant. The phase-space density can decrease, if the change is made non-adiabatically. However, a deformation to a non-harmonic potential shape can also lead to a local increase in phase-space density. This has been demonstrated by the Ketterle group at MIT [SK98] where a BEC of sodium atoms was reversibly created by deforming the trapping potential.

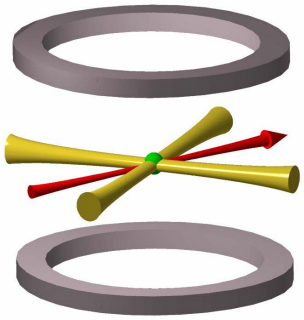

Figure 3.15.: Implementation of the dimple trap in our experiment. A tightly focused beam creates the dimple in the optical potential of the LevT.

In our setup, the deformation of the trapping potential is accomplished by a tightly focused far-off-resonance laser beam, which creates a "dimple" in the center of the LevT. This dimple trap is loaded by elastic collisions of the atoms. The LevT serves as an atom reservoir for the loading process, provided that the atom number in the dimple is always small compared to that in the LevT. Due to the tight confinement, the density in the dimple becomes much higher. However, the temperature remains almost constant, because the atoms in the dimple trap are in thermal contact with the larger reservoir. When the dimple trap is "full", the reservoir can be removed by switching off one of the CO_2-laser beams. The other CO_2-laser beam supplements the weak axial confinement of the dimple beam. We typically achieved a large local increase in phase space density, but not enough to reach quantum degeneracy.

In this trap forced evaporation can be easily implemented by lowering the laser power in the dimple. The evaporation is expected to be very efficient, since hot atoms can escape into almost the full solid angle, as a result of the magnetic levitation field.

A detailed description of the parameters used during the loading and evaporation process and the observed evaporation efficiencies will be summarized in Sec. 4.1.

3.5.1. FORT – Far Off-Resonance Trap

The dimple laser has a wavelength of 1064 nm and thus constitutes a far-off-resonant dipole trap. The detuning is larger than for a near-resonant dipole trap, such as the RC

lattice, but much smaller than the detuning for the CO_2-laser trap. In this regime, the dipole potential (U_{dip}) and the off-resonant photon scattering rate (Γ_{sc}) in a FORT are [Gri00]:

$$U_{\mathrm{dip,FORT}} = -\frac{3\pi c^2}{2\omega_{\mathrm{eff}}^3}\left(\frac{\Gamma}{\omega_{\mathrm{eff}}-\omega}+\frac{\Gamma}{\omega_{\mathrm{eff}}+\omega}\right)\cdot I, \tag{3.24}$$

$$\Gamma_{\mathrm{sc,FORT}} = \frac{3\pi c^2}{2\hbar\omega_{\mathrm{eff}}^3}\left(\frac{\omega}{\omega_{\mathrm{eff}}}\right)^3\left(\frac{\Gamma}{\omega_{\mathrm{eff}}-\omega}+\frac{\Gamma}{\omega_{\mathrm{eff}}+\omega}\right)^2\cdot I, \tag{3.25}$$

with ω being the frequency of the laser light and I its intensity. The effective transition frequency ω_{eff} and the effective line strength Γ_{eff} are defined in Sec. 3.4.1.

3.5.2. Yb fiber laser

The laser source for the dimple is an Yb fiber laser (IPG Laser PYL-2) which provides 2 W of laser light at a wavelength of 1064 nm, with a specified spectral width of about 1 nm. The fiber laser must be operated at full output power to avoid intensity fluctuations, which have been observed at lower power settings. The laser provides light with a stable linear polarization, which is important for branching off two beams using $\lambda/2$-plates and polarizing beam splitters. One beam with an intensity of 220 mW is used for the dimple beam, and 700 mW are used for the beam providing additional axial confinement, see below. Each beam passes through an AOM and the respective first order is coupled into a polarization-maintaining single mode optical fiber. To assure stable beam pointing and a perfect Gaussian beam shape, the light is transported through fibers to the experimental table. After the fiber a small fraction of the light of each beam is split off and is directed to a logarithmic photodiode which allows for precise determination of the intensity over several orders of magnitude with equal accuracy. The photodiode is connected to a computer programmable PID feedback loop device which controls the power of the AOM driver and allows for stabilization and accurate ramping of the intensity.

3.5.3. Trap configuration

A maximum of 160 mW after the fiber coupling is available for the dimple beam. The light is expanded to a beam waist of 8 mm and subsequently focused by a lens with a focal length of 300 mm to a waist of 34 µm at the experimental region. At the maximum power this provides a trap depth of 21 µK. The lens is mounted on a translation stage to shift the focus precisely into the experimental region. To fine-tune the beam pointing, the mirror before the lens is mounted on tunable piezo electric crystals.

The dimple beam D1 runs horizontally at a 30° angle to the x-axis which is defined by CO_2-laser beam L2. With a Rayleigh-length of 3.4 mm the dimple beam alone gives only a very weak axial confinement in the direction where additionally the magnetic

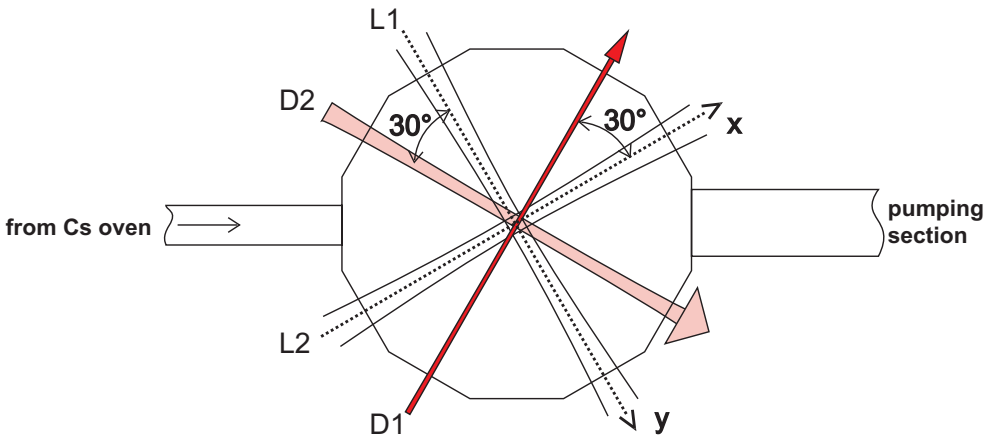

Figure 3.16.: Schematic of the beam configuration. The CO_2-laser beams Laser1 L1 and Laser2 L2 cross at an angle of 90°, the tightly focused dimple beam D1 propagates at 30° with respect to CO_2-laser beam L2. The additional 1064-nm laser beam D2 has an angle of 30° with respect to CO_2-laser beam L1 and is thus perpendicular to D1.

forces counteract the trapping potential. To supplement the confinement in the axial direction of the dimple laser beam, we use two additional laser beams. The beam configuration is shown in Fig. 3.16. The combination of CO_2-laser beam L1 with the dimple beam provides a deep potential of several μK as it is needed after the loading and in the early stage of the evaporation. However, due to the standing-wave problem described in Sec. 3.4.7, this combination is not suited at the end of the evaporation when the BEC is produced. The calculated potentials in the horizontal direction ($z = 0$) and in the vertical direction ($y = 0$) are illustrated in Fig. 3.17. The chosen intensities

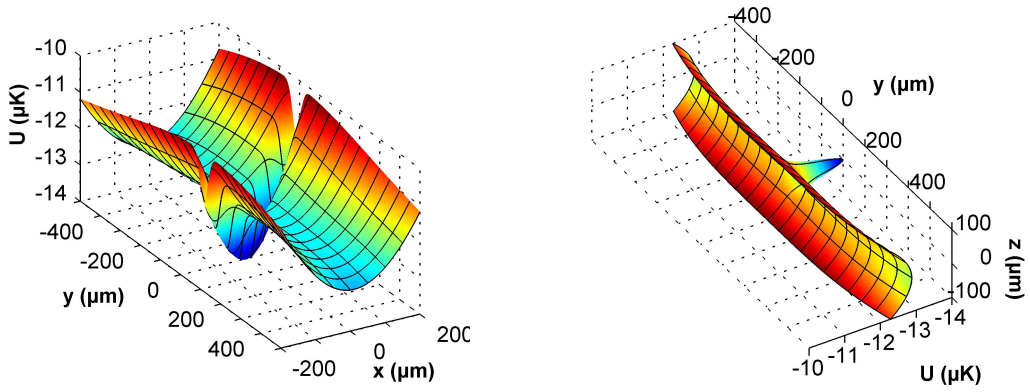

Figure 3.17.: Potential of the dimple trap in an intermediate stage of the evaporation. CO_2-laser beam L1 is on full power and the dimple beam D1 has a power of 10 mW. The additional 1064-nm beam D2, at a power of 220 mW, is barely visible. The levitation field and a bias field of 21 G are included which produce an anti-trapping potential, aiding the evaporation.

are typical for an intermediate stage of the evaporation. The plots visualize that the curvature produced by the magnetic gradient aids the evaporation because hot atoms that have escaped the trapping potential are quickly removed.

For the last stage of the evaporation we use the dimple beam in combination with the additional 1064-nm laser beam. The beam runs horizontally at an angle of 90° with respect to the dimple beam. The beam has a waist of 260 µm at the trap center. At the maximum available intensity of 500 mW the trap depth is only 1.2 µK, therefore the CO_2 laser is indispensable in the early stage of the evaporation. The additional 1064-nm beam is typically operated at 220 mW corresponding to a trap depth of 520 nK. The intensity is ramped up together with the intensity in the dimple beam. Its effect on the total potential is negligible compared to the CO_2 laser and the dimple beam. When the cloud is sufficiently cold, the intensity of the remaining CO_2 laser is adiabatically ramped to zero. The drift in the CO_2-laser beam position does not appear to be critical at this stage. The potential of the trap, consisting of the dimple beam and the additional 1064-nm beam, is illustrated in Fig. 3.18. The values for the intensities and the

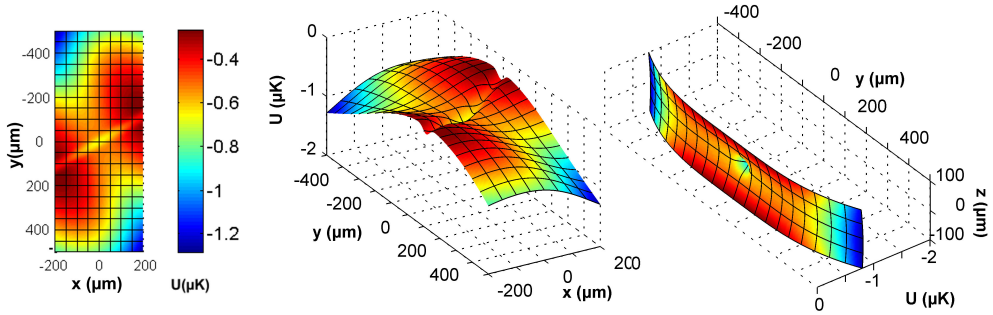

Figure 3.18.: These potentials represent the dimple trap when the BEC is produced. The CO_2 laser is completely turned off. The powers in the dimple and the additional 1064-nm beam are 1 mW and 220 mW, respectively. In the plan view of the potential (*left*) the potential created by the two beams crossing at 90° is visible. The bias field is 21 G.

magnetic bias field in the figure represent the trap at the end of the evaporation. The plots of the potential in the horizontal direction illustrate that due to the anti-trapping potential caused by the magnetic field gradient (cf. Eq. (3.11)) the beams have to cross in the center ($x = 0, y = 0$). Otherwise the magnetic forces are too strong and the trap is no longer confining. Also, the table inclination becomes a critical parameter at such small trap depths, as explained in Sec. 3.2.6.

This setup is well suited for efficient loading of the dimple trap and efficient forced evaporation. With the additional 1064-nm beam we have eliminated the standing-wave problem for experiments with the BEC. The trapping conditions in the final trap in which the BEC is stored can be flexibly varied to investigate the properties of the BEC. Furthermore, for certain types of experiments where a magnetic field gradient is undesirable, the intensity of the dimple beam can be raised to $\geq$ 35 mW where the trapping strength is sufficient to hold the atoms without the aid of the levitation field.

3.6. Experimental control

Our typical experimental cycles last several seconds. Within this time several digital channels, e.g. switching on/off of AOMs or optical shutters, and analog channels, for e.g. ramping laser intensities or magnetic fields, have to to be operated with microsecond precision.

We chose a real-time microprocessor board with onboard memory. The experimental sequence is prepared in a self-made computer interface and transferred to the microprocessor board. Once programmed the board can execute an experimental cycle independently.

During this work the experimental control setup was extended: For the latest experiments (Sec. 5.1.2) more analog channels were required, therefore an additional microprocessor card was installed. Furthermore, the reproducibility of the magnetic fields was limited by environmental field fluctuations. Therefore, the internal cycle of each card is triggered by an external clock, both synchronizing the cards to each other and to the power line.

3.6.1. Microprocessor board

We found that the microprocessor board ADwin-Gold (Keithley ADwin-Gold with option ADwin-Gold-DA) with 4 MB onboard memory fulfills the requirements of our experiment. The additionally installed ADwin board is similar (ADwin-Gold-ET, option ADwin-Gold-DA) except for an ethernet port used for programming the device and additional onboard memory which amounts to 16 MB. Each board features 32 digital TTL-compatible I/O channels and 8 analog output channels with a resolution of 16 bit and an output range of ±10 V. Further, 16 analog inputs on each board are available which are not used in our present setup. Details on the response times of the channels can be found in [Web03a].

The onboard memory allows storage of the complete sequence for an experimental cycle. It is executed by the built-in microprocessor, thus the timing is always precise down to 1 μs, independent of the load of the host computer.

3.6.2. Interface

To create, translate and transfer the program for the experimental sequence onto the ADwin board, an interface has been created in LabVIEW (National Instruments LabVIEW 6.1). It allows a flexible programming of events defining the state of digital channels and the output voltage of analog channels. The possibility to define nested loops provides a great flexibility to define a complete series of experiments. For instance a fully automated evaporation experiment can be carried out where the temperature (see Sec. 3.7.3) is measured at different values of the final laser power. The variable parameters are stored in a file on the hard drive.

For all the simplicity of the interface, it has so far fulfilled all experimental needs. Only small modifications have been made, e.g. to additionally program a signal generator (Stanford Research Systems DS345 30 MHz arbitrary waveform generator), and to address the second ADwin board.

3.6.3. Line trigger

Synchronizing the experimental timing with the power line significantly improves the reproducibility of the magnetic fields, because the main contribution of the residual alternating fields is synchronous to the power line, cf. Sec. 3.2.2.

The frequency of the power line is not stable and dithers around the central frequency of 50 Hz by 10^{-3}. Synchronizing the start of the experiment is thus not sufficient since the accumulated deviation over several seconds of the experimental cycle would become too large. As a solution, the frequency of the power line is constantly measured and divided into 20000 equal time steps by the *timing box*. These steps are used to externally trigger the 10 µs time steps of both ADwin boards. The jitter of each time step is measured to be on the order of 10^{-3}. To measure the effect of this synchronization, we probe environmental magnetic fluctuations by using short (4 ms) RF pulses, see Sec. 3.7.1. We can resolve magnetic field fluctuations with an amplitude of 4 mG, synchronous to the power line. This shows that the reproducibility of our magnetic fields is in the sub-mG range.

3.7. Detection and diagnosis

A precise knowledge of the trap properties, the magnetic fields, and the properties of the ensemble, i.e. the particle number and the density distribution, are crucial in every step of the experiment. The implemented tools for detection and diagnosis are described in the following.

3.7.1. Radio-frequency induced spin flips

The combination of a weak optical trap and magnetic levitation allows for the localized removal of atoms using radio-frequency induced spin flips. As shown in Fig. 3.19 the different magnetic substates $m_F = 3$ and $m_F = 2$ experience a different potential due to the difference in magnetic moment. While the magnetic field gradient is matched to levitate atoms in the state $m_F = 3$, the potential for atoms in $m_F = 2$ is not confining. An applied radio-frequency matching the difference in magnetic energy, transfers atoms from $m_F = 3$ to $m_F = 2$. Due to the vertical magnetic field gradient, the resonance frequency for those spin flip transitions varies with the vertical position in the trap.

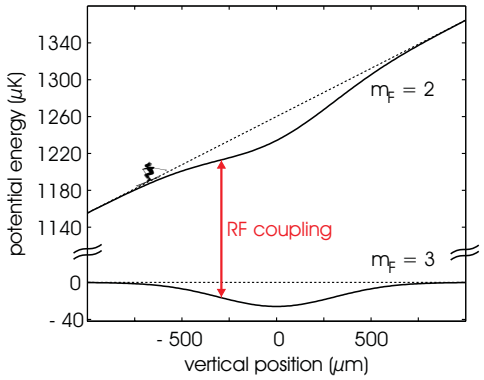

Figure 3.19.: The optical potential in the LevT where the gravitational potential is canceled by the magnetic levitation field for atoms in $F = 3, m_F = 3$. The corresponding potential for atoms in the state $F = 3, m_F = 2$ is not confining due to their different magnetic moment.

Magnetic field calibration

This constitutes an excellent tool to calibrate the magnetic field in the trap. In a levitated trap, the LevT or a weak dimple trap, the radio frequency directly leads to the removal of trapped atoms. An example is given in Fig. 3.20, which shows the calibration of the magnetic field at which the BEC is created. A fit reveals the center frequency of (7.317 ± 0.001) MHz.

Including the quadratic Zeeman effect, the corresponding magnetic field can be calculated:

$$B(\nu) = \frac{4h\nu}{\mu_B}\left(1 + \frac{h\nu}{\Delta E_0}\right) \tag{3.26}$$

$$B(\nu) = 2.85796\frac{\mathrm{G}}{\mathrm{MHz}}\nu\left(1 + 5\frac{\nu}{\nu_{\mathrm{HFS}}}\right). \tag{3.27}$$

Here ν is the determined center frequency and ν_{HFS} is the frequency splitting of the ^{133}Cs ground state, see Sec. 3.3.

In a "tight" trap, when the atoms can be trapped without levitation, this method can also be used. Applying the radio frequency in the trap with a subsequent free expansion in the presence of the levitation field separates the different magnetic substates. In both cases a fit to the remaining number of atoms in $m_F = 3$ versus the radio frequency reveals the magnetic field over the sample in the trap.

RF forced evaporation

The above described method can be used as a RF-knife for forced evaporation. Although the evaporation proceeds in only one dimension, this is a possible cooling mechanism as explained in Sec. 2.2.1. This path was pursued for an extended period of time and then dropped in favor of the more efficient dimple approach. We found

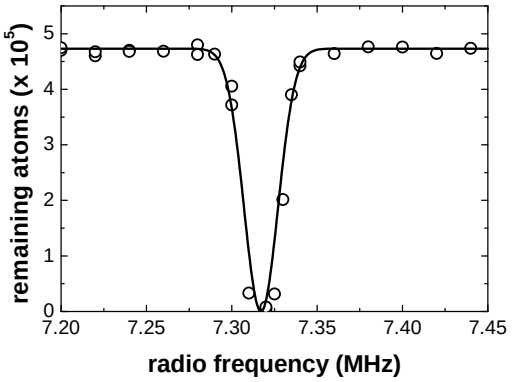

Figure 3.20.: Radio frequency calibration of the magnetic field value at which the BEC is created. A fit reveals the center frequency of (7.317 ± 0.001) MHz.

that due to three-body recombination heating [Web03c] the one-dimensionality of the evaporation is not sufficient to reach quantum degeneracy. A detailed description and discussion of these experiments can be found in [Web03a].

3.7.2. Imaging

After an experiment has been carried out it is necessary to extract information from the atomic cloud. The standard techniques we use both involve scattering photons on the sample. For *absorption imaging* the sample is irradiated with a resonant light pulse and the shadow of the cloud is imaged onto a CCD chip. This gives detailed information about the atom number and the density distribution of the sample. Alternatively *fluorescence* of the cloud in a MOT can be recorded with a photodiode or a CCD camera. The number of photons counted can be used to infer the number of atoms. Both methods impart several photon recoils onto each atom and are thus destructive.

Absorption imaging

Absorption imaging is easy to set up and a suitable technique to probe the atomic density distribution. The atoms are illuminated by light resonant with the $F = 4 \rightarrow F' = 5$ atomic transition and the shadow of the cloud is imaged onto a CCD chip. The amount of light absorbed is related to the column density of the atoms in the cloud giving rise to the atom number and the density distribution. The image is compared to a reference image taken under the same conditions but without atoms. This makes absorption imaging essentially independent of background light or the intensity distribution of the illuminating light. The image analysis is carried out according to [Ket99]. The axis of our main absorption imaging system lies in the horizontal plane and is perpendicular to the atomic beam. The camera system is a triggerable slow-scan frame transfer CCD camera (Theta System SIS-99/PH, 1024 × 1024 pixels, 14 bit resolution). The optical setup used for imaging is described in [Web03a]. The theoretical resolution limit,

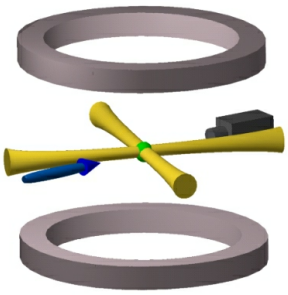

Figure 3.21.: Scheme for the horizontal absorption imaging. The imaging beam and the camera are indicated with respect to the crossed CO_2-laser trap.

given by the size of the observation viewport, is calculated to be 5 μm. The pixel size has been calibrated to correspond to 6.021 ± 0.015 μm by measuring the position of a free falling cloud.

When the imaging light is slightly detuned from resonance the atomic cloud has a index of refraction different from one. Additionally to absorption, a dense sample thus acts as a lens with index of refraction larger or smaller than one, depending on the sign of the detuning. The distortion of the resulting image is minimized when the sample is exactly in the focus. This effect was exploited to fine-tune the imaging system. By imaging objects with an extension well below the resolution, e.g. a small BEC, the resolution limit was experimentally determined to be ~ 8 μm.

For absorption imaging a weak probe laser pulse is needed, i.e. the intensity of the beam has to be well below saturation. By measuring the absorption vs. detuning of the laser frequency, the width of the resonance is determined. Through repeating this measurement for different intensities of the probe light, we could determine the maximum applicable intensity where the line is not broadened.

The validity of our atom number measurement could be independently confirmed by other measurements, see Sec. 4.2.2.

Absorption imaging at high magnetic field

Our standard absorption images are taken at zero magnetic field. The scattering rate is thus assumed to be the average over all possible transitions. Due to the relatively slow magnetic field response in our setup, cf. Sec. 3.2, absorption imaging is only possible after several milliseconds. Therefore it was not possible to image the ensemble directly in the trap. Additionally, for imaging a BEC which spends several milliseconds at large negative scattering length (below 17 G), see Sec. 2.4.4, the measured size of the cloud could be distorted.

These problems can be overcome by implementing an imaging technique that can be used at magnetic fields of several Gauss. The detuning of the probe laser can be tuned by the experimental control system. The polarization is adjusted to be in the

horizontal plane, perpendicular to the vertical magnetic field. It is evident that the choice of the polarization has no effect on the imaging at zero magnetic field where no quantization axis is assigned. For imaging at non-zero magnetic fields the absorption laser is tuned to resonance[3]. We use the same image analysis as described above, but due to the different optical transitions involved, the atom number was calibrated against the values measured for imaging at zero magnetic field.

Known problems

In spite of the improvements of the imaging system, e.g. fine-tuning of the focus and high field imaging, the measured size of a BEC in the trap was 50% larger than the calculated size as expected by the Thomas-Fermi approximation (given by Eq. (2.36)). Furthermore, the measured atom number drops for high atomic densities, e.g. at short expansion times.

This artefact could be caused by probe light that cannot be absorbed by the atoms. At low optical densities the contribution of this light is not significant. However, when the optical density is high, i.e. the absorption is close to 100%, the additionally counted photons lead to a strong underestimation of the column density. This effectively reduces the measured number of atoms and leads to a larger apparent size, explaining the observed effect.

Vertical imaging system

Another absorption imaging system has been installed whose optical axis runs at an angle of $\sim 20°$ to the vertical axis. The two systems together provide full spatial information. The image is taken by a triggerable video camera (Hitachi KP-F2A). In the current setup the resolution of the camera is limited by the pixel size of CCD chip to 11 μm.

Although the Hitachi camera has a higher sensitivity at 852 nm its signal-to-noise ratio makes it unsuitable for the observation of the BEC. Since all results presented in this thesis are taken using the Theta-System CCD camera, the reader interested in more details of the Hitachi system is referred to [Web03a].

Imaging sequence and analysis

To take an absorption image at the end of an experimental cycle, a sequence of events is defined, as described in Sec. 3.6. Since the atoms are in the $F = 3$, $m_F = 3$ and the imaging light is resonant to $F = 4 \rightarrow F' = 5$, additional light from the repumper is needed. We found that switching on the MOT repumper light 50 μs before the imaging is sufficient to bring all atoms into the resonant state. An imaging pulse of ≥ 100 μs gives an adequate signal-to-noise ratio. The imaging sequence includes an event which

[3]The variation in magnetic field over the sample due to the magnetic gradient is much smaller than the linewidth of the absorption and has no notable effect for small samples.

triggers the camera to take a picture. The exposure time of the camera is 2 ms. The reference image is taken under the same conditions a few hundred milliseconds later. Both images are immediately transferred to a computer and analyzed by a self-made LabVIEW application which processes and displays the resulting absorption image. Built-in fit functions give the atom number and the $1/e$-radii of a Gaussian distribution in the vertical and the horizontal direction. For experiments with a BEC we replenished the analysis by a fit to a bimodal density distribution giving atom number and the $1/e$-radii of the thermal distribution as well as the atom number and the Thomas-Fermi radii of the BEC.

The results are stored in a file together with the variable parameters of the experimental control system. Another LabVIEW interface can be used to read this file and to export and display the data. The convenient realtime visualization of the data is very valuable to quickly detect failures which occur during operation of the experiment and has greatly sped up the optimization cycle.

Fluorescence

In principle the two cameras used for absorption imaging can also take fluorescence images. For this the MOT is activated and the fluorescence of the atoms is detected by the CCD chip. This method, however, is inferior to the described absorption imaging since it does not give information about the spatial distribution of the atoms and was therefore rarely used. As an alternative, a calibrated photodiode is on hand but has not yet been installed.

We employ two small cameras (Conrad Electronics, CCD-MINI-FINGER-KAMERA S/W) to monitor the fluorescence of the MOT. Although no scientific data is gained from these, they serve as a reference for the experimentalist, because they immediately reveal the failure of a current supply or an unlocked laser.

3.7.3. Thermometry

To measure the temperature of a thermal ensemble in the trap or the release energy in the case of a BEC, we perform time-of-flight measurements. At the end of the experimental cycle the optical trapping potential is shut off and the cloud expands for a time t. The experiment is repeated and an image is taken after different expansion times, which yields the 1/e-radii of the expanding cloud ($\sigma_{x,y}(t)$). A fit to the measured widths of the cloud according to Eq. (3.28) yields the temperature, $T_{x,y}$, in the respective direction.

$$\sigma_{x,y}(t) = \sqrt{\sigma_0^2 + \frac{2k_B T_{x,y}}{m_{\mathrm{Cs}}}\, t^2} = \sqrt{\sigma_0^2 + T_{x,y}\, \frac{125\mu\mathrm{m}}{\mu\mathrm{K\ s}^2}\, t^2}, \tag{3.28}$$

with m_{Cs} being the mass of cesium and σ_0 the initial size at $t = 0$, which is a free parameter in the fit. The expansion energy (Sec. 2.4.4) of a BEC is determined analogously.

An expansion in the presence of the levitation field allows to measure at expansion times longer than 200 ms since the sample does not drop out of the field of view. In the vertical direction the temperature or the release energy can be directly inferred. In the horizontal direction the effects of the magnetic forces have to be taken into account, see Eq. (3.12) and Eq. (3.13).

3.7.4. Trap frequencies

A precise knowledge of the trap frequencies is crucial to determine the properties of a trapped sample, e.g. phase-space density, elastic collision rates, and 3-body loss rates. We established various methods to determine the trap frequencies which allow us to compare the results or adapt the adequate approach.

Center-of-mass oscillation

An adiabatic (and small) change in the magnetic levitation gradient pulls the trapped cloud in the vertical direction. A fast switch back to the perfectly matching levitation field leads to a center-of-mass oscillation of the cloud around its equilibrium position. Recording the position, directly yields the trap frequency in the vertical direction. An additional free expansion is a measure for the momentum of the oscillating cloud. This gives a better signal-to-noise ratio but in principle yields the same result. An example measurement is displayed in Fig. 3.22.

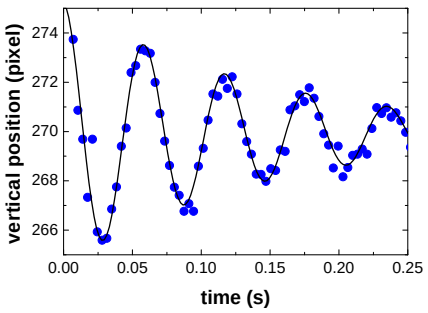

Figure 3.22.: Example for a trap frequency measurement of the vertical trap frequency in the LevT by exciting and observing the center-of-mass oscillation of the cloud.

This method also works for determining the horizontal trap frequencies. The excitation is accomplished by adding a horizontal bias field in x- and y-directions, respectively. The shifted quadrupole field adds a horizontal force. In contrast to the breathing oscillations, see below, this method is not affected by the two-body interactions [Pit03].

Parametric excitation

As outlined in Sec. 2.2.3 an oscillation of the center position of the potential with the trap frequency, or a modulation of the potential strength with twice the trap frequency,

finally leads to heating of the sample. The heating is typically accompanied by a loss of atoms due to plain evaporation. Both effects can easily detected.

A modulation of the potential strength can be accomplished by modulating the laser intensity of the respective beam. Modulating the gradient field strength constitutes a vertical oscillation of the trap center. The results obtained with this method must be more carefully interpreted since in a Gaussian shaped trap a hotter sample experiences a weaker potential.

Breathing oscillations

Breathing oscillations of the trapped sample can be excited by changing the strength of the trapping potential, e.g. by suddenly changing the trapping laser intensity or by switching off the trap for a short period of time. For an ideal thermal gas the frequency of the breathing oscillation is twice the trap frequency[4]. By either monitoring the breathing of the cloud directly or by monitoring the momentum distribution after a period of free expansion the trap frequency can be inferred.

Alternatively, a breathing oscillation in one direction is excited by switching off one laser beam for a short time. After a variable waiting time Δt the beam is shortly switched off again. If the switch-off happens in a period of expansion atoms will be lost, whereas in a period of contraction the atom loss is reduced. Monitoring the atom loss for different waiting times Δt, the trap frequency can be deduced. The advantage of the described method is that it is independent of the imaging method and that the trap frequency can be measured exactly perpendicular to the laser axis.

[4] In the case of a strongly interacting quantum gas this assumption is no longer valid [Dal99a].

4. BEC of Cesium - a Tunable Quantum Gas

One of the main experimental results of this thesis was the Bose-Einstein condensation of cesium. The project was started in summer 2000 with the aim to create the first cesium BEC. With the implementation of the levitated dipole trap it was possible to study the three-body recombination process of Cs atoms, described in [Web03c]. The results were fundamental for the strategy used for efficient evaporation towards BEC and led to the implementation of the dimple trap. In October 2002 the first milestone was reached and a BEC of 16000 Cs atoms was created [Web03b]. These experiments are in detail described in the thesis of Tino Weber [Web03a]. Subsequent improvements of the setup and an improved trap loading and evaporation scheme resulted in a BEC with ten times more atoms. This comparatively large BEC was used to probe the tunability of the BEC in several experiments [Kra04]. This BEC is an ideal starting point for the creation of ultracold molecules, which will be covered in the next chapter 5.

4.1. Optimized production of a cesium BEC

Our experimental strategy towards BEC of Cs has been detailed in Sec. 2.3.2. In short, we employ a sequence of optical traps in such a way that the loading from one trap to the next can be performed efficiently. A large and shallow optical dipole trap (LevT) provides excellent loading conditions for the pre-cooled sample. This trap serves as a reservoir for loading a tighter optical dipole trap. In this dimple trap evaporation towards Bose-Einstein condensation can be performed efficiently.

The central part of the experiment is the large volume CO_2-laser trap with magnetic levitation, the LevT. In the first setup a sample of 2×10^6 atoms at a temperature of $\sim$ 1 μK was available after loading and subsequent plain evaporation for 10 s. Our first attempts towards BEC of cesium were done in this trap using the RF-induced evaporation as described in Sec. 3.7.1. However, the achieved phase-space density never exceeded 0.1. The evaluation of measurements on the three-body recombination in our trap [Web03c] and a simulation of the evaporation process gave clear evidence that the one-dimensional evaporation process was a limiting factor. The search for a new strategy led to the implementation of the dimple trap. Shortly upon completion

of the dimple setup, in the early morning hours of October 5th 2002, we created the first BEC of cesium with 16000 atoms. To demonstrate the tunability of this quantum gas, we explored various regimes of condensate self-interaction. The experimental procedures are described in detail in [Web03b] and [Web03a].

Optimization of the experimental steps and of the evaporation strategy yielded an essentially pure BEC with 1.1×10^5 atoms. In the following I will focus on the optimized production of a Cs BEC and the experiments performed with this comparatively large condensate [Kra04]. Due to the ongoing optimization the number is still growing and has recently reached 2×10^5 atoms.

4.1.1. Pre-cooling

The initial collection and cooling of Cs atoms is achieved by conventional techniques which in combination are very well suited to load the first stage of optical trapping, the LevT (Sec. 3.4). The atoms are loaded into the MOT from the Zeeman slowed atomic beam until up to 3×10^8 atoms have accumulated after about 6 s. The MOT is compressed as described in Sec. 3.3.1. Subsequently, the MOT light is switched off. Due to the compression of the MOT a spatially much smaller but rather hot sample is produced. To cool the compressed cloud, we then apply Raman-sideband cooling (Sec. 3.3.2). The application of Raman-sideband cooling is advantageous in several ways: the spatial distribution is fixed by the optical lattice, the sample is further cooled, and the atoms are polarized in the desired $F = 3$, $m_F = 3$ state.

The ensemble is then adiabatically released from the lattice after 6 ms of cooling time. If the atomic cloud is released into free space, the temperature of the ensemble with up to 4×10^7 atoms is about 0.7 μK. For our typical atomic densities this corresponds to a phase space density of 1×10^{-3}.

4.1.2. Plain evaporation in the LevT

For transfer of the pre-cooled atoms into the LevT, we leave the light of the two CO_2-lasers on during the entire pre-cooling phase (Sec. 3.4.5). The trap is then activated by ramping up the magnetic levitation and the bias field. Due to the prior compression of the cloud, the better phase-space overlap with the LevT reduces the heating of the sample (cf. Fig. 3.14) during the transfer. As a result the number of atoms in the LevT 10 s of after plain evaporation is increased by more than a factor of two to $\geq 4 \cdot 10^6$ atoms. Furthermore, due to the reduced heating less time for plain evaporation is necessary. This speeds up the experimental cycle by several seconds and improves the number of atoms available for loading the dimple.

4.1.3. Dimple trap

The various stages of trap loading and evaporative cooling are illustrated in Fig. 4.1. After 2 s of plain evaporation in the LevT, we proceed with loading of the dimple trap

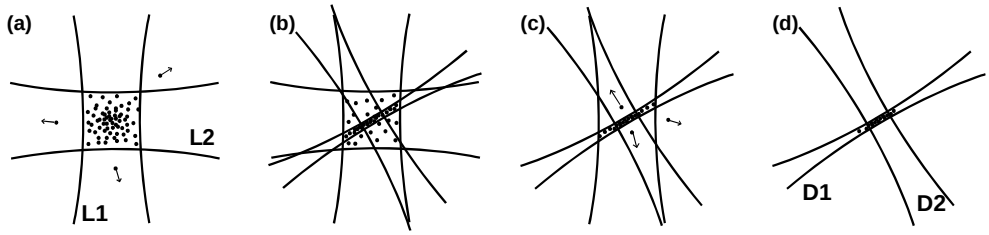

Figure 4.1.: Illustration of the various stages of trap loading and evaporative cooling as seen from above. (a) Plain evaporation in LevT at a scattering length of $a = 1200\ a_0$. The CO_2 lasers are labelled L1 and L2. (b) The dimple is created by ramping up the power in the dimple beam D1 and the additional 1064-nm beam D2. The dimple is loaded by elastic collisions. (c) Forced evaporative cooling after switching off CO_2-laser beam L2. The power of all remaining lasers is ramped down, and the power in CO_2-laser beam L1 is reduced to zero. (d) Final configuration of the dimple trap.

(Sec. 3.5). At this point the atom number in the LevT is 7.8×10^6 and the phase space density is 1.7×10^{-3} (see Fig. 4.3).

Loading

The powers in the beams D1 and D2 are ramped up within 1.5 s to a maximum power of 70 mW and 270 mW, respectively. The trapping in the dimple is now briefly done by all four laser beams with D1 providing most of the radial and L1 most of the axial confinement. After switching off beam L2 we measure the radial and axial trap frequencies in the dimple to (221.2 ± 1.6) Hz and (14.2 ± 0.1) Hz, respectively. During the ramping up phase we reduce the magnetic field offset to 23 G and thus the scattering length to 300 a_0 in order to reduce losses from three-body recombination. The dimple trap now contains about 1.7×10^6 atoms at a peak phase space density of approximately 1.3×10^{-1}. The increase in peak phase space density by a factor of ~ 100 demonstrates the efficiency of this strategy to load an optical dipole trap.

Forced evaporation

We start forced evaporative cooling by ramping down the power in all three remaining beams. Simultaneously we remove the reservoir by switching off the CO_2-laser L2 that is not responsible for axial confinement. The intensity ramps of the laser beams are plotted in Fig. 4.2 together with the variation of the scattering process. The CO_2-laser beam L1 is ramped to zero within 5.5 s so that D2 at the end of evaporation exclusively assures axial confinement. For the power in the dimple beam D1 we approximately follow an exponential ramp over 5.5 s. The power in beam D2 is only slightly reduced. The final powers in D1 and D2 are 0.5 mW and 220 mW, respectively.

We find and optimize this ramp by extending the ramp in discrete time steps of a few hundred milliseconds at the beginning and up to seconds towards the end of the

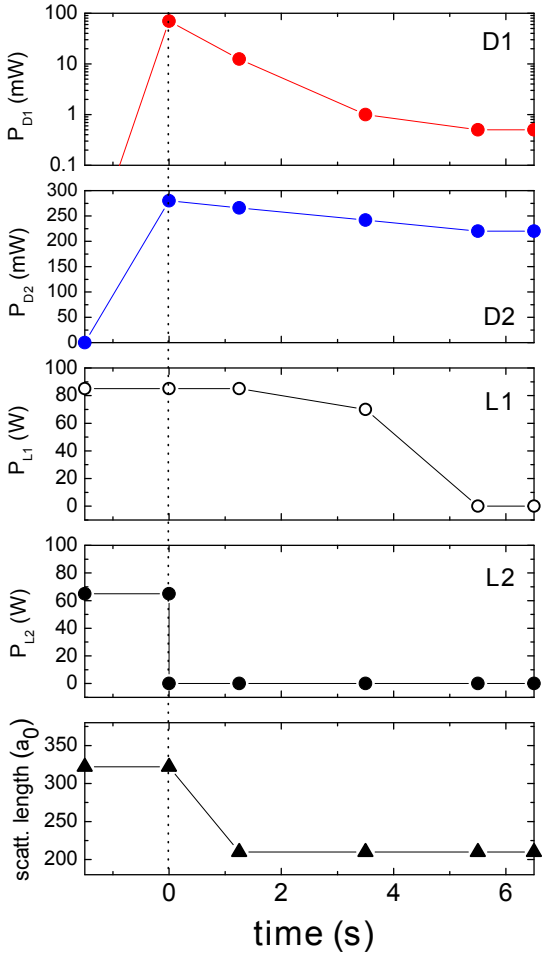

Figure 4.2.: Laser intensities in the dimple trap during loading and forced evaporation. Loading is achieved by ramping up the power in the dimple laser D1 and in D2 within 1.5 s. *Upper plot:* forced evaporation starts at $t = 0$ s and is mainly accomplished by reducing the laser power in D1 over several orders of magnitude. *Middle plot:* the power in D2 is only slightly reduced. *Lower plot:* The laser power of the remaining CO_2-laser beam L1 is reduced to transfer the atoms into the final dimple trap created by D1 and D2.

ramp. At each step we vary the final laser power in the dimple and the scattering length while searching for a maximum in evaporation efficiency ϵ according to Eq. (2.8). This results in an overall optimization of the evaporation path. We find that a magnetic field value of 21 G corresponding to a scattering length of $a = 210\ a_0$ is optimal during most of the forced evaporation phase, cf. Fig 4.2. As can be seen from Fig. 4.3 the evaporation efficiency ϵ lies around 3 during the forced evaporation ramp. We attribute this high efficiency to the fact that atoms can escape the trap into almost the full solid angle due to the levitation field.

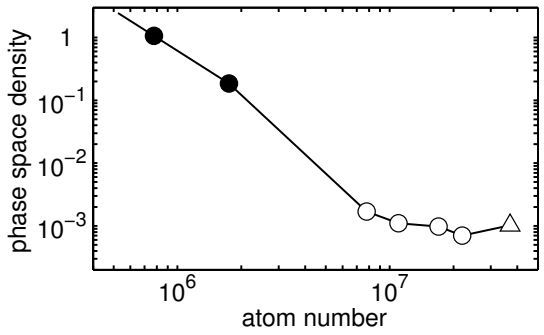

Figure 4.3.: Peak phase-space density as function of atom number. The path of evaporation proceeds from right to left. The *triangle* shows the atomic ensemble immediately after RC. The *open circles* show the ensemble in the LevT after 0.08, 0.22, 0.64, and 2.0 s. The *filled circles* correspond to the sample in dimple trap right after loading and after 1.5 s of evaporation. The phase transition occurs after 2 s of forced evaporation with $\sim 5 \times 10^5$ atoms left in the dimple trap.

Phase transition

Fig. 4.4 illustrates the momentum distribution of the ensemble at different phases of the evaporation. We observe the phase transition after 2 s of forced evaporative cooling with about 5×10^5 atoms at a temperature of (200 ± 10) nK. At this point the power in beams D1 and D2 are 1.0 mW and 240 mW. The duration of the ramp is relatively short. The inferred elastic collision rate is higher than expected. We attribute this to the corrugation of the dimple potential while CO_2-laser beam L1 is still on which effectively produces further local regions with high atomic density.

Our evaporation proceeds close to or within the hydrodynamic regime. Thus, significant improvement of the evaporation is not to be expected.

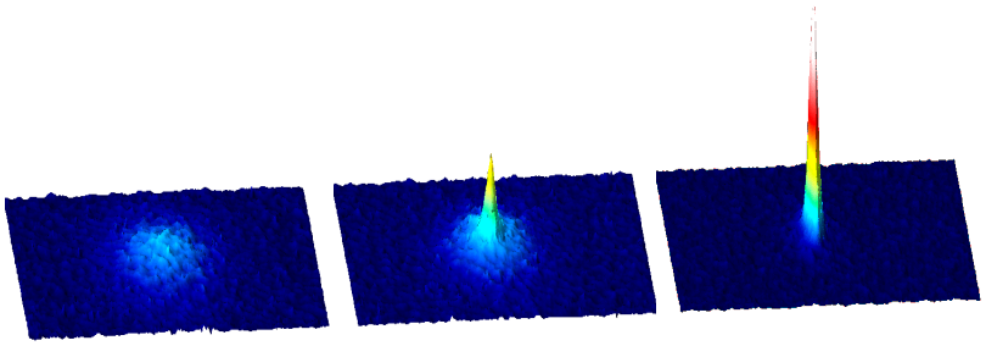

Figure 4.4.: Density distribution of the cloud after free expansion (for zero scattering length) at different stages of the evaporation. *Left*, a thermal distribution. *Middle*, bimodal distribution consisting of the condensed part and the thermal cloud. *Right*, almost pure condensate.

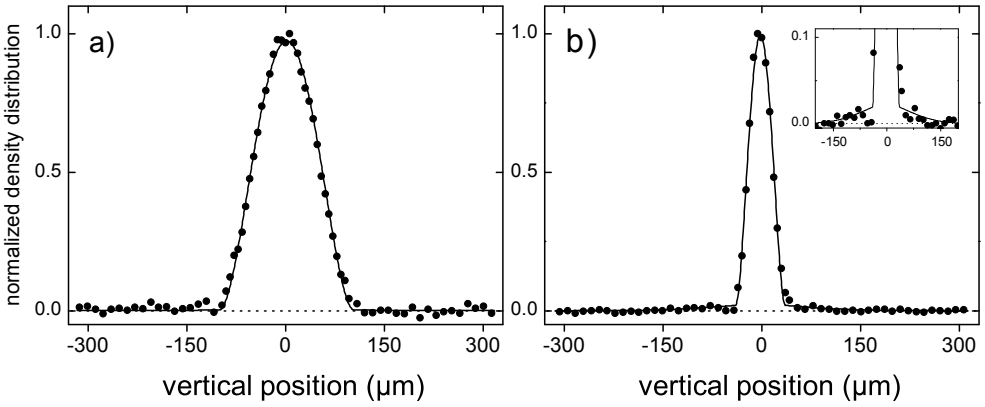

Figure 4.5.: Vertical density profiles of Cs condensates after 100 ms of free expansion in the levitation field. The solid curves are fits to the data for the Thomas-Fermi profiles which include possible thermal components. a) Expansion with no change in scattering length. The total number of atoms is $N = 1.1 \times 10^5$. b) Expansion near zero scattering length under the same conditions reveals a small thermal component, shown in the inset.

4.1.4. Condensate properties

Further evaporation leaves a cigar-shaped condensate with the long axis in the horizontal plane. In Fig. 4.5 we show vertical density profiles of expanding condensates. The tunability of the scattering length allows us to influence the expansion. For Fig. 4.5 a) we expand the condensate at the creation scattering length of 210 a_0. This is the usual type of self-similar expansion in which the condensate in the Thomas-Fermi regime retains its parabolic shape, see Sec. 2.4.4. For Fig. 4.5 b) we step the scattering length to zero at the moment of release from the trap. The mean-field interaction thus vanishes and the rate of expansion is greatly reduced. This exposes a small thermal component, for which a bimodal fit reveals a temperature of around 11 nK. The critical temperature at these trapping conditions is 24 nK, therefore the predicted condensate fraction of 90% (cf. Eq. (2.22)) agrees very well with the measured value of 91%. From the fit to the data in Fig. 4.5 we obtain that there are up to 1.1×10^5 atoms in the condensate with a 20% calibration error[1]. For this particular experiment we measure the final trap frequencies to (4.3 ± 0.2) Hz and (21.1 ± 0.2) Hz along the axial and radial direction, respectively. We thus infer for the initial Thomas-Fermi sizes $R_r^{TF} = (8.7 \pm 0.3)$ μm and $R_{ax}^{TF} = (42.5 \pm 1.2)$ μm along the radial and axial directions at a scattering length of $a = 210\ a_0$, cf. Eq. (2.36). The corresponding peak density of the condensate is $n_0 = (2.1 \pm 0.1) \times 10^{13}$ cm^{-3}.

By improving the setup and the adjustment it was possible to further raise the particle number in the BEC to more than 2^5. A large gain is attributed to extending the

[1]The error does not come from the fit but from the overall uncertainty in determining the atom number. Usually, the error from absorption imaging alone is around 50%, but we can calibrate the atom number from measurements on the chemical potential, see Sec. 4.2.

waist of the additional 1064-nm beam D2 to 340 μm and increasing the power of this beam to 500 mW.

4.2. A tunable quantum gas

The cesium atom is very attractive for experiments with tunable atomic interactions. As outlined in Sec. 2.1.4, the lowest internal quantum state of Cs, $F = 3$, $m_F = 3$, features a unique combination of wide and narrow Feshbach resonances which are easily accessible at low magnetic fields. This results in a great flexibility for tuning the atomic scattering properties. The tunability of the atomic interaction can be exploited in experiments where one might wish to adjust or to dynamically change the mean-field interaction of a Cs condensate.

We demonstrated the tunability of the condensate interaction in several experiments. In order to explore the different regimes of self-interaction, we switched to a variable magnetic field synchronously with the release of the condensate from the trap. In this first measurement, we realized imploding, exploding and a "frozen" condensate at positive, negative and vanishing scattering length, respectively. These measurements were done following the first realization of a Cs BEC.

Several technical improvements together with the optimized production of a large Cs BEC enabled more quantitative measurements. We studied the condensate expansion as a function of scattering length in two different ways: by either changing the scattering length slowly while the atoms were still trapped, or by stepping the scattering length quickly right after the release of the BEC from the trap. The results are compared to the theoretical predictions. We then specialized to the case when the interaction energy is switched off and present improved results on the ultra-slow expansion of a "frozen" condensate in comparison with our earlier measurements. Finally, we excited compression oscillations of the trapped condensate by suddenly stepping the scattering length to a lower value.

4.2.1. Different regimes of self-interaction

We explore the magnetic tunability of the Cs condensate in the range between 5 G and 65 G. These experiments are performed with the setup used for the first realization of a Cs BEC, and on a BEC with 16000 in the condensate phase.

In order to demonstrate the different regimes of self-interaction, we switch to a variable magnetic field synchronously with the release of the condensate. The variable field is applied for a short time interval of 10 ms, which is sufficiently long for the mean-field dynamics to take place. For subsequent expansion at fixed conditions, the magnetic bias field is switched to 17 G (0 a_0) where the self-interaction vanishes. After a total expansion time of 50 ms the vertical extension of the cloud and the total number of atoms are measured.

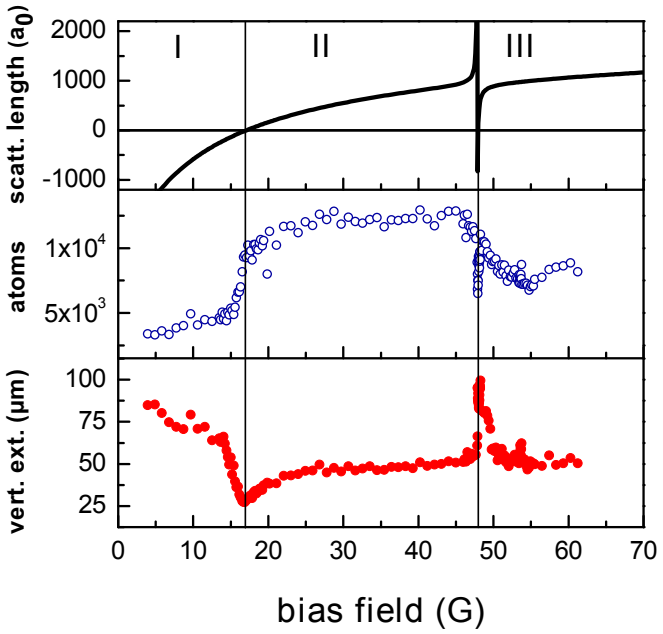

Figure 4.6.: Condensate expansion at different magnetic fields. The bias field has been applied for 10 ms after the release from the trap. The measurements are taken after a total expansion time of 50 ms. *Top*, the prediction for the scattering length, cf. Sec. 2.1.4. *Middle*, remaining number of atoms. *Bottom*, vertical extension (1/e half-width of a Gaussian fit) of the cloud. The three different regions refer to (I) negative scattering length; (II) positive scattering length; and (III) a regime dominated by the Feshbach resonance at 48 G.

The corresponding results (Fig. 4.6) show a marked dependence on the magnetic field with three distinct regions: Below 17 G (region I), the scattering length is negative and the BEC implodes, leading to a large momentum spread and a substantial loss of atoms, as described in Sec. 2.4.4.

The zero-crossing of the scattering length at 17 G, where the expansion shows a minimum, allows us to turn off the self-interaction and thus to realize a "frozen" condensate with an internal energy as low as $k_B \times 600$ pK. This experiment, repeated later with an improved setup, will be discussed in Sec. 4.2.3.

Between 17 G and 48 G (region II), the scattering length is positive and varies smoothly from zero to about 1000 a_0. An increase in width is observed, in agreement with the predicted behavior of the scattering length. This region will be more thoroughly examined in the next section.

For higher fields (region III), the behavior is dominated by the Feshbach resonance at 48 G. On this resonance, the cloud expands very rapidly as the condensate explodes in response to the strong sudden increase of its internal energy. In addition, a sharp loss feature is observed, which may indicate the formation of molecules in the BEC [Don02]. At even higher fields, the data show an asymmetry and broadening of the resonance together with a loss of atoms, which we attribute to the finite ramp speed

over the resonance [Cor00].

The smaller Feshbach resonances, e.g. at 19.8 G, see Fig. 2.7, are not represented by the data. We attribute this to the magnetic field fluctuations of a several mG which average out the effect from the small resonance with a with of a few mG.

4.2.2. Expansion energy

The following experiments are carried out using the optimized production scheme. The improved magnetic field setup features a better stability and faster field ramps. Additionally, the imaging system has been refined and imaging at high magnetic fields has been implemented. Finally, the realization of the final dimple trap with two crossed 1064-nm beams (D1 and D2) resolves the standing-wave problem (Sec. 3.4.7) and gives a well defined and flexible trapping potential. This allows for a quantitative study of the mean-field effects.

In this experiment we measure the release energy of the condensate for adiabatic ramping and for rapid switching of the scattering length.

Adiabatic ramping

In the first case, for a condensate in the Thomas-Fermi regime, the release energy E_{rel} directly corresponds to the chemical potential μ_{TF} given by Eq. (2.38) in combination with Eq. (2.39):

$$\frac{7}{2}E_{rel} = \mu_{TF} = \frac{\hbar\,\bar{\omega}}{2}\left(\frac{15\,N}{a_{ho}}\right)^{2/5} a^{2/5}. \tag{4.1}$$

For the experiment we produce a condensate with $N = 8.5 \times 10^4$ atoms at a creation scattering length of $a_c = 210\ a_0$. We then slowly ramp the magnetic field to values between 20 G and 35 G, setting the scattering length to a value between about 200 a_0 and 700 a_0. The slow ramping prohibits values beyond the Feshbach resonances at 19.9 G and 48.0 G. A combination of slow ramping and quick jumping at the Feshbach resonances would allow access to the full range of values for the scattering length. The condensate is then released from the trap and we measure the release energy. The results are shown in Fig. 4.7. Here we assume that the magnetic field strength translates into scattering length according to Fig. 2.7. The data is well fit by a function of the form $C\ a^{2/5}$, as expected from Eq. (4.1). From the fit parameter C we can deduce an independent estimate of the particle number $N = (8.2 \pm 1.3) \times 10^4$. The error is dominated by the error in determining the trap frequencies. The excellent agreement confirms the validity of our absorption imaging measurements.

Rapid switching

Alternatively, we rapidly switch the scattering length from the creation value a_c to some higher or lower value at the moment of condensate release. Thus, the interaction

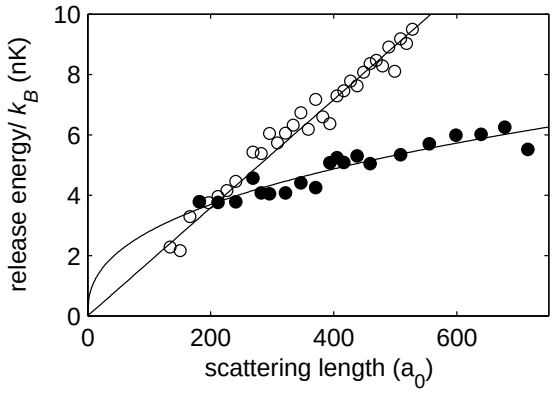

Figure 4.7.: Release energy of the condensate as a function of scattering length. The *filled circles* represent experimental data for the case of adiabatic ramping of a trapped condensate. The data, corresponding to 2/7 of the chemical potential at a given value of the scattering length, is fit by $C\ a^{2/5}$. The *open circles* represent data for rapid switching at the moment of condensate release. As discussed in the text, the straight line is not a fit. It connects the origin with the fitted value of the release energy at the creation scattering length.

energy of the condensate is either increased or decreased with respect to the equilibrium state. Since the mean-field interaction energy of the condensate scales linearly with the scattering length, as explained in Sec. 2.4.4, we expect a linear behavior of the release energy as a function of the final scattering length a.

In Fig. 4.7 we thus compare the data for the measured release energy to a straight line

$$E_{rel} = C\ a_c^{2/5}\ \frac{a}{a_c} \tag{4.2}$$

given by the origin and the fitted value of the release energy at the creation scattering length $a_c = 210\ a_0$ confirming the linear dependence.

4.2.3. Frozen BEC

We now study the expansion of the condensate near the zero-crossing of the scattering length. At the moment of condensate release, we rapidly switch the magnetic field from the creation field near 20 G to (17.17±0.05) G, corresponding to $a = (3.4\pm3.0)\ a_0$. The error in determining the precise magnetic field at the position of the condensate requires that we choose a slightly positive value of the scattering length to assure that no weakly attractive interactions modify the condensate expansion. The levitation field remains on, allowing for an extended observation period.

Fig. 4.8 shows the vertical and horizontal extent of a BEC with 1.2×10^5 atoms as a function of time after release from the trap. We only show the data after 75 ms of expansion when the optical density of the atomic cloud is sufficiently reduced to allow for reliable absorption imaging. The horizontal expansion is dominated by the magnetic anti-trapping potential, see Sec. 3.2.6.

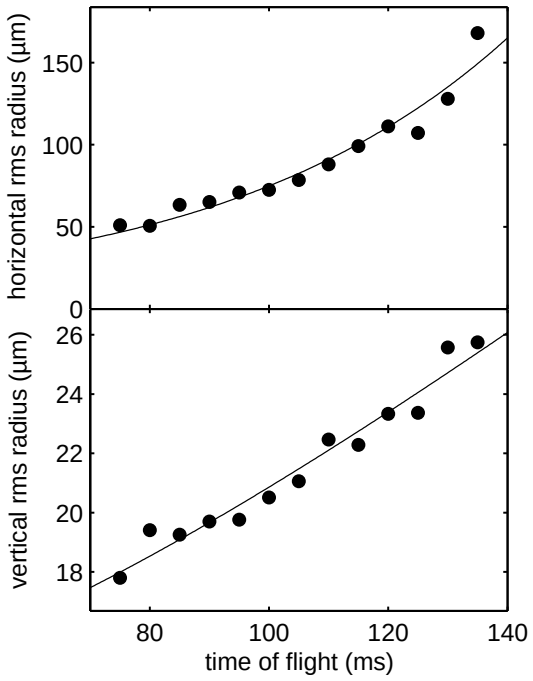

Figure 4.8.: Expansion of the non-interacting condensate. The data points show the horizontal (above) and vertical (below) rms radius of the BEC as a function of expansion time near the zero crossing of the scattering length. Note the different scales. The fit to the residual vertical expansion reveals a release energy of $k_B \times (51 \pm 3)$ pK. For the horizontal expansion the data is fit by $A \cosh(\alpha t)$ with $\alpha = 2\pi \times (3.20 \pm 0.23)$ Hz.

The measured rate of expansion $2\pi \times (3.20 \pm 0.23)$ Hz agrees reasonably well with the expected rate constant $\alpha = 2\pi \times 3.4$ Hz, given by Eq. (3.11). The vertical expansion corresponds to a release energy of $k_B \times (51 \pm 3)$ pK. It is remarkable that this is much lower than the kinetic energy of the ground state $\hbar\omega/4 = k_B \times 253$ pK given by a radial trap frequency of 21.1 Hz. The expectation is the following: Since the spatial extent of the condensate is much larger than the size of the ground state wave function of the harmonic oscillator, the momentum spread, limited by the uncertainty of the wave function of the initial condensate, is lower than that of the ground state.

4.2.4. Condensate oscillations

By rapidly changing the scattering length it is possible to excite oscillations of the condensate in the trap [Kag97]. In fact, in the limit of a cigar shaped condensate one expects radial "compression" or "expansion oscillations" at twice the trap frequency. Compression oscillations can be seen in Fig. 4.9 where we plot the vertical radius of the released condensate as a function of hold time t_h in the trap. To excite the oscillation we step the scattering length from a value of $a = 363\ a_0$ ($B = 24.4$ G)

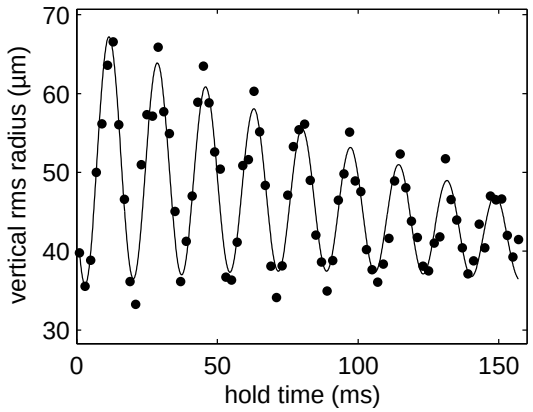

Figure 4.9.: Condensate oscillations after rapid switching of the scattering length. The *filled circles* show the vertical rms radius of an expanding BEC with 7×10^4 atoms after 80 ms of free expansion as a function of hold time in the trap. The scattering length has been switched rapidly from 363 a_0 to 25 a_0. The *solid curve* is a fit to the data giving an oscillation frequency of (58.3 ± 0.2) Hz. We independently measure the radial trap frequency to (28 ± 1) Hz.

to $a = 25\ a_0$ ($B = 17.6$ G) at time t_0. The condensate is then allowed to oscillate in the trap for a variable hold time t_h at the final value of the scattering length. We release the condensate at time $t_0 + t_h$ and take an image after 80 ms of free expansion. We fit the data by a sinusoidal function. The measured compression frequency of (58.3 ± 0.2) Hz agrees well with twice the radial trap frequency of $2 \times (28 \pm 1)$ Hz at a dimple power of 1 mW. To account for the deviation from a pure oscillation we had to introduce an exponential decay of the amplitude and of the offset value. The damping of the amplitude has a time constant of 126 ms. We have not yet identified the origin of this damping. Possibly the BEC samples different trapping frequencies due to the large amplitude of the oscillation, which would lead to an apparent damping. Also, damping might be caused by the interaction with a residual thermal cloud or by parametric processes [Che02].

5. Ultracold Quantum Gas of Cesium Molecules

For the creation of ultracold molecules, the large Cs BEC is an ideal starting point. In summer 2003 we created the first pure molecular quantum gas. By sweeping the magnetic field over a Feshbach resonance, we were able to convert 12% of the atoms in the BEC into ultracold Cs_2 molecules. The ability to separate the molecules by magnetic forces from the atoms permits direct observation of the pure molecular sample. We have measured ultra-low expansion energies, consistent with the presence of a macroscopic molecular matter wave [Her03].

An improved setup allowed better insight into the creation process. We found a novel magnetic field switching scheme, yielding unexpectedly high conversion efficiencies of up to 30% [Mar05], a factor three higher than conventional magnetic field ramps. We demonstrated transfer of the molecules to different internal states using avoided level crossings. A modified conversion scheme allows to create molecules in the CO_2-laser trap, where they remain trapped for several seconds.

5.1. Preparation of a pure molecular quantum gas

The rapid progress in controlling ultracold atomic gases, culminating in the creation of atomic Bose-Einstein condensates and opening the door to the realm of coherent matter wave physics [Cor02, Ket02, Nat02], has raised the question as to whether a similar level of control is possible with molecular samples. Starting with several experimental and theoretical break-throughs in 2003 the field of ultracold molecules has seen rapid progress.

In summer 2003 we were able to convert atoms in a BEC into ultracold molecules using a Feshbach resonance. It was possible, for the first time, to separate the two species and investigate the properties of a pure molecular quantum gas. Here I will discuss this work which has already been published in [Her03].

The results motivated several experimental improvements which permitted a deeper insight into the creation process, allowing for higher conversion efficiencies, and facilitated novel experiments which will be treated in the subsequent sections.

5.1.1. Introduction to ultracold molecules

Molecules, in contrast to atoms, have a much richer internal structure, and can possess permanent vector or tensor properties such as electric dipole moments, rotational angular momentum, or even chirality. Molecule-atom and molecule-molecule interactions are at least three- and four-body processes in nature which pose new challenges to our theoretical understanding. Exquisite control over the internal and external degrees of freedom of molecules could allow the experimental study of a new coherent chemistry [Hei00], where matter-wave interference, quantum tunneling and bosonic stimulation dominate the dynamics, and where the interaction properties can be externally controlled and engineered with electromagnetic fields. Quantum degenerate molecular gases with permanent dipole moments are also prime candidates for the precise investigation of strongly correlated quantum systems and for the study of novel quantum phase transitions [Gór02].

Several avenues have been investigated to cool and trap molecules. Slowing of a supersonic jet of polar molecules in time-varying electric fields [Bet00] and buffer gas loading and trapping [Wei98] in either electrostatic or magnetic traps both permit large molecular populations with temperatures in the mK-range. Alternatively, creation of molecules by photo-association of pre-cooled atoms has lead to molecular samples with temperatures in the μK-range [Van02]. For all these techniques, however, the resulting molecular phase-space density is still many orders of magnitude away from quantum degeneracy.

Concept of creating ultracold molecules

Starting with a sample of ultracold atoms, controlled production of molecules can be realized by coherently coupling an atom pair state to a molecular state. For example, a two-photon Raman transition has successfully been applied to produce molecules within an atomic BEC [Wyn00]. In a similar way, the coherent nature of atomic scattering can be exploited on a Feshbach resonance to transfer colliding atoms into molecules, which has been predicted to convert an atomic BEC into a molecular BEC [Abe99, Tim99, Mie00]. On a magnetic Feshbach resonance the atom-molecule coupling can be resonantly enhanced at a particular magnetic field value, and a sweep of the field near or across the resonance can convert the atoms into molecules in a single molecular quantum state, as illustrated in Fig. 5.1.

Experimental approaches

Prior to this work, existence of molecules created via atomic Feshbach resonances has been reported in a BEC of ^{85}Rb atoms [Don02], in thermal samples of ^{133}Cs [Chi03b] and in degenerate Fermi gases of ^{40}K [Reg03] and ^{6}Li [Cub03]. These studies demonstrate the quantum coherence of the Feshbach coupling [Don02] and the ability to detect molecules within the atomic sample by means of laser-induced [Chi03b], or radio-frequency-induced [Reg03], dissociation. However, the resulting molecular samples

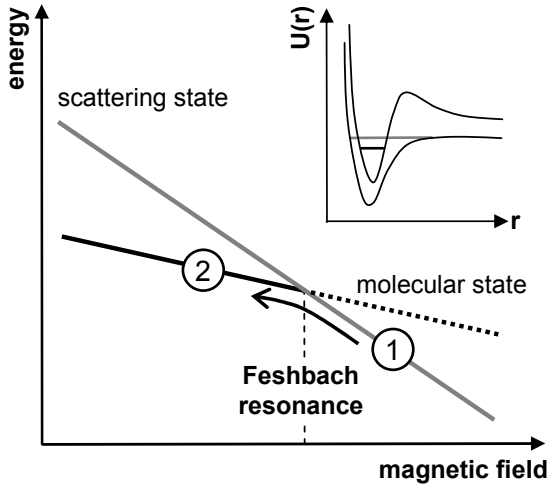

Figure 5.1.: Energy diagram for the atomic scattering state and the molecular bound state. The Feshbach resonance condition occurs near 20 G where. the Zeeman energy of the atomic scattering state becomes equal to that of a molecular bound state due to the difference in magnetic moments. Molecules at (2) are created from the BEC at (1) by a downward sweep of the magnetic field across the resonance.

could not be spatially distinguished from the atoms, nor could the molecular clouds be directly imaged and analyzed.

In contrast to the listed previous experiments with ultracold molecules, this work describes the creation of a pure molecular quantum matter by applying a Feshbach sweep to the atomic cesium BEC with immediate spatial Stern-Gerlach separation of the two species by the levitation field. This enables us to monitor directly the evolution of the coupled out molecular cloud. We measure ultra-low kinetic expansion energies consistent with the presence of a coherent molecular matter wave.

5.1.2. Creation of ultracold molecules

The starting point of this experiment is a pure BEC of up to 6×10^4 Cs atoms in the levitated dimple trap. The gradient for perfect levitation at the creation field of 21 G is 30.9 G/cm. The trap depth is $45 \times k_B$ nK with a radial (axial) trap frequency of 18 Hz (6 Hz). Accordingly, the BEC has a radial (axial) Thomas-Fermi radius of 8.6 μm (26.5 μm).

Feshbach sweep

For creation of the molecules we use a Feshbach resonance at 19.840(4) G, cf. Sec. 2.1.4.The resonance position has been determined by measuring the three-body loss in the trap, cf. Fig. 5.10. This value is consistent with a previous measurement measurement [Web03c]. However, the measurements do not reveal the width of the

resonance. The theoretically predicted width of the resonance is 5 mG [Jul03]. The corresponding molecular state is identified as a high-lying rovibrational state with internal angular momentum $f = 4$, magnetic quantum number $m_f = 4$, molecular orbital angular momentum $L = 4$, and angular momentum projection $m_L = 2$. According to Sec. 2.1.4 this state will be referred to as $4g$. The state has a predicted magnetic moment of $\mu = 0.93\ \mu_B$ with a small magnetic field dependence [Jul03]. These cesium molecules in this state are of special interest since they have a large orbital angular momentum ($l = 4$). Coupling from ultracold atoms in an s-wave scattering state to the g-wave molecular states is observed only for cesium atoms due to the large indirect spin-spin coupling [Mie96].

Molecules are produced from the atomic BEC by sweeping the magnetic field across the resonance from a higher field value (19.88 G) with a constant rate of typically 48 G/s according to the scheme outlined in Fig. 5.1, to a final value (B_f) of 19.74 G. The duration of the sweep is 3 ms. Immediately after the end of the ramp we switch off the optical trap. Simultaneously, the Feshbach coupling is turned off by lowering the magnetic field within 2 ms to a fixed hold field of 17 G where the molecules are allowed to expand under the influence of the gradient field. The ramping of the magnetic field is illustrated in Fig. 5.2.

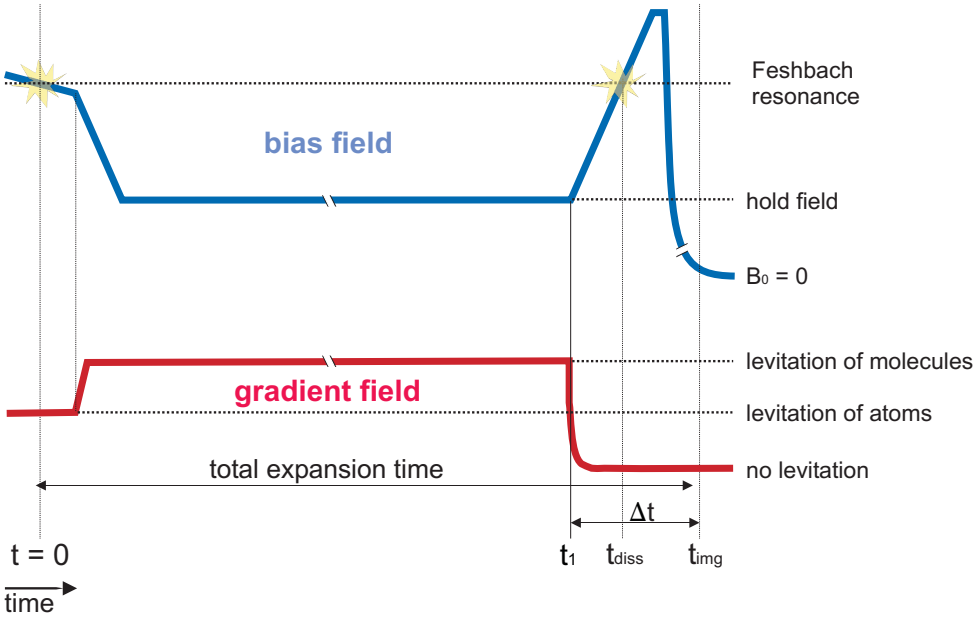

Figure 5.2.: Schematic of the magnetic field ramping for bias field (upper plot) and gradient field (lower plot).

Conversion in the magnetic gradient

Due to the large magnetic field gradient along the vertical direction and the narrow resonance width of 5 mG, the Feshbach resonance occurs only within a 2 μm thin horizontal layer. The conversion zone sweeps vertically through the condensate from below at a speed of 15 μm/ms, or equivalently, in 1.3 ms.

The newly created molecules immediately start falling with an acceleration of 0.38 g due to their reduced magnetic moment. This leads to a vertical center-of-mass velocity of typically a few mm/s, depending on the exact timing of the ramps. The molecular cloud is then completely separated from the atoms within 3 ms. By raising the magnetic field gradient quickly at the end of the sweep to approximately 50 G/cm we can levitate the molecules, see Fig. 5.2. In this case the atoms accelerate upwards at 0.61 g. Rapid molecule-atom separation and subsequent levitation permit long observation times to study the dynamics of the molecular sample.

5.1.3. Detection of molecules

To image the molecular cloud, we apply a reversed field sweep over the resonance with a ramp-speed of 1000 G/s. The reversed sweep brings the molecules above the scattering continuum, and they quickly dissociate into free atoms, see Fig. 5.2. The ramp takes 4 ms and reaches a final value of 21 G, well above the resonance.

For ramp-speeds ranging from 300 G/s up to 1100 G/s no influence was observed. The instant of time of the dissociation depends on the local magnetic field and thus on the vertical position of the molecular cloud in the gradient field. With a finite vertical velocity the position varies with expansion time. By switching off the gradient field at the start of the ramp (t_1), we ensure that the time of dissociation is fixed. Nevertheless, the exact time (t_{diss}) is not exactly known due to an unknown offset in the magnetic field caused by switching the gradient field. The expansion in the time between t_1 and t_{img} (Δt = 5.5 ms) takes place without the influence of the curvature of the gradient field. By varying the time between t_{diss} and t_{img} we can characterize the dynamics of the reconverted atoms. We observe a fast expansion with an energy of about $\frac{1}{2}k_B \times 1$ μK. This, together with the uncertainty in t_{diss}, leads to a fixed additional broadening (σ_{res}) of the cloud.

We switch off the magnetic bias field 1.5 ms before the imaging. The switching speed is much too fast to convert atoms into molecules when the Feshbach resonance is crossed again.

An absorption image of the reconverted atoms taken at at t_{img} thus reveals the spatial distribution of the molecules. The resolution limit caused by the dissociation process is measured to be in the order of about 10 μm, see Sec. 5.1.6. We apply a fit to the image to determine the center position, the size of the spatial distribution and the number of molecules. By varying the hold time the evolution of the molecular cloud is recorded.

The complete atom-molecule separation is clearly visible in absorption images (Fig. 5.3). For reference, the image of a levitated BEC after 12 ms of expansion time

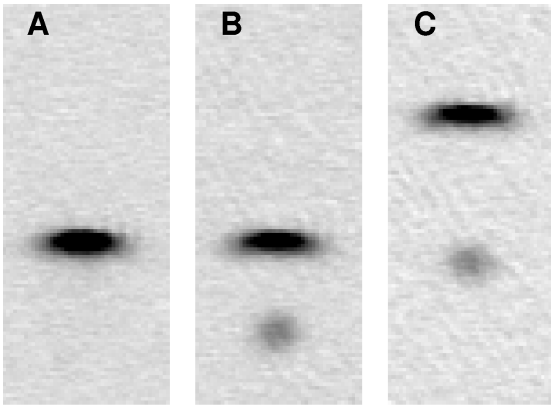

Figure 5.3.: Absorption images of (A) the levitated BEC without the Feshbach sweep, (B) the levitated BEC after the Feshbach sweep with a falling molecular cloud below and (C) the levitated molecular cloud with an upwards rising BEC above. In (B) and (C), 3000 molecules are produced at a sweep rate of 50 G/s. The separation between the atoms and the molecules is150 μm in (B) and 240 μm in (C).

is given in (A). In (B) and (C) a Feshbach sweep has been applied to the BEC. In (B), a coupled out molecular cloud with about 3000 molecules can be seen below the atomic BEC. With respect to (A), the number of atoms in the remaining BEC is reduced by 50% to about 25000. The molecular cloud is falling, because the magnetic field gradient needed to levitate the atoms is maintained. For (C), the magnetic field gradient is raised after the Feshbach sweep in order to levitate the molecules. Hence, the atomic BEC accelerates upwards and can be seen at the top of the image above the molecules.

5.1.4. Measurement of the molecular magnetic moment

Careful adjustment of the magnetic field gradient to null the molecular acceleration allows a precise determination of the magnetic moment of the molecular state. The basic idea is to derive this molecular moment by comparing the field gradient needed for levitation of the molecules with the one required for the atoms. Fig. 5.4 shows the vertical center-of-mass motion of the molecular cloud in a hold field of 17 G (at $z = 0$) with a gradient of 49.7 G/cm, close to the exact levitation condition. The gradient is calibrated via the current through the levitation coil with the atomic levitation condition serving as a precisely defined reference. A parabolic fit to the data yields a residual acceleration of 0.11(5) m/s^2. Taking this small correction into account we calculate a gradient of 50.2(3) G/cm for exact levitation of the molecules. The magnetic moment of the molecular state is then determined to 0.930(5) μ_B, which is in good agreement with the theoretical calculation [Jul03].

The fit to the data of Fig. 5.4 also yields an initial center-of-mass velocity of the molecular cloud of 4(1) mm/s. This velocity results from the downward acceleration before the field gradient increases to the molecule levitation value. The measured

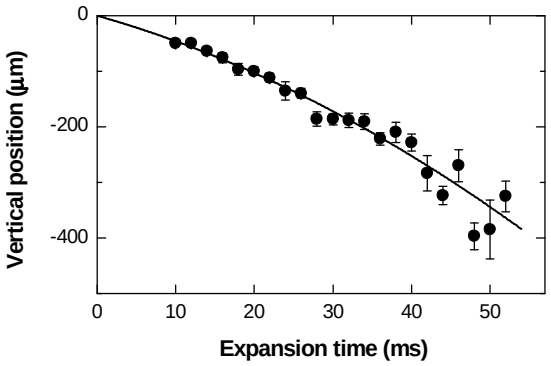

Figure 5.4.: Measurement of the molecular magnetic moment. The vertical center-of-mass position of the molecular cloud at a bias field of 17 G (at $z = 0$) is shown as a function of time together with a parabolic fit (solid line). The applied magnetic gradient field of 49.7 G/cm is slightly below the exact levitation condition so that a residual downward-directed acceleration is observed.

center-of-mass velocity suggests that the production of the molecules takes place in the center of the initial creation ramp, with an uncertainty of 1 ms. This defines the point where $t = 0$. Hence, the total time of expansion is measured from $t = 0$ until the time of imaging t_{img}.

5.1.5. Investigation of the conversion process

We investigate the atom-molecule conversion as a function of the end value B_f of the creation ramp. The ramp speed is kept constant at 50 G/s by varying B_f together with the duration of the ramp. We have checked that for final values B_f well above the resonance the rapid jump over the resonance to the hold field after the end of the creation ramp does not produce any molecules. As Fig. 5.5 shows, molecules are

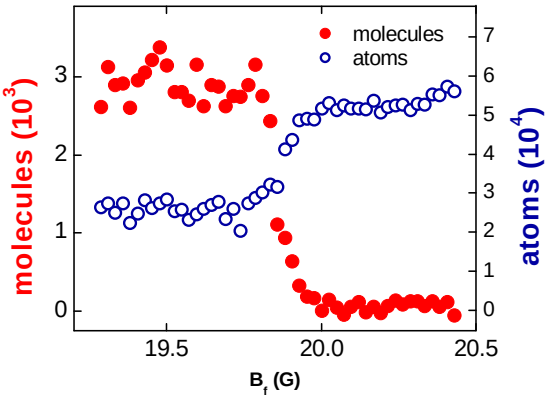

Figure 5.5.: Creation of molecules (filled circles) and simultaneous loss of atoms (open circles) as a function of the final value of the magnetic field ramp B_f for a fixed ramp speed of 50 G/s.

created in a step-like manner. Simultaneously, the atomic population in the BEC is reduced. The transition value agrees well with the resonance. From the plot of the atom number it can be seen that up to 50% of the atoms are lost from the condensate, corresponding to about 25000 atoms for this experiment. Hence, for a detected number of 3000 molecules, only about 24 of the lost atoms reappear as partners in molecule formation. Compared to the total initial number of atoms, this amounts to a conversion efficiency of 12% and a missing fraction of 38%.

Also, we have varied the speed of the downward magnetic field ramp across the Feshbach resonance and find that for decreasing ramp speed the number of detected molecules saturates at a value of about 3000 molecules for speeds less than 50 G/s. However, this measurement is limited by the finite ramp speeds in the used experimental setup[1]. The missing atoms and the saturation suggest that collisional relaxation into other molecular states occurs during the creation phase [Yur00]. After separation from the atoms, however, we do not detect any significant loss.

A more detailed study of the creation process is presented in Sec. 5.2 which gives a possible explanation and a remedy for the low conversion efficiency and suggests possible loss mechanisms explaining the missing fraction.

[1]The measurements were carried out before the implementation of the fast bias field setup, see Sec. 3.2.4.

5.1.6. Expansion measurement

We observe ultra-low expansion energies for the molecular cloud in both the vertical and the horizontal directions. This is done in time-of-flight expansion measurements by varying the hold time (t_{hold}) and hence the total expansion time. We plot the vertical and horizontal root-mean-square (rms) widths of the reconverted atomic cloud as a function of total expansion time (Fig. 5.6). An apparent anisotropy of the expansion can be seen. In the following I will detail the procedure to extract the relevant data from the expansion of the molecular cloud. The interpretation of the results is treated in the next section.

Vertical expansion

For the vertical size of the expanding cloud we use the fit function

$$\sigma_{z,\,\mathrm{img}} = \sqrt{\sigma_{\mathrm{res}}^2 + s_z^2 + u_z^2 t_{\mathrm{img}}^2}\,.$$

Here two free parameters are used: u_z denotes the initial rms velocity spread (predominantly resulting from the velocity dispersion), and σ_{res} is the spatial resolution limit that results from the dissociation energy in the detection phase. The fixed parameter $s_z = 3.7$ μm is the initial vertical rms position spread that we calculate from the Thomas-Fermi distribution of the BEC.

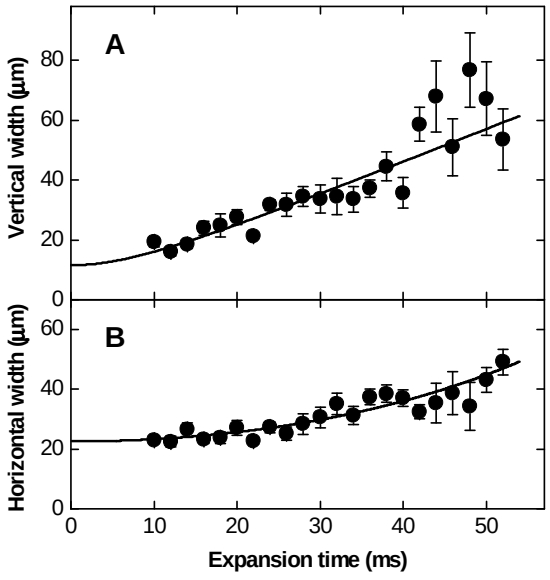

Figure 5.6.: Vertical rms-width (A) and horizontal rms-width (B) of the molecular cloud as a function of expansion time. From (A) a residual kinetic energy of $E_z = \frac{1}{2}\,k_B \times (40 \pm 3 \pm 2)$ nK and an imaging resolution of 11(3) μm is obtained. The fit in (B) then yields an initial horizontal expansion energy of $E_x = \frac{1}{2}\,k_B \times (2 \pm 2 \pm 3)$ nK.

For the velocity spread the fit yields $u_z = 1.12(5)$ mm/s, corresponding to a mean kinetic energy of $E_z = \frac{1}{2}\, k_\mathrm{B} \times 40(3)$ nK. For the resolution parameter we obtain $\sigma_\mathrm{res} = 11(3)$ µm. The given errors denote the one-standard-deviation (one sigma) values as resulting from the fit.

Horizontal expansion in the levitation field

To measure the energy in the horizontal direction, we have to take the influence of the levitation field into account, as described in Sec. 3.6. The trajectory of a particle in the levitation field with an initial position ρ_0 and an initial velocity of v_0 is given by Eq. (3.12) and Eq. (3.13).

In our experiment, the levitation field is turned off at time Δt before the image is taken at t_img. In this short time interval, beginning at $t_1 = t_\mathrm{img} - \Delta t$ and ending at t_img, a free motion in the field of gravity takes place. At the time of detection, the horizontal position of the particle is thus

$$\begin{aligned}\rho(t_\mathrm{img}) &= \rho(t_1) + v(t_1)\Delta t \\ &= \rho_0\Big[\cosh(\alpha t_1) + \alpha\Delta t \sinh(\alpha t_1)\Big] + v_0\Big[\alpha^{-1}\sinh(\alpha t_1) + \Delta t\cosh(\alpha t_1)\Big]\end{aligned}$$

For an ensemble of particles with statistical initial distributions of ρ_0 and v_0 we introduce s_x and u_x for the horizontal position spread and velocity spread (root-mean-square values). For the horizontal size of the cloud we then obtain the rms value

$$\sigma_x = \sqrt{s_x^2\left[\cosh(\alpha t_1) + \alpha\Delta t\sinh(\alpha t_1)\right]^2 + u_x^2\left[\alpha^{-1}\sinh(\alpha t_1) + \Delta t\cosh(\alpha t_1)\right]^2}\,. \quad (5.1)$$

For the horizontal expansion in the levitation field, we use the above expression for the cloud size σ_x together with the resolution parameter σ_res combined to the fit function

$$\begin{aligned}\sigma_{x,\,\mathrm{img}} &= \sqrt{\sigma_\mathrm{res}^2 + \sigma_x^2} \\ &= \sqrt{\sigma_\mathrm{res}^2 + s_x^2\left[\cosh(\alpha t_1) + \alpha\Delta t\sinh(\alpha t_1)\right]^2 + u_x^2\left[\alpha^{-1}\sinh(\alpha t_1) + \Delta t\cosh(\alpha t_1)\right]^2}\,,\end{aligned}$$

where $t_1 = t_\mathrm{img} - \Delta t$. The two free parameters of the fit are the initial horizontal cloud size, s_x, and an initial velocity spread, u_x. The parameter $\alpha = 27.2\ \mathrm{s}^{-1}$ is calculated for the effective horizontal curvature of the levitation field using Eq. (3.11). The resolution parameter $\sigma_\mathrm{res} = 11(3)$ µm is taken from the above fit to the vertical expansion and varied within its error range. From this fit procedure we obtain the initial horizontal cloud size $s_x = 20(2)$ µm. For the initial rms velocity spread the fit yields $u_x = 0.22(16)$ mm/s, which corresponds to a mean initial kinetic energy spread of $E_x = \frac{1}{2}\, k_\mathrm{B} \times 1.5^{+3.0}_{-1.4}$ nK. Rounding to one significant digit gives $E_x = \frac{1}{2}\, k_\mathrm{B} \times 2(2)$ nK.

Error estimation

In addition to the given statistical errors, systematic errors stem from the limited knowledge of the experimental parameters used in the above fits. A more detailed analysis shows that all systematic errors are far below the statistical errors with the exception of the origin of time, i.e. the instant at which the Feshbach conversion produces the molecules. The fits were repeated as before but introducing the maximum possible deviation with respect to the time origin of ±1 ms. The corresponding results indicate systematic deviations from the above fits which can be taken as the systematic errors.

For the most interesting quantities, the initial kinetic-energy spreads of the expanding molecular cloud, we finally obtain

$$\begin{aligned} E_z &= \tfrac{1}{2}\, k_\mathrm{B} \times (40 \pm 3 \pm 2)\ \mathrm{nK} \qquad \text{vertically,} \\ E_x &= \tfrac{1}{2}\, k_\mathrm{B} \times (2 \pm 2 \pm 3)\ \mathrm{nK} \qquad \text{horizontally,} \end{aligned}$$

where the two given error numbers denote the one-standard-deviation statistical error and the systematic error, respectively.

5.1.7. Discussion of the results

The results of the ultra-slow expansion presented in Fig. 5.6 require a detailed discussion. Regarding the conversion process in the presence of the levitation field the apparent anisotropy in the vertical and horizontal direction can be understood.

The origin of the **fast vertical expansion** of $\frac{1}{2}\, k_\mathrm{B} \times (40 \pm 3 \pm 2)$ nK is identified as the velocity dispersion of the molecules during the creation phase. The dispersion is caused by the fact that the conversion zone passes through the condensate at a finite speed from below. Hence, molecules created earlier (later) acquire a larger (smaller) velocity as a result of gravity. Taking into account the size of the BEC, the vertical expansion energy as a result of the velocity dispersion is calculated to be about $\frac{1}{2}\, k_B \times$ 30 nK for the molecular cloud, largely explaining the observed energy. In fact, vertical compression of the BEC does lead to a smaller vertical energy spread. By increasing the dipole trap depth to decrease the vertical extent of the BEC by a factor of 1.3 we find that the measured molecular kinetic energy is reduced in the expected way to a value of $E_z = \frac{1}{2}\, k_B \times (19 \pm 2 \pm 1)$ nK.

The **horizontal expansion** is unaffected by the velocity dispersion effect. However, a repulsive force due to the curvature of the levitation field acts on the molecules. This force results in an expansion of the cloud which follows a cosine hyperbolicus function and has been well characterized, cf. Sec. 4.2.3. Incorporating the resolution limit due to the dissociation and the cosine hyperbolicus expansion dynamics, the fit in Fig. 4B yields an extremely low kinetic energy of $E_x = \frac{1}{2}\, k_B \times (2 \pm 2 \pm 3)$ nK in the horizontal direction. Within the one-sigma errors given, the fit result is consistent with zero.

The slow expansion of the molecules is consistent with the behavior of a macroscopic matter wave. The horizontal expansion shows vanishing release energy while

the vertical expansion is dominated by the dispersive effect from gravity which in itself is coherent in its nature. In view of a possible quantum degeneracy of the molecular ensemble, we first estimate the peak molecular density right after the creation to be 1×10^{12} cm^{-3}, assuming 3000 molecules with a spatial density profile reflecting that of the atomic BEC given above. This is a reasonable assumption because no molecules can be created in the absence of atoms. Given the free-space degeneracy condition, the critical temperature is 6 nK. Comparing this value to the observed horizontal energy spread corresponding to $(2 \pm 2 \pm 3)$ nK, we raise the intriguing question as to whether a molecular cloud with macroscopic coherence has been created.

5.2. Efficient creation of molecules from a Cs BEC

We found a novel scheme to efficiently create weakly bound Cs_2 molecules from an atomic Bose-Einstein condensate. The method is based on switching the magnetic field to the narrow Feshbach resonance near 20 G and yields a high atom-molecule conversion efficiency of more than 30%, a factor of three higher than obtained with conventional magnetic-field ramps. The Cs_2 molecules are created in a single *g*-wave rotational molecular quantum state. The observed dependence of the conversion efficiency on the magnetic field and atom density shows scattering processes beyond two-body coupling to occur in the vicinity of the Feshbach resonance. The experiments discussed in this section have been published in [Mar05].

Further insight into the creation process was facilitated by technical improvements which were stimulated by the experimental results presented in the previous section. A tight dimple trap permits storing of the atomic BEC and conversion into molecules without the presence of the levitation gradient. In this way the Feshbach resonance applies to all atoms in the BEC simultaneously. We installed a new system providing better magnetic field stability and faster ramping (Sec. 3.2.4). The reduction of environmental magnetic fields (Sec. 3.2.2) and additional synchronization of the experimental cycle to the phase of the power line largely increases the precision and reproducibility of the magnetic fields, cf. Sec. 3.6.3. Furthermore, the implementation of imaging at high magnetic fields permits imaging directly after the dissociation process.

5.2.1. Investigations on the creation process

After the realization of the pure molecular quantum gas, described in Sec. 5.1 and [Her03], other experiments followed this approach. Xu *et al.* created Na_2 molecules from an atomic BEC. In this experiment the conversion efficiency was on the order of 4% [Xu03]. Dürr *et al.* converted about 7% of the atoms in a BEC into Rb_2 molecules and could determine their magnetic moment [Dür04b]. In the listed experiments the molecules are formed by ramping the magnetic field through a Feshbach resonance. The principle is illustrated in Fig. 5.7 and the corresponding magnetic field ramp is shown in Fig. 5.7. It is expected that during the ramping process the ground state atom population in the trap is adiabatically and efficiently converted into molecules in a weakly bound state [Abe99, Tie01, Kok01]. However, the reported efficiencies using this method are relatively low: Typically 5% $\sim$ 10% are observed, whereas 50% to 70% of the atoms are lost during the ramping process. The missing fraction (the lost atoms which are not converted into weakly bound molecules) is generally believed to result from the creation of molecules in states which cannot be detected by the conventional imaging method, or to consist of "hot" atoms which quickly leave the trap [Reg03, Her03].

We measure a high atom-molecule conversion efficiency in excess of 30% based on a novel magnetic field switching scheme. This scheme is illustrated in Fig. 5.1.

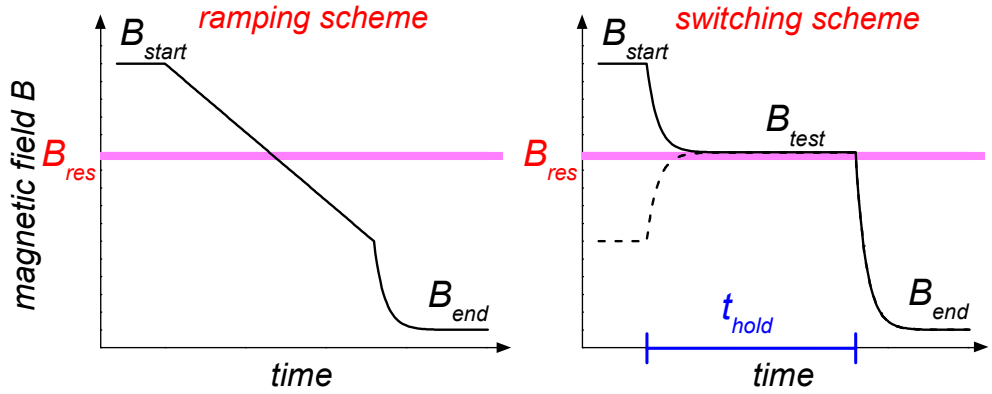

Figure 5.7.: Schemes for molecule creation near a Feshbach resonance, located at B_{res}. In the ramping scheme, we linearly ramp the magnetic field from B_{start}, well above the resonance, to B_{end}, well below the resonance. In the switching scheme, we first switch from B_{start} to B_{test}. After a hold time t_{hold}, we switch the field to B_{end}. The switching scheme also works for B_{start} below the resonance (dashed line). The finite response time of the magnetic field in our experiment is due to eddy currents in the stainless steel vacuum chamber.

The magnetic field is quickly switched from an off-resonant value B_{start} to a field B_{test}, near the resonance position B_{res}. After a variable hold time t_{hold}, the magnetic field is quickly lowered well below the resonance B_{end}, where atoms and molecules decouple and can be independently measured. Our new scheme works for initial magnetic fields B_{start} both well above or well below the resonance. In the latter case, the creation of molecules cannot be explained in terms of the two-body adiabatic conversion picture given above. An investigation of the atom loss and molecule creation efficiencies suggests that different scattering processes are involved near the narrow Feshbach resonance.

Preparation

Before we start the molecule creation, we first compress the condensate by adiabatically increasing the power of the tightly focused laser in 0.7 s to 35 mW. The higher laser power provides a stronger trapping force and allows us to turn off the levitation field. The absence of the magnetic field gradient is crucial to ensure that all atoms experience the same magnetic field and can simultaneously participate in the molecule formation process. In the compressed trap, the trap frequencies are $\omega_r/2\pi = 170$ Hz and $\omega_z/2\pi = 6.5$ Hz, the chemical potential is $k_B \times 86$ nK and the peak density is 1.7×10^{14} cm^{-3}. We then slowly change the magnetic field in 200 ms to a starting value of B_{start}, typically 0.5 G above the Feshbach resonance B_{res}. Note that this 0.5 G offset is much larger than the resonance width of a few mG. The condensate at B_{start} is not influenced by the resonance. We then switch off the dipole trap and release the atoms into free space and, at the same time, tune the magnetic field toward the Fesh-

bach resonance to create molecules. At the end of the molecule formation phase, we quickly lower the magnetic field down to $B_{\mathrm{end}} \approx 18$ G to decouple the molecules and atoms.

The resulting molecule and atom numbers can be determined independently. The atoms are directly imaged at 18 G. We verify that the molecules are insensitive to the imaging beam at this magnetic field. To detect the molecules, we first blast away the atoms at 18 G with a resonant beam[2] [Xu03], and then ramp the magnetic field back above the resonance to 21 G. The weakly bound molecular state is then above the continuum and the molecules quickly dissociate into free atoms [Muk04, Dür04a]. By imaging the resulting cloud of atoms, we can determine the number of molecules.

Comparing different ramping schemes

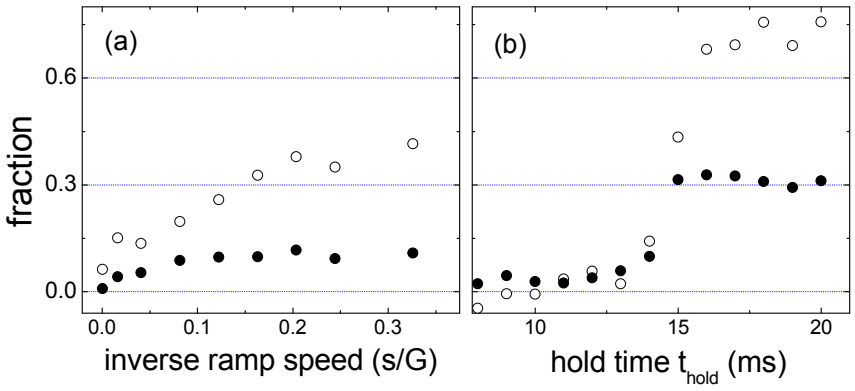

Figure 5.8.: Comparison of the two schemes of molecule creation. Molecule fraction (solid circles) and atom loss fraction (open circles) are shown for (a) the ramping scheme, where the fractions are measured for different ramp speeds, and for (b) the switching scheme for different hold times t_{hold}. In (b), B_{test} is set right on resonance.

We employ both the ramping scheme and the switching scheme for molecule production (see Fig. 5.7) and compare their performances. In the ramping scheme, we tune the magnetic field across the resonance with a constant ramping speed. Based on the resulting molecule number and the loss in atomic number, we calculate the conversion fractions, shown in Fig. 5.8 (a). A maximum molecule fraction of 10% is observed when the ramps are slower than 10 G/s. The atom loss for these ramps is about 40%, which indicates a missing fraction of about 30%. This result is similar to all previous experiments using the same method [Her03, Xu03, Dür04b].

For the switching scheme, we quickly tune the magnetic field onto the Feshbach resonance $B_{\mathrm{test}} \approx B_{\mathrm{res}}$, wait for various hold times t_{hold}, and quickly lower the magnetic

[2] In contrast to the preparation described in the previous section this is necessary, since here the two species are not separated by the levitation field.

field to $B_{\text{end}} = 18$ G. Due to the finite response time (cf. Fig. 3.5) of the magnetic field, the field approaches the Feshbach resonance after about 12 ms. We studied this behavior for different ramps and found that the time is determined by the magnetic field reaching the resonance region, as demonstrated in Fig. 5.9. For an end value of

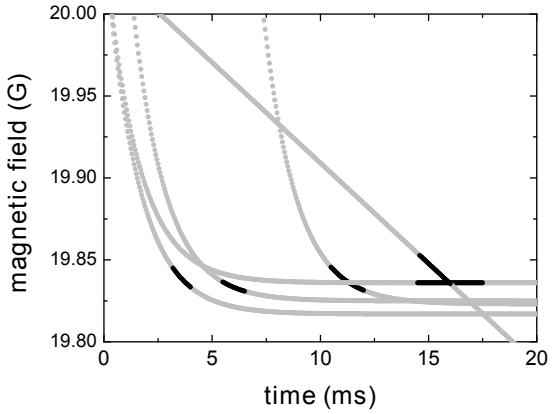

Figure 5.9.: The curves represent the calculated magnetic field for different parameters of the switching scheme and one linear ramp. The darker sections start where molecules are observed and end where the number of molecules levels out, see Fig. 5.8.

B_{test} below the resonance the molecules are created earlier with less efficiency.

At the creation at 12 ms the peak density of the expanding condensate reduces to 1.1×10^{12} cm^{-3}. For hold times $t_{\text{hold}} > 15$ms, molecule fractions of $30 \sim 35\%$ and atom loss fraction of $\sim 70\%$ are reached. The conversion efficiency is by more than a factor of three higher than obtained from the ramping scheme.

5.2.2. Creation and loss spectra in the switching scheme

To understand the different performance of the two schemes, we study the atom loss and molecule increase at different magnetic fields B_{test} based on the switching scheme, see Fig. 5.10 (a) and (b). For comparison, we also show the atom loss in the compressed trap in Fig. 5.10 (c), where the initial peak density is 1.9×10^{14} cm^{-3}. This value is slightly higher than the value given before because of the reduced scattering length. The calculated scattering length[3] is shown in Fig. 5.10 (d). For all measurements with B_{test} above the resonance, we prepare the condensate as previously described at $B_{\text{start}} = B_{\text{res}} + 0.5$ G. For B_{test} below the resonance, we prepare the condensate at a magnetic field below the resonance by quickly switching the magnetic field from the initial value to $B_{\text{res}} - 0.5$ G. No appreciable atom loss, molecule formation or

[3]The calculated resonance position is 20.1 G [Tie04]. To reflect the correct resonance position, we shift the numerical data by centering the resonance at our observed value of 19.84 G.The measure value agrees perfectly with our previously measured value, cf. Sec. 5.1.2.

condensate excitation is observed in this process. We then follow the same experimental procedure, but approach the resonance from below. These two different preparation procedures for magnetic fields above and below the resonance are necessary to avoid a slow field-sweep across the resonance, which can lead to systematic atom loss or molecule increase.

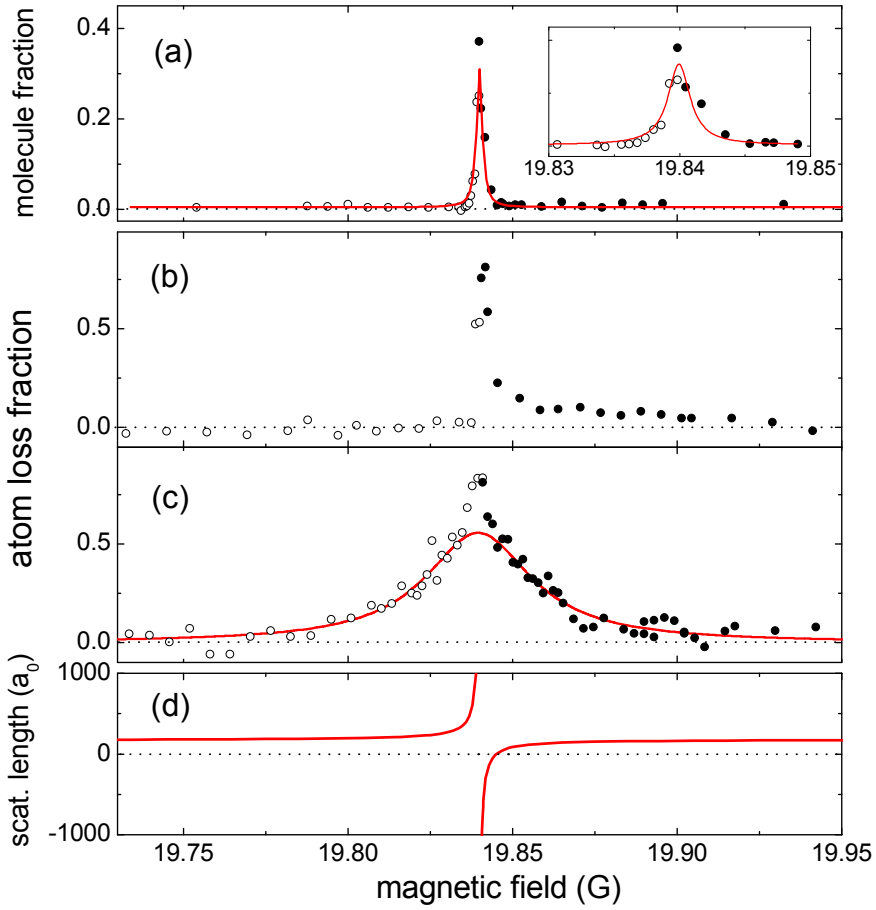

Figure 5.10.: Molecule creation and atom loss near the Feshbach resonance. Based on the switching scheme, molecule increase in t_{hold} = 18 ms (a) and atom loss in 18 ms (b) are measured for various test fields B_{test}. The inset shows the expanded view of the molecule signal. For comparison, the atom loss in the compressed trap is shown in (c). The scattering length is shown in (d) for reference. Solid circles (open circles) show the measurements above (below) the resonance. In (a), a Lorentzian fit (solid line) yields a width of 2.1 mG and the resonance position of B_{res} = 19.840 G, subject to a calibration uncertainty of 4 mG. Fitting both wings in (c) gives a Lorentzian width of 40(2) mG.

In the molecule creation spectrum (Fig. 5.10 (a)) we observe a very narrow linewidth of 2.1 mG, which is consistent with the predicted resonance width. Notably, our molecule creation scheme also works for B_{start} below the resonance, which

suggests that coupling beyond the adiabatic conversion model plays an important role in the creation process. In the adiabatic passage picture, molecules cannot be created when the creation field is below the resonance. The atom loss, shown in Fig. 5.10 (b), is asymmetric and seems to include two components, a narrow peak on resonance and a much broader and weaker loss feature for magnetic fields above the resonance. The narrow peak has a similar width as in the molecule production spectrum in Fig. 3 (a), and is clearly related to the observed molecule formation. The broad and weak feature on the high magnetic field side has a width of 80(20) mG as determined from a one-sided Lorentzian fit. To obtain further information about the atom loss process, we measure the atom loss in the compressed trap, where the atom density is higher by a factor of ~ 170 than in Fig. 5.10 (a) and (b). The result shown in Fig. 5.10 (c) displays a wide and symmetric loss feature. By fitting the two wings to a Lorentzian profile, we find a width of 40(2) mG.

The different line shapes suggest that different scattering processes are involved near the Feshbach resonance. The molecule formation width is close to the predicted width of the Feshbach resonance and can be interpreted in terms of the two-body Feshbach coupling. The asymmetric loss feature in Fig. 5.10 (b) and the trap loss may be due to three-body recombination or many-body effects. These broad atom loss features are puzzling, since they are a factor of 20 or more wider than the Feshbach resonance width of 2 mG. The physical origin of the associated loss mechanisms requires further investigation.

The large width of the atom loss feature, however, does provide a qualitative explanation of why the switching scheme is more efficient than the ramping scheme. In a linear ramp, atoms sample all magnetic fields near the resonance which, for a large fraction of time, leads to atom loss without molecule increase. Whereas in the switching scheme, the atoms spend more time in the magnetic field range where molecules can be created.

5.2.3. Dependency on density

To further investigate and differentiate the physical mechanisms that are responsible for the missing fraction and for the molecule creation, we measure the dependence of the atom loss fraction and molecule fraction on the atom number in the condensate, as shown in Fig. 5.11. Atom numbers ranging from 2.5×10^4 to 2.2×10^5 correspond to peak densities of 7.9×10^{13} cm^{-3} to 1.9×10^{14} cm^{-3} in the compressed trap and to 4.6×10^{11} cm^{-3} to 1.1×10^{12} cm^{-3} in free space at the moment the molecules are created. For the calculation of the densities in free space, we take into account the 12 ms expansion of the condensate in the Thomas-Fermi regime after the dipole trap is turned off.

Several interesting features show up in the density dependence. The molecule fraction grows and saturates to $\sim 30\%$ at densities higher than 5×10^{11} cm^{-3}. The saturation of the molecule fraction resembles observations in a thermal gas [Chi03b, Joc03], where a thermal equilibrium is reached with a constant molecule fraction in the sample

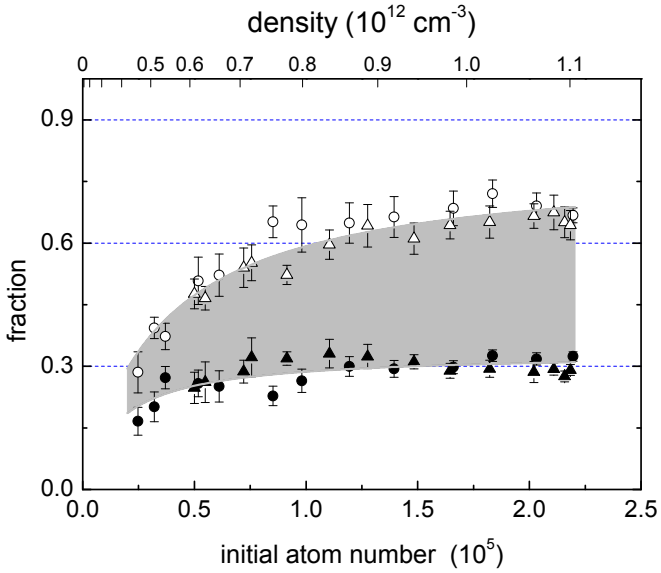

Figure 5.11.: Density dependence of the atom loss fraction (open symbols) and molecule fraction (solid symbols). The atom number in the BEC is varied by either adjusting optical cooling efficiencies (solid and open circles) or the loading efficiencies into the crossed dipole trap (solid and open triangles). The corresponding atomic density of the sample right before the molecule formation (after 12 ms expansion in free space) is given on the top axis. The shaded grey area is a guide to the eye to indicate the missing fraction.

[Chi03a]. The missing fraction is very small at low densities and continues to grow up to a density of 8×10^{12} cm^{-3}. The stronger density dependence of the missing fraction suggests that scattering processes involved in the atom loss are of higher order than for the molecule increase. Similar enhancement of the collision loss near the Feshbach resonance was also observed in a ^{85}Rb condensate [Rob00] and in a thermal Cs gas [Web03c]. A further analysis of the scattering dynamics and the possible thermal equilibrium condition is necessary.

The performance of this scheme is superior to the conventional linear magnetic field ramping scheme since the molecules are created only within the narrow Feshbach resonance width of 2 mG, while the atom are lost over a much large range of $\sim$ 40 mG. The density dependence of both the missing fraction and the molecule fraction suggests that in our scheme the molecules are created via Feshbach coupling, while the missing fraction comes from higher order scattering processes. Based on the new creation scheme, we are now able to obtain samples with up to 40000 ultracold molecules. This provides a good starting point to investigate the trapping, the interactions, and the matter-wave nature of ultracold molecules.

5.2.4. Expansion energy

We now investigate the expansion energy of the molecular sample. Here, we use the magnetic field switching scheme with an end value shortly below the resonance, which results in an earlier creation of the molecules, cf. Fig. 5.9, in this case after 7 ms.

We measure the $1/e$-widths of the expanding cloud. The results for the vertical, i.e. radial, expansion are displayed in Fig. 5.12. For comparison we record the vertical expansion of a BEC for which the magnetic field was kept constant instead of switching the field to produce molecules. The measured mean kinetic expansion energy for

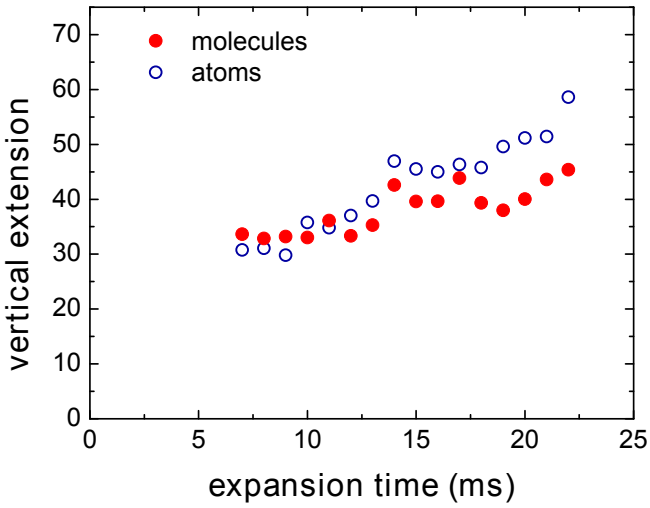

Figure 5.12.: The evolution of the vertical $1/e$-radii of the expanding molecular cloud and of an expanding BEC are displayed. The molecule creation takes place at $t = 0$. The BEC is released at $t = -7$ ms from the trap.

the molecular sample corresponds to $\frac{1}{2}\, k_B \times 32$ nK. At the same rate of expansion the measured energy of the atoms would be a factor of two lower due to the factor of two in mass. We observe a slightly higher rate of expansion for the undisturbed BEC. The accuracy is limited by the short observation time[4] of < 25 ms. For the BEC a more detailed measurement employing the levitation field is done, which reveals an expansion energy of $\frac{1}{2}\, k_B \times 16$ nK.

To investigate the correlation between expansion of the atoms and of the converted molecular cloud, we prepare atomic ensembles with different expansion energies. We create samples with a higher kinetic energies in one case by adiabatically increasing the dimple power to 70 mW, and in two other cases by a rapidly increasing the power to 35 mW and 70 mW, respectively. The resulting vertical expansion energies range from 30 nK to 75 nK. The conversion process is kept constant.

[4] All experiments are carried out without magnetic levitation. A falling cloud would sample different magnetic fields during the observation time, which could alter the the expansion.

In all cases we observe a slightly slower vertical expansion of the molecular sample compared to the atoms. Nevertheless, within the uncertainty the expansion rates almost agree. The difference could be explained by the density dependence of the conversion process, which would correspond to higher conversion efficiencies towards the center of the expanding cloud. Thus, predominantly less energetic atoms are converted.

The observation of the expansion in the horizontal (i.e. axial) direction agrees qualitatively with the measurement of the vertical direction for small atomic expansion energies: the molecular expansion rate is observed to be similar but always lower. Due to the short observation time a quantitative comparison is impossible. Surprisingly, for the conversion of a fast expanding atomic sample, the rate of expansion for the molecules seems to vanish in the horizonal direction. This effect is not yet understood, but could be explained by taking into account that the magnetic field is swept across a Feshbach resonance which can dramatically alter the expansion of a BEC.

Furthermore we observe a reduction in conversion efficiency for atomic samples with higher expansion energy. The conversion efficiency drops from 27% for a radial kinetic energy of $\frac{1}{2}\ k_B \times 16$ nK to 16% for an energy of $\frac{1}{2}\ k_B \times 75$ nK. Although the cloud expands faster in the latter case, the density at the time of molecule creation is in both cases still above 5×10^{11} cm^{-3}. Therefore the lower conversion efficiency cannot be explained by the density dependence alone, cf. Fig 5.11, and must be assigned to the higher expansion energy.

In conclusion, we observe that the molecules inherit the kinetic energy of the expanding atoms. We therefore assume that the molecular creation process is not exothermic.

5.3. Experiments with molecules

The efficient creation of ultracold molecules from a BEC opens the door to a novel class of experiments. Cs_2 molecules in particular offer a great versatility due to a rich spectrum of molecular energy levels at low magnetic fields.

This section presents a series of experiments performed with ultracold Cs_2 molecules. We have investigated the transfer of the molecules to other molecular states using avoided level crossings. We have discovered a molecular state with high orbital angular momentum, which, at the time, was not included in the theoretical picture. Furthermore, we have demonstrated trapping of molecules in the CO_2-laser trap. This allows to investigate the sample on extended time scales and yields the prospects of producing a trapped molecular BEC.

5.3.1. Transfer to other molecular states

The molecular binding energy for various states at low magnetic fields is shown in Fig. 5.13 and in a broader energy and magnetic field range in Fig. 2.8. The rich spec-

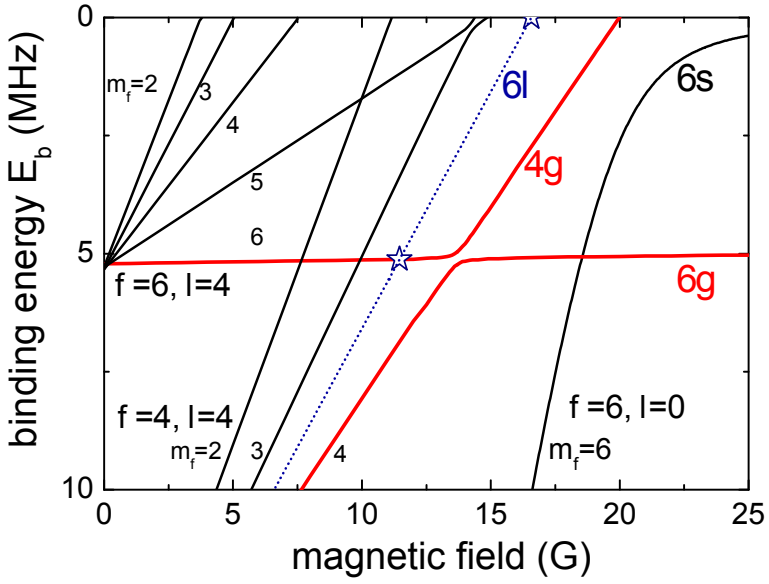

Figure 5.13.: Binding energy versus magnetic field for different molecular states. The quantum numbers of the states are indicated. For simplicity, the states relevant to the experiment are labelled $4g$, $6g$, $6s$, and $6l$, omitting the magnetic quantum numbers. The avoided crossing between $4g$ and $6g$ has been included in the calculation. The dashed line is fixed by the magnetic field for dissociation of a newly discovered state ($6l$) and the avoided crossing with $6g$, both indicated by stars. The figure is adapted from [Chi04].

trum of molecular states including several expected level crossings, presents many intriguing possibilities to transfer the molecules to and measure their properties in

various molecular states. Depending on the magnetic ramp speed and the coupling strength between two molecular states, a different fraction is transferred to each state. This allows a determination of the coupling strength and to control the population in the two states. By using slow adiabatic or fast non-adiabatic ramps, the level crossings can be used as controllable switches between the two states.

The state $4g$ is responsible for the Feshbach resonance at 19.84 G which we use to create molecules. The avoided level crossing between the states $4g$ and $6g$ is included in this picture. With regard to the the calculated splitting of 150 kHz, the realizable magnetic field ramps in our current setup are always slow and the sample will follow adiabatically into the $6g$ state and vice versa.

A new molecular state

To investigate the different molecular levels, we start by producing a sample of ultracold molecules using the efficient switching scheme, as described in Sec. 5.2. After the creation we separate the molecules from the atoms (Sec. 5.2.1) and ramp the magnetic field to B_{end} within 1 ms. After 3 ms we jump the field to a value above the resonance at 19.84 G to dissociate and detect the molecules. The absorption image of a typical molecular cloud is shown in Fig. 5.14 (a).

When the magnetic field is ramped to a value below $\sim$ 13.7 G the molecules are transferred to the state $6g$. Surprisingly, for a ramp to $\sim$ 11 G a second component becomes visible in the density distribution of the dissociated molecules, Fig. 5.14 (b). This second component can be explained by the partial transfer to another molecular state. However, the magnetic field is well above the value (10 G) at which the next avoided crossing is expected. The slow magnetic ramp transfers the molecules partially to the new state. In the fast ramp to the dissociation field the molecules in state $6g$ can follow to $4g$ and are dissociated at 19.84 G. On the other hand, we observe that molecules in the new state are already dissociated at lower magnetic fields. Therefore, a typical dissociation ramp to fields above 19.84 G can bring the molecules in the new state far above the dissociation continuum and thus they gain more energy in the dissociation process [Dür04a, Muk04]. Consequently, when the magnetic field is below the dissociation threshold for molecules in $4g$, only the molecules in the new state are dissociated, shown in Fig. 5.14 (c).

With the ability to measure the population of the two states independently, we can determine the exact value where the molecules start to dissociate and the position of the avoided crossing to the new state.

Avoided crossing

To determine the position of the avoided crossing we ramp the magnetic field in a slow ramp (2 ms) to a variable hold field. The reconversion field is set to 17 G, well below the $4g$ Feshbach resonance. Fig. 5.15 *(left)* shows the observed particle numbers against the hold field. We observe a strong increase in the population of the new state

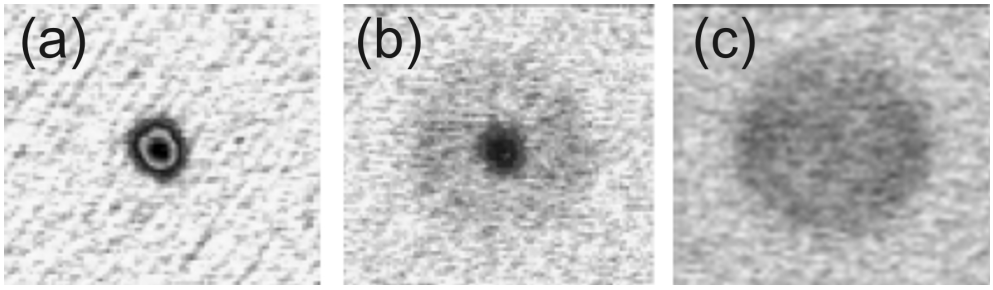

Figure 5.14.: Absorption images of dissociated molecules. In (b) and (c) the molecules were partly transferred to a new molecular state. In (c) the field for dissociation is below the threshold for molecules in $4g$. Above the threshold (b) both, a component of "hot" molecules from the new state, and a spatially smaller component from molecules in the $6g$ state are visible. As a reference a typical molecular cloud with all molecules in $6g$ is presented in (a).

for hold fields below (11.46 ± 0.01) G. Furthermore, we observe that for faster ramps we transfer only a fraction of the molecules into the new state. A detailed investigation of the coupling strength at this avoided crossing is currently in progress.

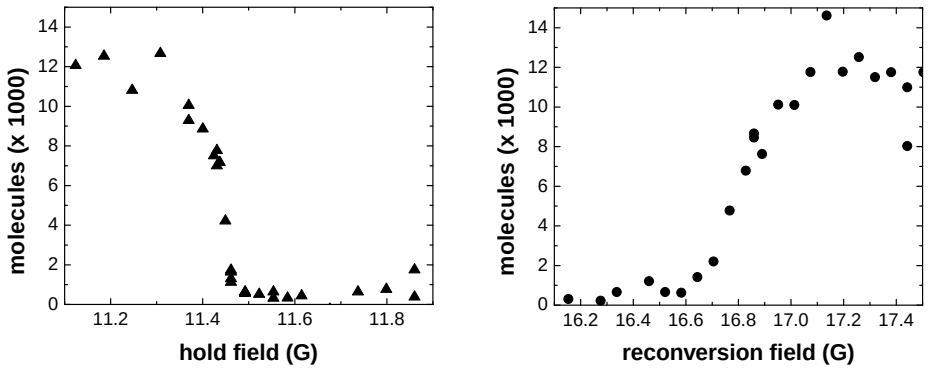

Figure 5.15.: Number of molecules in the new state $6l$ against the hold field *(left)*. This gives the position of the avoided crossing to be at (11.46 ± 0.01) G. *(Right)* number of molecules in the new state against the reconversion field. We observe that molecules are dissociated for fields above (16.57 ± 0.03) G. Both values have been determined by extrapolating the rising (falling) edge to the baseline.

Dissociation

To identify the magnetic value where the molecules start to dissociate we set the hold field to a fixed value of ∼ 11.2 G where most of the molecules are transferred to the new state and vary the reconversion field. We wait several milliseconds to allow a slow dissociation to take place. We detect molecules for reconversion fields above (16.57 ± 0.03) G, as shown in in Fig. 5.15 *(right)*.

The dissociation of molecules in the new state is significantly different from molecules dissociated at 19.84 G. The energy gained in the dissociation process is typically much larger than the expansion energy of the molecular sample. We observe a ring-like structure in the absorption image (Fig. 5.14 b and c), since the atoms expand on the surface of a hollow sphere [Dür04a]. A Gaussian fit[5] to the density distribution in a time-of-flight measurement reveals an energy of several μK. We attribute this high energy to a weak coupling of the new state to the continuum. The molecules can thus be ramped well above the continuum before they dissociate.

Furthermore, we conduct a thorough scan of the region around the dissociation value, measuring the lifetime of a dense, non-condensed sample of trapped atoms. In contrast to the $4g$ Feshbach resonance (Fig. 5.10) which shows a strong loss at the creation (dissociation) value, we do not observe any signature of a Feshbach resonance in the range of 15 G to 18 G. This supports the assumption of a very weak coupling of the new state to the continuum, resulting in an extremely narrow Feshbach resonance.

Identifying the new state

The position of the avoided crossing and of the dissociation field can be inserted into the energy diagram (Fig. 5.13). The binding energy is extrapolated by a straight line connecting the two points. This state is clearly distinguished from the next predicted state with the quantum numbers $f = 4, l = 4, m_f = 3$. New theoretical calculations including higher orbital angular momenta predict a state with $f = 6$ and $l = 8$ [Tie04], close to the observed position of the state we have discovered. According to the labelling of the relevant states we refer to this state as $6l$.

5.3.2. Trapping of molecules

So far our experiments on ultracold molecules have been performed in free space. We observed a strong reduction of the number of molecules when the 1064-nm dimple trap was on during the conversion process. However, we were able to trap the molecules for several seconds using the CO_2-laser trap. Furthermore, we observed a strong reduction in lifetime when the sample was irradiated with light from the 1064-nm Yb fiber laser, explaining the previously observed loss.

Conversion in the CO_2-laser trap

We start with the standard loading sequence of the dimple trap to create a dense sample of atoms. We load 1.7×10^6 atoms at a temperature of 1 μK. The corresponding density is 3.5×10^{13} cm^{-3} and the phase space density is 0.13. Instead of the standard evaporation, we leave both CO_2 lasers on and keep the power in the dimple constant. We adiabatically reduce the gradient field to zero. This removes the reservoir atoms in the LevT, while the atoms in the tight dimple trap remain.

[5] This can only be used as an estimate, since the distribution is not Gaussian.

For the conversion process we apply the magnetic field switching scheme, cf. Sec. 5.2.1. The atoms are released from the dimple at the start of the ramp. After the conversion the magnetic field is ramped to a hold field and the remaining atoms are removed with a resonant light pulse. To subsequently trap the molecules in the CO_2-laser trap, a levitation field of ~ 50 G/cm is applied in order to levitate molecules in the state $4g$ [Her03]. We measure 2×10^4 molecules after the creation, which corresponds to a conversion efficiency of $\sim 1.1\%$.

The vertical velocity accumulated during the creation process results in a strong center-of-mass oscillation in the CO_2-laser trap, which leads to an unacceptable heating of the sample. We therefore take several measures to reduce this effect: For the magnetic field ramp we choose an end value below the Feshbach resonance. This results in an earlier creation of the molecules, as shown in Fig. 5.9 while sacrificing some efficiency. Additionally, we optimize the time when the dimple trap is switched off. Furthermore, by monitoring the center-of-mass oscillation we can adjust the strength of the gradient in several steps to retard the motion of the molecular cloud and store it in the center of the trap. We can thereby reduce the amplitude of the center-of-mass motion by a factor of 10 down to 30 μm. The residual oscillation is damped and is no longer detectable after $\sim$ 1 s. At this point we detect a trapped thermal gas of 1.5×10^4 molecules with a temperature of 2.4 μK. The spatial $1/e$-with of the ensemble is 230 μm. This corresponds to a density of 10^9 cm^{-3}. In the case of a weakly bound molecule its static polarizability is close to that of two atoms [Tar92]. Due to the double mass the molecular trap frequencies in the LevT are the same as for atoms. We measure a vertical trap frequency of $\sim$ 16 Hz, agreeing reasonably well with the atomic trap frequency.

For this low-density sample we measure a lifetime of over 6 s. From these numbers we can give a first estimate of the inelastic collision rate of 5×10^{-9} cm^3/s. This value agrees with our later experiment [Chi05] at higher densities, but is still an order of magnitude below the value measured for Na molecules [Muk04].

Recent experiments demonstrate an improved method to produce a sample of trapped molecules, based on a standard BEC which is transferred to the LevT. The molecules are produced using the ramping scheme, since the LevT requires a levitation field. This method has a higher efficiency, due to the higher density and lower kinetic energy of the sample. However, the number of produced molecules is smaller due to the smaller initial number of atoms. The vertical acceleration experienced during the creation process [Her03] finally leads to a heating of the sample. However, the lower temperature and the smaller spatial extent of the resulting molecular sample is advantageous in some experiments.

Light induced losses

With the trapped sample of molecules it is now possible to study the properties of the molecular ensemble on extended timescales. To investigate the high losses during the creation process we illuminate the sample for 1 ms with 15 mW using a 1064-nm beam,

indicated as D2 in Fig. 3.16. This leads to a reduction of the lifetime to $\sim$ 300 ms. Due to the broad spectral width of this laser source of 1 nm around a wavelength of 1064 nm, the light can be resonant with several molecular bound-bound transitions. The excited molecules undergo a rapid radiative decay into lower molecular states, which cannot be reconverted into atoms and are thus not detectable. Molecules in these states are presumably lost from the trap, unless their magnetic moment is such that they are levitated. Since the spatial overlap of the illuminating beam with the trapped sample is unknown, we cannot deduce an excitation rate. Nevertheless, this observation explains the previously observed losses during the creation process in the presence of the 1064-nm light.

Prospects for a trapped BEC of Cs_2 molecules

Theoretical calculations of the molecular energy structure predict optical transitions up to a wavelength of $\sim$ 2.3 μm [Spi89]. The CO_2-laser trap is therefore well suited to trap a molecular sample. The need for a levitation gradient in this trap, on the other hand, hinders the conversion into molecules and finally leads to a hotter sample. The possibility to create a "tight" dimple using laser light above 2.3 μm would open up new possibilities for conversion within the trap. We have shown that no extra energy is released in the conversion process in free space, thus we expect that the conversion in the trap does not heat up the sample. Starting with a large atomic BEC this would result in a molecular sample with high phase space density. After the conversion magnetic levitation can be applied, which then allows to reduce the trapping strength and thus the density.

Furthermore, evaporative cooling in this dimple trap could be accomplished in the same way as for the atoms. The critical parameter determining the success of this method is the ratio between elastic and inelastic collisions which is yet unknown. However, our recent discovery of Feshbach-like resonances in a sample of ultracold Cs molecules [Chi05] may provide an instrument to control the intermolecular interaction.

5.3.3. Magnetic moment

The leviation field allows to probe the magnetic moment of the molecules at different magnetic bias fields. An experiment with a (fast) falling sample implies the complication that the cloud samples various magnetic bias fields during the interaction time, whereas a stationary, e.g. trapped, sample allows for an accurate measurement of the magnetic moment.

We start with a sample of thermal molecules in the trap in their equilibrium position. The levitation field is adjusted to levitate molecules in $4g$ [Her03]. We change the magnetic bias field upon release of the sample from the trap. After 5 ms of free expansion, the leviation field is shut off and the molecules are imaged. This additionally amounts to 2 ms without the influence of the levitation field. We measure the final

vertical position of the molecules. Using the equation of motion for this scenario, we can deduce the acceleration experienced by the molecules and thus the magnetic moment as a function of the applied bias field. The short expansion time ensures that the effect of different magnetic fields sampled by an accelerated ensemble is still small. In Fig. 5.16 we show the deduced magnetic moment at different magnetic fields. The

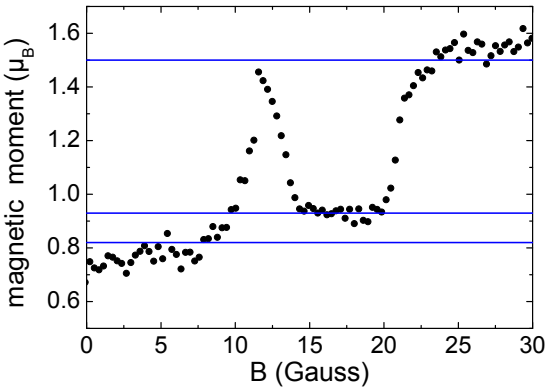

Figure 5.16.: Measurement of the magnetic moment of the molecules at different magnetic fields. A thermal cloud of molecules in the state $4g$ is levitated in the LevT. The magnetic offset field is changed upon release of the sample from the trap. The vertical position is determined after a period of free expansion in the gradient field. From the measured acceleration we infer the magnetic moment at the respective magnetic field. Above 19.8 G the the molecules are dissociated into atoms with a magnetic moment of 1.5 μ_B indicated by the upper line. The lowest line indicated the predicted magnetic moment of the state $6l$. The middle line matches the magnetic moment of the state $4g$.

measurement shows good agreement with the behavior expected from Fig. 5.13. The resolution is limited by the spread of the sample over a magnetic field of ~ 2 G. Above 19.8 the molecules dissociate into free atoms with a magnetic moment of 1.5 μ_B. Between 14 G and 19.8 G the sample is not accelerated as is expected for molecules in $4g$. At the avoided crossing at 13.7 G molecules are transferred from $4g$ to the state $6g$ which possesses a magnetic moment of 1.5 μ_B. The avoided crossing of $6g$ with the newly discovered state $6l$ and with the neighboring state ($f = 4, l = 4, m_F = 3$) are not clearly distinguishable due to the spread of the cloud in magnetic field.

The presented method provides a simple instrument to probe the magnetic moment of a sample over a large range of magnetic fields. The results show good agreement with a recent experiment, where the magnetic moment of molecules in $4g$ and $6g$ was measured with high precision [Chi05].

6. Summary and Outlook

The work presented in this thesis yielded two key experimental results: the realization of a Bose-Einstein condensate of cesium and the creation of a pure sample of ultracold Cs_2 molecules.

Bose-Einstein condensation of cesium

Our strategy to trap and cool cesium in an optical trap has led to the first realization of Bose-Einstein condensation of cesium. Our optical approach allows for trapping of the absolute ground state of cesium, $F = 3$, $m_F = 3$, thus evading the problem of high two body losses. Additionally, the magnetic field remains a free parameter to tune the interaction strength. The optimized loading and evaporation strategy yielded a BEC with 2×10^5 atoms, constituting an all optical way to produce large BECs, which is in no way inferior to magnetic trapping concepts. In fact, a new project has been started in our group to realize an optimized all optical trapping approach with the aim to produce large Cs BECs for various experimental approaches which could benefit from large atom numbers [Näg03].

Due to the unique tunability offered by cesium the BEC constitutes a tunable quantum gas, an ideal starting point for experiments where one might wish to adjust or to dynamically change the mean-field interaction of the condensate. As a demonstration, we measured the release energy of the condensate for abruptly and adiabatically changing the scattering length. We found excellent agreement with the theoretical expectations. Furthermore, by switching the scattering length to zero we realized a "frozen" condensate with vanishing expansion energy. Such a condensate represents an ideal source of cold atoms. It might be used in atom interferometers where one wishes to suppress any mean field effect [Gup02]. In the field of quantum gases, a Cs BEC can serve as the experimental key to explore new regimes beyond standard mean-field theory, like the strongly interacting regime with an interparticle spacing of the order of the scattering length, systems in reduced dimensionality, and the Mott-insulator phase [Jak98, Gre02]. Also, the modulation of the scattering length could be used as an alternative tool to probe the excitation spectrum of the condensate. Switching the scattering length to a large value, e.g. close to the resonance at 48 G, a strongly interacting quantum system could be realized which could be studied via the excitation of collective oscillations.

Ultracold Cs_2 molecules

With the BEC as a starting point, we created a pure molecular quantum gas by sweeping the magnetic field over a Feshbach resonance. This was the first time that a molecular sample could be spatially separated and imaged. The expansion energy of the molecular sample suggests the presence of a macroscopic molecular matter wave. Our capability to monitor the spatial distribution of the molecules could, in the future, allow us to detect interference patterns [And97] and thus to investigate the macroscopic coherence of the molecular matter wave.

A closer investigation of the conversion process resulted in a novel magnetic field switching scheme which yielded a conversion efficiency of 30%, a factor of three higher than obtained with conventional magnetic field ramps, which has already triggered further theoretical investigation [Mac05]. Our findings question the conventional adiabatic conversion picture. After the efficient creation of a pure sample of ultracold molecules, one might be able to coherently transfer the molecules to low-lying molecular states by two-photon Raman transitions. Hence, a complete and coherent control over the dynamics of molecular quantum matter can be envisaged.

In first experiments successfully demonstrated the transfer of the molecules into other molecular states using avoided level crossings. The multitude of available molecular states at low magnetic fields, including several avoided level crossings, constitutes a "molecular roadmap" with different tracks, crossings and switches. Furthermore, we discovered a state with higher orbital angular momentum ($l = 8$). We showed that molecules can be transferred to this state and from there be dissociated. Although the weak coupling to the continuum does not allow to convert atoms into molecules in this state, it could be populated through the "back-door". The unusual dissociation behavior can be interpreted as the discovery of a super narrow Feshbach resonance or alternatively as a more complex dissociation process which involves coupling to a shape resonance in another internal molecular state [Vol04]. In the molecular-roadmap picture this state represents a one-way street. In recent experiments the weak avoided crossing between the state $6l$ and $6g$ has been quantitatively measured. By varying the speed of the magnetic field ramp it has been possible to control the population of the two states. Using this "molecular beam splitter" a molecular interferometer has already been realized.

In first experiments, trapping of molecules was demonstrated in the CO_2-laser trap, presenting a concept to create a trapped molecular BEC. This would allow to study the transition from an atomic BEC to a molecular BEC, for which a quantum phase transition with an essentially topological character has been predicted [Rad04, Rom04]. In this respect, experiments using a laser source at 2.3 μm are scheduled.

Recently the lifetime of the trapped molecular sample has been studied at different magnetic bias fields. Two Feshbach-like resonances have been observed [Chi05]. These resonances can be interpreted as the formation of Cs_4 molecules. In analogy to atomic Feshbach resonances, the tunability of the interaction between molecules opens

up novel applications such as controlled chemical reactions and synthesis of ultracold quantum clusters.

A. Appendix

A.1. Diode laser system

In the experiment we employ several diode-laser systems to produce the laser light used in laser cooling and absorption imaging. In the following the different systems are described. More details can be found in [Web03a]. The laser setup, including sketches, is also described in [Mar03a].

The frequency of the light emitted by the laser diode can be tuned with high precision. The challenge is to precisely measure the frequency of the light and to actively keep it at the desired value using feedback-loops. Although the temperature of the diode has a strong effect on the emitted wavelength, the time constant of a temperature variation is too slow to be used for active control. Therefore the temperature is kept constant and the frequency is tuned by other means, such as the diode current.

We have installed acousto-optical modulators (AOM) in the path of every laser beam, except the Zeeman slower. This allows active control of the intensity and switching off of the light within a few μs. An AOM shifts the frequency of the light by its modulation frequency which is typically around 80 MHz. If not explicitly stated, I will refer to the frequencies including the shift by the AOM. All laser beams are coupled into single mode optical fibers to transport the light. Furthermore mechanical shutters are installed in all beam paths (except in those from the master laser) to physically block the light.

Master laser

The master laser consists of a 852 nm laser diode (SDL-5420) stabilized using a Littrow-type extended cavity [Ric95, Tha01] setup. The laser is locked to the $F = 4 \rightarrow F' = 5$ transition. The error signal is obtained by modulation transfer spectroscopy [Raj79, Ber01]. With this locking technique a laser linewidth of 100 kHz and an output power of 60 mW are obtained. The master laser serves three purposes. It is used as a reference for the MOT and Zeeman laser, it is the source of resonant light for the absorption imaging, and it is the master laser for the slave laser setup providing the RC lattice.

MOT and Zeeman laser

The MOT and Zeeman laser diodes are distributed Bragg reflector (DBR) type (SDL-5712-H1). The advantage of a DBR laser is that it incorporates a frequency-selective element that narrows its linewidth and causes it to lase near the desired wavelength. The frequency of the laser is coarsely tuned by changing the temperature. Fine-tuning is achieved by adjusting the diode current. Both lasers are locked using the so-called "beat lock" technique. The beat signal between the emitted light and the light from the master laser is detected by a photodiode. The beat frequency near 160 MHz is mixed down and compared to a reference signal given by a voltage-controlled oscillator (VCO). In this way the frequency can be easily tuned from −90 MHz to +60 MHz, with respect to the $F = 4 \rightarrow F' = 5$ transition. The laser linewidth obtained with this setup is $\sim$ 1 MHz. The lasers are located on a separate table to avoid resonant stray light on the experimental table. The powers after the fibers are 32 mW from the MOT and 32 mW from the Zeeman laser.

Repumper and polarizer

This DBR-type laser diode provides the laser light for repumping during the MOT ($F = 3 \rightarrow F' = 3$) and for polarizing in the RC phase ($F = 3 \rightarrow F' = 2$). Since the light is resonant for atoms in the $F = 3$ manifold, its frequency is over 9 GHz away from that of the master laser and a beat lock is not easily possible. Therefore, the laser is independently frequency stabilized the polarization lock scheme as described in [Cor98] and [Mos99]. This scheme is simple to set up and robust. It allows for stabilization of the laser frequency with a precision of a few MHz which is sufficient for repumping. For the polarizer a more precise locking scheme could improve the stability of the Raman-sideband cooling. A prototype has been tested, but due to its prototype character it is now only used as the "Zeeman repumper", see below. An improved polarizer is in preparation.

The laser is locked in between the $F = 3 \rightarrow F' = 2$ and $F = 3 \rightarrow F' = 3$ transition. The beam is split in two components which are shifted by AOMs to the desired transition. One beam is used as a MOT repumper. Its light is superimposed with the MOT light using a polarizing beam splitter (PBS) after which both are coupled into the same fiber. The maximum power of the repumper after the fiber is 6 mW. The other beam, used as a polarizer for RC, is coupled into a separate fiber, through which 3 mW are transported to the experimental table.

Zeeman repumper

The setup of the Zeeman repumper is similar to that of the master laser. It is resonant to the $F = 3 \rightarrow F' = 3$ transition. Its light is coupled into the same fiber as the Zeeman slower. The available laser power after the fiber is 11 mW.

RC lattice laser

The laser diode (SDL-5420) which provides light for the Raman-sideband cooling lattice is seeded by light from the master laser. Within a certain range of the laser current, known as the locking range, the laser light emitted by the RC laser has exactly the same frequency and linewidth as the light used for seeding. This allows for a high output power of 120 mW without additional feedback. The resulting laser light is resonant to the $F = 4 \rightarrow F' = 4$ transition.

Originally this laser was located on the experimental table and a pinhole was used to improve the beam quality. Due to instabilities in the beam pointing and/or the pinhole, a frequent readjustment of the pinhole and the laser beams was necessary. Therefore an single mode optical fibre transports the light of a new RC laser which was set up on a different table. This ensures an excellent beam quality and stable beam pointing. The power available on the experimental table is 65 mW.

Absorption imaging laser beams

The two beams used for absorption imaging are split off from the master laser. Both pass through double-pass AOMs and are coupled into optical fibers. This allows for a detuning from -10 MHz to $+60$ MHz from the $F = 4 \rightarrow F =' 5$ transition.

B. Publications

B.1. Three-Body Recombination at Large Scattering Lengths in an Ultracold Atomic Gas

Three-Body Recombination at Large Scattering Lengths in an Ultracold Atomic Gas

Tino Weber, Jens Herbig, Michael Mark, Hanns-Christoph Nägerl, and Rudolf Grimm
Institut für Experimentalphysik, Universität Innsbruck, Technikerstraße 25, A-6020 Innsbruck, Austria
(Received 14 April 2003; published 18 September 2003)

We study three-body recombination in an optically trapped ultracold gas of cesium atoms with precise magnetic control of the s-wave scattering length a. At large positive values of a, we measure the dependence of the rate coefficient on a and confirm the theoretically predicted scaling proportional to a^4. Evidence of recombination heating indicates the formation of very weakly bound molecules in the last bound energy level.

DOI: 10.1103/PhysRevLett.91.123201 PACS numbers: 34.50.–s, 32.80.Cy, 32.80.Pj, 33.80.Ps

Three-body recombination, the process of two particles forming a compound while interacting with a third particle, is of general importance in many-body systems. Understanding three-body processes has for a long time been a challenge in many areas of physics. In dilute ultracold atomic gases, where unique experimental access to interparticle interactions is available, three-body recombination leads to the formation of diatomic molecules. The possibility to trap and cool such molecules and thus to realize ultracold molecular ensembles [1] or atom-molecule mixtures [2] holds great prospects for future research in the field of quantum gases.

The main experimental challenge for measuring three-body recombination is to distinguish three-body losses from two-body losses. In magnetic traps, this is in general difficult, as dipolar relaxation is present as an inherent two-body loss mechanism. In the special case of magnetically trapped ^{87}Rb, experiments could nevertheless provide reliable data because of the anomalously weak two-body decay in this species [3,4]. As a more general approach, optical traps allow one to store atoms in the lowest internal state where two-body loss is fully suppressed for energetic reasons [5]. Three-body recombination in bosonic systems with large s-wave scattering length a has been explored in experiments utilizing Feshbach resonances in ^{23}Na [6] and ^{85}Rb [7]. The results demonstrate the dramatic enhancement of loss processes near such resonances.

In the case of large positive a, theoretical studies [8–11] predict formation of molecules in a weakly bound s level and deduce scaling of the three-body recombination rate with a to the fourth power. Recombination is discussed in terms of the event rate $\nu_{\mathrm{rec}} = \alpha_{\mathrm{rec}} n^3$ per unit volume and time, where n denotes the particle density. In the low-energy limit, the universal scaling law for the characteristic parameter α_{rec} is given as $\alpha_{\mathrm{rec}} = C\hbar a^4/m$ [8], where m is the mass of the atom, and C is a dimensionless factor. Predictions for C give values between 0 and ~70 [8–11], with oscillatory behavior between $C = 0$ and $C_{\mathrm{max}} = 67.9$ expected for strong variations of a on a Feshbach resonance [11]. Previously available experimental data on three-body recombination for various species roughly agree with the general trend of a universal a^4 scaling, with evidence for deviations from this scaling law near a Feshbach resonance [6].

In this work, we employ an optical trap to measure three-body recombination in an ultracold thermal gas of ^{133}Cs in the $6^2S_{1/2}$, $F = 3$, $m_F = 3$ absolute ground state. In this state, the scattering length varies strongly with an applied magnetic field B through a combination of broad and narrow Feshbach resonances at low field strengths [12,13]. The values of a as a function of B have been calculated to high precision [14]. This tunability allows us to conduct experiments in a range of precisely controlled large positive values of a, where the condition of recombination into a weakly bound s level is well fulfilled. Detailed measurements of the time evolution of both atom number and temperature allow us to quantify both three-body loss and heating.

The three-body loss rate coefficient L_3 is related to α_{rec} via $L_3 = n_l \alpha_{\mathrm{rec}}$, where n_l denotes the number of atoms lost from the trap per recombination event. Therefore, the central relationship for comparing measurements to theory is

$$L_3 = n_l C \frac{\hbar}{m} a^4. \tag{1}$$

In the recombination process, the molecular binding energy ε is set free as kinetic energy. The molecule and the third atom receive $\varepsilon/3$ and $2\varepsilon/3$, respectively. Since usually ε is large compared to the trapping potential depth, both are expelled from the trap, setting $n_l = 3$. However, the binding energy of the weakly bound last energy level of the dimer is given by $\varepsilon = \hbar^2/(ma^2)$ [15], and at very large scattering length values ε may be below the trap depth and the third atom cannot escape. If the potential of the atom trap does not confine the molecule, the dimer is lost and $n_l = 2$. If, however, the molecule is trapped and stays within the atom cloud, it may quickly quench its high vibrational excitation in an inelastic collision with a fourth trapped atom. The large amount of energy released in this situation expels the collision partners, making $n_l = 3$. In either case, the kinetic energy of

the remaining atom is distributed in the ensemble, giving rise to recombination heating.

Our measurements are conducted in a nearly isotropic optical dipole trap formed by two crossed 100 W CO_2-laser beams focused to a waist of 600 μm [16]. A vertical magnetic field gradient of 31 G/cm cancels gravity for the $6^2S_{1/2}$, $F = 3$, $m_F = 3$ absolute ground state of Cs. The optical trapping forces are so weak that no other m_F substate can be held against the gravitational force, thus perfect spin polarization of the sample is enforced by the trap itself. We have measured the trap frequencies by exciting small oscillations along the principal axes, the geometric average results to $\bar{\omega}/(2\pi) = 14.5 \pm 0.5$ Hz. The trap depth is $k_B \times 12$ μK; k_B denotes the Boltzmann constant. Trap heating is extremely weak; from long-time measurements we can give an upper bound for the heating rate of 0.2 nK/s. The background gas limited $1/e$ lifetime is $\sim$180 s.

After loading the dipole trap [16], the ensemble cools down by plain evaporation within the first 10 s to 3×10^6 atoms at $T = 1$ μK, 1/12 of the trap depth. To avoid further evaporative loss and cooling in our measurements, we cool the sample well below this limit. This is achieved by forced radio frequency evaporative cooling in the magnetic levitation field. We apply a radio frequency resonant with the Zeeman splitting between two m_F substates. In the vertical levitation gradient, this acts as height selective removal from the trap, effecting 1D evaporative cooling. Evaporation proceeds at a bias field of $B = 75$ G to tune the scattering length to $1200a_0$ ($a_0 = 0.053$ nm denotes Bohr's radius), which at the low initial peak density of 3×10^{11} cm^{-3} keeps the elastic scattering rate at $\sim$200 s^{-1}, high enough for efficient cooling. A simple 7 s two-segment linear sweep of the radio frequency provides 1.3×10^6 atoms at 450 nK (peak phase-space density $D \approx 4 \times 10^{-3}$). Some measurements have been taken at 200 nK starting temperature; to reach this, we appended another linear 5 s rf ramp, leaving 4×10^5 atoms in the trap ($D \approx 10^{-2}$). Temperature and atom number are measured by taking an absorption image with typically 50 ms of expansion in the levitation field after switching off the CO_2 lasers. For the expansion, the bias field is in all measurements set to 75 G to ensure constant conditions.

In a first set of measurements, we recorded the atom number and temperature of the trapped sample after a holding time of 10 s at fixed magnetic fields varied between 10 and 100 G [17]. Figure 1 shows the data in comparison to the calculated scattering length [14], which includes Feshbach resonances involving s- and d-wave channels. Additional resonances involving closed g-wave channels are marked by arrows. The Feshbach resonances have been observed in previous experiments through light-induced two-body losses [13,18] and described theoretically [12,18]. In our measurements, all resonances appear as prominent loss and heating features. Over the full range, both atom number and temperature show a clear correlation with the magnitude of the scattering length.

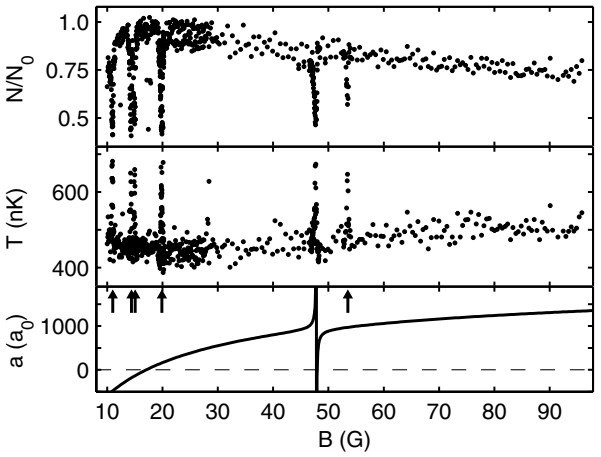

FIG. 1. Remaining fraction of atoms N/N_0 (upper curve) and temperature T (middle) after 10 s in the CO_2-laser trap in a range of magnetic bias fields. Initially $N_0 = 1.3 \times 10^6$ atoms are prepared at 450 nK. For comparison, the lower plot shows the calculated scattering length a with additional Feshbach resonances indicated by arrows (see text).

To obtain more quantitative results on recombination loss and heating, we have studied the time evolution of the atom number N and temperature T at various magnetic fields. Figure 2 shows a typical measurement at $B = 56$ G. Integrating the local three-body loss rate $L_3 n^3$ over the sample gives $\dot{N}/N = -L_3\langle n^2\rangle$. Expressing the average density in terms of the directly accessible quantities N and T, we replace $L_3\langle n^2\rangle$ by $\gamma N^2/T^3$, where $\gamma = L_3(m\bar{\omega}^2/2\pi k_B)^3/\sqrt{27}$. With an additional loss term $-\alpha N$ for background gas collisions, we obtain a differential equation for the atom number,

$$\frac{dN}{dt} = -\alpha N - \gamma \frac{N^3}{T^3}. \tag{2}$$

Atom loss through three-body recombination leads to "anti-evaporation" heating. With its n^3 dependence, three-body recombination predominantly happens in the region of highest density in the trap center. The mean

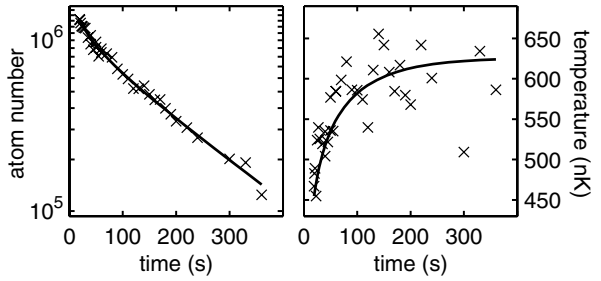

FIG. 2. Atom number and temperature as a function of time in the trap at a bias field of 56 G. The solid lines show a numerical fit to the data. The corresponding three-body loss coefficient is $L_3 = 7(2) \times 10^{-25}$ cm^6/s.

potential energy [19] of an atom undergoing a three-body process can be calculated by integrating over a thermal distribution with weights proportional to n^3, which yields $\frac{1}{2}k_BT$. As the ensemble average is $\frac{3}{2}k_BT$, for each lost atom an excess energy of $1k_BT$ remains in the sample. To account for recombination heating, we introduce an additional constant energy k_BT_h per lost atom. Relating the total heating energy $k_B(T + T_h)$ to the average energy $3k_BT$ of a trapped particle yields $\dot{T}/T = (\dot{N}/N)k_B(T + T_h)/(3k_BT)$, and we obtain an expression for the temperature evolution,

$$\frac{dT}{dt} = \gamma \frac{N^2}{T^3}\frac{(T + T_h)}{3}. \quad (3)$$

Equations (2) and (3) form a set of two coupled nonlinear differential equations for N and T. Using an iterative approach [20], we do a least-squares fit of the numerical solutions of both equations to the experimental data. For the data in Fig. 2, the fit is plotted as solid lines. Fit parameters are α, γ, and T_h. Error estimates for the fit parameters are based on varying one parameter up and down, respectively, to the points where χ^2 increases by one, while optimizing the other parameters [22].

The data obtained for L_3 as a function of magnetic field is plotted in Fig. 3. The inset shows an expanded view of data taken on the 48 G Feshbach resonance. The error bars represent the statistical errors derived from the fit as described above, which typically range around 20%. The systematic uncertainty is larger: Because of the scaling of L_3 with $N^2\bar{\omega}^6$, small errors in these values amount to large differences in the result obtained for L_3. Taking the uncertainty in the trap frequency and an estimated 30% in atom number, the systematic error can be up to a factor of 2.

In order to compare our data to theory, we do a least-squares fit of the expected scaling law [Eq. (1)] to our measurements, using the calculated $a(B)$ [14]. The single fit parameter is n_lC. The resulting curve is drawn as a solid line in Fig. 3. The data clearly confirm the universal a^4 scaling. In our experimental range, where a varies by less than a factor of 2, we do not find any indication of resonant behavior in C [23]. The result from the fit is $n_lC = 225$, corresponding to $C = 75$ for $n_l = 3$ or $C = 112$ for $n_l = 2$. In comparison to theory, both values are somewhat above the upper limit of $C_{\max} \approx 70$, but in good agreement within our systematic error limit.

The inset of Fig. 3 shows the data on the 48 G Feshbach resonance. In order to model the shape of the loss feature, we have to take into account the width of the sample in the vertical B field gradient and the unitarity limitation at the finite temperature. The theory curve is convoluted with a Gaussian of full $1/e$ width 260 mG, which is given by the vertical extension of the n^3 distribution of the trapped sample. A cutoff in a accounts for the unitarity limitation; the cutoff value of $1800a_0$ results from a least-squares fit to the data. Our B-field scale is slightly adjusted for an optimum match with theory by introducing a 40 mG shift, which is well within our calibration accuracy.

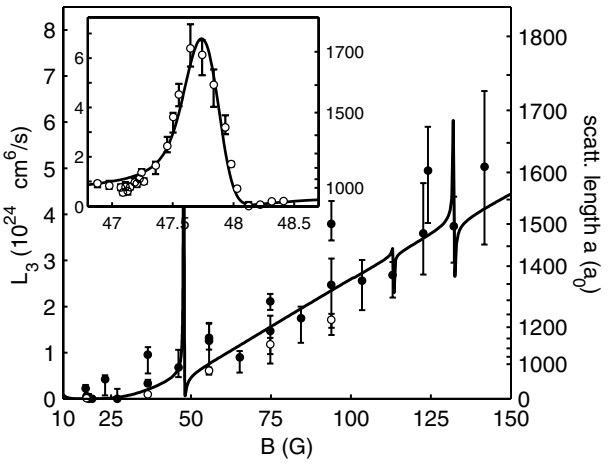

FIG. 3. Measured values of L_3 as a function of the bias field B. Filled symbols represent measurements taken at an initial temperature of 200 nK, open symbols at 450 nK. The solid line shows the calculation according to Eq. (1) with $n_lC = 225$. The scale on the right-hand side displays the corresponding scattering length values. The inset shows the region around the 48 G resonance with a model fit (see text).

Via the condition $ka \ll 1$, the inverse wave number $k^{-1} = [4k_BTm/(\pi\hbar^2)]^{-1/2}$ characterizes the crossover to the zero-energy limit. At 450 nK, $k^{-1} = 1500a_0$; at 200 nK, $k^{-1} = 2250a_0$. Correspondingly, the 450 nK data on the Feshbach resonance show a strong effect from the unitarity limitation, while the data taken at 200 nK starting conditions follow the expected scaling law up to the maximum $a \approx 1500a_0$.

Our results on recombination heating are displayed in Fig. 4. A trend towards smaller T_h at higher magnetic fields, corresponding to higher scattering lengths a, is

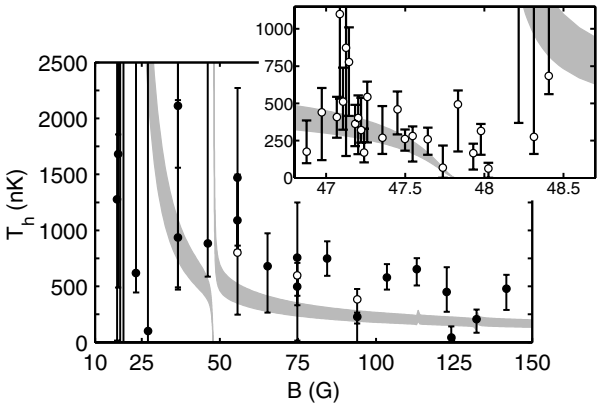

FIG. 4. Recombination heat T_h as a function of the bias field B. Filled symbols represent measurements taken at an initial temperature of 200 nK, open symbols at 450 nK. The inset shows the region around the 48 G resonance. The shaded area shows the expected range based on the calculated binding energy of the last bound state of the Cs_2 molecule (see text).

visible. At large values of a close to the Feshbach resonance, the values are correspondingly very small. We compare the data to the scenario that the recombination heating arises just from the binding energy ε of the last bound state of the dimer. As the atom involved in the three-body recombination process receives $2\varepsilon/3$, the recombination heat per lost atom results to $k_B T_h = 2\varepsilon/(3n_l)$. Therefore, we assume $k_B T_h$ to be between $2\varepsilon/9$ ($n_l = 3$) and $\varepsilon/3$ ($n_l = 2$). This range is shown as a shaded area in Fig. 4 [24]. This simple model shows reasonable agreement with the experimental data. Our heating measurements thus provide evidence of the formation of very weakly bound ultracold molecules.

From the apparent effect of recombination heating, we can draw an important conclusion for the efficiency of evaporative cooling towards quantum degeneracy in gases with large positive scattering length. If temperatures are very low ($k_B T \ll \varepsilon$) and the atom that carries $2\varepsilon/3$ cannot immediately escape from the trap, recombination heating has a detrimental effect much worse than mere three-body loss. For efficient evaporation, it is thus imperative to avoid the hydrodynamic collision regime and to implement a three-dimensional evaporation scheme. In our cooling experiments on optically trapped cesium [16], these conditions indeed turned out to be essential for the attainment of Bose-Einstein condensation.

The molecules formed in recombination are likely to remain trapped in our setup. A previous experiment shows evidence of trapping of the Cs_2 dimer in a CO_2-laser trap [26]. Away from Feshbach resonances, the magnetic dipole moment of the dimer in its last bound state has the same value as the sum of the dipole moments of two single Cs atoms, so that the levitation trap can hold the molecules under the same conditions as the atoms. This offers an intriguing way to study atom-molecule interactions both in ultracold thermal clouds and Bose-Einstein condensates. Moreover, the Feshbach resonances allow to change the molecular magnetic moment in a controlled way and thus to separate the molecules from the atoms to prepare pure molecular samples.

We thank C. Greene for useful discussions and P. Julienne for providing us with the scattering length data. We gratefully acknowledge support by the Austrian Science Fund (FWF) within SFB 15 (project part 16) and by the European Union in the frame of the Cold Molecules TMR Network under Contract No. HPRN-CT-2002-00290.

[1] F. Masnou-Seeuws and P. Pillet, Adv. At. Mol. Opt. Phys. **47**, 53 (2001).

[2] E. A. Donley, N. R. Claussen, S. T. Thompson, and C. E. Wieman, Nature (London) **417**, 529 (2002).

[3] J. Söding, D. Guéry-Odelin, P. Desbiolles, F. Chevy, H. Inamori, and J. Dalibard, Appl. Phys. B **69**, 257 (1999).

[4] E. Burt, R. Ghrist, C. Myatt, M. Holland, E. Cornell, and C. Wieman, Phys. Rev. Lett. **79**, 337 (1997).

[5] D. M. Stamper-Kurn, M. R. Andrews, A. P. Chikkatur, S. Inouye, H.-J. Miesner, J. Stenger, and W. Ketterle, Phys. Rev. Lett. **80**, 2027 (1998).

[6] J. Stenger, S. Inouye, M. R. Andrews, H.-J. Miesner, D. M. Stamper-Kurn, and W. Ketterle, Phys. Rev. Lett. **82**, 2422 (1999).

[7] J. L. Roberts, N. R. Claussen, S. L. Cornish, and C. E. Wieman, Phys. Rev. Lett. **85**, 728 (2000).

[8] P. O. Fedichev, M. W. Reynolds, and G. V. Shlyapnikov, Phys. Rev. Lett. **77**, 2921 (1996).

[9] E. Nielsen and J. H. Macek, Phys. Rev. Lett. **83**, 1566 (1999).

[10] B. D. Esry, C. H. Greene, and J. P. Burke, Jr., Phys. Rev. Lett. **83**, 1751 (1999).

[11] P. F. Bedaque, E. Braaten, and H.-W. Hammer, Phys. Rev. Lett. **85**, 908 (2000).

[12] P. J. Leo, C. J. Williams, and P. S. Julienne, Phys. Rev. Lett. **85**, 2721 (2000).

[13] C. Chin, V. Vuletic, A. J. Kerman, and S. Chu, Phys. Rev. Lett. **85**, 2717 (2000).

[14] Calculations by P. S. Julienne, E. Tiesinga, and C. J. Williams (2003), using the model of [12] (private communication).

[15] L. D. Landau and E. M. Lifshitz, *Quantum Mechanics: Non-Relativistic Theory* (Pergamon, Oxford, 1977), 3rd ed.

[16] T. Weber, J. Herbig, M. Mark, H.-C. Nägerl, and R. Grimm, Science **299**, 232 (2003).

[17] Below 10 G, the levitation gradient distorts the trapping potential too strongly for consistent measurements [16].

[18] C. Chin, Ph.D. thesis, Stanford University, 2001.

[19] In the low-temperature limit, the recombination process does not depend on the kinetic energy.

[20] Iteration steps are as follows: (i) Choose values for α and γ. (ii) Using these values, calculate a best fit of the solution of Eq. (3) to the temperature measurements, with T_h as the single fit parameter. (iii) Calculate the error sum of squares e_N between the atom number measurements and the solution of Eq. (2). Steps (i)–(iii) are repeated while varying α and γ to minimize e_N using a nonlinear optimization algorithm [21].

[21] MATLAB 6.5 R13, optimization toolbox, function *lsqnonlin*.

[22] P. R. Bevington and D. K. Robinson, *Data Reduction and Error Analysis for the Physical Sciences* (McGraw-Hill, New York, 1992), 2nd ed.

[23] C is predicted to undergo one full oscillation period between 0 and $C_{\max}$ when a varies by a factor of 22.7 [11].

[24] We include a correction [25] giving $\varepsilon = \hbar^2/[m(a - \bar{a})^2]$, with $\bar{a} = 95.5a_0$ for cesium.

[25] G. F. Gribakin and V. V. Flambaum, Phys. Rev. A **48**, 546 (1993).

[26] T. Takekoshi, B. M. Patterson, and R. J. Knize, Phys. Rev. Lett. **81**, 5105 (1998).

B.2. Bose-Einstein Condensation of Cesium

as being typical of the ionic state, whereas all the 200 K spectra showing the higher-lying peak (N; $\nu_N \sim 1430\ cm^{-1}$, red curves) indicate the neutral state, with $\rho \sim 0.2$. The 4.2 K spectrum of the 2,6-QBr_2Cl_2 complex, located at the NI QCP, reveals a blurred feature, implying that the dynamic distribution of the molecular ionicity, or equivalently the valence fluctuation with the time scale, is comparable to $(\nu_N - \nu_I)^{-1} \sim 30$ ps (*25*). Hence, the quantum paraelectric behavior in the DMTTF complex should originate from the quantum valence fluctuation rather than from the simple displacive (anti)ferroelectric transition. The dynamics of NI domain walls along the *DA* stacks, which can be related to the gigantic dielectric response above T_c in the NI transition system (*26*), may experience quantum motion and cause the collective fluctuation of the molecular valence.

The critical behavior, analogous to quantum ferroelectrics, provides evidence for the quantum valence fluctuation in the organic CT complexes. The phase transition near $T = 0$ can be driven by hydrostatic or equivalent chemical pressure. Such an anomalous variation of the molecular valence at $T = 0$ has not been observed previously for any conventional quantum ferroelectrics, and the phase transition may be distinguished as a quantum NI transition.

References and Notes

1. J. S. Miller, Ed., *Extended Linear Chain Compounds* (Plenum Press, New York, 1982), vols. 1 to 3.
2. T. Ishiguro, K. Yamaji, G. Saito, Eds., *Organic Superconductors* (Springer-Verlag, Berlin, ed. 2, 1998).
3. E. Coronado, P. Delhaes, D. Gatteschi, J. S. Miller, Eds., *Molecular Magnetism: From Molecular Assemblies to the Devices*, vol. E321, *NATO ASI Series* (Kluwer Academic, Dordrecht, Netherlands, 1996).
4. K. Nasu, Ed., *Relaxations of Excited States and Photo-Induced Phase Transitions* (Springer-Verlag, Berlin, 1997).
5. J. B. Torrance, J. E. Vazquez, J. J. Mayerle, V. Y. Lee, *Phys. Rev. Lett.* **46**, 253 (1981).
6. Y. Tokura *et al., Phys. Rev. Lett.* **63**, 2405 (1989).
7. M. H. Lemée-Cailleau *et al., Phys. Rev. Lett.* **79**, 1690 (1997).
8. T. Luty *et al., Europhys. Lett.* **59**, 619 (2002).
9. N. D. Mathur *et al., Nature* **394**, 39 (1998).
10. Q. Si, S. Rabello, K. Ingersent, J. L. Smith, *Nature* **413**, 804 (2001).
11. S. A. Grigera *et al., Science* **294**, 329 (2001).
12. S. Aoki, T. Nakayama, A. Miura, *Phys. Rev. B* **48**, 626 (1993).
13. S. Horiuchi, Y. Okimoto, R. Kumai, Y. Tokura, *J. Am. Chem. Soc.* **123**, 665 (2001).
14. K. A. Müller, H. Burkard, *Phys. Rev. B* **19**, 3593 (1979).
15. G. A. Samara, *Phys. Rev. Lett.* **27**, 103 (1971).
16. J. H. Barrett, *Phys. Rev.* **86**, 118 (1952).
17. S. Horiuchi, Y. Okimoto, R. Kumai, Y. Tokura, data not shown.
18. S. Aoki, T. Nakayama, A. Miura, *Synth. Met.* **70**, 1243 (1995).
19. T. Mitani *et al., Phys. Rev. B* **35**, 427 (1987).
20. N. Nagaosa, *J. Phys. Soc. Jpn.* **55**, 2754 (1986).
21. Concerning the low-*T* phase of DMTTF-QCl_4 crystal, E. Collet *et al.* (*27*) recently reported the doubling of one interchain axis of the triclinic unit cell, which originally contains only one *DA* pair. Furthermore, their structural analysis showed a layered ferrielectric ordering of antiparallel *DA* dimer by assuming that two (nonequivalent) *N* and *I* layers alternate along this doubled axis (noncentrosymmetric space group *P*1). However, both infrared and Raman spectroscopy (Fig. 4) have provided evidence in support of the homogeneous ρ without the mode splitting that would be expected for the modulated molecular environment and/or ionicity in the presence of nonequivalent *DA* stacks. In accord with these spectroscopic results, our latest structural analysis by synchrotron x-ray diffraction ($\lambda = 0.699$ Å) on our DMTTF-QCl_4 specimen at 14 K ($<T_c$) successfully demonstrated that two equivalent *DA* dimers in a centrosymmetic supercell (space group $P\bar{1}$) construct a layer-type antiferroelectric order (*28*). {$R = 0.063$, $R_w = 0.066$, based on 1387 observed reflections [$I > 3\sigma(I)$] and 237 variable parameters.}
22. T. Schneider, H. Beck, E. Stoll, *Phys. Rev.* **B13**, 1123 (1976).
23. Y. Nogami *et al., Synth. Met.* **70**, 1219 (1995).
24. A. Girlando, I. Zanon, R. Bozio, C. Pecile, *J. Chem. Phys.* **68**, 22 (1978).
25. S. Horiuchi, Y. Okimoto, R. Kumai, Y. Tokura, *J. Phys. Soc. Jpn.* **69**, 1302 (2002).
26. Y. Okimoto *et al., Phys. Rev. Lett.* **87**, 187401 (2001).
27. E. Collet *et al., Phys. Rev. B* **63**, 054105 (2001).
28. Supplementary material is available on *Science* Online.
29. A. Girlando, R. Bozio, C. Pecile, J. B. Torrance, *Phys. Rev.* **B26**, 2306 (1982).

30. We thank H. Okamoto, N. Nagaosa, S. Miyasaka, N. Takeshita, Y. Ogawa, and H. Sawa for enlightening discussions.

Supporting Online Material

www.sciencemag.org/cgi/content/full/299/5604/229/DC1
SOM Text
Figs. S1 to S3
Tables S1 to S6

15 July 2002; accepted 20 November 2002

Bose-Einstein Condensation of Cesium

Tino Weber, Jens Herbig, Michael Mark, Hanns-Christoph Nägerl, Rudolf Grimm

Bose-Einstein condensation of cesium atoms is achieved by evaporative cooling using optical trapping techniques. The ability to tune the interactions between the ultracold atoms by an external magnetic field is crucial to obtain the condensate and offers intriguing features for potential applications. We explore various regimes of condensate self-interaction (attractive, repulsive, and null interaction strength) and demonstrate properties of imploding, exploding, and non-interacting quantum matter.

Cesium (Cs) is an atom of particular interest in physics. It serves as our primary frequency standard (*1*) and has various important applications in fundamental metrology, such as measurements of the fine-structure constant (*2*), the electric dipole moment of the electron (*3*), parity violation (*4*), and the Earth's gravitational field (*5*). Cs, a heavy alkali atom with small photon recoil, is well suited for laser cooling and trapping methods. However, because of quantum-mechanical scattering resonances, collisions between Cs atoms at ultralow energy exhibit unusual properties with drastic consequences, such as large frequency shifts in atomic clocks (*1*). A further consequence of this resonant scattering is the fact that Cs has so far resisted all attempts to produce Bose-Einstein condensation (BEC) (*6*–*13*). In contrast, all other stable alkali species—^{87}Rb (*14*), ^{23}Na (*15*), ^{7}Li (*16*), ^{85}Rb (*17*), and ^{41}K (*18*)—have been condensed, along with hydrogen (*19*) and metastable ^{4}He (*20*).

We report the achievement of BEC of Cs (^{133}Cs, the only stable isotope) using optical trapping methods in combination with magnetic tuning of the scattering properties. With the condensate, we explore the tunability of its self-interaction that results from low-field Feshbach resonances (*21*, *22*). Across such a Feshbach resonance, the *s*-wave scattering length a shows a dispersive variation as a function of the applied magnetic field from very large positive to negative values. The magnetic tunability of the self-interaction has been exploited in experiments with magnetically trapped ^{85}Rb (*17*) and optically trapped ^{7}Li (*23*, *24*). Cs offers further flexibility because of a unique combination of resonances at low magnetic fields: One broad Feshbach resonance allows for precise tuning, whereas several narrow resonances enable very rapid control. With the magnetic field being a free parameter in our optical trapping approach to BEC, we can take full advantage of this tunability. By switching a to zero, we realize a non-interacting condensate that undergoes minimum expansion when released from the trap. By variations of the magnetic field, we observe an imploding BEC at negative a, a gently expanding BEC at moderate positive values of a, and an exploding condensate on a narrow Feshbach resonance.

Early experiments attempting BEC of Cs (*6*–*8*) followed magnetic trapping approaches similar to those used before in the realization of BEC in Rb and Na (*14*, *15*). Resonant elastic scattering with a large cross section was observed, but a rapid loss of atoms due to inelastic two-body collisions had a detrimental effect on evaporative cooling and prevent-

Institut für Experimentalphysik, Universität Innsbruck, Technikerstraβe 25, 6020 Innsbruck, Austria.

ed the experiments from reaching BEC (*6*, *7*). More recent magnetic trapping experiments have explored a range of magnetic fields, where two-body loss is relatively small, and have approached the phase-space density required for BEC to within a factor of 10 (*13*).

The use of optical dipole forces allows atoms to be trapped in their lowest internal state (*25*), where the absence of internal energy leads to full suppression of inelastic two-body loss processes. Because atoms in this state seek out regions of high magnetic fields, they are in general not trappable by magnetic forces. Experiments in optical dipole traps (*9*–*12*) have explored cooling of Cs in the corresponding state, which has a total angular momentum $F = 3$ and a magnetic quantum number $m_F = 3$. Evaporative cooling (*12*) has approached BEC to within a factor of 2, before running into limitations by three-body processes (*26*).

Knowledge of the *s*-wave scattering length of the lowest internal state of Cs originates from precise measurements of low-field Feshbach resonances (*21*) and their theoretical analysis (*22*). The scattering length a shows a pronounced dependence on the magnetic field B (*27*, *28*): It varies from a large negative value at zero field ($-3000\ a_0$ at 0 G) to large positive values at higher fields ($1000\ a_0$ at 55 G), going through zero at 17 G; $a_0 = 0.0529$ nm denotes Bohr's radius. This smooth variation over a wide magnetic field range can be interpreted as a result of a broad Feshbach resonance at about −8 G; here the negative field corresponds to a resonance position of +8 G (*22*) in the magnetically trappable state with $m_F = -3$. In addition to this broad one, several narrow Feshbach resonances occur (*27*, *29*), with the most prominent one at 48 G.

In our experiment, the starting point for evaporative cooling is a large-volume dipole trap that we realize by horizontally crossing two 100-W CO_2 laser beams (*30*). The trap has an effective volume of about 1 mm^3, is ~10 μK deep, and has a geometrically averaged trap frequency of $\bar{\omega}/2\pi = 14$ Hz. In contrast to the all-optical approach to BEC of (*31*), which uses tightly focused CO_2 laser beams and trap frequencies of the order of 1 kHz, our trap is shallow and designed for loading a large number of atoms rather than providing tight confinement. The CO_2 laser trap is loaded by adiabatical release of Cs atoms from an optical lattice. After Raman sideband cooling in the lattice according to (*32*) we start with a sample of 2×10^7 atoms with predominant polarization in the state $F = 3$, $m_F = 3$, a temperature of ~1 μK, and a phase-space density of a few 10^{-3}. Transfer losses and spatial mismatches, together with an excess potential energy of the trap, reduce the initial phase-space density to $\sim 10^{-4}$.

A magnetic levitation field (*30*) is applied to support the atoms against gravity (*12*, *14*). This field is essential to operate the large-volume CO_2 laser trap, which features optical forces far below the gravitational force on a Cs atom. Moreover, it is crucial for implementing efficient three-dimensional evaporation without being limited by gravitational sag. We combine the inhomogeneous levitation field with a freely adjustable bias field B_0 (*30*) to tune the scattering properties.

Evaporative cooling toward BEC proceeds in three stages (Fig. 1). In the first 10 s (Fig. 1A), the sample is cooled down by evaporation out of the CO_2 laser trap at constant trap depth. To obtain a sufficient collision rate at the rather low density of a few 10^{11} cm^{-3}, the scattering length is tuned to a large magnitude of $a = 1200\ a_0$ by setting the bias field to $B_0 = 75$ G. After 10 s, 2×10^6 atoms remain trapped at a temperature of ~1 μK and a phase-space density of about 10^{-3}.

In the following 5 s (Fig. 1B), an additional horizontal laser beam derived from a Yb fiber laser at a wavelength of 1064 nm is focused into the sample (waist, 30 μm) to create a narrow and deep potential well in the center of the CO_2 laser trap. Within these 5 s, the power is ramped up linearly from zero to 90 mW. The adiabatically deformed potential provides a strong local increase in the number density with a minor increase in the temperature, and a substantial gain in phase-space density is achieved (*33*, *34*). The magnetic bias field is set to $B_0 = 23$ G ($a = 300\ a_0$), which suppresses three-body loss as observed at higher values of a. Finally, one of the CO_2 lasers is turned off and about 3×10^5 atoms remain trapped in the combined field of the 1064-nm beam intersecting the CO_2 laser beam at an angle of 30°. This results in a cigar-shaped trap with tight radial confinement provided by the 1064-nm beam (radial trap frequency, 320 Hz). The axial confinement (axial frequency, 6 Hz) is essentially provided by the remaining CO_2 laser beam. In this way, a dense sample of Cs atoms (a few 10^{12} cm^{-3}) is prepared with a phase-space density on the order of 10^{-2}.

In the final stage (Fig. 1C), forced evaporative cooling is performed by ramping down the power of the 1064-nm beam to values of a few milliwatts within 17 s (*30*). The magnetic bias field is kept at 23 G ($a = 300\ a_0$), which is found to optimize the ratio of elastic collisions and inelastic three-body processes. We find that, for the given ramp, evaporative cooling toward BEC is possible only in a narrow magnetic field range between 21 and 25 G. Below 21 G, the cross

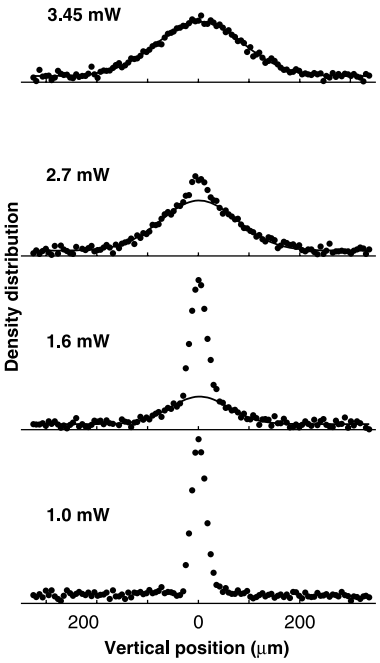

Fig. 2. Vertical density profiles of the released atom cloud observed after 50 ms of free expansion in the magnetic levitation field. The variable laser power at the end of the ramp is shown at left (in milliwatts). The profiles are obtained by horizontally integrating the measured column density in a 130-μm-wide region of interest. In these measurements, the magnetic bias field is switched to 17 G at the time of release to suppress the condensate expansion, which makes the appearance of the two-component distribution more pronounced. Gaussian fits to the thermal part of the distribution (solid lines in the upper three graphs) yield the temperatures.

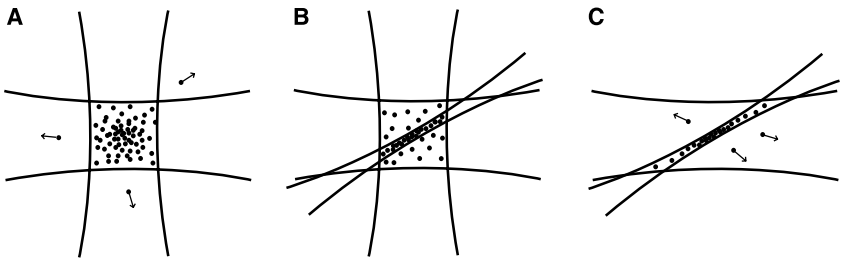

Fig. 1. Illustration of the three stages of evaporative cooling toward BEC of Cs. (**A**) Ten seconds of plain evaporation in two crossed CO_2 laser beams at a magnetic bias field of 75 G (scattering length tuned to 1200 a_0). (**B**) Five seconds of collisional loading of a tightly focused 1064-nm laser beam at 23 G (300 a_0). (**C**) Forced evaporative cooling by ramping down the power of the 1064-nm beam over 17 s, with the magnetic bias field kept at 23 G.

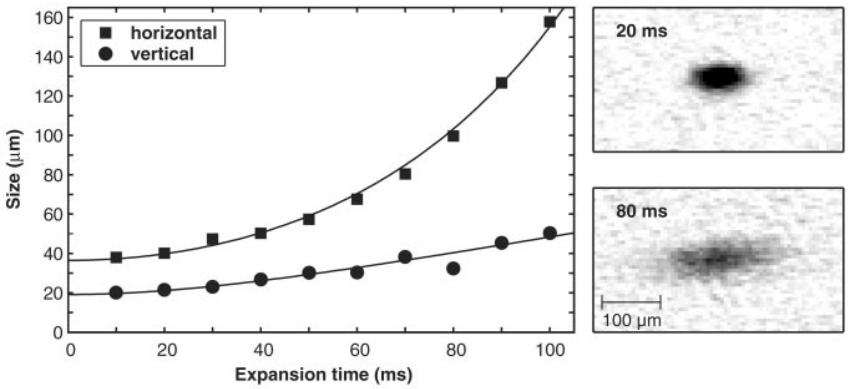

Fig. 3. Expansion of a non-interacting condensate at 17 G in the magnetic levitation field. The images at right show the condensate 20 ms (top) and 80 ms (bottom) after release. The data points at left show the 1/*e* half-widths of Gaussian fits to absorption images of the expanding cloud. The fit to the horizontal expansion shows the function $A\cosh(\alpha t)$, which describes the expansion with a calculated time constant of $\alpha^{-1} = 47$ ms (*30*) and an initial width $A = 36$ μm as the only adjustable parameter. The fit to the vertical expansion yields a mean kinetic energy of $k_B \times 600$ pK.

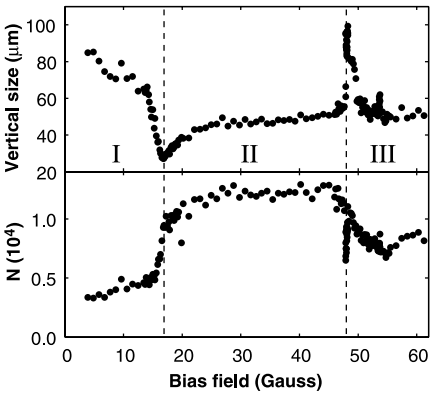

Fig. 4. Vertical extension (1/*e* half-width of a Gaussian fit) and atom number *N* of the expanding cloud as a function of the variable bias field applied in the first 10 ms after release. The measurements are taken after a total expansion time of 50 ms. The three different regions refer to (I) negative scattering length; (II) positive scattering length; and (III) a regime dominated by narrow Feshbach resonances, a prominent one at 48 G and a weaker one at 53 G.

section for elastic scattering is too small; and above 25 G, an increased rate of three-body processes in combination with the hydrodynamic collision regime leads to strong loss.

At the end of the ramp, the sample is released from the trap by simultaneously turning off both the CO_2 laser and the 1064-nm laser. In the magnetic levitation field, the atoms remain at a fixed vertical position. The observation time is typically limited to 100 ms by the horizontal spreading of the cloud that results from the weak transverse antitrapping force of the levitation field (*30*). For detection, absorption images are taken in a standard way (*14*, *15*) with a resonant probe beam that propagates horizontally at an angle of 30° with respect to the 1064-nm laser beam and 60° with respect to the CO_2 laser beam.

The BEC phase transition becomes obvious in the vertical density profiles of Fig. 2, which were taken 50 ms after release. Down to a final power of 3.45 mW (potential depth, 550 nK), a thermal cloud is observed; the corresponding profile shows a cloud of 65,000 atoms at temperature (T) = 46 nK. At final powers of 2.7 mW (450 nK) and 1.6 mW (260 nK), the profiles show a partially condensed cloud with T = 36 nK and 21 nK, respectively. At 1.0 mW (160 nK), an almost pure condensate is realized with 16,000 atoms. When the condensate with a peak density of 1.3×10^{13} cm^{-3} is kept in the trap, we measure a lifetime of ~15 s and infer an upper bound for the three-body loss coefficient of 2×10^{-27} cm^6 s^{-1}. This highlights the stability of the Cs BEC at the applied magnetic field.

We explore the magnetic tunability of the Cs condensate in the range between 5 and 65 G. The zero-crossing of the scattering length at 17 G allows us to turn off the self-interaction and thus to realize a "frozen" condensate with minimum internal energy. Figure 3 shows the measured expansion of the condensate, when B_0 is switched to 17 G at the time of release. In the vertical direction, a very slow expansion is observed, with a mean kinetic energy as low as $k_B \times 600$ pK (where k_B is Boltzmann's constant), which we attribute to residual self-interaction effects within the finite switching time. In the horizontal direction, the increasing width is fully determined by the horizontal magnetic force, which magnifies the initial cloud size according to the expected cosine hyperbolicus function (*30*). The non-interacting condensate can also be observed when the magnetic levitation field is turned off. Then, however, the observation of the falling BEC is limited to about 35 ms. We expect that with a few straightforward technical improvements in switching, the interaction energy of the "frozen" condensate could be reduced down to values of a few pK.

In order to demonstrate the other regimes of self-interaction, we switch to a variable magnetic field synchronously with the release of the condensate. The variable field is applied for a short time interval of 10 ms, which is sufficiently long for the mean-field dynamics to take place. For subsequent expansion at fixed conditions, the magnetic bias field is switched to 17 G. After a total expansion time of 50 ms, the vertical extension of the cloud and the total number of atoms are measured. The corresponding results (Fig. 4) show a marked dependence on the magnetic field with three distinct regions: Below 17 G (region I), the scattering length is negative and the BEC implodes, leading to a large momentum spread and a substantial loss of atoms. Between 17 and 48 G (region II), the scattering length is positive and varies smoothly from zero to about 1000 a_0. The expansion shows the minimum width at 17 G and a subsequent increase in width, in agreement with the predicted behavior of the scattering length. For higher fields (region III), the behavior is dominated by a narrow Feshbach resonance at 48 G. On this resonance, the cloud expands very rapidly as the condensate explodes in response to the strong sudden increase of its internal energy. In addition, a sharp loss feature is observed, which may indicate the formation of molecules in the BEC (*35*). At even higher fields, the data show an asymmetry and broadening of the resonance together with a loss of atoms, which we attribute to the finite ramp speed over the resonance (*17*).

The unique tunability offered by a Cs condensate is of great interest in various respects. In the field of quantum gases, it may serve as the experimental key to explore new regimes beyond standard mean-field theory, such as the strongly interacting regime with an interparticle spacing on the order of the scattering length, systems in reduced dimensionality, and the Mott insulator phase (*36*, *37*). Moreover, Cs is an interesting candidate for the creation of cold molecules and a molecular BEC (*35*, *38*). For applications in metrology, a "frozen" BEC without internal energy would represent an ideal source of cold atoms; for example, for precision measurements of the photon recoil (*39*). For future atomic clocks, one may envisage loading a very weak optical lattice with Cs atoms from a BEC. With one atom per site, such a system would provide long observation times with suppressed collisional frequency shifts.

Besides this particular interest in Cs, our experiments demonstrate that optical trapping methods allow BEC to be achieved with a species for which conventional magnetic trapping approaches have met severe difficulties.

References and Notes

1. C. Salomon *et al.*, *Proceedings of the 17th International Conference on Atomic Physics (ICAP 2000)*, E. Arimondo, P. D. Natale, M. Inguscio, Eds. (American Institute of Physics, Melville, NY, 2001), pp. 23–40.
2. J. M. Hensley, A. Wicht, B. C. Young, S. Chu, *Proceedings of the 17th International Conference on Atomic Physics (ICAP 2000)*, E. Arimondo, P. D. Natale, M. Inguscio, Eds. (American Institute of Physics, Melville, NY, 2001), pp. 43–57.
3. C. Chin, V. Leiber, V. Vuletic, A. J. Kerman, S. Chu, *Phys. Rev. A* **63**, 033401 (2001).
4. C. E. Wieman, *Proceedings of the 16th International Conference on Atomic Physics (ICAP 1998)*, W. E. Baylis, G. W. Drake, Eds. (American Institute of Physics, Woodbury, NY, 1999), pp. 1–13.
5. M. J. Snadden, J. M. McGuirk, P. Bouyer, K. G. Haritos, M. A. Kasevich, *Phys. Rev. Lett.* **81**, 971 (1998).
6. J. Söding, D. Guéry-Odelin, P. Desbiolles, G. Ferrari, J. Dalibard, *Phys. Rev. Lett.* **80**, 1869 (1998).
7. D. Guéry-Odelin, J. Söding, P. Desbiolles, J. Dalibard, *Europhys. Lett.* **44**, 26 (1998).
8. J. Arlt *et al.*, *J. Phys. B* **31**, L321 (1998).
9. H. Perrin, A. Kuhn, I. Bouchoule, C. Salomon, *Europhys. Lett.* **42**, 395 (1998).
10. A. J. Kerman, V. Vuletić C. Chin, S. Chu, *Phys. Rev. Lett.* **84**, 439 (2000).
11. D.-J. Han *et al.*, *Phys. Rev. Lett.* **85**, 724 (2000).
12. D. Han, M. T. DePue, D. Weiss, *Phys. Rev. A* **63**, 023405 (2001).
13. S. L. Cornish, S. Hopkins, A. M. Thomas, C. J. Foot, abstract from the 7th Workshop on Atom Optics and Interferometry, 28 September to 2 October 2002, Lunteren, Netherlands (book of abstracts).
14. M. Anderson, J. Ensher, M. Matthews, C. Wieman, E. Cornell, *Science* **269**, 198 (1995).
15. K. Davis *et al.*, *Phys. Rev. Lett.* **75**, 3969 (1995).
16. C. Bradley, C. Sackett, J. Tollett, R. Hulet, *Phys. Rev. Lett.* **75**, 1687 (1995).
17. S. Cornish, N. Claussen, J. Roberts, E. Cornell, C. Wieman, *Phys. Rev. Lett.* **85**, 1795 (2000).
18. G. Modugno *et al.*, *Science* **294**, 1320 (2001); published online 18 October 2001 (10.1126/science.1066687).
19. D. G. Fried *et al.*, *Phys. Rev. Lett.* **81**, 3811 (1998).
20. A. Robert *et al.*, *Science* **292**, 461 (2001); published online 22 March 2001 (10.1126/science.1060622).
21. C. Chin, V. Vuletic, A. J. Kerman, S. Chu, *Phys. Rev. Lett.* **85**, 2717 (2000).
22. P. J. Leo, C. J. Williams, P. S. Julienne, *Phys. Rev. Lett.* **85**, 2721 (2000).
23. L. Khaykovich *et al.*, *Science* **296**, 1290 (2002).
24. K. Strecker, G. Partridge, A. Truscott, R. Hulet, *Nature* **417**, 150 (2002).
25. R. Grimm, M. Weidemüller, Yu. B. Ovchinnikov, *Adv. At. Mol. Opt. Phys.* **42**, 95 (2000).
26. D. S. Weiss, personal communication.
27. A. J. Kerman *et al.*, *C. R. Acad. Sci. Paris IV* **2**, 633 (2001).
28. P. S. Julienne, E. Tiesinga, C. J. Williams, personal communication.
29. We observe the narrow Feshbach resonances at 11.0, 14.3, 15.0, 19.9, 47.7, and 53.4 G (accuracy ±0.2 G) as loss resonances in three-body decay of an uncondensed gas.
30. Materials and methods are available as supporting material on *Science* Online.
31. M. Barrett, J. Sauer, M. Chapman, *Phys. Rev. Lett.* **87**, 010404 (2001).
32. P. Treutlein, K. Y. Chung, S. Chu, *Phys. Rev. A* **63**, 051401 (2001).
33. D. Stamper-Kurn *et al.*, *Phys. Rev. Lett.* **81**, 2194 (1998).
34. M. Hammes, D. Rychtarik, H.-C. Nägerl, R. Grimm, *Phys. Rev. A* **66**, 051401(R) (2002).
35. E. A. Donley, N. R. Claussen, S. T. Thompson, C. E. Wieman, *Nature* **417**, 529 (2002).
36. D. Jaksch, C. Bruder, J. Cirac, C. Gardiner, P. Zoller, *Phys. Rev. Lett.* **81**, 3108 (1998).
37. M. Greiner, O. Mandel, T. Esslinger, T. W. Hänsch, I. Bloch, *Nature* **415**, 39 (2002).
38. F. Masnou-Seeuws, P. Pillet, *Adv. At. Mol. Opt. Phys.* **47**, 53 (2001).
39. S. Gupta, K. Dieckmann, Z. Hadzibabic, D. E. Pritchard, *Phys. Rev. Lett.* **89**, 140401 (2002).

40. We thank all members of the cold-atom group for support and a great team spirit. In particular, we thank the Cs surface trapping team, M. Hammes, D. Rychtarik, and B. Engeser, for fruitful interactions and for sharing the 1064-nm laser; A. Noga for assistance; and J. Hecker Denschlag for useful discussions. We are indebted to R. Blatt and his ion trapping group for support during our start-up phase in Innsbruck. We acknowledge financial support by the Austrian Science Fund (FWF) within project P15114 and within SFB 15 (project part 16).

Supporting Online Material
www.sciencemag.org/cgi/content/full/1079699/DC1
Materials and Methods
Figs. S1 to S3
References

23 October 2002; accepted 26 November 2002
Published online 5 December 2002;
10.1126/science.1079699
Include this information when citing this paper.

Anthropogenic CO_2 Uptake by the Ocean Based on the Global Chlorofluorocarbon Data Set

Ben I. McNeil,[1]* Richard J. Matear,[2] Robert M. Key,[1] John L. Bullister,[3] and Jorge L. Sarmiento[1]

We estimated the oceanic inventory of anthropogenic carbon dioxide (CO_2) from 1980 to 1999 using a technique based on the global chlorofluorocarbon data set. Our analysis suggests that the ocean stored 14.8 petagrams of anthropogenic carbon from mid-1980 to mid-1989 and 17.9 petagrams of carbon from mid-1990 to mid-1999, indicating an oceanwide net uptake of 1.6 and 2.0 ± 0.4 petagrams of carbon per year, respectively. Our results provide an upper limit on the solubility-driven anthropogenic CO_2 flux into the ocean, and they suggest that most ocean general circulation models are overestimating oceanic anthropogenic CO_2 uptake over the past two decades.

Despite improvements in our understanding of the partitioning of anthropogenic CO_2 between the atmosphere, ocean, and terrestrial biosphere, substantial uncertainties and insufficient direct observational constraints continue. Recent decadal-scale changes in oxygen concentrations that have been observed in the ocean (*1*, *2*) imply large and uncertain corrections (*3*–*5*) to the oceanic and terrestrial sinks for anthropogenic CO_2 that have been estimated based on atmospheric O_2/N_2 observations (*6*, *7*), which was the method used in the 2001 report by the Intergovernmental Panel on Climate Change (*8*). Because the O_2/N_2 technique is based on atmospheric observations, it inherently requires assumptions regarding the partitioning of anthropogenic CO_2 between the ocean and terrestrial biosphere. Ocean general circulation models (OGCMs) currently simulate oceanic anthropogenic CO_2 uptake, assuming a steady-state circulation and biological production (*9*). We present here an observational estimate of the decadal inventory of anthropogenic CO_2 in the ocean based on the global chlorofluorocarbon (CFC) data set. Our estimates provide independent observational insights into the contemporary global carbon budget and provide a framework that can be used for direct validation of ocean model predictions.

The most direct way of estimating anthropogenic CO_2 accumulation in the ocean is to compare dissolved inorganic carbon (DIC) measurements made at one time with those made later in the same region. To isolate the long-term trend from changes due to natural variability, DIC measurements along isopycnal surfaces (*10*) can be compared, or multiple linear regression (MLR) of DIC against hydrographic properties (*11*) can be used (Fig. 1C legend). Although these methods provide direct evidence for regional anthropogenic CO_2 accumulation (*10*, *12*, *13*), they currently cannot be used in the global context because of the lack of adequate historical DIC measurements.

Another way to estimate anthropogenic CO_2 is to study the distribution of CFCs in the ocean. The release of CFC-11 (CCl_3F) and CFC-12 (CCl_2F_2) to the atmosphere began in the 1930s and accelerated in the 1950s. CFCs are entirely anthropogenic and biologically inert in the ocean. The oceanic CFC distribution thus provides valuable information about the rates and pathways of water mass ventilation processes (*14*). As part of the World Ocean Circulation Experiment (WOCE) carried out in the 1990s, dissolved CFCs were measured with great accuracy and unprecedented global resolution (Fig. 2). The patterns of oceanic accumulation

[1]Atmospheric and Oceanic Science Program, Princeton University, Princeton, NJ 08544, USA. [2]Commonwealth Scientific and Industrial Research Organisation Marine Research and the Antarctic Co-operative Research Centre, Hobart, Tasmania, Australia. [3]Pacific Marine Environmental Laboratory, National Oceanic and Atmospheric Administration, Seattle, WA 98115, USA.

*To whom correspondence should be addressed.

Bose-Einstein Condensation of Cesium

Tino Weber, Jens Herbig, Michael Mark, Hanns-Christoph Nägerl, Rudolf Grimm

Materials and Methods

Crossed-beam CO_2 laser trap

The large-volume dipole trap is realized by horizontally crossing two 100-W beams derived from two separate, highly stable CO_2 lasers (Coherent-DEOS GEM-100L). In the intersection region the Gaussian beam waists are 0.6 mm, which results in a trap depth of $\sim 10\mu$K per beam and a geometrically averaged trap frequency of $\bar{\omega}/2\pi = 14$ Hz. The CO_2 lasers operate at a wavelength of 10.6μm, constituting a quasi-electrostatic trap (*S1–S3*). The photon scattering rates in this configuration are below one photon per hour. The magneto-optical trap which provides the initial ensemble of cold atoms is loaded from a Zeeman-slowed atomic beam. The dipole trap is operated in an ultra-high vacuum environment with a background pressure of $\sim 10^{-11}$mbar. We measure a rest-gas limited lifetime of the order of three minutes.

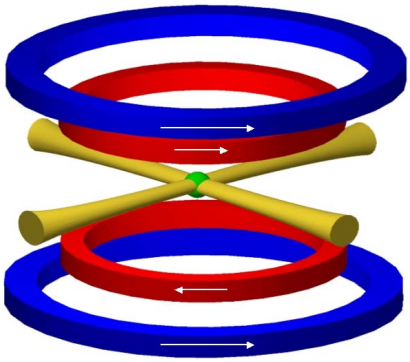

Fig. S1. Illustration of the crossed-beam CO_2 laser trap together with the coils for the magnetic field control: red, levitation coils; blue, Feshbach-tuning coils.

Magnetic field

The magnetic field for levitation and Feshbach tuning is applied immediately after loading the CO_2 laser trap. It is generated by a combination of two pairs of coils. The first pair (Fig. S1, red), in anti-Helmholtz configuration, produces a fixed vertical gradient of 31.3 G/cm to magnetically levitate the atoms in the $F = 3$, $m_F = 3$ state. The second pair (Fig. S1, blue), in Helmholtz configuration, provides the variable bias field B_0 up to 200 G, to tune the scattering length.

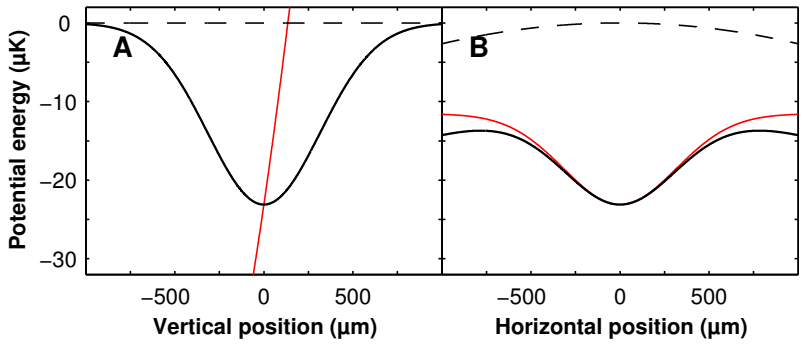

Fig. S2. Trapping potentials along the vertical axis (A) and horizontally along one of the laser beams (B). Red lines: potentials in the gravitational field without levitation. Black lines: trapping potentials, gravity compensated by the levitation field (bias field 23 G). Dashed lines: effect of the levitation field without optical potentials.

In Fig. S2 the trapping potentials are illustrated along the vertical axis (A) and horizontally along one of the CO_2 laser beams (B). The red lines indicate the total potentials without levitation, when the shallow optical trap is by far too weak to hold atoms against gravity in the vertical direction. If the levitation gradient is exactly matched to the magnetic moment to compensate for gravity (Fig. S2, black lines), the total potential is confining and the corresponding Stern-Gerlach selection ensures perfect spin polarization of the sample.

The combined field of both pairs of coils allows for complete cancellation of vertical forces, but horizontally exhibits a weak outward directed force $F_\rho = m\alpha^2\rho$ depending on the distance ρ from the symmetry axis (Fig. S2, B); the constant $\alpha = g\sqrt{m/(3\mu_B B_0)}$ is determined by the

atom's mass m, the gravitational acceleration g, and Bohr's magneton μ_B. This effect slightly reduces the trap depth but has negligible influence on the trap frequencies.

The dashed lines in Fig. S2 indicate the net effect of the weak horizontal anti-trapping force at a bias field of 23 G when the optical potential is turned off. As can be seen, F_ρ does affect the motion of free atoms after release from the trap. With an initial horizontal position of ρ_0 and a velocity v_0 the horizontal motion follows $\rho(t) = \rho_0 \cosh(\alpha t) + \alpha^{-1} v_0 \sinh(\alpha t)$. The vertical motion is not affected.

Evaporation procedure with the 1064-nm beam

To load the tightly focused 1064-nm laser beam (Gaussian beam waist $30\mu m$) from the crossed-beam CO_2 laser trap, its power is linearly increased to 90 mW within five seconds. For further

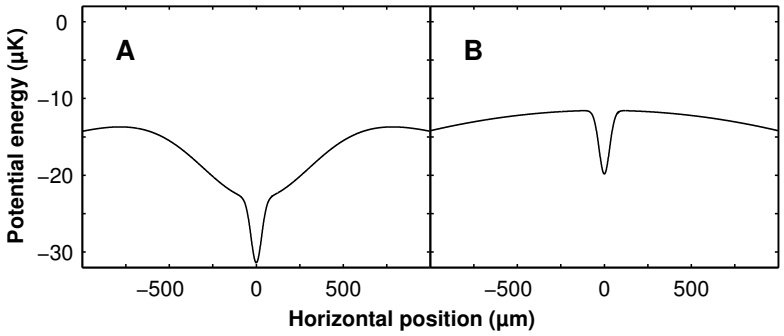

Fig. S3. Potential along one of the CO_2 laser beams with the 1064-nm laser at 50 mW and a bias field of 23 G. A. loading stage: both CO_2 lasers on; B. evaporation stage: the second CO_2 laser is switched off.

evaporation we switch off one of the CO_2 lasers and decrease the power of the 1064-nm beam over 17 s following four subsequent linear ramps connecting the points: 0 s, 90 mW; 2 s, 50 mW; 5 s, 10 mW; 10 s, 3.5 mW; 15 s, variable final power. In the last two seconds before release the power is kept at constant at the final level. The potential shapes during the loading stage and evaporation stage are illustrated in Fig. S3.

References

S1. T. Takekoshi, R. Knize, *Opt. Lett.* **21**, 77 (1996).

S2. H. Engler, T. Weber, M. Mudrich, R. Grimm, M. Weidemüller, *Phys. Rev. A* **62**, 031402(R) (2000).

S3. K. O'Hara *et al.*, *Phys. Rev. Lett.* **82**, 4204 (1999).

B.3. Preparation of a Pure Molecular Quantum Gas

One additional correction that cannot be added as a σ in quadrature is the LMC rotation. Several young and intermediate-age kinematic tracers have been measured in the LMC, including HII regions, PN, CH stars, Miras, and carbon stars. In the inner regions of the LMC bar, these populations are rotating as a solid body, with 25 km/s per kpc. For a scale of 1 kpc = 1.2°, our fields should not show a rotation component larger than 10 km/s.

In addition, a correction for rotation may not be necessary for the RR Lyrae population, because there is no evidence that this old population follows the LMC rotation. On the basis of the Milky Way RR Lyrae, one might suspect that the LMC RR Lyrae do not rotate like the rest of the stars. However, a composite RR Lyrae population may be present. For example, earlier interpretation of the RR Lyrae number counts indicated an exponential disk distribution (*31*). Multiple components (halo plus thick disk) cannot be ruled out without rotation measurements. Our fields are not spread out enough to measure the rotation. In order to measure the systemic rotation of the RR Lyrae population, one would need to observe $N \cong 50$ stars per field in fields located $>3°$ away on opposite sides of the bar. We estimate the correction in two ways: with the use of the velocities from HI maps (*32*) and with the use of the mean rotation fits of the disk (*22*, *24*). This correction does not change at all the LMC RR Lyrae velocity dispersion.

The large RR Lyrae velocity dispersion $\sigma_{true} = 53$ km/s implies that metal-poor old stars are distributed in a halo population. The velocity dispersion for the old RR Lyrae stars is higher than that for the old LMC clusters, although there are too few old clusters to measure the kinematics in the LMC. The presence of a kinematically hot, old, and metal-poor halo in the LMC suggests that galaxies like the Milky Way and small galaxies like the LMC have similar early formation histories (*33*).

The stellar halo traced by the RR Lyrae amounts only to 2% of the mass of the LMC, which is akin to the Milky Way halo (*1*, *22*). Consequently, its contribution to the microlensing optical depth should not be important (*26*, *34*). The ongoing Supermacho experiment will discover an order of magnitude more microlensing events toward the LMC (*35*), allowing us to test this prediction.

References and Notes

1. T. D. Kinman *et al.*, *Publ. Astron. Soc. Pac.* **103**, 1279 (1991).
2. M. Feast, in *Variable Stars and Galaxies*, Brian Warner, Ed. [Astronomical Society of the Pacific (ASP) Conference Series 30, San Francisco, 1992], p. 143.
3. E. W. Olszewski, N. B. Suntzeff, M. Mateo, *Annual Rev. Astron. Astrophys.* **34**, 511 (1996).
4. D. Minniti, *Astrophys. J.* **459**, 175 (1996).
5. A. Layden, in *Galactic Halos*, D. Zaritsky, Ed. (ASP Conference Series 136, San Francisco, 1998), p.14.
6. L. Searle, R. Zinn, *Astrophys. J.* **225**, 358 (1978).
7. O. Eggen, D. Lynden-Bell, A. Sandage, *Astrophys. J.* **136**, 748 (1962).
8. D. Minniti, A. A. Zijlstra, *Astrophys. J.* **467**, L13 (1996).
9. D. R. Alves, M. Rejkuba, D. Minniti, K. H. Cook, *Astrophys. J.* **573**, L51 (2002).
10. K. C. Freeman, G. Illingworth, A. Oemler, *Astrophys. J.* **272**, 488 (1983).
11. R. A. Schommer, E. W. Olszewski, N. B. Suntzeff, H. C. Harris, *Astron. J.* **103**, 447 (1992).
12. C. Alcock *et al.*, *Astrophys. J.* **490**, L59 (1997).
13. C. Alcock *et al.*, *Astrophys. J.* **482**, 89 (1997).
14. C. Alcock *et al.*, *Astrophys. J.* **542**, 257 (2000).
15. The MACHO RR Lyrae data are available online at the MACHO Project home page (www.macho.mcmaster.ca/). These RR Lyrae are classified on the basis of the MACHO light curves, with RRab being fundamental pulsators; RRc, first overtones; and RRe, double mode pulsators.
16. H. A. Smith, *The RR Lyrae Stars* (Cambridge Univ. Press, Cambridge, 1995).
17. C. M. Clement *et al.*, *Astron. J.* **122**, 2587 (2001).
18. M. Mayor *et al.*, *Astron. Astrophys.* **114**, 1087 (1997).
19. J. Kaluzny *et al.*, *Astron. Astrophys. Suppl. Ser.* **122**, 471 (1997).
20. J. E. Norris, K. C. Freeman, M. Mayor, P. Seitzer, *Astrophys. J.* **487**, 187 (1997).
21. D. S. Graff, A. Gould, N. B. Suntzeff, R. Schommer, E. Hardy, *Astrophys. J.* **540**, 211 (2000).
22. D. R. Alves, C. A. Nelson, *Astrophys. J.* **542**, 789 (2001).
23. E. Hardy, D. R. Alves, D. S. Graff, N. B. Suntzeff, R. A. Schommer, *Astrophys. J. Suppl. Ser.* **277**, 471 (2001).
24. R. P. van der Marel, D. R. Alves, E. Hardy, N. B. Suntzeff, *Astron. J.* **124**, 2639 (2002).
25. S. M. G. Hughes, P. R. Wood, I. N. Reid, *Astron. J.* **101**, 1304 (1991).
26. G. Gyuk, N. Dalal, K. Griest, *Astrophys. J.* **535**, 90 (2000).
27. We eliminated a low-velocity star, discrepant by more than 4σ from the mean, which could be a misidentified foreground star.
28. G. Clementini, R. Megighi, C. Cacciari, C. Gouiffes, *Mon. Not. R. Astron. Soc.* **267**, 83 (1994).
29. I. Skillen, J. A. Fernley, R. S. Stobie, R. F. Jameson, *Mon. Not. R. Astron. Soc.* **265**, 301 (1993).
30. We adopt a conservative error of 10 km/s for this quantity on the basis of uncertainties in the control samples.
31. C. Alcock *et al.*, *Astron. J.* **119**, 2194 (2000).
32. K. Rohlfs, J. Kreitschmann, B. C. Siegman, J. V. Feitzinger, *Astron. Astrophys.* **137**, 343 (1984).
33. The sample is not large enough and the velocities are not accurate enough to (i) detect tidal streams in front or behind the LMC and (ii) measure the systemic rotation of the halo RR Lyrae population. However, from a sample of this size, and with velocities measured to this accuracy, there is no difficulty in measuring the velocity dispersion and thus distinguishing a disk population from a halo population in the LMC.
34. C. Alcock *et al.*, *Astrophys. J.* **542**, 281 (2000).
35. C. Stubbs, in *The Galactic Halo*, B. K. Gibson, T. S. Axelrod, M. E. Putman, Eds. (ASP Conference Series 165, San Francisco, 2000), p. 503.

36. We gratefully acknowledge suggestions from E. Olszewski, A. Drake, M. Catelan, and C. Alcock and support by the Fondap Center for Astrophysics 15010003; by the U.S. Department of Energy National Nuclear Security Administration to University of California's Lawrence Livermore National Laboratory under contract W-7405-Eng-48; and by the Bilateral Science and Technology Program of the Australian Department of Industry, Technology, and Regional Development; and by ESO Program 70.B-0547.

27 June 2003; accepted 11 August 2003

Preparation of a Pure Molecular Quantum Gas

Jens Herbig, Tobias Kraemer, Michael Mark, Tino Weber, Cheng Chin, Hanns-Christoph Nägerl, Rudolf Grimm*

An ultracold molecular quantum gas is created by application of a magnetic field sweep across a Feshbach resonance to a Bose-Einstein condensate of cesium atoms. The ability to separate the molecules from the atoms permits direct imaging of the pure molecular sample. Magnetic levitation enables study of the dynamics of the ensemble on extended time scales. We measured ultralow expansion energies in the range of a few nanokelvin for a sample of 3000 molecules. Our observations are consistent with the presence of a macroscopic molecular matter wave.

Rapid progress in controlling ultracold atomic gases, culminating in the creation of atomic Bose-Einstein condensates (BECs) and opening the door to the realm of coherent matter-wave physics (*1*–*3*), has raised the question of whether a similar level of control is possible with molecular samples. Molecules, in contrast to atoms, have a much richer internal structure and can possess permanent vector or tensor properties, such as electric dipole moments, rotational angular momentum, and even chirality. Molecule-atom and molecule-molecule interactions are at least three- and four-body processes in nature, posing new challenges to our theoretical understanding. Exquisite control over the internal and external degrees of freedom of molecules could allow the experimental study of a new coherent chemistry (*4*), where matter-wave interference, quantum tunneling, and bosonic stimulation dominate the dynamics and where the interaction properties can be externally controlled and engineered with electromagnetic fields. Quantum degenerate molecular gases with permanent dipole moments are also prime candidates for the precise investigation of strongly correlated quantum

Institut für Experimentalphysik, Universität Innsbruck, Technikerstraβe 25, 6020 Innsbruck, Austria.

*To whom correspondence should be addressed. E-mail: rudolf.grimm@uibk.ac.at

systems and for the study of novel quantum phase transitions (*5*).

Several avenues have been investigated to cool and trap molecules. Slowing of a supersonic jet of polar molecules in time-varying electric fields (*6*) and buffer gas loading and trapping (*7*) in either electrostatic or magnetic traps both permit large molecular populations with temperatures in the mK range. Alternatively, creation of molecules by photoassociation of precooled atoms has led to molecular samples with temperatures in the μK range (*8*). For all these techniques, however, the resulting molecular phase-space density is still many orders of magnitude away from quantum degeneracy.

Starting with a sample of ultracold atoms, controlled production of molecules can be realized by the coherent coupling of an atom pair state to a molecular state. For example, a two-photon Raman transition has successfully been applied to produce molecules within an atomic BEC (*9*). Similarly, the coherent nature of atomic scattering can be exploited on a Feshbach resonance to transfer colliding atoms into molecules, which has been predicted to convert an atomic BEC into a molecular BEC (*10*–*12*). A Feshbach resonance occurs when the energy of the atomic scattering state is tuned into degeneracy with that of a bound molecular state (*13*). Experimentally, Feshbach resonances can be induced by an external magnetic field when both states feature different Zeeman shifts. Consequently, the atom-molecule coupling can be resonantly enhanced at a particular magnetic field value, and a sweep of the field near or across the resonance can convert the atoms into molecules in a single molecular quantum state. Existence of molecules created through atomic Feshbach resonances has been reported previously in a BEC of ^{85}Rb atoms (*14*), in thermal samples of ^{133}Cs (*15*), and in degenerate Fermi gases of ^{40}K (*16*) and ^{6}Li (*17*). These studies demonstrate the quantum coherence of the Feshbach coupling (*14*) and the ability to detect molecules within the atomic sample by means of laser-induced (*15*) or radiofrequency-induced (*16*) dissociation. However, the resulting molecular samples could not be spatially distinguished from the atoms, nor could the molecular clouds be directly imaged and analyzed. Here, we report the observation of pure molecular quantum matter, achieved by applying a Feshbach sweep to an atomic Cs BEC (*18*) with immediate spatial Stern-Gerlach separation of the two species. By monitoring the evolution of the coupled-out molecular cloud, we measure ultralow kinetic expansion energies that are consistent with the presence of a coherent molecular matter wave.

The starting point of our experiment was a pure BEC of up to 6×10^4 Cs atoms in an optical trap (*19*) with a radial Thomas-Fermi radius of 8.6 μm and an axial Thomas-Fermi radius of 26.5 μm. The atoms were in the hyperfine ground state with total angular momentum $F = 3$ and magnetic quantum number $m_F = 3$. As the optical trap was by far too weak to support the atoms against gravity during the evaporative cooling process, a magnetic field gradient of 30.9 G/cm was applied to levitate the atoms (*20*). This levitation is very sensitive to the magnetic moment of the trapped particles, and a small change of 1% in either the gradient or in the magnetic moment of the trapped particles is sufficient to render the trap unstable. The state $F = 3$, $m_F = 3$ features a narrow Feshbach resonance near 20 G (*21*) with an estimated resonance width of 5 mG (*22*). According to an analysis of the Cs scattering properties (*23*, *24*), the corresponding molecular state (*25*) has a predicted magnetic moment of $\mu = 0.93\ \mu_B$, where μ_B is Bohr's magneton, with a small magnetic field dependence (*22*). We produced molecules from the atomic BEC by sweeping the magnetic field across the resonance from a higher field value with a constant rate of typically 50 G/s (Fig. 1). The duration of the sweep was 3 ms. To turn off the Feshbach coupling, the field was then quickly lowered to a hold field at 17 G for a variable hold time while the optical trap was shut off (*20*). Because of the large magnetic field gradient along the vertical direction and the narrow resonance width of 5 mG, the Feshbach resonance occurred only within a 2-μm-thin horizontal layer. The conversion zone swept through the condensate from below at a speed of 15 μm/ms, or equivalently, in 1.3 ms. The newly created molecules immediately started falling with an acceleration of 0.38*g* due to their reduced magnetic moment. The molecular cloud was then completely separated from the atoms within 3 ms. By raising the magnetic field gradient quickly at the end of the sweep to about 50 G/cm, we levitated the molecules. In this case, the atoms accelerated upward at 0.61*g*. Rapid molecule-atom separation and subsequent levitation permit long observation times for studying the dynamics of the molecular sample.

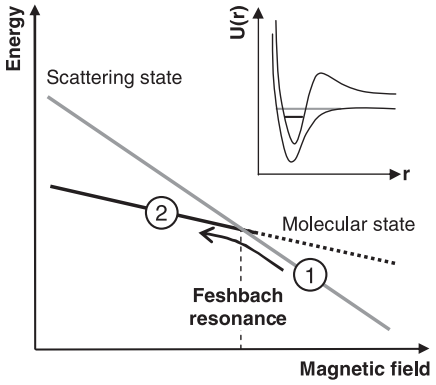

Fig. 1. Energy diagram for the atomic scattering state and the molecular bound state. The Feshbach resonance condition occurs near 20 G, where the Zeeman energy of the atomic scattering state becomes equal to that of a molecular bound state because of the difference in magnetic moments. Molecules at (2) are created from the BEC at (1) by a downward sweep of the magnetic field across the resonance. For detection, a reversed sweep brings the molecules above the dissociation limit. The inset schematically shows the molecular potential that corresponds to the open channel (lower curve) and the molecular potential that supports the bound state (upper curve). U, potential energy; r, interatomic distance.

To image the molecular cloud, we applied a reversed field sweep across the Feshbach resonance. The reversed sweep brought the molecules above the scattering continuum, and they quickly dissociated into free atoms. An immediate absorption image of the reconverted atoms thus reveals the spatial distribution of the molecules. A resolution limit of about 10 μm was caused by an energy on the order of $k_B \times 1$ μK released in the dissociation process (*20*), where k_B is the Boltzmann constant. We applied a fit to the image to determine the center position, the size of the spatial distribution, and the number of molecules. The evolution of the molecular cloud was recorded by variation of the hold time.

The complete atom-molecule separation is clearly visible in absorption images (Fig. 2). For reference, the image of a levitated BEC after 12 ms of expansion time is given in Fig. 2A. In Fig. 2, B and C, a Feshbach sweep has been applied to the BEC. In Fig. 2B, a coupled-out molecular cloud with ~3000 molecules can be seen below the atomic BEC. The number of atoms in the remaining BEC is reduced by 50% from those shown in Fig. 2A, to ~25,000. The molecular cloud is falling, because the magnetic field gradient needed to levitate the atoms was maintained. For Fig. 2C, the magnetic field gradient was

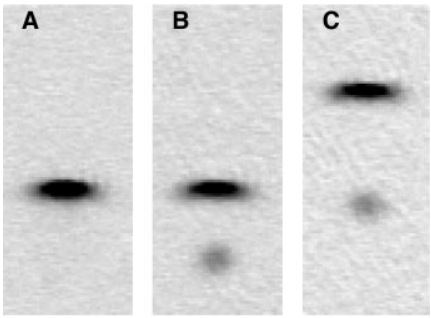

Fig. 2. Absorption images of (**A**) the levitated BEC without the Feshbach sweep, (**B**) the levitated BEC after the Feshbach sweep with a falling molecular cloud below, and (**C**) the levitated molecular cloud with an upward-rising BEC above. In (B) and (C), 3000 molecules are produced at a sweep rate of 50 G/s. The separation between the atoms and the molecules is 150 μm in (B) and 240 μm in (C).

raised after the Feshbach sweep in order to levitate the molecules. Hence, the atomic BEC accelerates upward and can be seen at the top of the image above the molecules. Careful adjustment of the magnetic field gradient to null the molecular acceleration allowed a precise determination of the molecular magnetic moment. We find that $\mu = 0.930(5)\ \mu_B$ (*20*), which is in good agreement with the theoretical calculation (*22*).

We investigated the atom-molecule conversion as a function of the end value B_f of the creation ramp. The ramp speed was kept constant at 50 G/s by variation of B_f together with the duration of the ramp. We have checked that for final values of B_f well above the resonance, the rapid jump over the resonance to the hold field after the end of the creation ramp did not produce any molecules. As Fig. 3 shows, molecules were created in a steplike manner. Simultaneously, the atomic population in the BEC is reduced. The transition value agrees well with the resonance position of 19.83(2) G as determined from three-body recombination loss measurements (*26*). From the plot of the atom number, it can be seen that up to 50% of the atoms were lost from the condensate, corresponding to ~25,000 atoms for this experiment. Hence, for a detected number of 3000 molecules, only about 24% of the lost atoms reappeared as partners in molecule formation. Also, we varied the speed of the downward magnetic field ramp across the Feshbach resonance and found that for decreasing ramp speed, the number of detected molecules saturated at a value of ~3000 molecules for speeds less than 50 G/s. The missing atoms and the saturation suggest that collisional relaxation into other molecular states occurs during the creation phase (*27*). After separation from the atoms, however, we did not detect any substantial loss.

We observed ultralow expansion energies for the molecular cloud in both the vertical and the horizontal directions. This was done in time-of-flight expansion measurements by variation of the hold time and hence the total expansion time. We plotted the vertical and horizontal root-mean-square (rms) widths of the reconverted atomic cloud as a function of total expansion time (Fig. 4, A and B). An apparent anisotropy of the expansion can be seen. The faster vertical expansion corresponds to a mean kinetic energy of $E_z = \frac{1}{2}\ k_B \times (40 \pm 3 \pm 2)$ nK (*20*), where the first one-standard-deviation error is statistical and the second one is systematic. The origin of this vertical energy was identified as the velocity dispersion of the molecules during the creation phase. The dispersion was caused by the fact that the conversion zone passes through the condensate at a finite speed from below. Hence, molecules created earlier acquire a larger velocity, and those created later acquire a smaller velocity, as a result of the gravity pulling. When the size of the BEC was taken into account, the vertical expansion energy as a result of the velocity dispersion was calculated to be about $\frac{1}{2}\ k_B \times 30$ nK for the molecular cloud, largely explaining the observed energy. In fact, vertical compression of the BEC did lead to a smaller vertical energy spread. By increasing the dipole trap depth to decrease the vertical extent of the BEC by a factor of 1.3, we found that the measured molecular kinetic energy was reduced in the expected way to a value of $E_z = \frac{1}{2}\ k_B \times (19 \pm 2 \pm 1)$ nK.

The horizontal expansion shown in Fig. 4B was unaffected by the velocity dispersion effect. However, a repulsive force due to the curvature of the levitation field acted on the molecules. This force resulted in an expansion of the cloud that follows a cosine hyperbolicus function and has been characterized previously (*18*). When the resolution limit due to the dissociation and the cosine hyperbolicus expansion dynamics (*20*) is incorporated, the fit in Fig. 4B yields an extremely low kinetic energy of $E_x = \frac{1}{2}\ k_B \times (2 \pm 2 \pm 3)$ nK in the horizontal direction.

The slow expansion of the molecules is consistent with the behavior of a macroscopic matter wave, as the horizontal expansion showed vanishing release energy and the vertical expansion was dominated by the dispersive gravity pulling effect, which is coherent in its nature. In view of a possible quantum degeneracy of the molecular ensemble, we first estimated the peak molecular density right after creation to $1 \times 10^{12}\ \mathrm{cm}^{-3}$, assuming 3000 molecules with a spatial density profile that reflects that of the atomic BEC (*28*). Given the free-space degeneracy condition, the critical temperature is 6 nK. Comparing this value to the observed horizontal energy spread that corresponds to $(2 \pm 2 \pm 3)$ nK, we raise the question whether a molecular cloud with macroscopic coherence has been created. Our capability to monitor the spatial distribution of the molecules should allow us to detect interference patterns (*29*) and thus to investigate the macroscopic coherence of the molecular matter wave.

To create molecules coherently with high efficiency, it will be advantageous to load the atomic BEC into an optical lattice (*30*), which allows the preparation of a Mott insulator phase (*31*) with exactly two atoms per lattice site. Molecules created by a subsequent Feshbach sweep will therefore be individually isolated and immune to collisional losses. After the creation of a pure molecular matter wave, one might be able to coherently transfer the molecules to low-lying molecular states by two-photon Raman transitions. Hence, a complete and coherent control over the dynamics of molecular quantum matter can be envisaged.

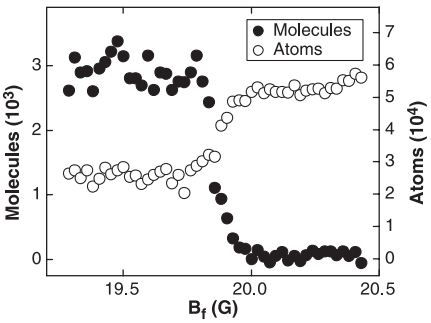

Fig. 3. Creation of molecules (solid circles) and simultaneous loss of atoms (open circles) as a function of the final value of the magnetic field ramp B_f for a fixed ramp speed of 50 G/s.

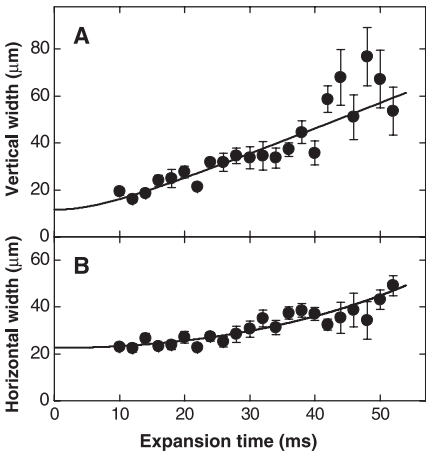

Fig. 4. (**A**) Vertical rms width and (**B**) horizontal rms width of the molecular cloud as a function of expansion time. From (A), a vertical expansion energy of $E_z = 1/2\ k_B \times (40 \pm 3 \pm 2)$ nK and an imaging resolution of 11(3) μm is obtained. The fit in (B) then yields an initial horizontal expansion energy of $E_x = 1/2\ k_B \times (2 \pm 2 \pm 3)$ nK.

References and Notes

1. E. A. Cornell, C. E. Wieman, *Rev. Mod. Phys.* **74**, 875 (2002).
2. W. Ketterle, *Rev. Mod. Phys.* **74**, 1131 (2002).
3. Nature Insight on Ultracold Matter, *Nature* **416**, 205 (2002).
4. D. J. Heinzen, R. Wynar, P. D. Drummond, K. V. Kheruntsyan, *Phys. Rev. Lett.* **84**, 5029 (2000).
5. K. Góral, L. Santos, M. Lewenstein, *Phys. Rev. Lett.* **88**, 170406 (2002).
6. H. L. Bethlem *et al.*, *Nature* **406**, 491 (2000).
7. J. D. Weinstein, R. deCarvalho, T. Guillet, B. Friedrich, J. M. Doyle, *Nature* **395**, 148 (1998).
8. N. Vanhaecke, W. de Souza Melo, B. L. Tolra, D. Comparat, P. Pillet, *Phys. Rev. Lett.* **89**, 063001 (2002).
9. R. Wynar, R. S. Freeland, D. J. Han, C. Ryu, D. J. Heinzen, *Science* **287**, 1016 (2000).
10. F. A. van Abeelen, B. J. Verhaar, *Phys. Rev. Lett.* **83**, 1550 (1999).
11. E. Timmermans, P. Tommasini, M. Hussein, A. Kerman, *Phys. Rep.* **315**, 199 (1999).
12. F. H. Mies, E. Tiesinga, P. S. Julienne, *Phys. Rev. A* **61**, 022721 (2000).
13. S. Inouye *et al.*, *Nature* **392**, 151 (1998).
14. E. A. Donley, N. R. Claussen, S. T. Thompson, C. E. Wieman, *Nature* **417**, 529 (2002).
15. C. Chin, A. J. Kerman, V. Vuletić, S. Chu, *Phys. Rev. Lett.* **90**, 033201 (2003).
16. C. A. Regal, C. Ticknor, J. L. Bohn, D. S. Jin, *Nature* **424**, 47 (2003).

17. C. Salomon, talk presented at the Quantum Electronics and Laser Science Conference, Baltimore, MD, 5 June 2003.
18. T. Weber, J. Herbig, M. Mark, H.-C. Nägerl, R. Grimm, *Science* **299**, 232 (2003); published online 5 Dec 2002 (10.1126/science.1079699).
19. The optical trap has a depth of $k_B \times 45$ nK with a radial trap frequency of 18 Hz and an axial trap frequency of 6 Hz. The axial direction of the BEC is oriented in the horizontal plane. At 20 G, the Cs scattering length is $a = 163\ a_0$, with a_0 denoting Bohr's radius. The resulting chemical potential for the BEC is $k_B \times 7$ nK.
20. Materials and methods are available as supporting material on *Science* Online.
21. V. Vuletić, C. Chin, A. J. Kerman, S. Chu, *Phys. Rev. Lett.* **83**, 943 (1999).
22. P. S. Julienne, E. Tiesinga, private communication (2003).
23. C. Chin, V. Vuletić, A. J. Kerman, S. Chu, *Phys. Rev. Lett.* **85**, 2717 (2000).
24. P. J. Leo, C. J. Williams, P. S. Julienne, *Phys. Rev. Lett.* **85**, 2721 (2000).
25. The molecular state was identified as a high-lying rovibrational state with internal angular momentum $f = 4$, magnetic quantum number $m_f = 4$, molecular orbital angular momentum $L = 4$, and angular momentum projection $m_L = 2$.
26. T. Weber, J. Herbig, M. Mark, H.-C. Nägerl, R. Grimm, *Phys. Rev. Lett.*, in press (available at http://arXiv.org/abs/physics/0304052).
27. V. A. Yurovsky, A. Ben-Reuven, P. S. Julienne, C. J. Williams, *Phys. Rev. A* **62**, 043605 (2000).
28. This is a reasonable assumption, because no molecules can be created in the absence of atoms.
29. M. R. Andrews *et al.*, *Science* **275**, 637 (1997).
30. D. Jaksch, V. Venturi, J. I. Cirac, C. J. Williams, P. Zoller, *Phys. Rev. Lett.* **89**, 040402 (2002).
31. M. Greiner, O. Mandel, T. Esslinger, T. W. Hänsch, I. Bloch, *Nature* **415**, 39 (2002).
32. We thank P. S. Julienne for very helpful discussions. Supported by the Austrian Science Fund (FWF) within Spezialforschungsbereich 15 (project part 16) and by the European Union through the Cold Molecules Training and Mobility of Researchers Network under contract no. HPRN-CT-2002-00290.

Supporting Online Material
www.sciencemag.org/cgi/content/full/1088876/DC1
Materials and Methods
Figs. S1 to S3

7 July 2003; accepted 11 August 2003
Published online 21 August 2003;
10.1126/science.1088876
Include this information when citing this paper.

Cooling Bose-Einstein Condensates Below 500 Picokelvin

A. E. Leanhardt,* T. A. Pasquini, M. Saba, A. Schirotzek, Y. Shin, D. Kielpinski, D. E. Pritchard, W. Ketterle

Spin-polarized gaseous Bose-Einstein condensates were confined by a combination of gravitational and magnetic forces. The partially condensed atomic vapors were adiabatically decompressed by weakening the gravito-magnetic trap to a mean frequency of 1 hertz, then evaporatively reduced in size to 2500 atoms. This lowered the peak condensate density to 5×10^{10} atoms per cubic centimeter and cooled the entire cloud in all three dimensions to a kinetic temperature of 450 ± 80 picokelvin. Such spin-polarized, dilute, and ultracold gases are important for spectroscopy, metrology, and atom optics.

The pursuit of lower temperatures is motivated by the quest to observe phenomena that occur on very low energy scales, in particular, phase transitions to new forms of matter. The achievement of temperatures near 1 K in solids and in liquids led to the discoveries of superconductivity (*1*) and superfluidity (*2*), respectively. The advent of laser cooling resulted in microkelvin temperature atomic vapors (*3*–*5*), subsequently cooled to nanokelvin temperatures by evaporative cooling to form dilute Bose-Einstein condensates (*6*, *7*) and quantum degenerate Fermi gases (*8*). Collectively, these low-temperature systems have a host of applications, including superconducting quantum interference devices (SQUIDs) (*9*), superfluid gyroscopes (*10*, *11*), and atomic clocks (*12*).

Temperature is a quantity that parameterizes how energy is distributed across the available states of a system, and effective temperatures can be defined for decoupled degrees of freedom or subsets of particles. For example, nuclear spins isolated from the kinetic motion of their respective atoms have been cooled by adiabatic demagnetization to an effective temperature of 280 pK (*13*). Spin ensembles have a finite number of available states, such that a spin-polarized sample, as in our work, would be characterized by zero effective temperature. In contrast, the motion of free particles is subject to a continuum of states, and the kinetic temperature of an ensemble can only asymptotically approach absolute zero.

Effective temperatures in atomic vapors are defined by the widths of velocity distributions, which can be much smaller than the mean velocity of the sample. Raman cooling (*14*, *15*) and velocity-selective coherent population trapping (VSCPT) (*16*) have generated velocity distributions with very narrow peaks, corresponding to nanokelvin and picokelvin effective temperatures. However, these temperatures were associated with the motion of only a subset of the atoms in the cloud and/or with atomic motion in only one dimension.

For trapped, partially condensed atomic vapors, the condensate fraction has zero entropy and the kinetic temperature of the sample is determined by the velocity distribution of the thermal (noncondensed) component. When released, the condensate fraction expands more slowly than the thermal component and has been characterized by picokelvin effective temperatures for anisotropic (*17*) and noninteracting (*18*) gases.

Cooling the atomic motion of entire ensembles in all three dimensions has proven difficult. To date, kinetic temperatures of a few hundred nanokelvin have been achieved with adiabatic and optical cooling (*19*, *20*), and evaporative cooling techniques have produced condensates with temperatures of 3 nK (*21*). By adiabatic expansion and subsequent evaporation, we have cooled partially condensed atomic vapors to picokelvin kinetic temperatures.

Our thermometry is calibrated by the Bose-Einstein condensation (BEC) phase transition temperature, T_c, which in the thermodynamic limit for a harmonically trapped ideal Bose gas is (*22*)

$$k_B T_c = \hbar\bar{\omega}\left(\frac{N}{\zeta(3)}\right)^{1/3} \approx 0.94\hbar\bar{\omega}N^{1/3} \qquad (1)$$

where k_B is Boltzmann's constant, $\hbar$ is Planck's constant h divided by 2π, $\zeta(n)$ is the Riemann Zeta function, $\bar{\omega} = (\omega_x\omega_y\omega_z)^{1/3}$ is the geometric mean of the harmonic trap frequencies, and N is the total number of atoms, both condensed and noncondensed. Thus, the atom number and the trap frequencies set an upper limit for the temperature of a confined Bose-Einstein condensate. In our work, adiabatically weakening the trapping potential to a mean frequency of $\bar{\omega} = 2\pi \times (1.12 \pm 0.08)$ Hz guaranteed that partially condensed atomic vapors with $N \leq 8000$ atoms had picokelvin temperatures ($T_c \leq 1$ nK).

Bose-Einstein condensates containing more than 10^7 ^{23}Na atoms were created in the weak field seeking $|F = 1, m_F = -1\rangle$ state in a magnetic trap, captured in the focus of an optical tweezers laser beam, and transferred into an auxiliary "science" chamber as described in (*23*). In the science chamber, condensates containing 2×10^6 to 3×10^6 atoms were transferred from the optical tweezers into a gravito-magnetic trap (Fig. 1A). A small coil carrying current I_S generated a vertical bias field B_z and supported the condensates against gravity with a vertical magnetic field gradient, $B_z' = 2\ mg/$

Department of Physics, MIT-Harvard Center for Ultracold Atoms, and Research Laboratory of Electronics, Massachusetts Institute of Technology, Cambridge, MA 02139, USA.

*To whom correspondence should be addressed. E-mail: ael@mit.edu

Preparation of a Pure Molecular Quantum Gas

Jens Herbig, Tobias Krämer, Michael Mark, Tino Weber,
Cheng Chin, Hanns-Christoph Nägerl, Rudolf Grimm

Materials and Methods

Magnetic levitation field

For the compensation of gravity by a magnetic gradient force, we use a quadrupole field symmetric with respect to a vertical axis (z-axis) through the center of the atomic or molecular cloud. The field is produced by two pairs of coils, which provide independent control of the vertical field gradient B' and the bias field B_0. While the inner anti-Helmholtz pair provides the gradient B', the outer Helmholtz pair generates the bias field B_0. The field experienced by a particle at a vertical position z on the symmetry axis is given by $B_0 + B'z$.

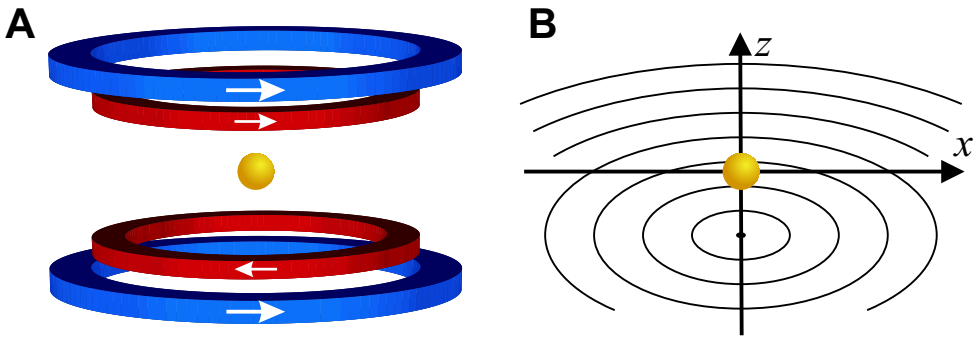

Fig. S1. Illustration of the magnetic levitation field. (A) Two pairs of coils facilitate independent control of the magnetic bias field B_0 (blue) and the vertical field gradient B' (red). (B) The contour lines of equal magnetic fields are centered around the magnetic zero, which is located at a distance of B_0/B' below the ultracold cloud. The curvature leads to a weak outward directed antitrapping force, depending on the distance x from the symmetry axis.

The levitation of a high-field seeking particle can be understood by looking at the repulsive effect of the magnetic quadrupole which forms an axially symmetric antitrap with its center located below the levitated particles. Above the magnetic-field zero, the increasing magnetic field pushes the particles upwards. On the symmetry axis, gravity can be exactly cancelled in this way. Off axis, however, the magnetic force is not directed exactly in vertical direction. To

first order in the distance x from the symmetry axis, the levitation condition is not affected, but a weak outward directed force occurs in the horizontal direction with anti-trapping character. This horizontal force can be written as

$$F_x = m\alpha^2 x\,.$$

For exact levitation, the characteristic rate is given by

$$\alpha = \frac{g}{2}\sqrt{\frac{m}{\mu B_0}}\,,$$

where m and μ are the particle's mass and magnetic moment, respectively, and g denotes the gravitational acceleration.

Experimental timing and magnetic-field ramps

The starting point of the ramp is above the resonance at $19.88\,$G. With a ramp-speed of $48\,$G/s the field is swept over the resonance to a final field value of $19.74\,$G. Immediately after the end of the ramp we switch off the optical trap and ramp the gradient field within $0.5\,$ms to about $50\,$G/cm to cancel the gravitational force for the molecules. Simultaneously the magnetic field is lowered in $2\,$ms to a fixed hold field of $17\,$G where the molecules are allowed to expand under the influence of the gradient field.

In the time between the production of the molecules and the end of the gradient field ramp, the molecules are initially accelerated with $0.38\,$g. This leads to a vertical center-of-mass velocity of typically a few mm/s, depending on the exact timing of the ramps.

For detection we dissociate the molecules to atoms by ramping back over the resonance with a ramp-speed of $1000\,$G/s. The ramp takes $4\,$ms and reaches a final value of $21\,$G, well above the resonance. For ramp-speeds ranging from $300\,$G/s up to $1100\,$G/s, we did not find any influence on the dissociation process. The instant of time of the dissociation depends on the local magnetic field and thus on the vertical position of the molecular cloud in the gradient field. With a finite vertical velocity the position varies with expansion time. By switching off the gradient field at the start of the ramp (t_1), we ensure that the time of dissociation is fixed. Nevertheless the exact time (t_{diss}) is not exactly known due to an unknown offset in the magnetic field caused by switching the gradient field. The expansion in the time between t_1 and t_{img} ($\Delta t = 5.5\,$ms) takes place without the influence of the curvature of the gradient field.

By varying the time between t_{diss} and t_{img} we can characterize the dynamics of the reconverted atoms. We observe a fast expansion with an energy of about $\frac{1}{2}k_B \times 1\mu$K. This, together

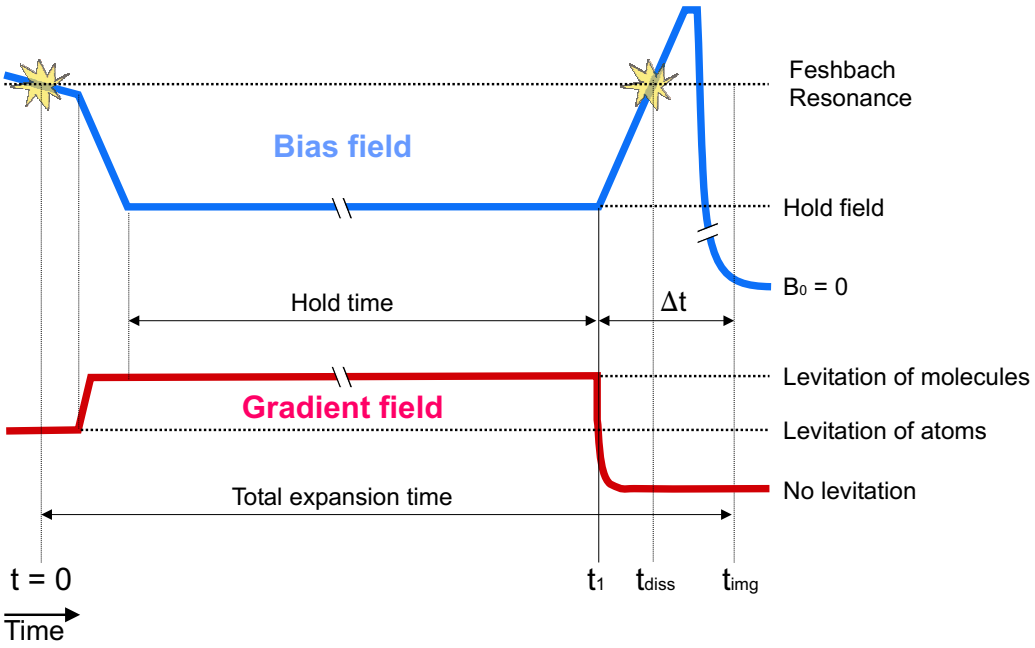

Fig. S2. Schematic of the magnetic field ramping for bias field (blue) and gradient field (red).

with the uncertainty in t_{diss}, leads to a fixed additional broadening (σ_{res}) of the cloud. We switch off the magnetic bias field $1.5\,$ms before the imaging. The switching speed is much too fast to convert atoms into molecules when the Feshbach resonance is crossed again. At t_{img} the cloud is imaged using a $100\,\mu$s resonant absorption pulse.

The measured center-of-mass velocity suggests that the production of the molecules takes place in the center of the initial creation ramp, with an uncertainty of $1\,$ms, and this defines the point where $t = 0$. Hence, the total time of expansion is measured from $t = 0$ until the time of imaging t_{img}.

Measurement of the magnetic moment

The compensation of gravity by the magnetic gradient field facilitates a precise measurement of the magnetic moment of the molecular state. The basic idea is to derive this molecular moment by comparing the field gradient needed for levitation of the molecules with the one required for the atoms. The known magnetic moment of the atoms serves as a reference.

Figure S3 shows the vertical center-of-mass motion of the molecular cloud in a magnetic field of 17 G (at $z = 0$) with a gradient of $49.7\,$G/cm, close to the exact levitation condition. A

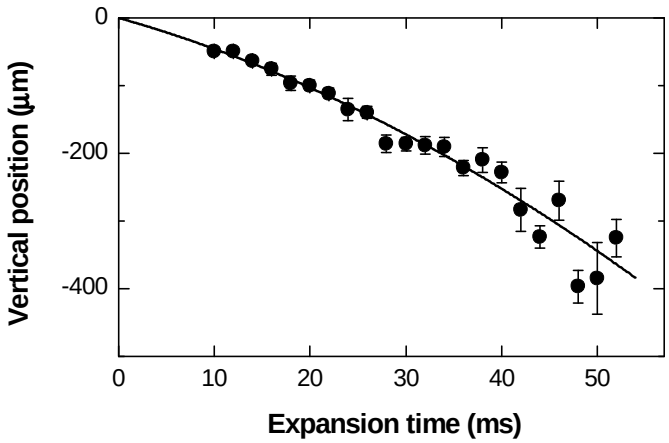

Fig. S3. Measurement of the molecular magnetic moment. The vertical center-of-mass position of the molecular cloud at a bias field of 17 G (at $z = 0$) is shown as a function of time together with a parabolic fit (solid line). The applied magnetic gradient field of 49.7 G/cm is slightly below the exact levitation condition so that a residual downward-directed acceleration is observed.

parabolic fit to the data yields a residual acceleration of $0.11(5)$ m/s^2. Taking this small correction into account we calculate a gradient of $50.2(3)$ G/cm for exact levitation of the molecules. The magnetic moment of the molecular state is then determined to $0.930(5)\,\mu_{\rm B}$.

The fit to the data of Fig. S3 also yields an initial center-of-mass velocity of the molecular cloud of $4(1)$ mm/s. This velocity results from the downward acceleration before the field gradient increases to the molecule levitation value.

Horizontal expansion in the levitation field

According to the equation of motion $F_x = m\alpha^2 x$ for the horizontal degrees of freedom, a particle released at $t = 0$ in the levitation field with an initial horizontal position x_0 and an initial horizontal velocity v_0 follows

$$\begin{aligned} x(t) &= x_0 \cosh(\alpha t) + \alpha^{-1} v_0 \sinh(\alpha t)\,, \\ v(t) &= \alpha x_0 \sinh(\alpha t) + v_0 \cosh(\alpha t)\,. \end{aligned}$$

In our experiment, the levitation field is turned off a time Δt before the image is taken at $t_{\rm img}$. In this short final time interval, beginning at $t_1 = t_{\rm img} - \Delta t$ and ending at $t_{\rm img}$, a free motion in the field of gravity takes place. At the time of detection, the horizontal position of the

particle is

$$\begin{aligned} x(t_{\rm img}) &= x(t_1) + v(t_1)\Delta t \\ &= x_0\Big[\cosh(\alpha t_1) + \alpha\Delta t \sinh(\alpha t_1)\Big] + v_0\Big[\alpha^{-1}\sinh(\alpha t_1) + \Delta t\cosh(\alpha t_1)\Big] \end{aligned}$$

For an ensemble of particles with statistical initial distributions of x_0 and v_0 we introduce s_x and u_x for the horizontal position spread and velocity spread (root-mean-square values). For the horizontal size of the cloud we then obtain the rms value

$$\sigma_x = \sqrt{s_x^2\left[\cosh(\alpha t_1) + \alpha\Delta t\sinh(\alpha t_1)\right]^2 + u_x^2\left[\alpha^{-1}\sinh(\alpha t_1) + \Delta t\cosh(\alpha t_1)\right]^2}\,.$$

Expansion data: fit procedure and error analysis

In order to extract the relevant parameters from the observed expansion of the molecular cloud (Fig. 4) we proceed in the following way.

Vertical expansion. For the vertical size of the expanding cloud we use the fit function

$$\sigma_{z,\,\rm img} = \sqrt{\sigma_{\rm res}^2 + s_z^2 + u_z^2 t_{\rm img}^2}\,.$$

Here two free parameters are used: u_z denotes the initial rms velocity spread (predominantly resulting from the velocity dispersion), and $\sigma_{\rm res}$ is the spatial resolution limit that results from the dissociation energy in the detection phase. The fixed parameter $s_z = 3.7\,\mu$m is the initial vertical rms position spread that we calculate from the Thomas-Fermi distribution of the BEC.

For the velocity spread the fit yields $u_z = 1.12(5)$ mm/s, corresponding to a mean kinetic energy of $E_z = \frac{1}{2}k_{\rm B} \times 40(3)$ nK. For the resolution parameter we obtain $\sigma_{\rm res} = 11(3)\,\mu$m. The given errors denote the one-standard-deviation (one sigma) values as resulting from the fit.

Horizontal expansion. For the horizontal expansion in the levitation field, we use the above expression for the cloud size σ_x together with the resolution parameter $\sigma_{\rm res}$ combined to the fit function

$$\begin{aligned} \sigma_{x,\,\rm img} &= \sqrt{\sigma_{\rm res}^2 + \sigma_x^2} \\ &= \sqrt{\sigma_{\rm res}^2 + s_x^2\left[\cosh(\alpha t_1) + \alpha\Delta t\sinh(\alpha t_1)\right]^2 + u_x^2\left[\alpha^{-1}\sinh(\alpha t_1) + \Delta t\cosh(\alpha t_1)\right]^2}\,, \end{aligned}$$

where $t_1 = t_{\rm img} - \Delta t$. The two free parameters of the fit are the initial horizontal cloud size s_x and an initial velocity spread u_x. The parameter $\alpha = 27.2\,{\rm s}^{-1}$ is calculated for the effective horizontal curvature of the levitation field. The resolution parameter $\sigma_{\rm res} = 11(3)\,\mu$m is taken from the above fit to the vertical expansion and varied within its error range. From this fit procedure we obtain the initial horizontal cloud size $s_x = 20(2)\,\mu$m. For the intial rms velocity spread the fit yields $u_x = 0.22(16)$ mm/s, which corresponds to a mean initial kinetic energy spread of $E_x = \frac{1}{2}k_{\rm B} \times 1.5^{+3.0}_{-1.4}$ nK. Rounding to one significant digit gives $E_x = \frac{1}{2}k_{\rm B} \times 2(2)$ nK.

Expansion energies and total error budget. In addition to the given statistical errors, systematic errors stem from the limited knowledge of the experimental parameters used in the above fits. A more detailed analysis shows that all systematic errors are far below the statistical errors with the exception of the origin of time, i.e. the instant at which the Feshbach conversion produces the molecules. We have therefore repeated the above fits with a time origin varied in the maximum possible error range of ± 1 ms. The corresponding results indicate systematic deviations from the above fit results which can be taken as the systematic errors.

For the most interesting quantities, the initial kinetic-energy spreads of the expanding molecular cloud, we finally obtain

$$\begin{aligned} E_z &= \tfrac{1}{2}k_{\rm B} \times (40 \pm 3 \pm 2)\,{\rm nK} \qquad \text{vertically}, \\ E_x &= \tfrac{1}{2}k_{\rm B} \times (2 \pm 2 \pm 3)\,{\rm nK} \qquad \text{horizontally}, \end{aligned}$$

where the two given error numbers denote the one-standard-deviation statistical error (first error) and the systematic error (second error).

B.4. Optimized production of a cesium Bose-Einstein condensate

Appl. Phys. B 79, 1013–1019 (2004)
DOI: 10.1007/s00340-004-1657-5

Applied Physics B
Lasers and Optics

T. KRAEMER[1]
J. HERBIG[1]
M. MARK[1]
T. WEBER[1]
C. CHIN[1]
H.-C. NÄGERL[1,✉]
R. GRIMM[1,2]

Optimized production of a cesium Bose–Einstein condensate

[1] Institut für Experimentalphysik, Universität Innsbruck, Technikerstraße 25, 6020 Innsbruck, Austria
[2] Institut für Quantenoptik und Quanteninformation, Österreichische Akademie der Wissenschaften, 6020 Innsbruck, Austria

Received: 11 August 2004
Published online: 6 October 2004 •

ABSTRACT We report on the optimized production of a Bose–Einstein condensate of cesium atoms using an optical trapping approach. Based on an improved trap loading and evaporation scheme we obtain more than 10^5 atoms in the condensed phase. To test the tunability of the interaction in the condensate we study the expansion of the condensate as a function of scattering length. We further excite strong oscillations of the trapped condensate by rapidly varying the interaction strength.

PACS 03.75.Kk; 32.80.Pj

1 Introduction

Much of the present work in the field of quantum gases relies on optical trapping techniques and on the ability to tune atomic interactions. Optical approaches have been recently employed in several atomic Bose–Einstein condensation experiments [1–5] and in experiments on the production of ultracold molecular samples [6–10] and on molecular Bose–Einstein condensates [11, 12]. The major advantages in optical traps are the possibility to trap atoms in any sublevel of the electronic ground state and the ease to adjust the interaction strength using magnetically induced Feshbach resonances.

The cesium atom is very attractive for experiments with tunable atomic interactions. The lowest internal quantum state of Cs features a unique combination of wide and narrow Feshbach resonances which are easily accessible at low magnetic fields [13]. This results in a great flexibility for tuning the atomic scattering properties. In particular, magnetic tuning of the interaction strength has recently allowed the first realization of a Bose–Einstein condensate (BEC) with Cs atoms [4] and the realization of a two-dimensional condensate very close to a dielectric surface [5]. The tunability of the atomic interaction can be exploited in experiments where one might wish to adjust or to dynamically change the mean-field interaction of the condensate. Also, the Feshbach resonances can be used to produce molecules from an atomic BEC [8–10, 14] and to study the transition from an atomic BEC to a molecular BEC. In this context, a quantum phase transition with an essentially topological character has been predicted [15, 16]. For such and many other intriguing experiments it is desirable to have a large BEC of Cs atoms as a starting point.

In this paper we report on the optimized production of an essentially pure Cs BEC in the lowest internal quantum state with more than 10^5 atoms. Since this state cannot be trapped by purely magnetic means, the path to condensation relies on a sequence of optical traps. We discuss the loading and transfer from one trap to the next and give a detailed description of the evaporation path and of the resulting condensate. As a demonstration for tunability, we measure the expansion energy as a function of scattering length in time-of-flight experiments. In particular, we show the ultra-slow expansion of the condensate after release from the trap for nearly vanishing scattering length. The release energy corresponds to ~ 50 pK. Finally, we present first results when the scattering length is suddenly stepped and the condensate then starts to oscillate freely in the trap.

2 Cesium scattering properties and Feshbach resonances

Early experiments [17, 18] towards condensation of cesium focused on samples in magnetic traps polarized either in the upper hyperfine ground state $F = 4$, magnetic sublevel $m_F = 4$, or in the lower hyperfine state $F = 3$, $m_F = -3$. Here, F denotes the total angular momentum and m_F the magnetic quantum number. The spin relaxation rates were measured to be several orders of magnitude higher than expected [19–21]. It was later understood that this is caused by the dipolar relaxation process induced by the second-order spin–orbit interaction [22]. The maximum phase-space density in a small sample of Cs atoms was a factor of about four away from condensation [23].

The problem of the strong inelastic two-body losses can be overcome by using the lowest internal state of cesium, $F = 3$, $m_F = 3$ [24–27]. In this state, all inelastic two-body processes are endothermic and are thus fully suppressed at sufficiently low temperature. This state requires optical trapping since it cannot be captured in a magnetic trap. Optically trapped atoms can only be efficiently evaporated by lowering the total potential depth. This process weakens the confine-

✉ Fax: +43-512-507-2921, E-mail: christoph.naegerl@uibk.ac.at

ment of the trapped sample and thus makes it difficult to achieve sufficiently high elastic collision rates for effective evaporation. Hence, adjustability of the collisional properties is very helpful for a fast evaporation strategy.

The success in condensing Cs [4] largely relies on the fact that the s-wave scattering length for the $F = 3, m_F = 3$ state can be tuned to moderate and positive values by the application of relatively low dc magnetic fields [13]. As Fig. 1 shows, an external magnetic field allows for precise tuning of the atomic scattering length a from negative to positive values. Positive scattering lengths in the range between zero and one thousand a_0 are attained for magnetic fields of a few ten Gauss; a_0 denotes Bohr's radius. In particular, there is a gentle zero-crossing of the scattering length near 17 G [25]. Here, the interaction of atoms in a BEC is effectively switched off. Several narrow higher-order Feshbach resonances [13], caused by coupling to d- and g-wave molecular states, enable very rapid control of the atomic scattering properties. With the magnetic field being a free parameter in our optical trapping approach, we can take full advantage of this tunability of the s-wave scattering length.

For Cs in the $F = 3, m_F = 3$ ground state the process of three-body recombination is the dominant loss and heating mechanism [28]. In a recombination process, three atoms collide, two of them form a molecule, and the third atom takes away two thirds of the binding energy according to energy and momentum conservation. The atoms that form the molecule are usually lost, and the third atom is either lost or it deposits its share of the binding energy in the sample. Heating of the sample is the combination of "anti-evaporation" and recombination heating [28]. To a good approximation, the three-body recombination rate scales with the fourth power of the scattering length. Unfortunately, the prefactor in this scaling law is measured to be relatively large [28]. To minimize this heating, the recombination products should be removed quickly from the trap. It is thus important to assure that the sample is not operated too deeply in the hydrodynamic regime and that the evaporation is efficient in all directions. Arbitrarily increasing the scattering length to speed up the forced evaporation is therefore not possible without sacrificing cooling efficiency. Within these limits, tuning the scattering length allows for an optimization of the evaporation for given trap parameters. For example, for the low initial densities in a large reservoir trap the evaporation may be sped up by increasing the scattering length. In a later trapping stage with a higher atomic density the scattering length should be reduced to optimize the ratio of good to bad collisions.

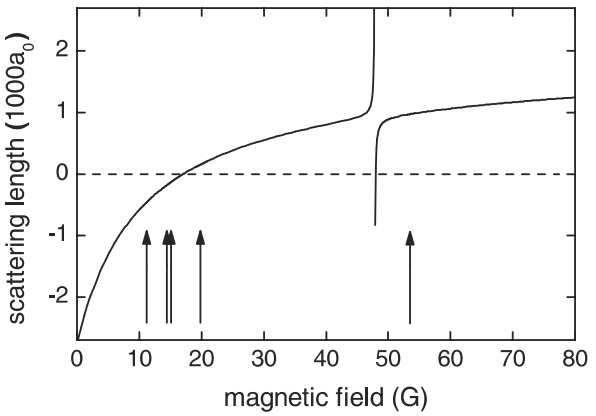

FIGURE 1 Scattering length as a function of magnetic field for the state $F = 3, m_F = 3$. There is a relatively broad Feshbach resonance at 48.0 G due to coupling to a d-wave molecular state. The *arrows* indicate several very narrow resonances at 11.0, 14.4, 15.0, 19.9 and 53.5 G, which result from coupling to g-wave molecular states. The data are taken from [13]

3 BEC production

3.1 *Overview of experimental strategy*

For producing large condensates in optical dipole traps, it is necessary to independently optimize both trap loading and evaporative cooling. For initial loading of as many atoms as possible, an optical trap with large volume is needed which, in view of limited laser power, implies a shallow trapping potential. For subsequent forced evaporative cooling, however, high densities and fast elastic collisions require much tighter confinement. These two requirements in general demand dynamical changes of the trapping potential. A possible way to implement this is a spatial compression of the optical trap using e.g., a zoom-lens system [29]. Our approach is based on an alternative way where a sequence of optical trapping schemes is used to provide optimized loading together with optimized evaporative cooling.

We first use a shallow, large volume CO_2-laser trap as a "reservoir" for collecting the atoms before forced evaporative cooling is implemented in a tighter trap. The reservoir trap can be efficiently loaded with atoms that are precooled by Raman-sideband cooling [30]. This approach allows for the collection of atoms at moderate densities with little loss from three-body collisions and with negligible heating from either photon scattering or trap vibrations. It serves as a good starting point for the final transfer into a tighter optical trap. The tighter trap is adiabatically increased and adds a "dimple" to the trapping potential of the reservoir. Collisional loading of this dimple already yields a significant enhancement of the local number and phase-space density [31]. After turning off the reservoir trap excellent conditions for further forced evaporative cooling are obtained.

The different trap stages of optical trapping used in our experiments are illustrated in Fig. 2. An overview of the evolution of phase-space density and particle number for the various trapping stages is shown in Fig. 3.

The use of relatively weak optical trapping necessitates the implementation of magnetic "levitation" where a magnetic field gradient along the vertical direction compensates for the gravitational force. This levitation turns out to be very useful in two ways: First, in the limit of very weak optical trapping only one spin state is held in the trap. This assures perfect spin polarization of the sample[1]. Further, efficient evaporation can be performed without the effect of gravitational sag in the trap. The dc magnetic field offset remains a free parameter for flexible tuning of the scattering length.

[1] This Stern–Gerlach separation technique also allows for radio-frequency evaporation along the vertical direction. Although one-dimensional, this type of evaporation has been applied to produce ultracold Cs atoms for studying three-body collisions [28].

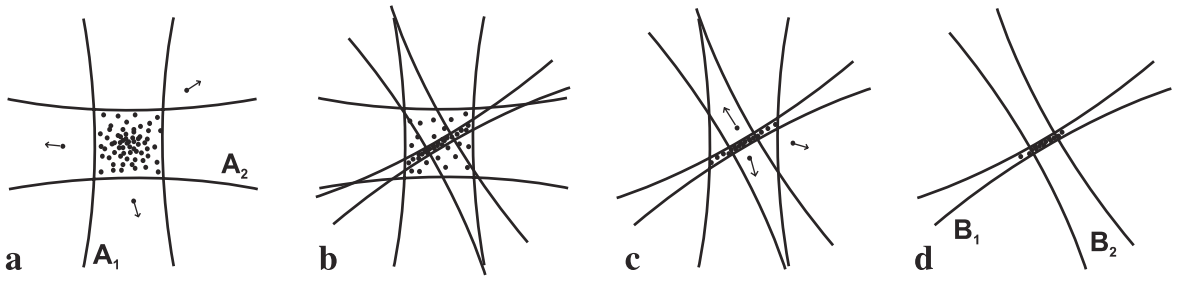

FIGURE 2 Illustration of the various stages of trap loading and evaporative cooling as seen from above. (**a**) Plain evaporation in a crossed CO_2-laser trap generated by beams A_1 and A_2 at a scattering length of $a = 1215\,a_0$. (**b**) 1.5 s of ramping and collisional loading into a crossed 1064-nm fibre laser trap generated by beams B_1 and B_2 with a final scattering length $a = 210\,a_0$. (**c**) Forced evaporative cooling after switching off CO_2-laser beam A_2. The power of all remaining lasers is ramped down, and the power in CO_2-laser beam A_1 is reduced to zero. (**d**) Final configuration of the crossed 1064-nm trap. Imaging is done in the horizontal plane at an angle of 30° with respect to the long axis of the cigar-shaped atomic cloud

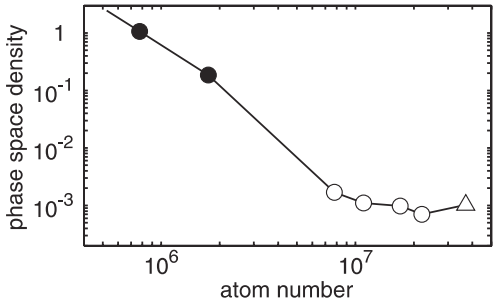

FIGURE 3 Peak phase space density as function of atom number. The path of evaporation proceeds from right to left. The *triangle* shows the atomic ensemble immediately after lattice cooling. The *open circles* show the ensemble in the reservoir trap after 0.08, 0.22, 0.64, and 2.0 s. The *filled circles* correspond to the sample in dimple trap right after loading and after 1.5 s of evaporation. The phase transition occurs after 2 s of forced evaporation with $\sim 5 \times 10^5$ atoms left in the dimple trap

3.2 *Laser cooling*

The initial collection and cooling of Cs atoms is achieved by conventional techniques. In a stainless steel vacuum chamber [32] atoms are loaded into a magneto-optical trap (MOT) from a Zeeman slowed atomic beam with up to 3×10^8 atoms after about 6 s. The MOT is operated on the $6^2S_{1/2}$, $F = 4$ to $6^2P_{3/2}$, $F' = 5$ transition. The ultra-high vacuum of less than 1×10^{-11} mbar gives 200 s for the 1/e-lifetime of the MOT. The MOT light is derived from a high power laser diode[2] referenced via beat-lock to a grating-stabilized master diode laser. Standard absorption imaging is used to determine particle numbers and temperatures.

We compress the atomic cloud by ramping up the magnetic field gradient in the MOT by a factor of five to 33 G/cm within 40 ms. Simultaneously we linearly change the detuning of the MOT laser from around 10 MHz to 30 MHz. At the end of the ramp, we switch off the MOT light and the magnetic field gradient. To cool the compressed cloud, we then apply degenerate Raman-sideband cooling [30] in an optical lattice to further cool and to polarize the atoms in the desired $F = 3, m_F = 3$ state. We have adapted the technique as described in [33] to our setup. This cooling scheme is particularly suited for polarizing atoms in the $F = 3, m_F = 3$ state because this is a dark state for which photon scattering is suppressed. Four laser beams derived from an injection locked slave laser resonant with the $F = 4$ to $F' = 4$ transition produce a three-dimensional optical lattice, drive Raman-sideband transitions and repump out of the $F = 4$ ground state manifold. The total power of all the four beams is 65 mW and their $1/e^2$-beam radii are about 1 mm. The oscillation frequency in the lattice is on the order of 100 kHz. A small magnetic field offset of several hundred mG is applied to induce the Raman-sideband cooling. We succeed in polarizing 90% of the atoms. The ensemble is then adiabatically released from the lattice after 6 ms of cooling time. If the atomic cloud is released into free space, the temperature of the ensemble with up to 4×10^7 atoms is about 0.7 μK. For our typical atomic densities this corresponds to a phase space density of 1×10^{-3}.

3.3 *Reservoir trap*

We generate the large reservoir trap by horizontally crossing two CO_2-laser beams A_1 and A_2 at right angles as shown in Fig. 2a. At the same time we apply a magnetic gradient field in the vertical direction to levitate the atoms against gravity. The delivered powers in laser beams A_1 and A_2 are 90 W and 65 W, respectively. The light comes from two separate, highly stable linearly polarized single-frequency CO_2-lasers[3]. Switching of the beams is done by external acousto-optical modulators[4] (AOMs). A_1 is downshifted in frequency by 40 MHz, whereas A_2 is upshifted by 40 MHz to prevent any interference. To avoid mode-hops the cooling water for the lasers needs to be stabilized to better than ±20 mK. Still, a slow mode drift changes the power of the lasers by a few percent over the time scale of minutes. At the crossing point the $1/e^2$-beam radii of the two lasers are (605 ± 35) μm and (690 ± 35) μm.

The magnetic fields for levitation and for Feshbach tuning are generated by two pairs of coils aligned with their axes parallel to the vertical direction. One pair in anti-Helmholtz configuration produces the vertical magnetic field gradient near 31.3 G/cm to levitate the atoms in the $F = 3, m_F = 3$ state. Another pair in Helmholtz configuration provides a variable bias field B_0 of up to 200 G. The combined field results in a weak outward directed force $F(\varrho) = m\alpha^2\varrho$ depend-

[2] SDL-5712-H1

[3] Coherent-DEOS GEM-100L

[4] Intraaction AGM-408BB1M

ing on the horizontal distance ϱ from the vertical symmetry axis. For perfect levitation of our atoms the constant $\alpha = g\sqrt{m/(3\mu_B B_0)}$ describes the curvature of the parabolic anti-trapping potential. The levitation field thus slightly reduces the trap depth along the horizontal direction. Here, m is the mass of Cs, g is the gravitational acceleration, and μ_B is Bohr's magneton. At $B_0 = 17$ G we have $\alpha = 2\pi \times 3.4$ Hz. The horizontal trap frequencies $\omega_{x,y}$ are reduced according to $\omega'_{x,y} = \sqrt{\omega^2_{x,y} - \alpha^2}$. This is usually a very small effect for all but the lowest trap frequencies. Note that levitation also affects the horizontal motion of free atoms after the optical trap is shut off. The horizontal motion follows $\varrho(t) = \varrho_0 \cosh(\alpha t) + \alpha^{-1} v_0 \sinh(\alpha t)$ for initial position ϱ_0 and initial velocity v_0. The vertical motion is not affected.

We excite vertical trap oscillations by briefly changing the vertical magnetic field gradient and hence tilting the trap. For exciting horizontal trap oscillations we shift the equilibrium position of the atoms by adding a horizontal magnetic field component. In both cases we monitor the center-of-mass oscillation of the atomic cloud after 50 ms time-of-flight. The geometrically averaged trap frequency $\bar{\nu}$ is calculated to be (12.6 ± 1.5) Hz which is in good agreement with the experimental value of (13.2 ± 0.2) Hz. Together with the levitation and the magnetic bias field the lasers provide an effective trap depth of about $k_B \times 7$ μK. This trap depth is given by the weaker of the two CO_2-lasers as the atoms can escape along the direction of the stronger beam.

For transfer of the precooled atoms into the reservoir trap, we leave the light of the two CO_2-lasers on during the entire pre-cooling phase. This is because the CO_2-lasers show strong variations in beam pointing and beam shape as a function of radio-frequency power to the AOMs. We have checked that the small light shift introduced by the lasers does not affect the initial loading and cooling efficiency. The reservoir trap is then activated by ramping up the magnetic field and its gradient. The 1/e-rise time of the magnetic fields is limited to 1.5 ms because of eddy currents in the stainless steel chamber. We, therefore, do not expect the transfer to be fully adiabatic.

We find that the atoms are heated to about 2.2 μK by the transfer into the reservoir trap. A clear measurement on the trapped sample is only possible after about 50 ms since the system initially is not in thermal equilibrium and since the untrapped atoms need to disappear from the field of view. We largely attribute the heating to imperfect phase space matching. In fact, the atomic cloud after Raman-sideband cooling to 0.7 μK has a 1/e-radius of ~ 350 μm. In comparison, an equilibrium distribution in the reservoir trap at 0.7 μK would have a 1/e-radius of ~ 100 μm. Potential energy is thus gained which is then turned into kinetic energy, effectively heating the cloud of atoms. Subsequently, the hot atoms evaporate out of the trap. For this phase of plain evaporation we set the magnetic bias field to 73.5 G. The scattering length is then $1215\, a_0$. The temperature is reduced to less than 1 μK within 10 s. After this time, we measure more than 4×10^6 atoms, corresponding to a peak phase space density of 2×10^{-3}.

3.4 *Dimple trap*

We proceed with loading of the dimple trap after 2 s of plain evaporation in the reservoir trap. At this point the atom number is 7.8×10^6 and the phase space density is 1.7×10^{-3} (see Fig. 3). The dimple trap is generated by horizontally intersecting one tightly focused laser beam B_1 with 34-μm waist and another less focused beam B_2 with 260-μm waist at right angles, rotated by 30° in the horizontal plane with respect to the CO_2-laser beams as shown in Fig. 2d. This is different from our earlier work [4] where we have used CO_2-laser beam A_2 for axial confinement. We introduce the B_2 beam because some weak back reflections of the CO_2-laser beams led to a slight undesirable corrugation of the optical potential. This complicated the quantitative analysis of the BEC. Beams B_1 and B_2 are derived from a broadband fiber laser[5] at 1064 nm. The powers in these beams are ramped up within 1.5 s to a maximum power of 70 mW for B_1 and 270 mW for B_2. The trapping in the dimple is now briefly done by all four laser beams with B_1 providing most of the radial and A_1 most of the axial confinement. After switching off beam A_2, we measure the radial and axial trap frequencies in the dimple to (221.2 ± 1.6) Hz and (14.2 ± 0.1) Hz, respectively. During the ramping up phase of B_1 and B_2 we reduce the magnetic field offset to 23 G and thus the scattering length to $300\, a_0$ in order to reduce losses from three-body recombination [28]. The trap now contains about 1.7×10^6 atoms at a peak phase space density of approximately 0.13.

3.5 *Forced evaporation towards BEC*

We start forced evaporative cooling by ramping down the power in all three remaining beams. Simultaneously we remove the reservoir by switching off the CO_2-laser A_2 that is not responsible for axial confinement. To assure a well-defined ramp over a large intensity range we control the light power of the near-infrared beam B_1 by means of a logarithmic photodiode and a servo loop. The power in CO_2-laser beam A_1 is ramped to zero within 5.5 s so that B_2 at the end of evaporation exclusively assures axial confinement. The change in beam pointing for A_2 does not affect the evaporation. For B_1 we approximately follow an exponential ramp over 5.5 s. The power in beam B_2 is only slightly reduced. The final power in B_1 and B_2 is 0.5 mW and 220 mW. We find and optimize this ramp by extending the ramp in discrete time steps of a few hundred milliseconds at the beginning and up to one second towards the end of the ramp.

At each step we search for a maximum in evaporation efficiency $\gamma = \log(D'/D)/\log(N/N')$ as a function of the trap depth and scattering length [34]. Here, D and D' are the phase-space densities at the beginning and end of each step, N and N' denote the respective particle numbers. Maximizing γ at each step results in an overall optimization of the evaporation path. We find that a magnetic field value of 21 G with scattering length $a = 210\, a_0$ is optimal during the forced evaporation phase. As can be seen from Fig. 3 the efficiency γ lies around 3 during the forced evaporation ramp. We attribute this high efficiency to the fact that atoms can escape the trap into almost all directions because of the levitation field.

We observe the phase transition after 2 s of forced evaporative cooling with about 5×10^5 atoms at a temperature of (200 ± 10) nK. At this point the power in beams B_1 and B_2 is

[5] IPG Laser PYL-10

8.7 mW and 250 mW. The duration of the ramp is relatively short. Our evaporation proceeds close to the hydrodynamic regime. Thus, significant improvement of the evaporation is not to be expected.

Further evaporation leaves a cigar-shaped condensate with the long axis in the horizontal plane. In Fig. 4 we show vertical density profiles of expanding condensates. The tunability of the scattering length allows us to explore different regimes of expansion. For Fig. 4a we expand the condensate at the creation scattering length of $210\,a_0$. This is the usual type of self-similar expansion in which the condensate in the Thomas–Fermi regime retains its parabolic shape [35]. For Fig. 4b we step the scattering length to zero at the moment of release from the trap. The mean-field interaction thus vanishes and the rate of expansion is greatly reduced. This exposes a small thermal component, for which a bimodal fit reveals a temperature of around 10 nK. The critical temperature at these trapping conditions is 24 nK; therefore, the expected condensate fraction agrees well with the measured value of 91%. From the fit to the data in Fig. 4 we obtain that there are up to 1.1×10^5 atoms in the condensate with a 20% calibration error. The error does not come from the fit but from the overall uncertainty in determining the atom number. Usually, the error from absorption imaging alone is around 50%, but we can calibrate the atom number from measurements on the chemical potential, see Sect. 4.1. For this particular experiment we measure the final trap frequencies to (4.3 ± 0.2) Hz and (21.1 ± 0.2) Hz along the axial and radial direction, respectively. We thus infer for the initial Thomas–Fermi sizes $R_{\rm r}^{\rm TF} = (8.7 \pm 0.3)$ μm and $R_{\rm a}^{\rm TF} = (42.5 \pm 1.2)$ μm along the radial and axial directions at a scattering length of $a = 210\,a_0$. The peak density of the condensate is $n_0 = (2.1 \pm 0.1)\,10^{13}\,{\rm cm}^{-3}$.

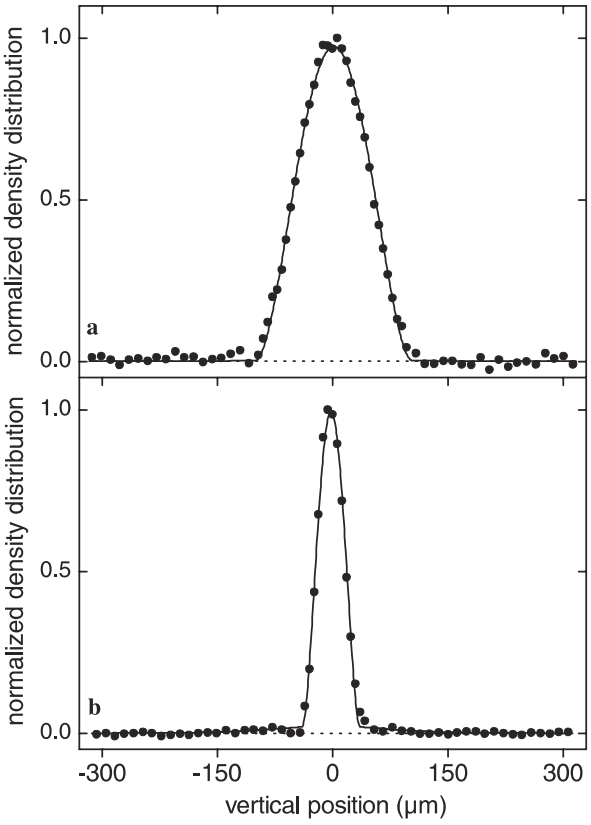

FIGURE 4 Vertical density profiles of Cs condensates after 100 ms of free expansion in the levitation field. The *solid curves* are fits to the data for the Thomas–Fermi profiles which include possible thermal components. For better distinction the baseline is dashed. (**a**) Expansion with no change in scattering length. The total number of atoms in the condensate is $N = 1.1 \times 10^5$. (**b**) Expansion near zero scattering length under the same conditions reveals a small thermal component with a temperature of about 10 nK

4 Tunable quantum gas

We now test the tunability of the condensate interaction. We first study the condensate expansion as a function of scattering length [36] in two different ways. We then specialize to the case when the interaction energy is switched off and present improved results on the ultra-slow expansion of the condensate in comparison with earlier measurements in [4]. Finally, we excite compression oscillations of the trapped condensate by suddenly stepping the scattering length to a lower value.

4.1 *Expansion energy as a function of scattering length*

We measure the release energy of the condensate for slow and fast changes of the scattering length. When we slowly vary the scattering length the wave function of the trapped condensate can follow adiabatically and the condensate remains in equilibrium. The release energy is proportional to the chemical potential of the condensate at the given value of the scattering length. The situation is different when we rapidly switch the scattering length at the moment of condensate release. The condensate then expands from a non-equilibrium state because the wave function has not had time to adjust to the change in interaction energy. This leads to strong changes for the rate of condensate expansion in comparison to the expansion from equilibrium.

We first consider a condensate in the Thomas–Fermi regime for which we adiabatically ramp the scattering length to a new value. For such a condensate, the release energy $E_{\rm rel}$ directly corresponds to the chemical potential $\mu_{\rm TF}$ through $\frac{7}{2}E_{\rm rel} = \mu_{\rm TF}$ [35], which is given by

$$\mu_{\rm TF} = \frac{h\bar{\nu}}{2}\left(\frac{15N}{a_{\rm ho}}\right)^{2/5} a^{2/5}. \qquad (1)$$

Here, $\bar{\nu}$ is the geometric average of the trap frequencies, N is the particle number in the condensate, and $a_{\rm ho} = \sqrt{\hbar/(m2\pi\bar{\nu})}$ is the oscillator length. For the experiment we produce a condensate with $N = 8.5 \times 10^4$ atoms at a creation scattering length of $a_{\rm c} = 210\,a_0$. We then slowly ramp the magnetic field to values between 20 and 35 G, setting the scattering length to a value between about 200 and 700 a_0. The slow ramping excludes values below the Feshbach resonance at 19.9 and above the one at 48.0 G because of strong loss[6]. The condensate is then released from the trap and we measure the release energy. The results are shown in Fig. 5. Here we assume that the magnetic field strength translates into scattering length according to Fig. 1. The data is well fit by a function of the

[6] A combination of slow ramping and quick jumping at the Feshbach resonances would allow access to the full range of values for the scattering length.

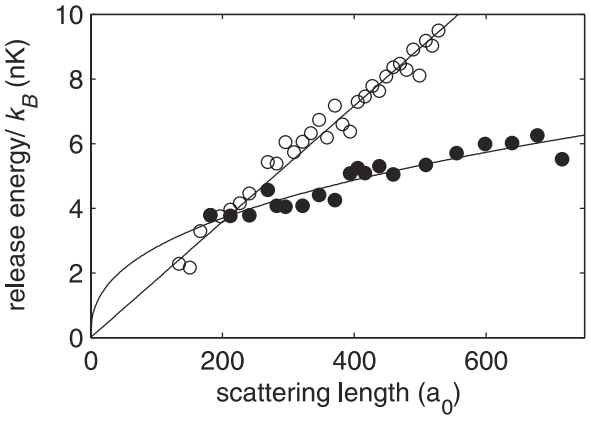

FIGURE 5 Release energy of the condensate as a function of scattering length a. The *filled circles* represent experimental data for the case of adiabatic ramping of a trapped condensate. The data, corresponding to 2/7 of the chemical potential at a given value of the scattering length, are fit by $C\,a^{2/5}$. The *open circles* represent data for rapid switching at the moment of condensate release. As discussed in the text, the straight line is not a fit. It connects the origin with the fitted value of the release energy at the creation scattering length

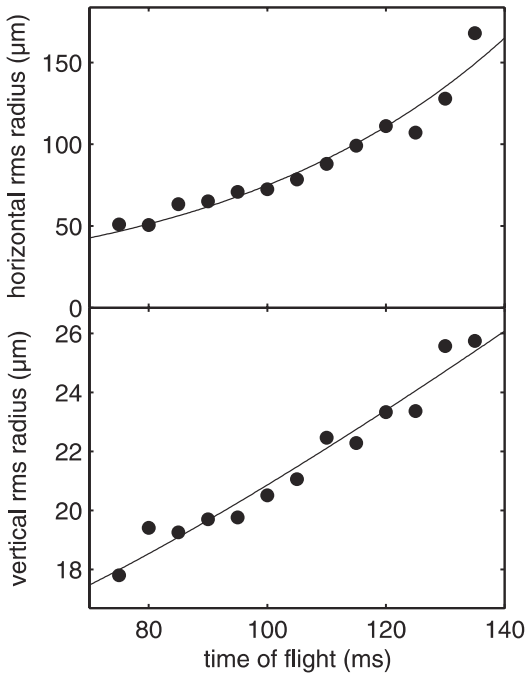

FIGURE 6 Expansion of the non-interacting condensate. The data points show the horizontal (above) and vertical (below) rms radius of the BEC as a function of expansion time near the zero crossing of scattering length. Note the different scales. The fit to the residual vertical expansion reveals a release energy of $k_B \times (51 \pm 3)$ pK. For the horizontal expansion the data are fit by $A \cosh(\alpha t)$ with $\alpha = 2\pi \times (3.20 \pm 0.23)$ Hz

form $Ca^{2/5}$ according to (1). From the fit parameter C we can deduce an independent estimate of the particle number $N = (8.2 \pm 1.3) \times 10^4$. The error is dominated by the error in determining the trap frequencies.

For a sudden change of the scattering length the condensate wave function has no time to react. For example, for an increase of the scattering length the density distribution is too narrow in comparison to the equilibrium density distribution at the new value of the scattering length. The condensate thus expands more rapidly than a condensate in equilibrium at this new value. Since the mean-field interaction energy of the condensate scales linearly with the scattering length for a given density profile [35], we expect a linear behavior of the release energy as a function of the final scattering length a. In Fig. 5 we thus compare the data for the measured release energy to a straight line $Ca_c^{2/5} a/a_c$ given by the origin and the fitted value of the release energy at the creation scattering length $a_c = 210\,a_0$. We find good agreement with the linear dependence.

4.2 *Ultra-slow condensate expansion*

We now study the expansion of the condensate near the zero-crossing of the scattering length. At the moment of condensate release, we rapidly switch the magnetic field from the creation field near 20 G to (17.17 ± 0.05) G, corresponding to $a = (3.4 \pm 3.0)\,a_0$. The error in determining the precise magnetic field at the position of condensate requires that we choose a slightly positive value of the scattering length to assure that no weakly attractive interactions modify the condensate expansion. The levitation field remains on, allowing for an extended observation period because the atoms then do not fall under gravity. Figure 6 shows the vertical and horizontal extent of a BEC with 1.2×10^5 atoms as a function of time after release from the trap. We only show the data after 75 ms of expansion when the optical density of the atomic cloud is sufficiently reduced to allow for reliable absorption imaging. The horizontal expansion is dominated by the magnetic anti-trapping potential which derives from the presence of the levitation field and which magnifies the atomic cloud according to the cosine hyperbolicus function, see Sect. 3.3. The measured rate of expansion $2\pi \times (3.20 \pm 0.23)$ Hz agrees reasonably well with the expected rate constant $\alpha = 2\pi \times 3.4$ Hz. The vertical expansion corresponds to a release energy of $k_B \times (51 \pm 3)$ pK. Note that this is much lower than the kinetic energy of the ground state $\hbar\omega_r/4 = k_B \times 253$ pK given by a radial trap frequency of $\omega_r = 2\pi \times 21.1$ Hz. It is remarkable that the release energy is less than the zero-point energy of the ground state. Since the spatial extent of the condensate is much larger than the size of the ground state wave function of the harmonic oscillator, the momentum spread, limited by the uncertainty of the wave function of the initial condensate, is lower than that of the ground state.

4.3 *Condensate oscillations*

By rapidly ramping the scattering length it is possible to excite oscillations of the condensate in the trap [37]. In fact, in the limit of a cigar shaped condensate one expects radial "compression" or "expansion oscillations" at twice the trap frequency. Compression oscillations can be seen in Fig. 7 where we plot the vertical radius of the released condensate as a function of hold time t_h in the trap. To excite the oscillation we step the scattering length from a value of $a = 363\,a_0$ ($B = 24.4$ G) to $a = 25\,a_0$ ($B = 17.6$ G) at time t_0. The condensate is then allowed to oscillate in the trap for a variable hold time t_h at the final value of the scattering length. We release the condensate at time $t_0 + t_h$ and take an image after 80 ms of free expansion. We fit the data

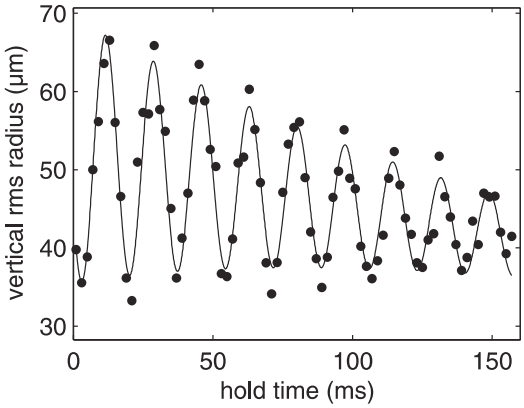

FIGURE 7 Condensate oscillations after rapid switching of the scattering length. The *filled circles* show the vertical rms radius of an expanding BEC with 7×10^4 atoms after 80 ms of free expansion as a function of hold time in the trap. The scattering length has been switched rapidly from $363\,a_0$ to $25\,a_0$. The *solid curve* is a fit to the data giving an oscillation frequency of (58.3 ± 0.2) Hz. We independently measure the radial trap frequency to (28 ± 1) Hz

by a sinusoidal function. The measured compression oscillation frequency of (58.3 ± 0.2) Hz agrees well with twice the radial trap frequency of $2 \times (28 \pm 1)$ Hz at the given trapping power. To account for the damping we have to introduce an exponential decay of the amplitude and of the offset value. The damping of the amplitude has a time constant of 126 ms. We have not yet identified the origin of this damping. Possibly the BEC samples different trapping frequencies due to the large amplitude of the oscillation, which would lead to an apparent damping. Also, damping might be caused by the interaction with a residual thermal cloud or by parametric processes [38].

5 Conclusion

We have shown that essentially pure Cs condensates can be produced with more than 10^5 atoms. In our optical trap it is possible to flexibly change the atomic scattering properties. The atomic condensate can now be used as the starting point for experiments where a tuning and ramping of the scattering properties can be exploited. It will be interesting to study the case of a non-interacting condensate at the zero-crossing of the scattering length. Such a condensate might be used in atom interferometers where one wishes to suppress any mean-field effects [39]. On the other hand, tuning to large values of the scattering length might allow the investigation of effects beyond the mean-field approximation [35]. Also, modulation of the scattering length could be used as an alternative tool to probe the excitation spectrum of the condensate. Finally, ultracold Cs_2 molecules can be created by ramping across one of the Feshbach resonances [8] and the transition from an atomic to a molecular condensate could then be studied.

ACKNOWLEDGEMENTS This work is supported by the Austrian "Fonds zur Förderung der wissenschaftlichen Forschung" (FWF) within SFB 15 (project part 16) and by the European Union in the frame of the Cold Molecules TMR Network under Contract No. HPRN-CT-2002-00290. M.M. is supported by DOC [Doktorandenprogramm der Österreichischen Akademie der Wissenschaften]. C.C. is supported by a Lise-Meitner-Fellowship from the FWF.

REFERENCES

1 M. Barrett, J. Sauer, M. Chapman: Phys. Rev. Lett. **87**, 010404 (2001)
2 Y. Takasu, K. Maki, K. Komori, T. Takano, K. Honda, M. Kumakura, T. Yabuzaki, Y. Takahashi: Phys. Rev. Lett. **91**, 040404 (2003)
3 G. Cennini, G. Ritt, C. Geckeler, M. Weitz: Phys. Rev. Lett. **91**, 240408 (2003)
4 T. Weber, J. Herbig, M. Mark, H.-C. Nägerl, R. Grimm: Science **299**, 232 (2003)
5 D. Rychtarik, B. Engeser, H.-C. Nägerl, R. Grimm: Phys. Rev. Lett. **92**, 173003 (2004)
6 C. Chin, A.J. Kerman, V. Vuletic, S. Chu: Phys. Rev. Lett. **90**, 033201 (2003)
7 C.A. Regal, C. Ticknor, J.L. Bohn, D.S. Jin: Nature **424**, 47 (2003)
8 J. Herbig, T. Kraemer, M. Mark, T. Weber, C. Chin, H.-C. Nägerl, R. Grimm: Science **301**, 1510 (2003)
9 S. Dürr, T. Volz, A. Marte, G. Rempe: Phys. Rev. Lett. **92**, 020406 (2004)
10 K. Xu, T. Mukaiyama, J.R. Abo-Shaeer, J.K. Chin, D.E. Miller, W. Ketterle: Phys. Rev. Lett. **91**, 210402 (2003)
11 S. Jochim, M. Bartenstein, A. Altmeyer, G. Hendl, S. Riedl, C. Chin, J. Hecker Denschlag, R. Grimm: Science **302**, 2101 (2003)
12 M. Greiner, C.A. Regal, D.S. Jin: Nature **426**, 537 (2003)
13 C. Chin, V. Vuletic, A.J. Kerman, S. Chu, E. Tiesinga, P.J. Leo, C.J. Williams: Phys. Rev. A **70**, 032701 (2004)
14 E.A. Donley, N.R. Claussen, S.T. Thomson, C.E. Wieman: Nature **417**, 529 (2002)
15 L. Radzihovsky, J. Park, P.B. Weichman: Phys. Rev. Lett. **92**, 160402 (2004)
16 M.W.J. Romans, R.A. Duine, S. Sachdev, H.T.C. Stoof: Phys. Rev. Lett. **93**, 020405 (2004)
17 J. Söding, D. Guéry-Odelin, P. Desbiolles, G. Ferrari, J. Dalibard: Phys. Rev. Lett. **80**, 1869 (1998)
18 J. Arlt, P. Bance, S. Hopkins, J. Martin, S. Webster, A. Wilson, K. Zetie, C.J. Foot: J. Phys. B **31**, L321 (1998)
19 D. Guéry-Odelin, J. Söding, P. Desbiolles, J. Dalibard: Europhys. Lett. **44**, 26 (1998)
20 D. Guéry-Odelin, J. Söding, P. Desbiolles, J. Dalibard: Optics Express **2**, 323 (1998)
21 S.A. Hopkins, S. Webster, J. Arlt, P. Bance, S. Cornish, O. Maragò, C.J. Foot: Phys. Rev. A. **61**, 032707 (2000)
22 P.J. Leo, E. Tiesinga, P.S. Julienne, D.K. Walter, S. Kadlecek, T.G. Walker: Phys. Rev. Lett. **81**, 1389 (1998)
23 A.M. Thomas, S. Hopkins, S.L. Cornish, C.J. Foot: J. Opt. B **5**, S107 (2003)
24 H. Perrin, A. Kuhn, I. Bouchoule, C. Salomon: Europhys. Lett. **42**, 395 (1998)
25 V. Vuletić, A.J. Kerman, C. Chin, S. Chu: Phys. Rev. Lett. **82**, 1406 (1999)
26 M. Hammes, D. Rychtarik, V. Druzhinina, U. Moslener, I. Manek-Hönninger, R. Grimm: J. Mod. Opt. **47**, 2755 (2000)
27 D.-J. Han, M.T. DePue, D.S. Weiss: Phys. Rev. A **63**, 023405 (2001)
28 T. Weber, J. Herbig, M. Mark, H.-C. Nägerl, R. Grimm: Phys. Rev. Lett. **91**, 123201 (2003)
29 D.-J. Han, M.T. DePue, D.S. Weiss: Phys. Rev. A **63**, 023405 (2001)
30 A.J. Kerman, V. Vuletić, C. Chin, S. Chu: Phys. Rev. Lett. **84**, 439 (2000)
31 D.M. Stamper-Kurn, H.-J. Miesner, A.P. Chikkatur, S. Inouye, J. Stenger, W. Ketterle: Phys. Rev. Lett. **81**, 2194 (1998)
32 T. Weber: PhD thesis, Univ. Innsbruck 2003
33 P. Treutlein, K.Y. Chung, S. Chu: Phys. Rev. A **63**, 051401 (2001)
34 W. Ketterle, N.J. Van Druten: Adv. At. Mol. Opt. Phys. **37**, 181 (1996)
35 L. Pitaevskii, S. Stringari: *Bose–Einstein Condensation* (Clarendon Press, Oxford 2003)
36 S.L. Cornish, N.R. Claussen, J.L. Roberts, E.A. Cornell, C.E. Wieman: Phys. Rev. Lett. **85**, 1795 (2000)
37 Y. Kagan, E.L. Surkov, G.V. Shlyapnikov: Phys. Rev. Lett. **79**, 2604 (2001)
38 F. Chevy, V. Bretin, P. Rosenbusch, K.W. Madison, J. Dalibard: Phys. Rev. Lett. **88**, 250402 (2002)
39 S. Gupta, K. Dieckmann, Z. Hadzibabic, D.E. Pritchard: Phys. Rev. Lett. **89**, 140401 (2002)

B.5. Efficient creation of molecules from a cesium Bose-Einstein condensate

EUROPHYSICS LETTERS

OFFPRINT

Vol. 69 • Number 5 • pp. 706–712

Efficient creation of molecules from a cesium Bose-Einstein condensate

* * *

M. Mark, T. Kraemer, J. Herbig, C. Chin
, H.-C. Nägerl and R. Grimm

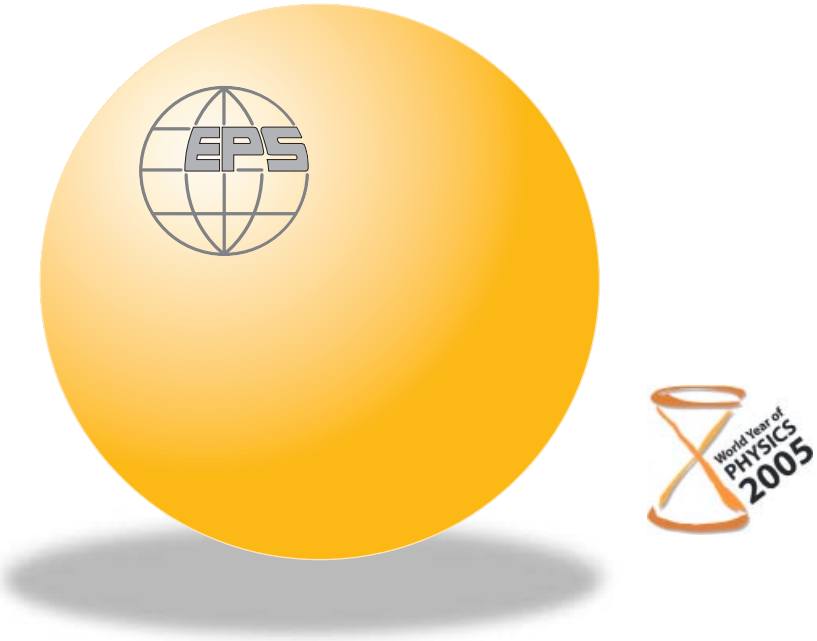

Published under the scientific responsability of the
EUROPEAN PHYSICAL SOCIETY
Incorporating
JOURNAL DE PHYSIQUE LETTRES • LETTERE AL NUOVO CIMENTO

Europhys. Lett., **69** (5), pp. 706–712 (2005)
DOI: 10.1209/epl/i2004-10427-7

Efficient creation of molecules from a cesium Bose-Einstein condensate

M. Mark[1], T. Kraemer[1], J. Herbig[1], C. Chin[1]
, H.-C. Nägerl[1] and R. Grimm[1,2]

[1] *Institut für Experimentalphysik, Universität Innsbruck*
Technikerstraße 25, 6020 Innsbruck, Austria
[2] *Institut für Quantenoptik und Quanteninformation*
Österreichische Akademie der Wissenschaften - 6020 Innsbruck, Austria

received 29 September 2004; accepted in final form 12 January 2005
published online 2 February 2005

PACS. 03.75.-b – Matter waves.
PACS. 34.50.-s – Scattering of atoms and molecules.
PACS. 32.80.Pj – Optical cooling of atoms; trapping.

Abstract. – We report a new scheme to create weakly bound Cs_2 molecules from an atomic Bose-Einstein condensate. The method is based on switching the magnetic field to a narrow Feshbach resonance and yields a high atom-molecule conversion efficiency of more than 30%, a factor of three higher than obtained with conventional magnetic-field ramps. The Cs_2 molecules are created in a single g-wave rotational quantum state. The observed dependence of the conversion efficiency on the magnetic field and atom density shows scattering processes beyond two-body coupling to occur in the vicinity of the Feshbach resonance.

The newly emerging field of quantum-degenerate molecules provides intriguing possibilities for controlled studies of multicomponent matter-wave systems. Chemical reactions are expected to show effects of coherence, matter-wave interference, quantum tunneling, and bosonic stimulation. Recently, coherent atom-molecule couplings [1] have been observed in a Bose-Einstein condensate (BEC), and molecular quantum gases [2,3] and molecular BECs [4] have been realized. The key ingredient in these experiments has been the presence of magnetically induced Feshbach resonances [5]. These resonances provide the variable coupling between atoms and molecules as a function of an external magnetic field and allow the conversion of atoms to molecules and vice versa.

In the previous experiments on the creation of ultracold Cs_2, Na_2 and Rb_2 molecules from the corresponding atomic BECs [2, 3, 6] the molecules are formed by ramping the magnetic field through a Feshbach resonance; see illustration in fig. 1. It is expected that during the ramping process the ground-state atom population in the trap is adiabatically and efficiently converted into molecules in a weakly bound state [7]. However, the reported efficiencies using this method are relatively low: Typically 5%–10% are observed, whereas up to 50% to 70% of the atoms are lost during the ramping process. The missing fraction, the lost atoms which are not converted into weakly bound molecules, is generally believed to result from the creation

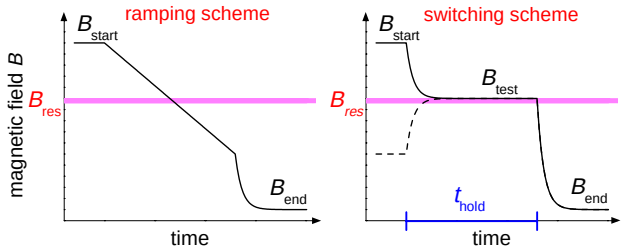

Fig. 1 – Schemes for molecule creation near a Feshbach resonance, located at $B_{\rm res}$. In the ramping scheme, we linearly ramp the magnetic field from $B_{\rm start}$, well above the resonance, to some value well below the resonance, and then quickly to $B_{\rm end}$. In the switching scheme, we first switch from $B_{\rm start}$ to $B_{\rm test}$. After a hold time $t_{\rm hold}$, we switch the field to $B_{\rm end}$. The switching scheme also works for $B_{\rm start}$ below the resonance (dashed line). The finite response time of the magnetic field in our experiment is due to eddy currents in the stainless-steel vacuum chamber.

of molecules in states which cannot be detected by the conventional imaging method, or to consist of "hot" atoms which quickly leave the trap [2, 8].

In this paper, we report a high atom-molecule conversion efficiency in excess of 30% from an atomic BEC based on a novel switching scheme. This scheme is illustrated in fig. 1. The magnetic field is quickly switched from an off-resonant value $B_{\rm start}$ to a field $B_{\rm test}$, near the resonance position $B_{\rm res}$. After a variable hold time $t_{\rm hold}$, the magnetic field is quickly lowered well below the resonance $B_{\rm end}$, where atoms and molecules decouple and can be independently measured. Our new scheme works for initial magnetic fields $B_{\rm start}$ both well above or well below the resonance. In the latter case, the creation of molecules cannot be explained in terms of the two-body adiabatic conversion picture [7]. An investigation on the atom loss and molecule creation efficiencies suggests that different scattering processes are involved near the narrow Feshbach resonance.

The cesium molecules we create are of special interest since they have a large orbital angular momentum ($l = 4$). Coupling from ultracold atoms in an s-wave scattering state to the g-wave molecular states is observed only for cesium atoms due to the large indirect spin-spin coupling [9]. Many narrow Feshbach resonances of this kind were observed at low magnetic fields for cesium atoms polarized in the lowest internal state $|F = 3, m_F = 3\rangle$ [10], where F is the total angular momentum and m_F is the magnetic quantum number. Based on these narrow resonances, the formation of thermal molecules was investigated [11] and a pure molecular quantum gas was created from an atomic BEC [2].

Our experiments start with a pure BEC of cesium with up to 2.2×10^5 atoms in the ground state $|F = 3, m_F = 3\rangle$ [12, 13]. The magnetic field is set to 21 G, corresponding to an atomic scattering length of $210a_0$, where a_0 is the Bohr radius. The magnetic field gradient is set to 31.3 G/cm for levitation of the atoms [12]. The condensate is confined in a crossed dipole trap formed by two horizontally intersecting laser beams, which are derived from a broad-band Yb fiber laser at 1064 nm. One tightly focused beam with a waist of 35 μm and a power of 0.5 mW essentially provides the radial confinement; the other beam with a waist of 300 μm and power of 350 mW essentially provides the axial confinement. The radial and axial trap frequencies are $\omega_r/2\pi = 17.5$ Hz and $\omega_z/2\pi = 4.7$ Hz, respectively. The chemical potential is $k_{\rm B} \times 11$ nK, where $k_{\rm B}$ is Boltzmann's constant.

Before we start the molecule creation, we first compress the condensate by adiabatically increasing the power of the tightly focused laser in 0.7 s to 40 mW. The higher laser power provides a stronger trapping force and allows us to turn off the levitation field. The absence

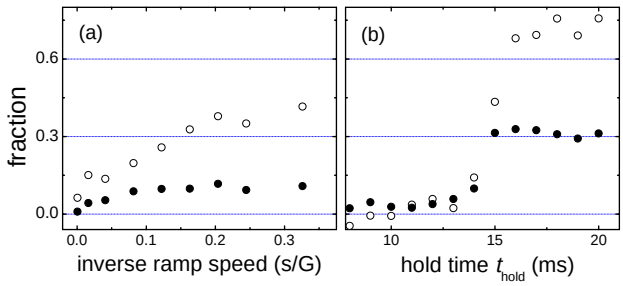

Fig. 2 – Comparison of the two schemes of molecule creation. Molecule fraction (solid circles) and atom loss fraction (open circles) are shown for (a) the ramping scheme, where the fractions are measured for different ramp speeds, and for (b) the switching scheme for different hold times $t_{\rm hold}$. In (b), $B_{\rm test}$ is set right on resonance.

of the magnetic field gradient is crucial to ensure that all atoms experience the same magnetic field and can simultaneously participate in the molecule formation process. In the compressed trap, the trap frequencies are $\omega_r/2\pi = 170\,\text{Hz}$ and $\omega_z/2\pi = 6.5\,\text{Hz}$, the chemical potential is $k_{\rm B} \times 86\,\text{nK}$ and the peak density is $1.7 \times 10^{14}\,\text{cm}^{-3}$. We then slowly change the magnetic field in 200 ms to a starting value of $B_{\rm start}$, typically 0.5 G above the Feshbach resonance $B_{\rm res}$. Note that this 0.5 G offset is much larger than the resonance width of a few mG. The condensate at $B_{\rm start}$ is not influenced by the resonance. We then switch off the dipole trap and release the atoms into free space and, at the same time, tune the magnetic field toward the Feshbach resonance to create molecules. At the end of the molecule formation phase, we quickly lower the magnetic field down to $B_{\rm end} \approx 18\,\text{G}$ to decouple the molecules and atoms.

The resulting molecule and atom numbers can be determined independently by absorption imaging [2]. The atoms are directly imaged at 18 G. We verify that the molecules are insensitive to the imaging beam at this magnetic field. To detect the molecules, we first blast away the atoms at 18 G with a resonant beam [3], and then ramp the magnetic field back above the resonance to 21 G. The weakly bound molecular state is then above the continuum and the molecules quickly dissociate into free atoms [14]. By imaging the cloud of the resulting atoms, we can determine the molecule number. We define the corresponding molecule fraction as the number of atoms detected after dissociation normalized to the initial atom number. This is then, by definition, equal to the atom-molecule conversion efficiency.

We employ both the ramping scheme and the switching scheme for molecule production (see fig. 1) and compare their performances. In the ramping scheme, we tune the magnetic field across the resonance with a constant ramping speed. Based on the resulting molecule number and the loss in atomic number, we calculate the conversion fractions, shown in fig. 2(a). A maximum molecule fraction of 10% is observed when the ramps are slower than 10 G/s. The atom loss for these ramps is about 40%, which indicates a missing fraction of about 30%. This result is similar to all previous experiments using the same method [2,3,6]. For the switching scheme, we quickly tune the magnetic field onto the Feshbach resonance $B_{\rm test} \approx B_{\rm res}$, wait for various hold times $t_{\rm hold}$, and quickly lower the magnetic field to $B_{\rm end} = 18\,\text{G}$. Due to the finite response time of the magnetic field, the field approaches the Feshbach resonance after about 12 ms [15]. At this time, the peak density of the expanding condensate reduces to $1.1 \times 10^{12}\,\text{cm}^{-3}$ [16]. For hold times $t_{\rm hold} > 15\,\text{ms}$, molecule fractions of $30 \sim 35\%$ and atom loss fractions of $\sim 70\%$ are reached as shown in fig. 2(b). The conversion efficiency is by more than a factor of three higher than obtained from the ramping scheme. Note that in order

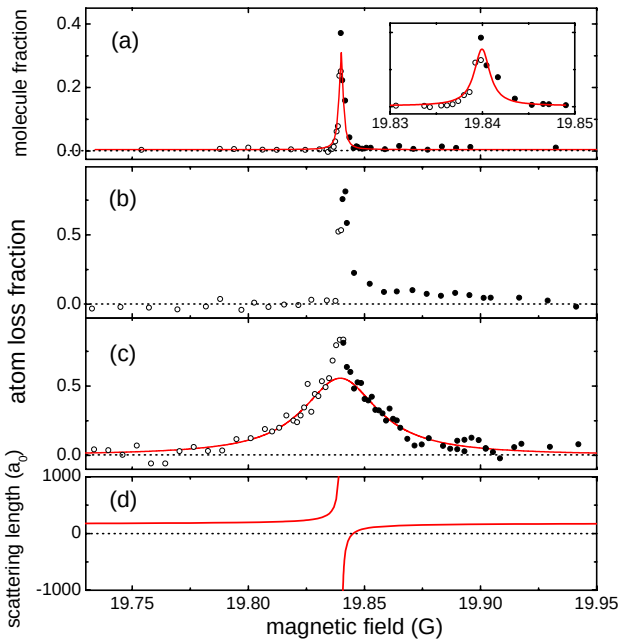

Fig. 3 – Molecule creation and atom loss near the Feshbach resonance. Based on the switching scheme, molecule increase in $t_{\rm hold} = 18\,\rm ms$ (a) and atom loss in 18 ms (b) are measured for various test fields $B_{\rm test}$. The inset shows the expanded view of the molecule signal. For comparison, the atom trap loss in the compressed trap is shown in (c). The scattering length is shown in (d) for reference. Solid circles (open circles) show the measurements above (below) the resonance. In (a), a Lorentzian fit (solid line) yields a width of 2.1 mG and the resonance position of $B_{\rm res} = 19.840\,\rm G$, subject to a calibration uncertainty of 4 mG. Fitting both wings in (c) gives a Lorentzian width of 40(2) mG.

to precisely set the magnetic field right on the narrow Feshbach resonance, we synchronize the experiment with the 50 Hz line voltage to reduce the effects of the ambient magnetic-field ripple, for which we measure an amplitude of 4 mG. This suppresses uncontrolled magnetic-field variations to about 1 mG.

To understand the different performance of the two schemes, we study the atom loss and molecule increase at different magnetic fields $B_{\rm test}$ based on the switching scheme, see fig. 3(a) and (b). For comparison, we also show the atom loss in the compressed trap in fig. 3(c), where the initial peak density is $1.9 \times 10^{14}\,\rm cm^{-3}$ [17]. The calculated scattering length is shown in fig. 3(d) [18]. For all measurements with $B_{\rm test}$ above the resonance, we prepare the condensate as previously described at $B_{\rm start} = B_{\rm res} + 0.5\,\rm G$. For $B_{\rm test}$ below the resonance, we prepare the condensate at a magnetic field below the resonance by quickly switching the magnetic field from the initial value to $B_{\rm res} - 0.5\,\rm G$. No appreciable atom loss, molecule formation or condensate excitation is observed in this process. We then follow the same experimental procedure, but approach the resonance from below. These two different preparation procedures for magnetic fields above and below the resonance are necessary to avoid a slow field-sweep across the resonance, which can lead to systematic atom loss or molecule increase.

In the molecule creation spectrum (fig. 3(a)) we observe a very narrow linewidth of 2.1 mG, which is consistent with the predicted resonance width. Notably, our molecule creation scheme also works for $B_{\rm start}$ below the resonance, which suggests that coupling beyond the adiabatic

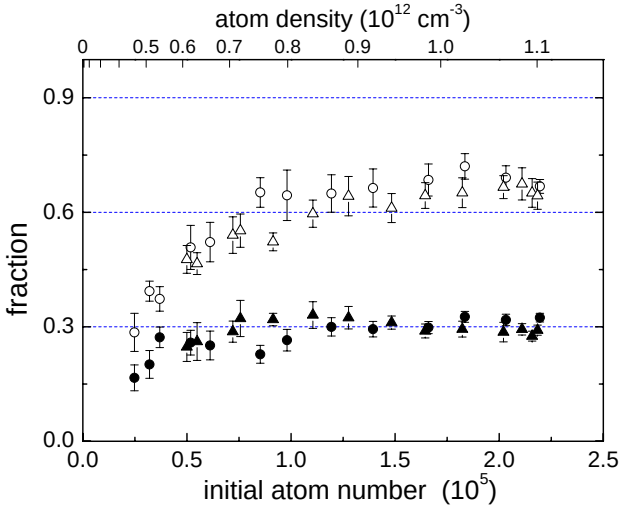

Fig. 4 – Density dependence of the atom loss fraction (open symbols) and molecule fraction (solid symbols). The atom number in the BEC is varied by either adjusting optical cooling efficiencies (solid and open circles) or the loading efficiencies into the crossed dipole trap (solid and open triangles). The corresponding atomic density of the sample right before the molecule formation (after 12 ms expansion in free space) is given on the top axis.

conversion model plays an important role in the creation process. In the adiabatic passage picture, molecules cannot be created when the creation field is below the resonance. The atom loss, shown in fig. 3(b), is asymmetric and seems to include two components, a narrow peak on resonance and a much broader and weaker loss feature for magnetic fields above the resonance. The narrow peak has a similar width as in the molecule production spectrum in fig. 3(a), and is clearly related to the observed molecule formation. The broad and weak feature on the high magnetic-field side has a width of 80(20) mG as determined from a one-sided Lorentzian fit. To obtain further information about the atom loss process, we measure the atom loss in the compressed trap, where the atom density is higher by a factor of ~ 170 than in fig. 3(a) and (b). The result shown in fig. 3(c) displays a wide and symmetric loss feature. By fitting the two wings to a Lorentzian profile, we find a width of 40(2) mG.

The different lineshapes suggest that different scattering processes are involved near the Feshbach resonance. The molecule formation width is close to the predicted width of the Feshbach resonance and can be interpreted in terms of the two-body Feshbach coupling. The asymmetric loss feature in fig. 3(b) and the trap loss may be due to three-body recombination or many-body effects. These broad atom loss features are puzzling, since they are a factor of 20 or more wider than the Feshbach resonance width of 2 mG. The physical origin of the associated loss mechanisms requires further investigation.

The large width of the atom loss feature, however, does provide a qualitative explanation why the switching scheme is more efficient than the ramping scheme. In a linear ramp, atoms sample all magnetic fields near the resonance which, for a large fraction of time, leads to atom loss without molecule increase. With the switching scheme, the atoms spend more time in the magnetic-field range where the molecules can be created.

To further investigate and differentiate the physical mechanisms that are responsible for the missing fraction and for the molecule increase, we measure the dependence of the atom loss

fraction and molecule fraction on the atom number in the condensate, as shown in fig. 4. Atom numbers ranging from 2.5×10^4 to 2.2×10^5 correspond to peak densities of $7.9 \times 10^{13}\,\mathrm{cm}^{-3}$ to $1.9 \times 10^{14}\,\mathrm{cm}^{-3}$ in the compressed trap and to $4.6 \times 10^{11}\,\mathrm{cm}^{-3}$ to $1.1 \times 10^{12}\,\mathrm{cm}^{-3}$ in free space at the moment the molecules are created. For the calculation of the densities in free space, we take into account the 12 ms expansion of the condensate in the Thomas-Fermi regime after the dipole trap is turned off.

Several interesting features show up in the density dependence. The molecule fraction grows and saturates to $\sim 30\%$ at densities higher than $5 \times 10^{11}\,\mathrm{cm}^{-3}$. The saturation of the molecule fraction resembles observations in a thermal gas [11,19], where a thermal equilibrium is reached with a constant molecule fraction in the sample [20]. The missing fraction is very small at low densities and continues to grow up to a density of $8 \times 10^{12}\,\mathrm{cm}^{-3}$. The stronger density dependence of the missing fraction suggests that scattering processes involved in the atom loss are of higher order than for the molecule increase. Similar enhancement of the collision loss near the Feshbach resonance was also observed in a ^{85}Rb condensate [21] and in a thermal Cs gas [22]. A further analysis on the scattering dynamics and the possible thermal equilibrium condition is necessary.

In conclusion, we show that an atom-molecule conversion fraction of more than 30% can be reached based on a magnetic-field switching scheme. The performance of this scheme is superior to the conventional linear magnetic-field ramping scheme since the molecules are created only within the narrow Feshbach resonance width of 2 mG, while the atoms are lost over a much large range of ~ 40 mG. The density dependence of both the missing fraction and the molecule fraction suggests that in our scheme the molecules are created via Feshbach coupling, while the missing fraction comes from higher-order scattering processes. Based on the new creation scheme, we are now able to obtain samples with up to 40000 ultracold molecules. This provides a good starting point to investigate the trapping, the interactions, and the matter-wave nature of ultracold molecules.

* * *

We acknowledge support by the Austrian Science Fund (FWF) within SFB 15 (project part 16) and by the European Union in the frame of the Cold Molecules TMR Network under Contract No. HPRN-CT-2002-00290. MM is supported by DOC (Doktorandenprogramm der Österreichischen Akademie der Wissenschaften). CC is a Lise-Meitner research fellow of the FWF.

REFERENCES

[1] DONLEY E. A., CLAUSSEN N. R., THOMPSON S. T. and WIEMAN C., *Nature*, **412** (2002) 295.
[2] HERBIG J., KRAEMER T., MARK M., WEBER T., CHIN C., NÄGERL H.-C. and GRIMM R., *Science*, **301** (2003) 1510.
[3] XU K., MUKAIYAMA T., ABO-SHAEER J. R., CHIN J. K., MILLER D. E. and KETTERLE W., *Phys. Rev. Lett.*, **91** (2003) 210402.
[4] JOCHIM S., BARTENSTEIN M., ALTMEYER A., HENDL G., RIEDL S., CHIN C., HECKER DENSCHLAG J. and GRIMM R., *Science*, **302** (2003) 2101; published online November 13, 2003 (10.1126/science.1093280); GREINER M., REGAL C. A. and JIN D. S., *Nature*, **426** (2003) 537; ZWIERLEIN M. W., STAN C. A., SCHUNCK C. H., RAUPACH S. M. F., GUPTA S., HADZIBABIC Z. and KETTERLE W., *Phys. Rev. Lett.*, **91** (2003) 250401.
[5] TIESINGA E., VERHAAR B. J. and STOOF H. T. C., *Phys. Rev. A*, **47** (1993) 4114; INOUYE S., ANDREWS M., STENGER J., MIESNER H.-J., STAMPER-KURN S. and KETTERLE W., *Nature*, **392** (1998) 151.

[6] Dürr S., Volz T., Marte A. and Rempe G., *Phys. Rev. Lett.*, **92** (2004) 020406.
[7] Kokkelmans S. J. J. M. F., Vissers H. M. J. and Verhaar B. J., *Phys. Rev. A*, **63** (2001) 031601(R); van Abeelen F. A. and Verhaar B. J., *Phys. Rev. Lett.*, **83** (1999) 1550; Tiesinga E., Williams C. J., Mies F. H. and Julienne P. S., *Phys. Rev. A*, **61** (2000) 063416.
[8] Regal C. A., Ticknor C., Bohn J. L. and Jin D. S., *Nature*, **424** (2003) 47.
[9] Mies F. H., Williams C. J., Julienne P. S. and Krauss M., *J. Res. Natl. Inst. Stand. Technol.*, **101** (1996) 521.
[10] Chin C., Vuletić V., Kerman A. J., Chu S., Tiesinga E., Leo P. and Williams C. J., *Phys. Rev. A*, **70** (2004) 032701.
[11] Chin C., Vuletić V., Kerman A. J. and Chu S., *Phys. Rev. Lett.*, **90** (2003) 033201.
[12] Weber T., Herbig J., Mark M., Nägerl H.-C. and Grimm R., *Science*, **299** (2003) 232.
[13] Kraemer T., Herbig J., Mark M., Weber T., Chin C., Nägerl H.-C. and Grimm R., *Appl. Phys. B*, **79** (2004) 1013. For the present experiment, we have improved the atom number in the BEC by another factor two using the higher power from a new Yb fiber laser.
[14] Mukaiyama T., Abo-Shaeer J. R., Xu K., Chin J. K. and Ketterle W., *Phys. Rev. Lett.*, **92** (2004) 180402; Dürr S., Volz T. and Rempe G., *Phys. Rev. A*, **70** (2004) 031601(R).
[15] The response time of $t_{1/e} = 1.54\,\mathrm{ms}$ for the magnetic field is limited by the eddy currents from the vacuum chamber. Starting from 500 mG above the resonance, we estimate the magnetic field will take $\ln(500\,\mathrm{mG}/2\,\mathrm{mG})t_{1/e} \approx 9\,\mathrm{ms}$ to settle within the resonance width. This result is close to the measured delay time of 12 ms.
[16] We observe that the expansion rate of the molecules is very close to that of the expanding condensate.
[17] This value is slightly higher than the value given before because of the reduced scattering length.
[18] The calculated resonance position is 20.1 G. To reflect the correct resonance position, we shift the numerical data by centering the resonance at our observed value of 19.84 G.
[19] Jochim S., Bartenstein M., Altmeyer A., Hendl G., Chin C., Hecker Denschlag J. and Grimm R., *Phys. Rev. Lett.*, **91** (2003) 240402.
[20] Chin C. and Grimm R., *Phys. Rev. A*, **69** (2004) 033612.
[21] Roberts J. L., Claussen N. R., Cornish S. L. and Wieman C. E., *Phys. Rev. Lett.*, **85** (2000) 728.
[22] Weber T., Herbig J., Mark M., Nägerl H.-C. and Grimm R., *Phys. Rev. Lett.*, **91** (2003) 123201.

B.6. Observation of Feshbach-Like Resonances in Collisions Between Ultracold Molecules

Observation of Feshbach-Like Resonances in Collisions between Ultracold Molecules

C. Chin,[1,*] T. Kraemer,[1] M. Mark,[1] J. Herbig,[1] P. Waldburger,[1] H.-C. Nägerl,[1] and R. Grimm[1,2]
[1]*Institut für Experimentalphysik, Universität Innsbruck, Technikerstraße 25, 6020 Innsbruck, Austria*
[2]*Institut für Quantenoptik und Quanteninformation, Österreichische Akademie der Wissenschaften, 6020 Innsbruck, Austria*
(Received 10 November 2004; published 1 April 2005)

We observe magnetically tuned collision resonances for ultracold Cs_2 molecules stored in a CO_2-laser trap. By magnetically levitating the molecules against gravity, we precisely measure their magnetic moment. We find an avoided level crossing which allows us to transfer the molecules into another state. In the new state, two Feshbach-like collision resonances show up as strong inelastic loss features. We interpret these resonances as being induced by Cs_4 bound states near the molecular scattering continuum. The tunability of the interactions between molecules opens up novel applications such as controlled chemical reactions and synthesis of ultracold complex molecules.

DOI: 10.1103/PhysRevLett.94.123201 PACS numbers: 34.50.−s, 05.30.Jp, 32.80.Pj, 67.40.Hf

The synthesis of ultracold molecules from ultracold atoms has opened up new possibilities for studies on molecular matter waves [1–3], strongly interacting superfluids [4], high-precision molecular spectroscopy [5] and coherent molecular optics [6]. In all these experiments, control of the interatomic interaction by magnetic fields plays an essential role in the association process. When a two-atom bound state is magnetically tuned near the quantum state of two scattering atoms, coupling from the atomic to the molecular state can be resonantly enhanced. This is commonly referred to as a Feshbach resonance [7].

The success in controlling the interaction of ultracold atoms raises the question whether a similar level of control can be achieved for ultracold molecules. Resonant interactions between molecules may lead to synthesis of complex objects beyond atomic dimers. Furthermore, scattering processes for molecules involve many novel reactive channels in comparison to the atomic counterpart, e.g., collision induced dissociation, rearrangement, or displacement chemical reactions. Magnetic tunability of the molecular interactions, similar to that resulting from atomic Feshbach resonances, will lead to exciting perspectives for investigating these chemical processes in regimes where quantum statistics and quantum coherence play an important role.

In this Letter, we report the observation of magnetically tuned collision resonances in an ultracold gas of Cs_2 molecules. The ultracold dimers are created from an atomic Bose-Einstein condensate (BEC) by use of a Feshbach ramp [1] and are trapped in a CO_2-laser trap. We precisely measure the magnetic moment of the molecules and observe an avoided crossing [8] which allows us to transfer the molecules into another state. In the new state, we discover two narrow inelastic collision resonances. The resonance structure suggests that bound states of two cesium molecules, or equivalently Cs_4 states, induce the resonant scattering of molecules. These resonances, which we interpret as Feshbach resonances for ultracold molecules, may open the door to the synthesis of more complex molecules and to the control of their chemical reactions.

The relevant molecular energy structure shown in Fig. 1 is based on calculations done at NIST [9,10]. The dissociation threshold, providing the energy reference $E_b = 0$, is associated with two Cs atoms in the lowest ground state sublevel $|F = 3, m_F = 3\rangle$, where F and m_F are the quantum number of the atomic angular momentum and its projection, respectively. As a result of the strong indirect spin-spin interaction of Cs atoms [11], coupling to molecular states with large orbital angular momentum $l = 4$ [10,12] leads to the complexity of the energy structure shown in Fig. 1. This type of coupling is generally referred to as g-wave Feshbach coupling.

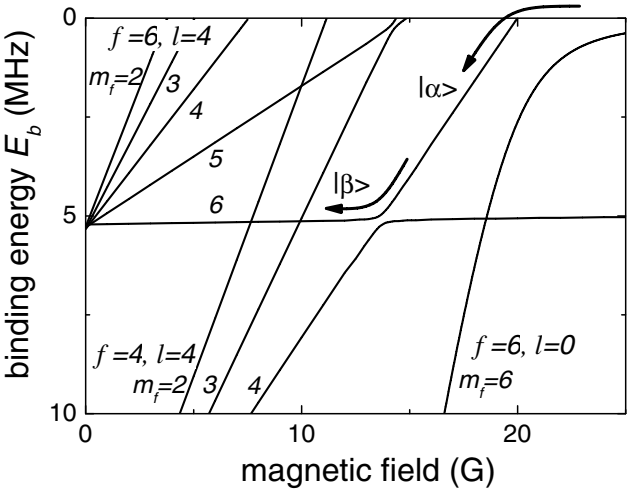

FIG. 1. Molecular energy structure below the scattering continuum of two cesium atoms in the $|F = 3, m_F = 3\rangle$ state. The energy of the dissociation threshold corresponds to $E_b = 0$. The arrows mark the paths to the molecular states we explore, which include the creation of the molecules in $|\alpha\rangle$ via the atomic Feshbach resonance at 19.84 G [1,19] and an avoided crossing to $|\beta\rangle$ at ~13.6 G. Included are only molecular states which can couple to the continuum via Feshbach couplings up to g-wave interaction ($l \leq 4$, $m_f + m_l = 6$ and $m_f \geq 2$).

We create the molecules in the bound state $|\alpha\rangle \equiv |f = 4, m_f = 4; l = 4, m_l = 2\rangle$ via g-wave Feshbach coupling at 19.84 G [1]; see Fig. 1. Here, f is the internal angular momentum of the molecule, and m_f and m_l are the projections of f and l, respectively. The molecular state $|\alpha\rangle$ is stable against spontaneous dissociation for magnetic fields below 19.84 G and acquires larger binding energies at lower magnetic fields. This is due to the small magnetic momentum of $\sim 0.95\mu_B$ of this state as compared to the atomic scattering continuum with $\sim 1.5\mu_B$. At about 14 G, an avoided crossing to another state $|\beta\rangle \equiv |f = 6, m_f = 6; l = 4, m_l = 0\rangle$ is induced by the indirect spin-spin coupling. In this work, we ramp the magnetic field adiabatically and explore the upper branch of the avoided crossing.

Our experiment starts with an essentially pure atomic BEC with up to 2.2×10^5 atoms in a crossed dipole trap formed by two CO_2 laser beams [13,14]. We apply a magnetic field of 20 G, slightly above the Feshbach resonance, and a magnetic field gradient of 31 G/cm to levitate the atoms [15]. The CO_2-laser trap is roughly spherically symmetric with a trapping frequency of $\omega \approx 2\pi \times 20$ Hz and a trap depth of 7 μK. The atomic density is 6×10^{13} cm^{-3} and the chemical potential is $k_B \times 20$ nK, where k_B is Boltzmann's constant.

To create the molecules, we first ramp the magnetic field from 20.0 to 19.5 G in 8 ms and then quickly change the field to 17 G to decouple the molecules from the atoms. Simultaneously, we ramp the magnetic field gradient from 31 up to 50 G/cm. The latter field gradient levitates the molecules [1] and removes all the atoms from the trap in 3 ms. As a consequence, we obtain a pure molecular sample in the CO_2-laser trap with typically 10^4 molecules. The magnetic field ramping process also leads to a small momentum kick on the molecules, which start oscillating in the trap. After ~ 100 ms, the oscillations are damped out and the sample comes to a new equilibrium at a temperature of 250 nK with a peak density of 5×10^{10} cm^{-3} and a phase space density of 10^{-2} to 10^{-3}. To measure the molecule number, we dissociate the molecules into free atoms by reversely ramping the magnetic field back above the resonance to 21 G. We then image the resulting atoms [1].

A key parameter for a perfect levitation of the Cs_2 molecules is the precise value of their magnetic moment [1]. The levitation field is crucial because the gravitational force is much stronger than the trapping force of the CO_2 lasers. In contrast to ground state atoms with only slow-varying magnetic moment, the magnetic moment of the molecules can sensitively depend on the magnetic field as a result of the complex interactions between molecular states; see Fig. 1. Therefore, the prerequisite to perform Cs_2 molecule experiments at different magnetic fields is the knowledge of the molecular magnetic moment for an accurate setting of the levitation field.

We map out the magnetic moment of the molecules over the range of 11.5 to 19.8 G. This is realized by a two-step process: First, we slowly tune the magnetic field in 60 ms to a desired value and find a corresponding magnetic field gradient which can approximately keep the molecules near the center of the CO_2-laser trap. Second, after a hold time of 500 ms needed for the ensemble to come to an equilibrium, we measure the position of the cloud. The location of the molecular cloud provides a very sensitive probe to the residual imbalance of the magnetic force and gravity. Given a small vertical displacement of the molecules relative to the trap center δz for a local magnetic field B and a field gradient B', the magnetic moment is then $\mu(B) = (2m\omega^2\delta z + 2mg)/B'$. Here $2m$ is the molecular mass, and g is the gravitational acceleration. Independent measurements based on releasing the molecules into free space [1] confirm the accuracy of the above method to $0.01\mu_B$.

The measured magnetic moments of the molecules show the expected behavior in the range of 11.5 to 19.8 G; see Fig. 2. We find that the magnetic moment slowly decreases from $0.98\mu_B$ to $0.93\mu_B$ as the magnetic field is lowered from 19.8 G. For magnetic fields below ~ 14 G, the magnetic moment quickly rises and levels off at $1.5\mu_B$. This behavior is readily explained by the avoided crossing at 13.6 G (Figs. 1 and 2), which transfers the molecules from state $|\alpha\rangle$ with $\mu \approx 0.9\mu_B$ to $|\beta\rangle$ with $\mu \approx 1.5\mu_B$. Below 11.5 G, a new avoided crossing to a very weakly coupled $l = 8$ molecular state occurs [16]. We observe fast loss of the molecules since our current apparatus cannot produce a sufficient levitation field to support the molecules against gravity in this new state.

Our measurement agrees excellently with the NIST calculation [9,10] within the 200 mG uncertainty from the multichannel calculation; see Fig. 2. We evaluate the

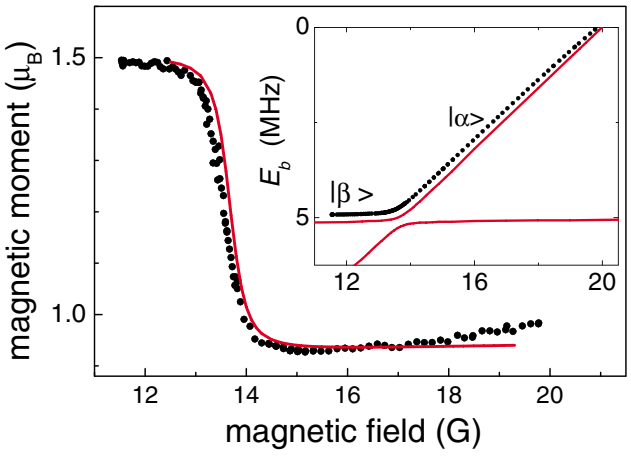

FIG. 2 (color online). Magnetic moment of the Cs_2 molecules. The measured magnetic moment (solid circles) is compared to the NIST calculation (solid line). The fast change at ~ 13.6 G is associated with an avoided crossing. In the inset, we derive the molecular binding energy (solid circles) by integrating the measured magnetic moment. Binding energies from the NIST calculation (solid lines) for both branches of the avoided crossing between state $|\alpha\rangle$ and state $|\beta\rangle$ are shown; see also Fig. 1.

molecular binding energy based on integrating the measured magnetic moments. Here the integration constant is fixed by the fact that the molecular binding energy is zero at the atomic Feshbach resonance $B = 19.84$ G. The result shown in the inset of Fig. 2 gives very good agreement with the theoretical calculation within the energy uncertainty of 0.25 MHz [9]. By fitting our binding energies to a simple avoided crossing model, we determine the crossing to be $B_{\mathrm{cross}} = 13.55(4)$ G and the coupling strength, half the energy splitting between the two eigenstates at B_{cross}, to be $h \times 150(10)$ kHz. Here h is Planck's constant.

To investigate the interactions between molecules, we measure the inelastic collision loss after a trapping time of 300 ms (Fig. 3). For molecules in state $|\alpha\rangle$ ($14\ \mathrm{G} < B < 19.8$ G), the fractional loss is about ~40%. In this molecular state, we do not see any strong magnetic field dependence. When the magnetic field is tuned near the Feshbach resonance at 19.8 G, molecules dissociate into free atoms, which leave the trap.

In state $|\beta\rangle$ ($11.5\ \mathrm{G} < B < 13.6$ G), the behavior of the molecules is strikingly different. We observe a weaker background loss of ~20% and two pronounced resonances with a fractional loss of up to 60%. An expanded view in the inset of Fig. 3 shows that the "double peak" structure can be well fit by a sum of two Lorentzian profiles. From the fit, we determine the resonance positions to be 12.72(1) and 13.15(2) G with full widths of 0.25 and 0.24 G, respectively. Note that due to the levitation gradient field, the inhomogeneity across the molecular sample is as large as 0.15 G in state $|\beta\rangle$, which suggests that the intrinsic widths of these resonances are less than the observed values.

The observed resonances cannot be explained by single-molecule effects based on the Cs_2 energy structure, which is precisely known to very high partial waves [9,10]. Beyond single-molecule effects, the observed resonance structure strongly suggests that bound states of two Cs_2 molecules (Cs_4 tetramer states) are tuned in resonance with the scattering state of the molecules and induce Feshbach-like couplings to inelastic decay channels. Other possible scattering processes, e.g., direct coupling to a trimer and an atom or a dimer and two atoms, should result in a threshold behavior in the loss spectrum instead of the observed resonance structure. For Cs_2 molecules, the appearance of Cs_4 bound states near the scattering continuum is not surprising considering the complexity of interaction between Cs atoms and the additional rotational and vibrational degrees of freedom.

To confirm that the loss is indeed due to collisions between molecules, we observe the decay of the molecular population in the CO_2-laser trap. Starting with 11 000 molecules prepared at different magnetic fields, we record the molecule number after various wait times, as shown in Fig. 4. Three magnetic field values are chosen here: 15.4 G where the molecules are in state $|\alpha\rangle$, 12.1 G where the molecules are in state $|\beta\rangle$ and are away from the resonance, and 12.7 G where the molecules are on the strong molecular resonance; see Fig. 4. The number of trapped molecules shows a nonexponential decay, which provides a clear signature of the density-dependent processes.

To further investigate the underlying molecular collision processes, we model the loss based on a two-body or a three-body loss equation. Assuming a Gaussian distribution for the thermal ensemble in a harmonic trap with a constant temperature and that the collision loss rate is slow compared to the thermalization rate, we fit the measured molecule numbers to the two-body and three-body decay equation; see in Fig. 4. For 15.4 and 12.1 G, we find that the two-body equation provides excellent fits. The two-body

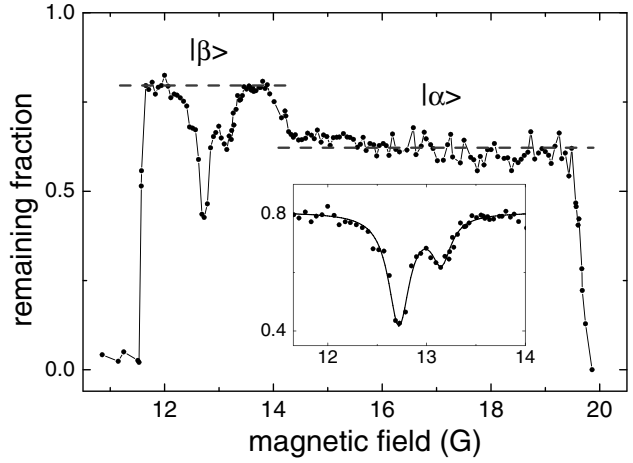

FIG. 3. Remaining fraction of optically trapped molecules after a storage time of 300 ms. Initially, there are 11 000 molecules at a peak density of 6×10^{10} cm^{-3} and a temperature of 250 nK. The dashed lines mark the background loss rates in state $|\alpha\rangle$ and in state $|\beta\rangle$. The two loss resonances for $|\beta\rangle$ are fit by a sum of two Lorentzian profiles (inset).

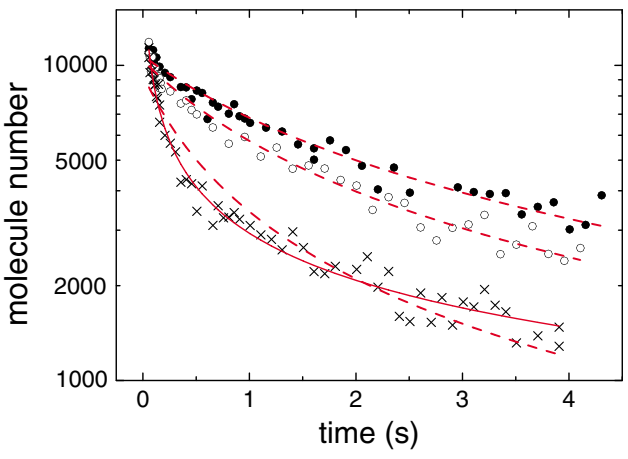

FIG. 4 (color online). Time evolution of the molecule number in the CO_2-laser trap for molecules in state $|\alpha\rangle$ at 15.4 G (open circles), in state $|\beta\rangle$ at 12.1 G (off resonance, solid circles) and at 12.7 G (on resonance, crosses). Fits based on two-body loss (dashed lines) work well for 15.4 and 12.1 G. A fit based on three-body loss (solid line) works better for 12.7 G.

coefficients are 5×10^{-11} cm^3/s at 15.4 G and 3×10^{-11} cm^3/s at 12.1 G. We cannot, however, rule out the possibility that three-body processes also play a role. The measured collision rate coefficients are similar to the measurements from the MIT group on Na_2 [17], and are an order of magnitude below the unitarity limit of $2h/mk = 4 \times 10^{-10}$ cm^3/s, where k is the characteristic collision wave number associated with the temperature of the sample.

At 12.7 G, where the molecules are on the strong resonance, we find that the three-body equation actually provides a better fit than the two-body fit with a three-body loss coefficient at 6×10^{-20} cm^6/s; see Fig. 4. This value, however, is much too high compared to the three-body unitarity limit of $96\pi h/mk^4 = 2 \times 10^{-23}$ cm^6/s [18]. One alternative explanation is that on resonance, the fast collision loss rate might leave the molecules insufficient time to reach thermal equilibrium. By fitting the resonance data in the first 200 ms with the two-body loss model, we determine the two-body loss coefficient to be 2×10^{-10} cm^3/s, which indeed approaches the unitarity limit of 4×10^{-10} cm^3/s.

In conclusion, we have observed magnetically tuned collision resonances in a trapped ultracold sample of Cs_2 dimers. The density-dependent inelastic decay and the resonance structure strongly suggest a resonant coupling to Cs_4 tetramer states. Our observations are reminiscent of Feshbach resonances in atom-atom scattering. The controlled use of such resonances for interaction tuning and molecule formation in atomic ensembles has opened up new avenues in research on ultracold quantum gases. Our observation of magnetically tuned Feshbach-like resonances in molecule-molecule scattering brings in fascinating prospects for a controlled synthesis of ultracold tetramers in a single four-body quantum state in analogy to the formation of ultracold dimers near atomic Feshbach resonances. The tunability of the interactions in molecular quantum gases can potentially open up the door to few-body physics beyond simple atoms and diatomic molecules and to a new ultracold chemistry.

We greatly thank E. Tiesinga and P. S. Julienne for stimulating discussions, and, in particular, for providing us with the theoretical calculation on the Cs_2 energy structure. We acknowledge support by the Austrian Science Fund (FWF) within SFB 15 and the Lise Meitner program, and by the European Union in the frame of the Cold Molecules TMR Network under Contract No. HPRN-CT-2002-00290. M. M. is supported by DOC [Doktorandenprogramm der Österreichischen Akademie der Wissenschaften].

*Present address: Department of Physics and James Franck Institute, University of Chicago, Chicago, IL 60637, USA.

[1] J. Herbig, T. Kraemer, M. Mark, T. Weber, C. Chin, H.-C. Nägerl, and R. Grimm, Science **301**, 1510 (2003).

[2] K. Xu, T. Mukaiyama, J. R. Abo-Shaeer, J. K. Chin, D. E. Miller, and W. Ketterle, Phys. Rev. Lett. **91**, 210402 (2003).

[3] S. Jochim, M. Bartenstein, A. Altmeyer, G. Hendl, S. Riedl, C. Chin, J. Hecker Denschlag, and R. Grimm, Science **302**, 2101 (2003); M. Greiner, C. A. Regal, and D. S. Jin, Nature (London) **426**, 537 (2003); M. W. Zwierlein, C. A. Stan, C. H. Schunck, S. M. F. Raupach, S. Gupta, Z. Hadzibabic, and W. Ketterle, Phys. Rev. Lett. **91**, 250401 (2003).

[4] M. Bartenstein, A. Altmeyer, S. Riedl, S. Jochim, C. Chin, J. Hecker Denschlag, and R. Grimm, Phys. Rev. Lett. **92**, 120401 (2004); C. A. Regal, M. Greiner, and D. S. Jin, Phys. Rev. Lett. **92**, 040403 (2004); M. W. Zwierlein, C. A. Stan, C. H. Schunck, S. M. F. Raupach, A. J. Kerman, and W. Ketterle, Phys. Rev. Lett. **92**, 120403 (2004); T. Bourdel, L. Khaykovich, J. Cubizolles, J. Zhang, F. Chevy, M. Teichmann, L. Tarruell, S. J. J. M. F. Kokkelmans, and C. Salomon, Phys. Rev. Lett. **93**, 050401 (2004).

[5] M. Bartenstein, A. Altmeyer, S. Riedl, R. Geursen, S. Jochim, C. Chin, J. Hecker Denschlag, R. Grimm, A. Simoni, E. Tiesinga, C. J. Williams, and P. S. Julienne, Phys. Rev. Lett. **94**, 103201 (2005); cond-mat/0408673.

[6] J. R. Abo-Shaeer, D. E. Miller, J. K. Chin, K. Xu, T. Mukaiyama, and W. Ketterle, Phys. Rev. Lett. **94**, 040405 (2005).

[7] E. Tiesinga, B. J. Verhaar, and H. T. C. Stoof, Phys. Rev. A **47**, 4114 (1993); S. Inouye, M. Andrews, J. Stenger, H.-J. Miesner, S. Stamper-Kurn, and W. Ketterle, Nature (London) **392**, 151 (1998).

[8] S. Dürr, T. Volz, A. Marte, and G. Rempe, Phys. Rev. Lett. **92**, 020406 (2004).

[9] E. Tiesinga and P. S. Julienne (private communication).

[10] C. Chin, V. Vuletić, A. J. Kerman, S. Chu, E. Tiesinga, P. J. Leo, and C. J. Williams, Phys. Rev. A **70**, 032701 (2004).

[11] F. H. Mies, C. J. Williams, P. S. Julienne, and M. Krauss, J. Res. Natl. Inst. Stand. Technol. **101**, 521 (1996).

[12] C. Chin, A. J. Kerman, V. Vuletić, and S. Chu, Phys. Rev. Lett. **90**, 033201 (2003).

[13] T. Kraemer, J. Herbig, M. Mark, T. Weber, C. Chin, H.-C. Nägerl, R. Grimm, Appl. Phys. B **79**, 1013 (2004).

[14] We adiabatically transfer the atomic BEC from a near-infrared laser trap, where the atomic BEC is formed [13], to the CO_2-laser trap by simultaneously reducing the near-infrared laser power to zero and ramping the CO_2 lasers to full power in 1 s.

[15] T. Weber, J. Herbig, M. Mark, H.-C. Nägerl, and R. Grimm, Science **299**, 232 (2003).

[16] This $l = 8$ state, not shown in Fig. 1, is very weakly coupled to the state $|\beta\rangle$. Investigations on this state are currently in progress.

[17] T. Mukaiyama, J. R. Abo-Shaeer, K. Xu, J. K. Chin, and W. Ketterle, Phys. Rev. Lett. **92**, 180402 (2004).

[18] H. Suno, B. D. Esry, and C. H. Greene, Phys. Rev. Lett. **90**, 053202 (2003).

[19] M. Mark, T. Kraemer, J. Herbig, C. Chin, H.-C. Nägerl, and R. Grimm, Europhys. Lett. **69**, 706 (2005); cond-mat/0409737.

References

[Abe99] F. A. van Abeelen and B. J. Verhaar, *Time-Dependent Feshbach Resonance Scattering and Anomalous Decay of a Na Bose-Einstein Condensate*, Phys. Rev. Lett. **83**, 1550 (1999).

[And95] M. H. Anderson, J. R. Ensher, M. R. Matthews, C. E. Wieman, and E. A. Cornell, *Observation of Bose-Einstein Condensation in a Dilute Atomic Vapor*, Science **269**, 198 (1995).

[And97] M. R. Andrews, C. G. Townsend, H.-J. Miesner, D. S. Durfee, D. M. Kurn, and W. Ketterle, *Observation of Interference Between Two Bose-Einstein Condensates*, Science **275**, 637 (1997).

[Arl98] J. Arlt, P. Bance, S. Hopkins, J. Martin, S. Webster, A. Wilson, K. Zetie, and C. J. Foot, *Suppression of collisional loss from a magnetic trap*, J. Phys. B **31**, L321 (1998).

[Arn97] M. Arndt, M. B. Dahan, D. Guéry-Odelin, M. W. Reynolds, and J. Dalibard, *Observation of a Zero-Energy Resonance in Cs-Cs Collisions*, Phys. Rev. Lett. **79**, 625 (1997).

[Ber01] F. Bertinetto, P. Cordiale, G. Galzerano, and E. Bava, *Frequency Stabilization of DBR Diode Laser Against Cs Absorption Lines at 852 nm Using the Modulation Transfer Method*, IEEE Transactions on Instrumentation and Measurement **50**, 490 (2001).

[Bet00] H. L. Bethlem, G. Berden, F. M. H. Crompvoets, R. T. Jongma, A. J. A. van Roij, and G. Meijer, *Electrostatic trapping of ammonia molecules*, Nature **406**, 491 (2000).

[BIP98] BIPM, *Le System Interational d'Unites (SI)*, Tech. rep., Bureau International des Poids at Measures, Sevres, France (1998).

[Bog47] N. Bogoliubov, *On the theory of superfluidity*, J. Phys. **11**, 23 (1947).

[Bon02] K. Bongs and K. Sengstock, *Introduction to Bose-Einstein Condensation*, in: M. Weidemüller and C. Zimmermann (Eds.), *Interactions in Ultracold Gases*, Wiley-VCH, Weinheim, 2002.

[Bos24] S. Bose, *Plancks Gesetz und Lichtquantenhypothese*, Z. Phys. **26**, 178 (1924).

[Bou82] M. Bouchiat, J. Guena, L. Hunter, and L. Pottier, *Observation of a parity violation in cesium*, Physics Letters B **117**, 358 (1982).

[Bra95] C. C. Bradley, C. A. Sackett, J. J. Tollett, and R. G. Hulet, *Evidence of Bose-Einstein Condensation in an Atomic Gas with Attractive Interactions*, Phys. Rev. Lett. **75**, 1687 (1995), *ibid.* **79**, 1170 (1997).

[Bur99] S. Burger, K. Bongs, S. Dettmer, W. Ertmer, K. Sengstock, A. Sanpera, G. V. Shlyapnikov, and M. Lewenstein, *Dark Solitons in Bose-Einstein Condensates*, Phys. Rev. Lett. **83**, 5198 (1999).

[Cas96] Y. Castin and R. Dum, *Bose-Einstein Condensates in Time-Dependent Traps*, Phys. Rev. Lett. **77**, 5315 (1996).

[Che02] F. Chevy, V. Bretin, P. Rosenbusch, K. W. Madison, and J. Dalibard, *Transverse Breathing Mode of an Elongated Bose-Einstein Condensate*, Phys. Rev. Lett. **88**, 250402 (2002).

[Chi00] C. Chin, V. Vuletic, A. J. Kerman, and S. Chu, *High Resolution Feshbach Spectroscopy of Cesium*, Phys. Rev. Lett. **85**, 2717 (2000).

[Chi01a] C. Chin, *Cooling, Collisions and Coherence of Cold Cesium Atoms in a Trap*, Ph.D. thesis, Stanford University (2001).

[Chi01b] C. Chin, V. Leiber, V. Vuletić, A. J. Kerman, and S. Chu, *Measurement of an electron's electric dipole moment using Cs atoms trapped in optical lattices*, Phys. Rev. A **63**, 033401 (2001).

[Chi03a] C. Chin and R. Grimm, *Thermal equilibrium and efficient evaporation of an ultracold atom-molecule mixture*, Phys. Rev. A **69**, 033612 (2003), submitted for publication.

[Chi03b] C. Chin, A. J. Kerman, V. Vuletic, and S. Chu, *Sensitive Detection of Cold Cesium Molecules Formed on Feshbach Resonances*, Phys. Rev. Lett. **90**, 033201 (2003).

[Chi04] C. Chin, V. Vuletic, A. J. Kerman, S. Chu, E. Tiesinga, P. J. Leo, and C. J. Williams, *Precision Feshbach spectroscopy of ultracold Cs_2*, Phys. Rev. A **70**, 032701 (2004), doi:10.1103/PhysRevA.70.032701.

[Chi05] C. Chin, T. Kraeme, M. Mark, J. Herbig, P. Waldburger, H.-C. Nägerl, and R. Grimm, *Observation of Feshbach-like resonances in collisions between ultracold molecules*, Phys. Rev. Lett. **94**, 123201 (2005), doi:10.1103/PhysRevLett.94.123201.

[Chu86] S. Chu, J. E. Bjorkholm, A. Ashkin, and A. Cable, *Experimental Observation of Optically Trapped Atoms*, Phys. Rev. Lett. **57**, 314 (1986).

[Cor98] K. L. Corwin, Z.-T. Lu, C. F. Hand, R. J. Epstein, and C. E. Wieman, *Frequency-stabilized diode laser with Zeeman shift in an atomic vapor*, Appl. Opt. **37**, 3295 (1998).

[Cor99] E. A. Cornell, J. R. Ensher, and C. E. Wieman, *Experiments in dilute atomic Bose-Einstein condensation*, in: M. Inguscio, S. Stringari, and C. E. Wieman (Eds.), *Proceedings of the International School of Physics - Enrico Fermi*, 15, IOS Press, 1999, arXiv:cond-mat/9903109.

[Cor00] S. L. Cornish, N. R. Claussen, J. L. Roberts, E. A. Cornell, and C. E. Wieman, *Stable ^{85}Rb Bose-Einstein Condensates with Widely Tunable Interactions*, Phys. Rev. Lett. **85**, 1795 (2000).

[Cor02] E. A. Cornell and C. E. Wieman, *Nobel Lectures in Physics 2001*, Rev. Mod. Phys. **74**, 875 (2002).

[Cub03] J. Cubizolles, , T. Bourdel, S. J. J. M. F. Kokkelmans, G. V. Shlyapnikov, and C. Salomon, *Production of Long-Lived Ultracold Li2 Molecules from a Fermi Gas*, Phys. Rev. Lett. **91**, 240401 (2003).

[Dal97] F. Dalfovo, C. Minniti, S. Stringari, and L. Pitaevskii, *Nonlinear dynamics of a Bose condensed gas*, Phys. Lett. A **227**, 259 (1997).

[Dal99a] F. Dalfovo, *Dynamics of trapped Bose-condensed gases in mean-field theory*, in: M. Inguscio, S. Stringari, and C. E. Wieman (Eds.), *Proceedings of the International School of Physics - Enrico Fermi*, 555, IOS Press, 1999.

[Dal99b] F. Dalfovo, S. Giorgini, L. P. Pitaevskii, and S. Stringari, *Theory of Bose-Einstein condensation in trapped gases*, Rev. Mod. Phys. **71**, 463 (1999), arXiv:cond-mat/9806038.

[Dal99c] J. Dalibard, *Collisional dynamics of ultra-cold atomic gases*, in: M. Inguscio, S. Stringari, and C. E. Wieman (Eds.), *Proceedings of the International School of Physics - Enrico Fermi*, 321, IOS Press, 1999.

[Dav95a] K. B. Davis, M.-O. Mewes, M. R. Andrews, N. J. van Druten, D. S. Durfee, D. M. Kurn, and W. Ketterle, *Bose-Einstein Condensation in a Gas of Sodium Atoms*, Phys. Rev. Lett. **75**, 3969 (1995).

[Dav95b] K. B. Davis, M.-O. Mewes, and W. Ketterle, *An analytical model for evaporative cooling of atoms*, Appl. Phys. B **60**, 155 (1995).

[DeM02] D. DeMille, *Quantum Computation with Trapped Polar Molecules*, Phys. Rev. Lett. **88**, 067901 (2002), doi:10.1103/PhysRevLett.88.067901.

[Den99] L. Deng, E. W. Hagley, J. Wen, M. Trippenbach, Y. Band, P. S. Julienne, J. E. Simsarian, K. Helmerson, S. L. Rolston, and W. D. Phillips, *Four-wave mixing with matter waves*, Nature **398**, 218 (1999).

[Den00] J. Denschlag, J. E. Simsarian, D. L. Feder, C. W. Clark, L. A. Collins, J. Cubizolles, L. Deng, E. W. Hagley, K. Helmerson, W. P. Reinhardt, S. L. Rolston, B. I. Schneider, and W. D. Phillips, *Generating Solitons by Phase Engineering of a Bose-Einstein Condensate*, Science **287**, 97 (2000).

[Don02] E. A. Donley, N. R. Claussen, S. T. Thompson, and C. E. Wieman, *Atom-molecule coherence in a Bose-Einstein condensate*, Nature **417**, 529 (2002).

[Dür04a] S. Dürr, T. Volz, , and G. Rempe, *Dissociation of ultracold molecules with Feshbach resonances*, Phys. Rev. A **70**, 031601(R) (2004).

[Dür04b] S. Dürr, T. Volz, A. Marte, and G. Rempe, *Observation of Molecules Produced from a Bose-Einstein Condensate*, Phys. Rev. Lett. **92**, 020406 (2004).

[Ein25] A. Einstein, *Quantentheorie des einatomigen idealen Gases. Zweite Abhandlung*, Sitzungber. Preuss. Akad. Wiss. **1925**, 3 (1925).

[Eng00] H. Engler, *A quasi-electrostatic trap for neutral atoms*, Ph.D. thesis, Ruprecht-Karls-Universität Heidelberg (2000).

[Fes62] H. Feshbach, *A Unified Theory of Nuclear Reactions. II*, Ann. Phys. **19**, 287 (1962).

[Fri98] D. G. Fried, T. C. Killian, L. Willmann, D. Landhuis, S. C. Moss, D. Kleppner, and T. J. Greytak, *Bose-Einstein Condensation of Atomic Hydrogen*, Phys. Rev. Lett. **81**, 3811 (1998).

[GO98] D. Guéry-Odelin, J. Söding, P. Desbiolles, and J. Dalibard, *Is Bose-Einstein condensation of atomic cesium possible?*, Europhys. Lett. **44**, 26 (1998).

[Gór02] K. Góral, L. Santos, and M. Lewenstein, *Quantum Phases of Dipolar Bosons in Optical Lattices*, Phys. Rev. Lett. **88**, 170406 (2002).

[Gre02] M. Greiner, O. Mandel, T. Esslinger, T. W. Hänsch, and I. Bloch, *Quantum phase transition from a superfluid to a Mott insulator in a gas of ultracold atoms*, Nature **415**, 39 (2002).

[Gri] A. Griesmaier, J. Werner, S. Hensler, J. Stuhler, and T. Pfau, *Bose-Einstein condensation of chromium*, arXiv:cond-mat/0503044 .

[Gri00] R. Grimm, M. Weidemüller, and Y. Ovchinnikov, *Optical dipole traps for neutral atoms*, Adv. At. Mol. Opt. Phys. **42**, 95 (2000), arXiv:physics/9902072.

[Gro61] E. P. Gross, *Structure of a Quantized Vortex in Boson Systems*, Il Nuovo Cimento **20**, 454 (1961).

[Gry93] G. Grynberg, B. Lounis, P. Verkerk, J. Courtois, and C. Salomon, *Quantized motion of cold cesium atoms in two- and three-dimensional optical potentials*, Phys. Rev. Lett. **70**, 2249 (1993).

[Gup02] S. Gupta, K. Dieckmann, Z. Hadzibabic, and D. E. Pritchard, *Contrast Interferometry using Bose-Einstein Condensates to Measure h/m and alpha*, Phys. Rev. Lett. **89**, 140401 (2002).

[Ham02] M. Hammes, *Optical Surface Microtraps based on Evanescent Waves*, Ph.D. thesis, Universität Innsbruck (2002).

[Han01] D. J. Han, M. T. DePue, and D. Weiss, *Loading and compressing Cs atoms in a very far-off-resonant light trap*, Phys. Rev. A **63**, 023405 (2001).

[Hei00] D. J. Heinzen, R. Wynar, P. D. Drummond, and K. V. Kheruntsyan, *Superchemistry: Dynamics of Coupled Atomic and Molecular Bose-Einstein Condensation*, Phys. Rev. Lett. **84**, 5029 (2000).

[Hen00] J. Hensley, A. Whicht, B. Young, and S. Chu, *Progress towards a Measurement of h/M*, in: E. Arimondo, P. D. Natale, and M. Inguscio (Eds.), *Proc. 17th Int. Conf. Atomic Physics*, 43–57, AIP, Melville, New York, 2000.

[Her03] J. Herbig, T. Kraemer, M. Mark, T. Weber, C. Chin, H.-C. Nägerl, and R. Grimm, *Preparation of a Pure Molecular Quantum Gas*, Science **301**, 1510 (2003), published online 21 Aug 2003 (doi:10.1126/science.1088876).

[Hes86] H. F. Hess, *Evaporative cooling of magnetically trapped and compressed spin-polarized hydrogen*, Phys. Rev. B **34**, 3476 (1986).

[Hol97] M. J. Holland, D. S. Jin, M. L. Chiofalo, and J. Cooper, *Emergence of Interaction Effects in Bose-Einstein Condensation*, Phys. Rev. Lett. **78**, 3801 (1997).

[Hop00] S. A. Hopkins, S. Webster, J. Arlt, P. Bance, S. Cornish, O. Maragò, and C. J. Foot, *Measurement of elastic cross section for cold cesium collisions*, Phys. Rev. A **61**, 032707 (2000).

[Ino98] S. Inouye, M. R. Andrews, J. Stenger, H.-J. Miesner, D. M. Stamper-Kurn, and W. Ketterle, *Observation of Feshbach resonances in a Bose-Einstein condensate*, Nature **392**, 151 (1998).

[Jak98] D. Jaksch, C. Bruder, J. I. Cirac, C. W. Gardiner, and P. Zoller, *Cold Bosonic Atoms in Optical Lattices*, Phys. Rev. Lett. **81**, 3108 (1998).

[Joc03] S. Jochim, M. Bartenstein, A. Altmeyer, G. Hendl, C. Chin, J. H. Denschlag, and R. Grimm, *Pure Gas of Optically Trapped Molecules Created from Fermionic Atoms*, Phys. Rev. Lett. **91**, 240402 (2003).

[Jul02] P. S. Julienne, *Cold collision basics: Threshold phenomena*, Talk at the university of Innsbruck (2002).

[Jul03] P. Julienne and E. Tiesinga, *private comunication* (2003).

[Kag96] Y. Kagan, E. L. Surkov, and G. V. Shlyapnikov, *Evolution of a Bose-condensed gas under variations of the confining potential*, Phys. Rev. A **54**, R1753 (1996).

[Kag97] Y. Kagan, E. L. Surkov, and G. V. Shlyapnikov, *Evolution and Global Collapse of Trapped Bose Condensates under Variations of the Scattering Length*, Phys. Rev. Lett. **79**, 2604 (1997).

[Kas95] M. Kasevich, H. J. Lee, C. Adams, and S. Chu, *Optical traps for ultracold atoms*, in: M. Inguscio, M. Allegrini, and A. Sasso (Eds.), *Laser Spectroscopy, XII International Conference*, 13, World Scientific, 1995.

[Ker00] A. J. Kerman, V. Vuletić, C. Chin, and S. Chu, *Beyond Optical Molasses: 3D Raman Sideband Cooling of Atomic Cesium to High Phase-Space Density*, Phys. Rev. Lett. **84**, 439 (2000).

[Ket96] W. Ketterle and N. J. van Druten, *Evaporative Cooling of Trapped Atoms*, Adv. At. Mol. Opt. Phys. **37**, 181 (1996).

[Ket99] W. Ketterle, D. S. Durfee, and D. M. Stamper-Kurn, *Making, probing and understanding Bose-Einstein condensates*, in: M. Inguscio, S. Stringari, and C. E. Wieman (Eds.), *Proceedings of the International School of Physics - Enrico Fermi*, 67, IOS Press, 1999, arXiv:cond-mat/9904034.

[Ket02] W. Ketterle, *Nobel lecture: When atoms behave as waves: Bose-Einstein condensation and the atom laser*, Rev. Mod. Phys. **74**, 1131 (2002).

[Kha02] L. Khaykovich, F. Schreck, G. Ferrari, T. Bourdel, J. Cubizolles, L. D. Carr, Y. Castin, and C. Salomon, *Formation of a Matter-Wave Bright Soliton*, Science **296**, 1290 (2002).

[Kok01] S. J. J. M. F. Kokkelmans, H. M. J. Vissers, and B. J. Verhaar, *Formation of a Bose condensate of stable molecules via a Feshbach resonance*, Phys. Rev. A **63**, 031601(R) (2001).

[Kot00] S. Kotochigova, E. Tiesinga, and P. S. Julienne, *Relativistic ab initio treatment of the second-order spin-orbit splittin of the $a^3\Sigma_u^+$ potential of rubidium and cesium dimers*, Phys. Rev. A **63**, 012517 (2000), doi:10.1103/PhysRevA.63.012517.

[Kra04] T. Kraemer, J. Herbig, M. Mark, T. Weber, and C. Chin, *Optimized production of a cesium Bose-Einstein condensate*, Appl. Phys. B **79**, 1013 (2004), arXiv:cond-mat/0408268.

[Lan77] L. D. Landau and E. M. Lifshitz, *Quantum Mechanics: Non-Relativistic Theory*, Pergamon Press, Oxford, 1977, 3rd ed.

[Leo98] P. J. Leo, E. Tiesinga, P. S. Julienne, D. K. Walter, S. Kadlecek, and T. G. Walker, *Elastic and Inelastic Collisions of Cold Spin-Polarized* ^{133}*Cs Atoms*, Phys. Rev. Lett. **81**, 1389 (1998).

[Leo00] P. J. Leo, C. J. Williams, and P. S. Julienne, *Collision Properties of Ultracold* ^{133}*Cs Atoms*, Phys. Rev. Lett. **85**, 2721 (2000).

[Lid97] D. R. Lide (Ed.), *Handbook of Chemistry and Physics*, CRC Press, 1997, 78th ed.

[Mac05] M. Mackie, *Coherent Population Trapping in a Feshbach-Resonant* ^{1}33*Cs Condensate*, arXiv:cond-mat/0502269 (2005).

[Mad00] K. W. Madison, F. Chevy, W. Wohlleben, and J. Dalibard, *Vortex Formation in a Stirred Bose-Einstein Condensate*, Phys. Rev. Lett. **84**, 806 (2000).

[Man99] I. Manek, *Gravito-optical Surface Trap for Cesium Atoms*, Ph.D. thesis, Ruprecht-Karls Universität, Heidelberg (1999).

[Mar02] A. Marte, T. Volz, J. Schuster, S. Dürr, G. Rempe, E. G. M. van Kempen, and B. J. Verhaar, *Feshbach Resonances in Rubidium 87: Precision Measurements and Analysis*, Phys. Rev. Lett. **89**, 283202 (2002).

[Mar03a] M. Mark, *Bose-Einstein-Kondensation von Cäsium*, Diploma thesis, Universität Innsbruck (2003).

[Mar03b] A. Marte, *Feshbach-Resonanzen bei Stößen ultrakalter Rubidium atome*, Coordinator: G. rempe, Technische Universität München, Max-Planck-Institut für Quantenoptik (2003).

[Mar04] H. Marion, S. Bize, L. Cacciapuoti, D. Chambon, F. P. D. Santos, G. Santarelli, P. Wolf, A. Clairon, A. Luiten, M. Tobar, S. Kokkelmans, and C. Salomon, *First observation of Feshbach resonances at very low magnetic field in a* ^{133}*Cs fountain*, arXiv:physics/0407064 (2004).

[Mar05] M. Mark, T. Kraemer, J. Herbig, C. Chin, H.-C. Nägerl, and R. Grimm, *Effcient creation of molecules from a cesium Bose-Einstein condensate*, Europhysics Letters **69** (2005), submitted, arXiv:cond-mat/0409737, doi:10.1209/epl/i2004-10427-7.

[Mat99] M. R. Matthews, B. P. Anderson, P. C. Haljan, D. S. Hall, C. E. Wieman, and E. A. Cornell, *Vortices in a Bose-Einstein Condensate*, Phys. Rev. Lett. **83**, 2498 (1999).

[Met99] H. J. Metcalf and P. van der Straten, *Laser cooling and trapping*, Springer-Verlag, New York, 1999.

[Mew96] M.-O. Mewes, M. R. Andrews, N. J. van Druten, D. M. Kurn, D. S. Durfee, and W. Ketterle, *Bose-Einstein Condensation in a Tightly Confining dc Magnetic Trap*, Phys. Rev. Lett. **77**, 416 (1996).

[Mew97] M.-O. Mewes, M. R. Andrews, D. M. Kurn, D. S. Durfee, C. G. Townsend, and W. Ketterle, *Output Coupler for Bose-Einstein Condensed Atoms*, Phys. Rev. Lett. **78**, 582 (1997).

[Mie96] F. H. Mies, C. J. Williams, P. S. Julienne, and M. Krauss, *Estimating Bounds on Collisional Relaxation Rates of Spin-Polarized ^{87}Rb Atoms at Ultracold Temperatures*, J. Res. Natl. Inst. Stand. Tech. **101**, 521 (1996).

[Mie00] F. H. Mies, E. Tiesinga, and P. S. Julienne, *Manipulation of Feshbach resonances in ultracold atomic collisions using time-dependent magnetic fields*, Phys. Rev. A **61**, 022721 (2000).

[Mil93] J. D. Miller, R. A. Cline, and D. J. Heinzen, *Far-off-resonance optical trapping of atoms*, Phys. Rev. A **47**, R4567 (1993).

[Mod01] G. Modugno, G. Ferrari, G. Roati, R. J. Brecha, A. Simoni, and M. Inguscio, *Bose-Einstein Condensation of Potassium Atoms by Sympathetic Cooling*, Science **294**, 1320 (2001).

[Mos99] U. Moslener, *Weiterentwicklung der gravitooptischen Oberflächenfalle (GOST)*, Diploma thesis, Universität Heidelberg and Max-Planck-Institut für Kernphysik (1999).

[Muk04] T. Mukaiyama, J. R. Abo-Shaeer, K. Xu, J. K. Chin, and W. Ketterle, *Dissociation and Decay of Ultracold Sodium Molecules*, Phys. Rev. Lett. **92**, 180402 (2004).

[Näg03] H.-C. Nägerl, *Verstimmbare Quantenmaterie für Präzisionsmessungen*, Presseaussendung, FWF, Der Wissenschaftsfond **START-Preis 2003** (2003), http://www.fwf.ac.at/de/press/naegerl.html.

[Nat02] *Nature Insight on Ultracold Matter*, Nature **418**, 205 (2002).

[Pet02] C. J. Pethick and H. Smith, *Bose-Einstein Condensation in Dilute Gases*, Cambridge University Press, 2002.

[Phi82] W. Phillips and H. Metcalf, *Laser Decelaration of an Atomic Beam*, Phys. Rev. Lett. **48**, 596 (1982).

[Pit61] L. P. Pitaevskii, *Vortex lines in an imperfect Bose gas*, Sov. Phys. JETP **13**, 451 (1961).

[Pit99] L. P. Pitaevskii, *Trapped Bose-Einstein condensed gas: mean-field approximation and beyond*, in: M. Inguscio, S. Stringari, and C. E. Wieman (Eds.), *Proceedings of the International School of Physics - Enrico Fermi*, 287, IOS Press, 1999.

[Pit03] L. Pitaevskii and S. Stringari, *Bose-Einstein Condensation*, International Series of Monographs on Physics 116, Oxford University Press, 2003.

[Raa87] E. L. Raab, M. Prentiss, A. Cable, S. Chu, and D. E. Pritchard, *Trapping of Neutral Sodium Atoms with Radiation Pressure*, Phys. Rev. Lett. **59**, 2631 (1987).

[Rad04] L. Radzihovsky and J. Park, *Superfluid Transitions in Bosonic Atom-Molecule Mixtures near a Feshbach Resonance*, Phys. Rev. Lett. **92**, 160402 (2004), doi:10.1103/PhysRevLett.92.160402.

[Raj79] R. K. Raj, D. Bloch, J. J. Sydner, G. Camy, and M. Ducloy, *High-Frequency Optically Heterodyned Saturation Spectroscopy Via Resonant Degenerate Four-Wave Mixing*, Phys. Rev. Lett. **32**, 145 (1979).

[Reg03] C. A. Regal, C. Ticknor, J. L. Bohn, and D. S. Jin, *Creation of ultracold molecules from a Fermi gas of atoms*, Nature **424**, 47 (2003).

[Ric95] L. Ricci, M. Weideüeller, T. Esslinger, A. Hemmerich, C. Zimmermann, V. Vuletic, W. König, and T. Hänsch, *A compact grating-stabilized diode laser system for atomic physics*, Opt. Comm. **117**, 541 (1995).

[Rob00] J. L. Roberts, N. R. Claussen, S. L. Cornish, and C. E. Wieman, *Magnetic Field Dependence of Ultracold Inelastic Collisions near a Feshbach Resonance*, Phys. Rev. Lett. **85**, 728 (2000).

[Rob01] A. Robert, O. Sirjean, A. Browaeys, J. Poupard, S. Nowak, D. Boiron, C. I. Westbrook, and A. Aspect, *A Bose-Einstein Condensate of Metastable Atoms*, Science **292**, 461 (2001).

[Rom04] M. W. J. Romans, R. A. Duine, S. Sachdev, and H. T. C. Stoof, *Quantum Phase Transition in an Atomic Bose Gas with a Feshbach Resonance*, Phys. Rev. Lett. **93**, 020405 (2004), doi:10.1103/PhysRevLett.93.02040.

[Rup95] P. A. Ruprecht, M. J. Holland, K. Burnett, and M. Edwards, *Time-dependent solution of the nonlinear Schrödinger equation for Bose-condensed trapped neutral atoms*, Phys. Rev. A **51**, 4704 (1995).

[Ryc04] D. Rychtarik, B. Engeser, H.-C. Nägerl, and R. Grimm, *Two-Dimensional Bose-Einstein Condensate in an Optical Surface Trap*, Rhys. Rev. Lett. **92**, 173003 (2004), doi:10.1103/PhysRevLett.92.173003.

[Sak94] J. J. Sakurai, *Modern Quantum Mechanics*, Addison-Wesley, 1994, revised ed.

[SK98] D. M. Stamper-Kurn, H.-J. Miesner, A. P. Chikkatur, S. Inouye, J. Stenger, and W. Ketterle, *Reversible Formation of a Bose-Einstein Condensate*, Phys. Rev. Lett. **81**, 2194 (1998).

[Sna98] M. J. Snadden, J. M. McGuirk, P. Bouyer, K. G. Haritos, and M. A. Kasevich, *Measurement of the Earth's Gravity Gradient with an Atom Interferometer-Based Gravity Gradiometer*, Phys. Rev. Lett. **81**, 971 (1998).

[Söd98] J. Söding, D. Guéry-Odelin, P. Desbiolles, G. Ferrari, and J. Dalibard, *Giant Spin Relaxation of an Ultracold Cesium Gas*, Phys. Rev. Lett. **80**, 1869 (1998).

[Spi89] N. Spies, (unpublished), Universität Kaiserslautern, Fachbereich Chemie (1989).

[Ste02] D. A. Steck, *Cesium D Line Data*, `http://steck.us/alkalidata` , revision 1.5 (2002).

[Stö04] T. Stöferle, H. Moritz, C. Schori, M. Köhl, and T. Esslinger, *Transition from a Strongly Interacting 1D Superfluid to a Mott Insulator*, Phys. Rev. Lett. **92**, 130403 (2004).

[Tak95] T. Takekoshi, J. R. Yeh, and R. J. Knize, *Quasi-electrostatic trap for neutral atoms*, Opt. Commun. **114**, 421 (1995).

[Tak98] T. Takekoshi, B. M. Patterson, and R. J. Knize, *Observation of Optically Trapped Cold Cesium Molecules*, Phys. Rev. Lett. **81**, 5105 (1998).

[Tak03] Y. Takasu, K. Maki, K. Komori, T. Takano, K. Honda, M. Kumakura, T. Yabuzaki, and Y. Takahashi, *Spin-Singlet Bose-Einstein Condensation of Two-Electron Atoms*, Phys. Rev. Lett. **91**, 040404 (2003).

[Tar92] V. Tarnovsky, M. Bunimovicz, L. Vuskovic, B. Stumpf, and B. Bederson, *Measurements of the dc electric dipole polarizabilities of the alkali dimer molecules, homonuclear and heteronuclear*, The Journal of Chemical Physics **98**, 3894 (1992), doi:10.1063/1.464017.

[Tha01] G. Thalhammer, *Frequenzstabilisierung von Diodenlasern bei 850, 854 und 866 nm mit Linienbreiten im Kilohertz-Bereich*, Diploma thesis, Universität Innsbruck (2001).

[Tho03] A. M. Thomas, S. Hopkins, S. L. Cornish, and C. J. Foot, *Strong evaporative cooling towards Bose-Einstein condensation of a magnetically trapped caesium gas*, J. Opt. B: Quantum Semiclass. Opt. **5**, S107 (2003).

[Thr93] Threshold and resonance phenomena in ultracold ground-state collisions, *E. Tiesinga and B.J. Verhaar and H. T. C. Stoof*, Phys. Rev. A **47**, 4114 (1993).

[Tie92] E. Tiesinga, A. Moerdijk, B. J. Verhaar, and H. T. C. Stoof, *Conditions for Bose-Einstein condensation in magnetically trapped atomic cesium*, Phys. Rev. A **46**, R1167 (1992).

[Tie01] E. Tiesinga, C. J. Williams, F. H. Mies, and P. S. Julienne, *Interacting atoms under strong quantum confinement*, Phys. Rev. A **61**, 063416 (2001).

[Tie04] E. Tiesinga, (private communication) (2004).

[Tim99] E. Timmermans, P. Tommasini, R. Côté, M. Hussein, and A. Kerman, *Rarified Liquid Properties of Hybrid Atomic-Molecular Bose-Einstein Condensates*, Phys. Rev. Lett. **83**, 2691 (1999).

[Tre01] P. Treutlein, K. Y. Chung, and S. Chu, *High-brightness atom source for atomic fountains*, Phys. Rev. A **63**, 051401 (2001).

[Van02] N. Vanhaecke, W. de Souza Melo, B. L. Tolra, D. Comparat, and P. Pillet, *Accumulation of Cold Cesium Molecules via Photoassociation in a Mixed Atomic and Molecular Trap*, Phys. Rev. Lett **89**, 063001 (2002).

[Vol04] T. Volz, S. Dürr, N. Syassen, and G. Rempe, *Tuning a Feshbach Resonance through a Shape Resonance in the Dissociation of Ultracold Molecules*, arXiv:cond-mat/0410083 (2004).

[Vul99] V. Vuletić, A. J. Kerman, C. Chin, and S. Chu, *Observation of Low-Field Feshbach Resonances in Collisions of Cesium Atoms*, Phys. Rev. Lett. **82**, 1406 (1999).

[Web00] T. Weber, *Langzeitspeicherung verschiedener atomarer Spezies in einer quasi-elektrostatischen Dipolfalle*, Diploma thesis, Ruprecht-Karls-Universität Heidelberg (2000).

[Web03a] T. Weber, *Bose-Einstein Condensation of Optically Trapped Cesium*, Ph.D. thesis, University of Innsbruck, University of Innsbruck, Technikerstrasse 25/4, 6020 Innsbruck, Austria (2003).

[Web03b] T. Weber, J. Herbig, M. Mark, H.-C. Nägerl, and R. Grimm, *Bose-Einstein Condensation of Cesium*, Science **299**, 232 (2003), published online 5 Dec 2002 (doi:10.1126/science.1079699).

[Web03c] T. Weber, J. Herbig, M. Mark, H.-C. Nägerl, and R. Grimm, *Three-body recombination at large scattering lengths in an ultracold atomic gas*, Phys. Rev. Lett. **91**, 123201 (2003), doi:10.1103/PhysRevLett.91.123201.

[Wei98] J. D. Weinstein, R. deCarvalho, T. Guillet, B. Friedrich, and J. M. Doyle, *Magnetic trapping of calcium monohydride molecules at millikelvin temperatures*, Nature **395**, 148 (1998).

[Wei02] D. S. Weiss, private communication (2002).

[Win84] W. Wing, *On Neutral Particle Trapping in Quasielectrostatic Electromagnetic Fields*, Prog. Quant. Elect. **8**, 181 (1984).

[Wyn00] R. Wynar, R. S. Freeland, D. J. Han, C. Ryu, and D. J. Heinzen, *Molecules in a Bose-Einstein Condensate*, Science **287**, 1016 (2000).

[Xu03] K. Xu, T. Mukaiyama, J. R. Abo-Shaeer, J. K. Chin, D. E. Miller, and W. Ketterle, *Formation of Quantum-Degenerate Sodium Molecules*, Phys. Rev. Lett. **91**, 210402 (2003).

[Yur00] V. A. Yurovsky, A. Ben-Reuven, P. S. Julienne, and C. J. Williams, *Atom loss and the formation of a molecular Bose-Einstein condensate by Feshbach resonance*, Phys. Rev. A **62**, 043605 (2000).

Dankeschön

Die Kriterien zur Auswahl meiner Doktorarbeit waren eine angenehme Gruppenatmosphäre, ein Projekt mit Potential, eine gute Betreuung und eine ansprechende Umgebung. All das wurde in Innsbruck mehr als erfüllt.

Ich möchte mich daher als erstes bei Rudi bedanken, der mich in seine Gruppe aufgenommen hat. Sein Interesse an unserem Experiment war mir stets ein Ansporn. Sein Wissen und seine Intuition haben entscheident zum Erfolg des Experiments beigetragen. Er hatte immer den richtigen Riecher, wenn große Durchbrüche zu erwarten waren und stand uns sogar bis in die frühen Morgenstunden zur Seite.

Tino hat die Grundsteine des Experiments gelegt. Es ist seiner umsichtigen Planung und seinem technischen Geschick zu verdanken, dass wir in Rekordzeit ein robustes und erfolgreiches Experiment aufgebaut haben. Mit ihm zu arbeiten hat immer viel Spaß gemacht. Zusammen haben wir die Höhen und Tiefen des Forscherlebens überwunden. Ich habe ihm vieles zu verdanken, als Kollege und als Freund.

Hanns-Christoph hat als Assistent das Experiment von Anfang an betreut und es tatkräftig unterstützt. Dank seiner fundierten Erfahrung waren viele Probleme schneller gelöst als sie auftauchten.

Michael und Tobias, die zweite Generation am Experiment, haben die gute Arbeit und die prima Stimmung im Labor fortgesetzt.

Cheng, der über ein Jahr Gastwissenschaftler bei uns war, hat das Experiment ständig mit neuen Ideen versorgt. Durch sein tiefes Verständnis der experimentellen und theoretischen Aspekte des Experiments war er für uns ein wandelndes Nachschlagewerk für physikalische Fragen.

Markus H. hat mich am Anfang an der GOST in die hohe Kunst der Quantenoptik eingeweiht. Er und die anderen Männern der ersten Stunde haben die Grundsteine für eine großartige Gruppe gelegt.

Mit Matthias das Büro zu teilen, war schon vor Innsbruck eine gute Idee. Er hat mit mir den Frust des Zusammenschreibens geteilt und mit kritischen Fragen meine Wissenslücken ausgeleuchtet. Stefan „Stiegl“, der Dritte im Büro, war immer für einen Schmäh und anregende Diskussionen gut.

Der ganzen Gruppe danke ich für eine sehr angenehme und inspirierende Arbeitsatmospäre, unterhaltsame Diskussionen beim Kaffeetrinken und eine sehr schöne Zeit im Institut und außerhalb. Bei Christine, den „SFB Ladies“ und der Werkstatt möchte ich mich bedanken, dass sie uns mit ihrer kompetent Arbeit zur Seite standen.

Meine Eltern haben mich während meiner ganzen Studienzeit unterstützt. Dieser Rückhalt gab mir viel Kraft.

Danke, Gavin und dem Rest der „Bagage“ für viel Spaß in der Vergangenheit und auch in der Zukunft und meiner WG, die sich oft geändert hat, aber immer super war.

Und ich danke Patty, die mich durch Höhen und Tiefen begleitet und mir beigebracht hat, dass man die „Moleküle auch mal rasen lassen soll“.